Astrophysikalisches Institut Potsdam

The role of binary stars in searches for extrasolar planets by microlensing and astrometry

by

Dijana Dominis

A thesis submitted in partial fulfillment of the requirements
for the degree of
Doctor Rerum Naturalium
in Astrophysics
at the Mathematisch-Naturwissenschaftliche Fakultät
der Universität Potsdam

Potsdam, July 2006

Abstract

When Galactic microlensing events of stars are observed, one usually measures a symmetric light curve corresponding to a single lens, or an asymmetric light curve, often with caustic crossings, in the case of a binary lens system. In principle, the fraction of binary stars at a certain separation range can be estimated based on the number of measured microlensing events. However, a binary system may produce a light curve which can be fitted well as a single lens light curve, in particullary if the data sampling is poor and the errorbars are large. We investigate what fraction of microlensing events produced by binary stars for different separations may be well fitted by and hence misinterpreted as single lens events for various observational conditions. We find that this fraction strongly depends on the separation of the binary components, reaching its minimum at between $0.6R_E$ and $1.0R_E$, where it is still of the order of 5% (R_E is the Einstein radius, corresponding to few A.U. for typical Galactic microlensing scenarios). The rate for misinterpretation is higher for short microlensing events lasting up to few months and events with smaller maximum amplification. For fixed separation it increases for binaries with more extreme mass ratios.

Problem of degeneracy in photometric light curve solution between binary lens and binary source microlensing events was studied on simulated data, and data observed by the PLANET collaboration. The fitting code BISCO using the PIKAIA genetic algorithm optimizing routine was written for optimizing binary-source microlensing light curves observed at different sites, in I, R and V photometric bands. Tests on simulated microlensing light curves show that BISCO is successful in finding the solution to a binary-source event in a very wide parameter space. Flux ratio method is suggested in this work for breaking degeneracy between binary-lens and binary-source photometric light curves. Models show that only a few additional data points in photometric V band, together with a full light curve in I band, will enable breaking the degeneracy. Very good data quality and dense data sampling, combined with accurate binary lens and binary source modeling, yielded the discovery of the lowest-mass planet discovered outside of the Solar System so far, OGLE-2005-BLG-390Lb, having only 5.5 Earth masses. This was the first observed microlensing event in which the degeneracy between a planetary binary-lens and an extreme flux ratio binary-source model has been successfully broken. For events OGLE-2003-BLG-222 and OGLE-2004-BLG-347, the degeneracy was encountered despite of very dense data sampling. From light curve modeling and stellar evolution theory, there was a slight preference to explain OGLE-2003-BLG-222 as a binary source event, and OGLE-2004-BLG-347 as a binary lens event. However, without spectra, this degeneracy cannot be fully broken.

No planet was found so far around a white dwarf, though it is believed that Jovian planets should survive the late stages of stellar evolution, and that white dwarfs will retain planetary systems in wide orbits. We want to perform high precision astrometric observations of nearby white dwarfs in wide binary systems with red dwarfs in order to find planets around white dwarfs. We selected a sample of observing targets (WD-RD binary systems, not published yet), which can possibly have planets around the WD component, and modeled synthetic astrometric orbits which can be observed for these targets using existing and future astrometric facilities. Modeling was performed for the astrometric accuracy of 0.01, 0.1, and 1.0 mas, separation between WD and planet of 3 and 5 A.U., binary system separation of 30 A.U., planet masses of 10 Earth masses, 1 and 10 Jupiter masses, WD mass of $0.5M_{\odot}$ and $1.0M_{\odot}$, and distances to the system of 10, 20 and 30 pc. It was found that the PRIMA facility at the VLTI will be able to detect planets around white dwarfs once it is operating, by measuring the astrometric wobble of the WD due to a planet companion, down to 1 Jupiter mass. We show for the simulated observations that it is possible to model the orbits and find the parameters describing the potential planetary systems.

Zusammenfassung

Bei von Sternen verursachten Mikrolinsen-Ereignissen beobachtet man meist symmetrische Lichtkurven einer einzelnen Linse oder asymmetrische Lichtkurven (oftmals mit Kaustik-Crossing), die durch Doppel-Linsen hervorgerufen werden. Im Prinzip kann aus der Zahl der gemessenen unsymmetrischen Ereignisse der Anteil der Doppelstern-Systeme in Abhängigkeit vom Winkelabstand abgeschätzt werden. Allerdings kann auch ein Doppelsystem Lichtkurven erzeugen, die gut mit einer Einzellinsen-Lichtkurve gefittet werden können. Die gilt insbesondere bei lückenhafter Messung oder großen Messfehlern. In dieser Arbeit wird für verschiedene Beobachtungsbedingungen untersucht, wie häufig Lichtkurven, die von Doppellinsen mit unterschiedlichen Abständen erzeugt werden, gut mit Einzellinsen-Lichtkurven gefittet werden können und damit fehlinterpretiert werden. Es wurde gefunden, daß der Anteil fehlinterpretierter Lichtkurven stark von der Separation der Komponenten abhägig ist: das Minimum liegt zwischen $0.6R_E$ und $1.0R_E$, wo der Anteil immer noch 5% beträgt (R_E ist das Einstein Durchmesser). Die Rate der Fehlinterpretationen ist höher für kurze Mikrolinsen-Ereignisse (bis zu wenigen Monaten) und für Ereignisse mit geringer Maximalverstärkung. Bei gleicher Separation steigt die Rate mit extremeren Massenverhältnissen an.

Das Problem der Degenerierung zwischen den Lichtkurven für doppelte Linsensysteme und doppelte Hintergrund-Quellen wurde anhand simulierter Daten und mit Beobachtungsdaten des PLANET Projekts untersucht. Der Fit-Code BISCO, der den genetischen Algorithmus PIKAIA nutzt, wurde geschrieben, um Doppel-Linsen Lichtkurven, die von verschiedenen Observatorien in den photometrischen Bändern I, R, und V gemessen wurden, zu modellieren. Tests mit simulierten Daten haben gezeigt, daß BISCO in der Lage ist, in einem sehr weiten Parameterbereich die korrekte Lösung für die Lichtkurve einer Doppel-Linsen zu finden. In dieser Arbeit wird die Flußverhältnis-Methode empfohlen, um die Degenerierung zwischen Doppel-Linse und Doppel-Quelle aufzulösen. Modellierungen zeigen, daß nur wenige zusätzliche Datenpunkte im V-Band genügen, um zusammen mit einer vollständigen Lichtkurve im I-Band die Degenerierung aufzubrechen. Mit sehr guter Datenqualität und zeitlich dichten Messungen, kombiniert mit genauer Modellierung von Doppel-Linsen und Doppel-Quellen, gelang die Entdeckung des bisher masseärmsten Planeten ausserhalb des Sonnensystems: OGLE-2005-BLG-390Lb, mit nur 5.5 Erdmassen. Dies war das erste Mikrolinsen-Ereignis, bei dem die Degenerierung zwischen plantarer Doppel-Linse und einer Doppel-Quelle mit extremem Flußverhältnis erfolgreich aufgelöst wurde. Für die Ereignisse OGLE-2003-BLG-222 und OGLE-2004-BLG-347 besteht die Degenerierung trotz sehr dichter Messungen. Aufgrund der Lichtkurvenmodellierung und Argumenten

aus der Theorie der Sternentwicklung ist die Erklärung von OGLE-2003-BLG-222 als Doppel-Quelle und OGLE-2004-BLG-347 als Doppel-Linsen Ereignis vorzuziehen. Allerdings kann die Degenerierung ohne spektrale Daten nicht vollständig aufgelöst werden.

Bisher wurde kein Planet als Begleiter eines Weissen Zwerges gefunden, obwohl es möglich sein sollte, daß jupiterähnliche Planeten die Spätstadien der Sternentwicklung überleben und daß sich Weisse Zwerge Planetensysteme mit weiten Umlaufbahnen erhalten können. Wir planen hochgenaue astrometrische Beobachtungen von nahen Weissen Zwergen in weiten Doppelsystemen, um Planeten um Weisse Zwerge zu finden. Wir haben eine Stichprobe von Systemen zusammengestellt, in denen möglicherweise Planeten gefunden werden könnten. Wir haben synthetische astrometrische Orbits modelliert, die für diese Systeme mit existierenden und zukünftigen astrometrischen Instrumenten beobachtbar sind. Die Modellierungen wurden für astrometrische Genauigkeiten von 0.01, 0.1, und 1 Milibogensekunden gerechnet. Als Abstände zwischen Weissem Zwerg und Planet wurden 3 und 5 Astronomische Einheiten angenommen, für den Abstand zwischen den Doppelsternkomponenten 30 A.E. Als Planetenmassen wurden 10 Erdmassen, bzw. 1 und 10 Jupitermassen gewählt, als Masse für den Weissen Zwerg $0.5M_{\odot}$ und $1.0M_{\odot}$. Die Distanzen zum System betragen 10, 20 und 30 parsec. Als Resultat dieser Untersuchung wurde gefunden, daß das PRIMA Instrument am VLTI in der Lage sein wird, die astrometrischen Oszillationen, die ein Planet ab einer Jupitermasse verursacht, zu detektieren. Wir zeigen, daß es möglich sein wird, die Umlaufbahnen solcher Planeten zu modellieren und damit die Parameter dieser Planetensysteme zu bestimmen.

Contents

Introduction

> How do we know that the reality is not just another computer simulation?
>
> - From "The Matrix", based upon "Simulacra and Simulations" by Jean Baudrillard, 1983

About half of the stars in our Milky Way are bound in binary systems. Some of these systems have planets, increasing their complexity. Extrasolar planets can be detected mainly by indirect methods. Two of these methods will be described in this work, gravitational microlensing and astrometry. In both cases the presence of the gravitational field will uncover the invisible companions to the stars. In the case of microlensing events, the stellar systems acting as gravitational lenses will bend the light coming from the background source to the observer. Often these systems acting as lenses will be binary systems. Sometimes the sources will show a signature of binarity. In the case of astrometric measurements, we will be able to detect the astrometric wobble of the host star due to its orbiting planet mass. If the host star has a binary companion, the companion can be helpful for determining the accurate astrometric position changes of the host star.

These two methods are complementary considering the time scales. Microlensing events have often very short durations, of the order of months, weeks, even days. The most exciting signals, coming from low-mass planets, last in many cases only few hours, as will be shown by the example of a 5.5 Earth mass planet discovery OGLE-2005-BLG-390Lb. Since they cannot be repeated, we need very dense data sampling when observing the light curves. On the other hand, astrometric measurements require time and patience for measuring the orbit, since it takes several years for a planet at the orbital separation of few astronomical units to revolve around its host star, more than a time span of one PhD thesis.

One of the important goals of this work is to compare numerical simulations with real observations, to find out what is indeed the "reality". On one side we have to make models and simulations as realistic as possible. On the other hand, observations can be performed in different ways. We want to find the limiting observational constraints for different types of detections, in order to make decisions about the optimal use of the available observing facilities.

This work is divided into three parts. In the first part, numerical simulations of microlensing events were performed to study the probability of misinterpreting of binary lens single source microlensing events by single lens single source events. In the second part, the problem of binary source single lens microlensing events is discussed, stressing the degeneracy of photometric light curve solutions produced by binary source

single lens events and by single source binary lens events. This is based on simulations, suggesting the new flux ratio method to break this degeneracy, and on modeling three microlensing events observed by the PLANET collaboration. In the third part, simulations of astrometric observations of white dwarfs in wide binary systems are presented. The goal was to find out whether using the new VLTI astrometric facility PRIMA to be operating in near future will be able to detect planets around white dwarfs. Introductionary chapters, theory, and descriptions of numerical methods are incorporated into the different parts in such a way to lead the reader through this work gradually, and compare theory, modeling, and observations explaining different scientific problems without separating them.

CHAPTER 1

Extrasolar planets

A planet is an object that has a mass between that of Pluto and the Deuterium-burning threshold and that forms in orbit around an object that can generate energy by nuclear reactions, as defined by The International Astronomical Union. The discovery of the first extra-solar planet surrounding a main-sequence star was announced in 1995 based on very precise radial velocity (Doppler) measurements. Michel Mayor and Didier Queloz of the University of Geneva succeeded in the first definitive detection of an exoplanet orbiting an ordinary main-sequence star 51 Pegasi (Mayor and Queloz 1995). This discovery ushered in the modern era of exoplanetary discoveries. In the years immediately following, exoplanets began to be discovered in large numbers.

The vast majority of exoplanets found so far have high masses (Fig. 1.1.1). Ninety percent of them have more than 10 times the mass of Earth. Many are considerably more massive than Jupiter. However, these high masses are in large part an observational selection effect, since all detection methods are much more likely to discover massive planets. That observational selection effect makes statistical analysis difficult, but it appears plausible that in most exoplanetary systems, the largest planets are comparable in size to Jupiter or Saturn. Also, the fact that few planets only a few times more massive than Earth have been found (Beaulieu et al. 2006, Mayor et al. 2004), despite the great difficulty of detecting them, indicates that such planets are fairly common. Most known exoplanets have quite eccentric orbits (Marcy et al. 2005, Fig. 1.0.1). This is not an observational selection effect, since a planet can be detected equally well regardless of how eccentric its orbit is. The prevalence of elliptical orbits is a major puzzle, since current theories of planetary formation strongly suggest planets should form with circular (non-eccentric) orbits. This is also an indication that our own Solar System may be unusual, since almost all of its planets do all follow basically circular orbits. Of the 90 extrasolar planets that reside beyond 0.15 AU, their average orbital eccentricity is 0.32. In contrast, planets orbiting within 0.1 AU of their host star all reside in nearly circular orbits, no doubt enforced by tidal circularization. Various theories have been proposed to explain the orbital eccentricities. Planet-planet interactions, eccentricity induced by protoplanetary disk, gravitational perturbations from a companion star, gravitational perturbations from passing stars, formation by disk Instability, just to mention some.

Improvements in telescope technology, such as CCD and computer-based image processing, made the searches for extrasolar planets much more feasible. These advances allowed for more accurate measurements of stellar motion, allowing astronomers to detect planets, by measuring gravitational influences upon stars. Extrasolar planets were also be detected by measuring the variation in a star's apparent luminosity as a

FIGURE 1.0.1. Eccentricity vs. Semimajor axis for extrasolar planets. The 75 planets shown were found in a Doppler survey of 1300 FGKM main sequence stars using the Lick, Keck, and AAT telescopes. The survey was carried out by the California-Carnegie planet search team (Marcy et al. 2005)

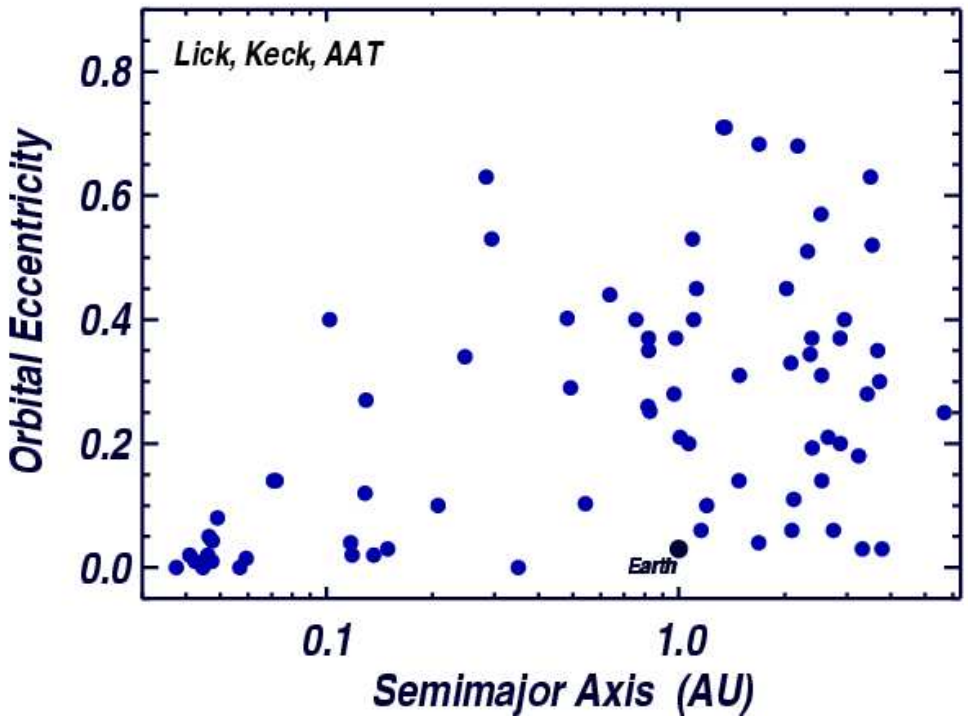

planet passes in front of it. Up to date (June 2006) 194 extrasolar planets have been detected, using different methods. We will briefly describe the most important methods.

1.1. Methods for detecting extrasolar planets

1.1.1. Astrometry. Astrometry is the oldest search method for extrasolar planets. It consists of precisely measuring a star's position in the sky and observing how that position changes over time. If the star has a planet, then the gravitational influence of the planet will cause the star itself to move in a tiny circular or elliptical orbit. Effectively, star and planet each orbit around their mutual center of mass (barycentre), as explained by solutions to the two-body problem. Since the star is much more massive, its orbit will be much smaller. Unfortunately, the changes in stellar position are so small that even the best ground-based telescopes cannot produce precise enough measurements. More on possible detecting of extrasolar planets through high-precision astrometry will be one of the topics discussed in this work.

1.1.2. The radial velocity method. Like the astrometric method, the radial velocity method uses the fact that a star with a planet will move in its own small orbit

in response to the planet's gravity. The goal is to measure variations in the speed with which the star moves towards or away from Earth. In other words, the variations are in the component along the line of sight of the radial velocity of the star with respect to Earth. The radial velocity can be deduced from the displacement in the parent star's spectral lines due to the Doppler effect. The velocity of the star around the barycentre is much smaller than that of the planet because the radius of its orbit around the center of mass is so small. Velocity variations down to 1 m/s can be detected with modern spectrometers. This has been by far the most productive technique used by planet hunters. It is also known as the "Doppler method" or "Wobble method". The method is distance independent, but requires high signal-to-noise ratios to achieve high precision, and so is generally only used for relatively nearby stars out to about 160 light-years from Earth. It easily finds massive planets that are close to stars, but detection of those orbiting at great distances requires many years of observation. Planets with orbits perpendicular to the line of sight from Earth produce smaller wobbles, and are thus more difficult to detect. One of the main disadvantages of the radial-velocity method is that it can only estimate a planet's minimum mass, because we measure only the projection of the radial velocity $v \sin i$, where i is the orbital inclination of the planetary system to the observer. Usually the true mass will be within 20% of this minimum value, but occasionally the true mass may be much higher.

1.1.3. The transit method. This method can be used to measure the radius of a planet. If a planet crosses (transits) in front of its parent star's disk, then the observed visual brightness of the star drops a small amount. The amount the star dims depending on its size and on the size of the planet. This method has two major disadvantages. First of all, planetary transits are only observable for the small percentage of planets whose orbits have very small angles of inclination. This is a problem in case of large orbits. Such alignment is especially unlikely for planets with large orbits. Secondly, the method suffers from a high rate of false detections. At least at present, a transit detection requires confirmation from some other method. The main advantage of the transit method is that when combined with the radial velocity method, one can determine the density of the planet, and hence learn something about the planet's physical structure. The nine planets that have been studied by both methods are by far the best-characterized of all known exoplanets. The transit method also makes it possible to study the atmosphere of the transiting planet. When the planet transits the star, light from the star passes through the upper atmosphere of the planet. By studying the stellar spectrum carefully, one can detect elements present in the planet's atmosphere.

1.1.4. Circumstellar disks. An even newer approach is the study of circumstellar disks . Many solar systems contain a significant amount of space dust that is present due to frequent dust generation activity such as comets, asteroid and planetary collisions. This dust forms as a disk around a star and absorbs regular star light and re-emits it as infrared radiation. These dust clouds can provide invaluable information through studies of their density and distortion, caused either by an orbiting planet "catching" the dust, or distortion due to gravitational influences of orbiting planets. Unfortunately this method can only be employed by space-based observations because our atmosphere

absorbs most infrared radiation, making ground based observation impossible. The Solar system contains a lot of dust. Although its mass is negligible, its surface area is so great that at a distance, its infrared emissions would outshine all our planets by a factor of 100. The Hubble Space Telescope is capable of these observations using its NICMOS (Near Infrared Camera and Multi-Object Spectrometer) instrument. Even better images were then taken by its sister instrument, the Spitzer Space Telescope (formerly SIRTF, the Space Infrared Telescope Facility), in 2003. The Spitzer Telescope was designed specifically for use in the infrared range and probes far deeper into the spectrum than the Hubble Space Telescope can.

1.1.5. Direct imaging. Detecting planets by direct imaging is difficult, taken in account their low brightness compared to their parent stars. In a few unusual cases, however, current telescopes may be capable of directly imaging planets. Specifically, this may be possible when the planet is especially large (considerably larger than Jupiter), widely separated from its parent star, and young (so that it is hot and emits intense infrared radiation). In early 2005, two groups (Neuhauser et al. 2005 and Chauvin et al. 2005), both using the European Southern Observatory Very Large Telescope array in Chile announced direct infrared images of extrasolar planets: GQ Lupi b and 2M1207b. Both planets are believed to be several times the mass of Jupiter and orbit at distances greater than 50 AU from their primary star. However, their status as planetary objects (as opposed to being small brown dwarfs) has not been firmly established.

1.1.6. Gravitational microlensing. Planet detection using the gravitational microlensing effect will be discussed in more detail later, as this is one of the main topic of this work. So far there have been four planets detected by microlesning (Bond et al. 2004, Udalski et al. 2005, Beaulieau et al 2006, Gould et al. 2006), the third being the first low-mass planet (5.5 Earth masses) in a wide orbit, OGLE-2005-BLG-390Lb. Up to date (2006) there is no other technique capable of detecting low-mass and Earth-like planets. In Fig. 1.1.1 the masses of 169 extrasolar planets detected by radial velocity, transit method and microlensing up to 2005 are plotted against the orbital separations from the parent stars. Dashed lines in colors corresponding to the methods in the plot, bordering the discovery spaces for the present and future facilities of these methods. We see that the shown methods have rather complementary discovery spaces, with only microlesning being able to detect low-mass planets in wide orbits. The three red points are the planets detected by microlensing so far, with OGLE-2005-BLG-390Lb considerably separated from all other planets in the discovery space.

FIGURE 1.1.1. Extrasolar planets detected by different methods up to 2005, plotted as orbital radius vs. planet mass (Horne 2005)

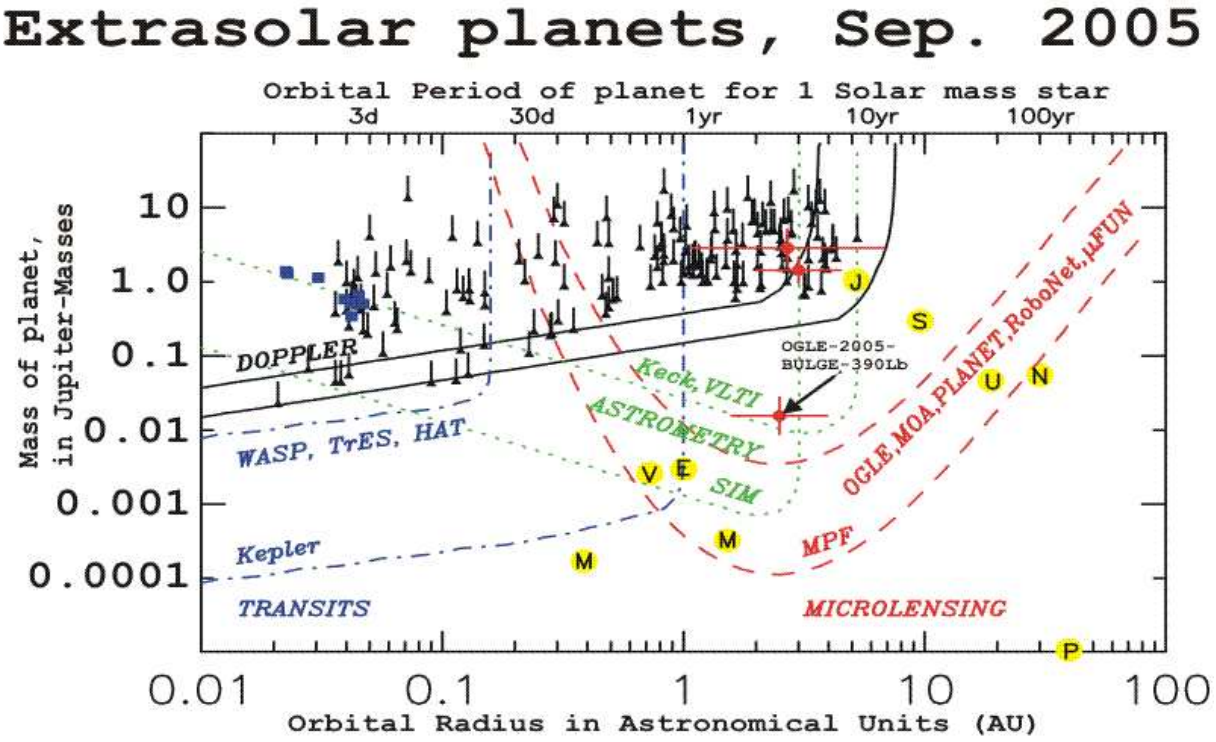

Black lines and markers: Radial Velocity search limits and planets (158)
Blue lines and markers: Transit search limits and planets (8)
Green lines and markers: Astrometry search limits and planets (0)
Red lines and markers: Microlensing search limits and planets (3)
M,V,E,M,J,S,N,U,P: The planets in our Solar System (Mercury, Venus, Earth, etc)

Part 1

On the probability of misinterpreting microlensing light curves produced by binary stars as single lens light curves

CHAPTER 2

Gravitational lensing and microlensing

In general relativity, the presence of matter (energy density) can curve spacetime, and the path of a light ray will be deflected as a result. This process is called gravitational lensing and in many cases can be described in analogy to the deflection of light by lenses in optics. Many useful results for cosmology have come out of using this property of matter and light. For many of the cases of interest one does not need to fully solve the general relativistic equations of motion for the coupled spacetime and matter, because the bending of spacetime by matter is small.

Consider an observer O observing a light source S. If an object L, acting as the gravitational lens, is placed between the observer and the source, the bending of light due to gravitational field of the lens will produce images of the source, S_1 and S_2 (Fig. 2.0.1).

FIGURE 2.0.1. Gravitational lensing effect. The light of the source S is deflected as it passes close to the lens L. To the observer O, it appears as if the source S has two additional images S_1 and S_2.

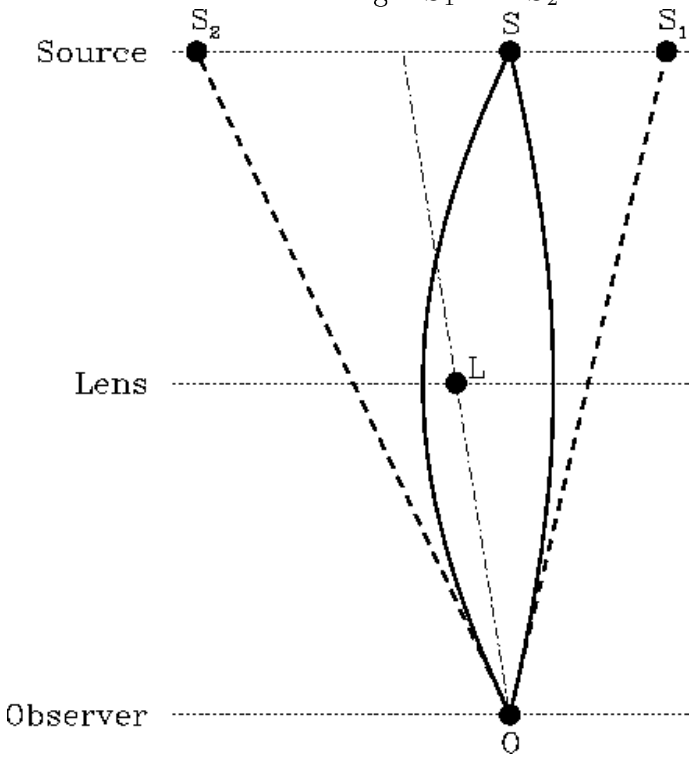

There are 3 different regimes of gravitational lensing: strong lensing, weak lensing, and microlensing. The distinction between these regimes depends on the positions of the source, lens and observer, and the mass and shape of the lens. The most extreme bending of light is when the lens is very massive and the source is close enough to it: in this case light can take different paths to the observer and more than one image of the source will appear. This regime is called *strong lensing*. In many cases the lens is not strong enough to form multiple images or arcs. In these case we speak about *weak lensing*. However, the source can still be distorted: both stretched (shear) and magnified (convergence). If all sources were well known in size and shape, one could just use the shear and convergence to deduce the properties of the lens. However, usually one does not know the intrinsic properties of the sources, but has information about the average properties. The statistics of the sources can then be used to get information about the lens. For instance, galaxies in general aren't perfectly spherical, but if one has a collection of galaxies one doesn't expect them all to be lined up. Thus, if this set of galaxies is lensed, on average, or statistically, there will be some overall shear and/or convergence imposed on the distribution, which will give information about the intervening lens(es). In some cases the lensing is of an image that is so small or faint that one doesn't see the multiple images. The additional light bent towards the observer adds up to the light of the source, which increases the brightness of the source during some finite time interval. This is the case of *microlensing* which will be explained in Section 2.2.

2.1. The basics of gravitational lensing

The standard gravitational lensing theory is valid for weak stationary gravitational fields. For small angle deviations, and when the typical size of the deflector is much smaller than the propagation medium, it is possible to use the thin lens approximation. In the thin-lens approximation, the hyperbolic paths are approximated by their asymptotes. The basics of gravitational lensing are described systematically in a review by Wambsganss (1998).

For a spherically symmetric lens (Fig. 2.1.1), what is a good approximation for a star or a planet, the deflection angle is:

$$\hat{\alpha}(\zeta) = \frac{4MG(\zeta)}{c^2\zeta} \tag{2.1.1}$$

where $M(\zeta)$is the mass inside the radius ζ. From Fig. 2.1.1, it is obvious that for very small angles, which are typical in astrophysical situations:

$$\theta D_S = \beta D_S + \alpha \hat{D}_{LS} \tag{2.1.2}$$

If we define the reduced angle as:

$$\alpha(\theta) = \frac{D_{LS}}{D_S}\hat{\alpha(\theta)}$$

Equation 2.1.2 becomes the so-called *lens equation*:

FIGURE 2.1.1. A spherically symmetric lens. O is the observer position, L position of the lens, S is the source position, and S_1 and S_2 position of the two images. The source and the observer are separated by the distance D_S, the source and the lens by D_{LS}, and the lens and the observer by D_L.

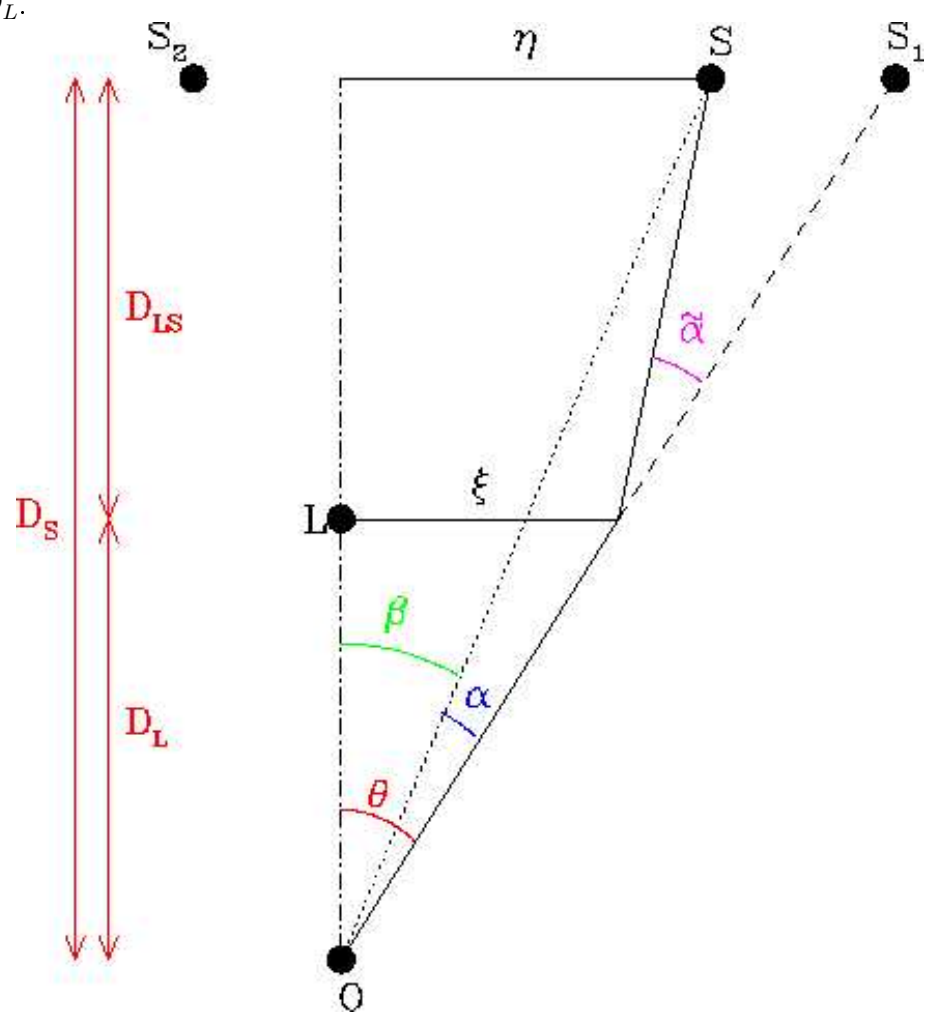

$$\beta = \theta - \alpha(\theta) \tag{2.1.3}$$

If the source, the lens and the observer were aligned on the same axis ($\beta = 0$) the image of the source would be a ring, the so-called Einstein ring. This ring has a radius (Einstein radius) defined as:

$$R_E = \sqrt{\frac{4GM_{tot}}{c^2}\frac{D_{LS}}{D_L D_S}} \tag{2.1.4}$$

where D_S is distance to the source, D_{LS} distance to the lens and, and $M_{tot}$is the total lens mass.

FIGURE 2.1.2. Changes in the image of an extended source in dependence on the projected angular separation of the source and the lens. As the angle decreases (from left to right), the two images merge and form the Einstein ring. The extended source is shown in spectrum colors, to see the mapping of the source in dependance to the angle.

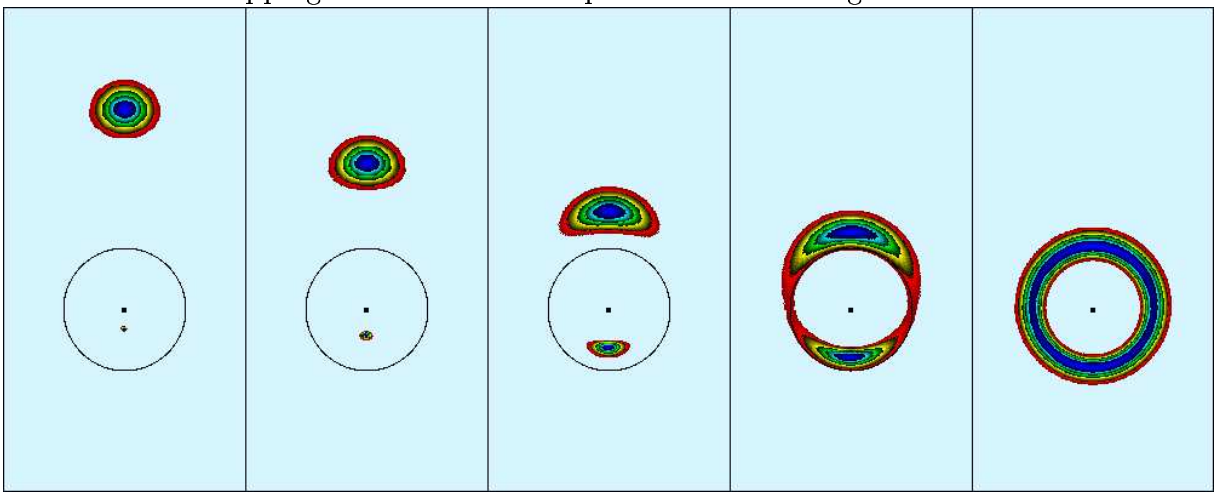

For a point-mass lens (or Schwarzschild lens) the lens equation 2.1.3 expressed through the Einstein radius R_E becomes a quadratic equation:

$$\beta = \theta - \frac{R_E}{\theta}$$

The two solutions of this equation are the image positions, one within, and one outside the Einstein ring:

$$\theta_{\pm} = \frac{1}{2}(\beta \pm \sqrt{\beta^2 + 4R_E^2})$$

In gravitational lensing, the number of photons is preserved. In case of a presence of a gravitational lens, we can receive more photons, what is called magnification of amplification, or less photons (de-magnification). Magnification is defined as:

$$A = \frac{1}{\det J}$$

where J is the Jacobian matrix of the lens mapping (Eq. 2.1.3). For the regions where the Jacobian vanishes, we have a very high magnification (for a perfectly point source and point lens it will become infinite, however, this is never a case in reality). The set of the points in the lens plane which satisfies this criteria is called critical curves. The corresponding set of point in the source plane, mapped though the lens equation (Eq. 2.1.3) is called the caustics.

FIGURE 2.1.3. Critical curves (left) and corresponding caustics (right). for an elliptical lens. The numbers in the right panels identify regions in the source plane that correspond to 1, 3 or 5 images, respectively.

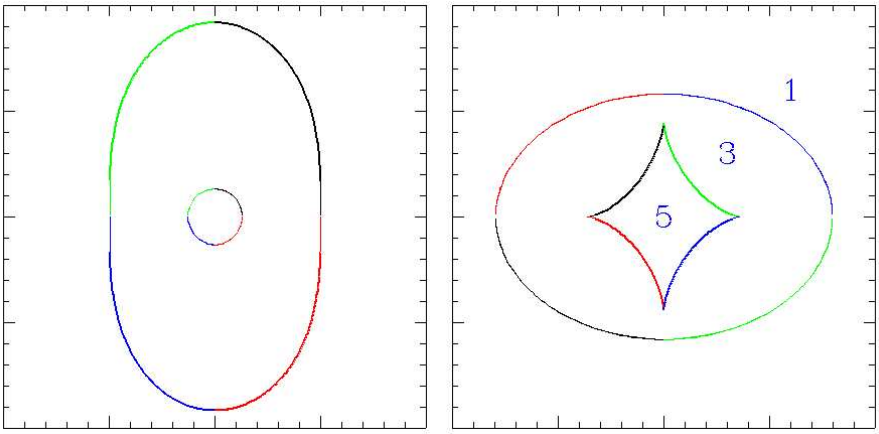

2.2. Microlensing

A limit of strong gravitational lensing in which the separation of multiple images is too small to be resolved is called microlensing. The intensity variation of a macroimage is made of unresolved micro-images. The basic idea was pointed out by Bohdan Paczynski ('The Father of microlensing') in 1986. If the galactic halo contains dark objects, called massive compact halo objects (machos), with masses between that of Jupiter (about 1/1000 of a solar mass) and very dim stars (e.g., brown dwarfs) with masses too small (less than 1/10 of a solar mass) to trigger thermonuclear ignition, then once in a while these massive halo objects should cross the line of sight between the earth and a more distant luminous star. If the halo object gets close enough to the line-of-sight we should see a noticeable lensing effect, characterized by a temporary brightening of the light from the distant star, called microlensing. In 1992 several teams started monitoring the Magellanic Clouds and the Galactic Bulge. The latter was at the beginning meant to be a check on the detection efficiency. If no microlensing events would be discovered toward the Magellanic Clouds, it could be because of a very low detection efficiency. Since the Galactic Bulge contains a lot of matter, it can be a perfect test of the method. After roughly a decade of monitoring, only about 20 microlensing events were detected towards the Magellanic Clouds. On the other hand, the initial 'test-method', observing microlensing events towards the Galactic Bulge (Paczynski 1996), yielded with thousands of observed microlensing events and valuable discoveries including few extrasolar planet discoveries (Bond et al. 2004, Udalski et al. 2005, Beaulieau et al. 2006, Gould et al. 2006), increasing our knowledge about single and binary stars in both Galactic plane, and the Galactic Bulge.

2.3. Microlensing galactic surveys

Various teams observe microlensing events towards the Galactic Bulge. Survey teams like OGLE (The Optical Gravitational Lensing Experiment, Udalski et al. 1992)

and MOA (Microlensing Observations in Astrophysics, Muraki 1999, Yock 2000) observe wide fields towards the Galactic Bulge, searching for signatures of microlensing events. Based upon their alerts, several teams select interesting events for high precision follow-up observations (like PLANET/RoboNet, MPS, MicroFUN etc.).

PLANET collaboration (Probing Lensing Anomalies NETwork, Albrow et al. 1998), is concentrated in studying in detail different aspects of microlensing towards the Galactic Bulge, especially searching for extrasolar planets and binary stars. PLANET maintains a network of telescopes on the Southern Hemisphere (in Chile, Australia and South Africa) to enable 24h continuous observations of the targets. Such follow-up is necessary for observing precisely short-lasting binary lens signatures such as caustic crossings, and especially for planet detection. A low-mass planetary signal lasts only few hours. The PLANET observing seasons last from April to September, when the Bulge is best observable from the Southern Hemisphere.

The author of this work is a PLANET member since 2003, working on data modeling, and has performed two observational runs (Mt. Canopus, Tasmania 2003, and La Silla, Chile 2004).

2.4. Single lens single source microlensing events

Let us consider a single point-like source passing behind a single point-lens with the transverse velocity v_T (Fig. 2.4.1). The angular separation between the lens and the source as a function of time is $u(t)$. At the time of the closest approach t_0, $u(t)$ will reach its minimum value u_0 (or u_{min}), called *the impact parameter.*

For a galactic microlensing scenario in which stars in the disk of the Milky Way act as lenses for Bulge stars close to the center of the Milky Way, the scale defined by the Einstein radius (Eq. 2.1.4) is:

$$R_E \sim 0.5\sqrt{\frac{M}{M_\odot}}[mas]$$

where $M_\odot$ is the Solar mass.

The time it takes for the source to pass through the Einstein radius, is depending on the transverse velocity v_T, and is called Einstein crossing time:

$$t_E = \frac{R_E}{v_T} \tag{2.4.1}$$

Magnification $A(t)$ (amplification) of the source star as a function of time is:

$$A(t) = \frac{u^2(t)+2}{u(t)\sqrt{u^2(t)+4}} \tag{2.4.2}$$

where $u(t)$ is depending on the impact parameter u_{min}:

$$u(t) = \sqrt{u_{min}^2 + (\frac{t-t_0}{t_E})^2} \tag{2.4.3}$$

FIGURE 2.4.1. A single lens single source microlensing event, also called a point source point lens (PSPL) event. u_{min} is the impact parameter, $R_0$the Einstein radius, and v_T the transverse velocity of the source relative to the lens. The magnification (amplification) inside the Einstein ring is larger than 0.3 mag.

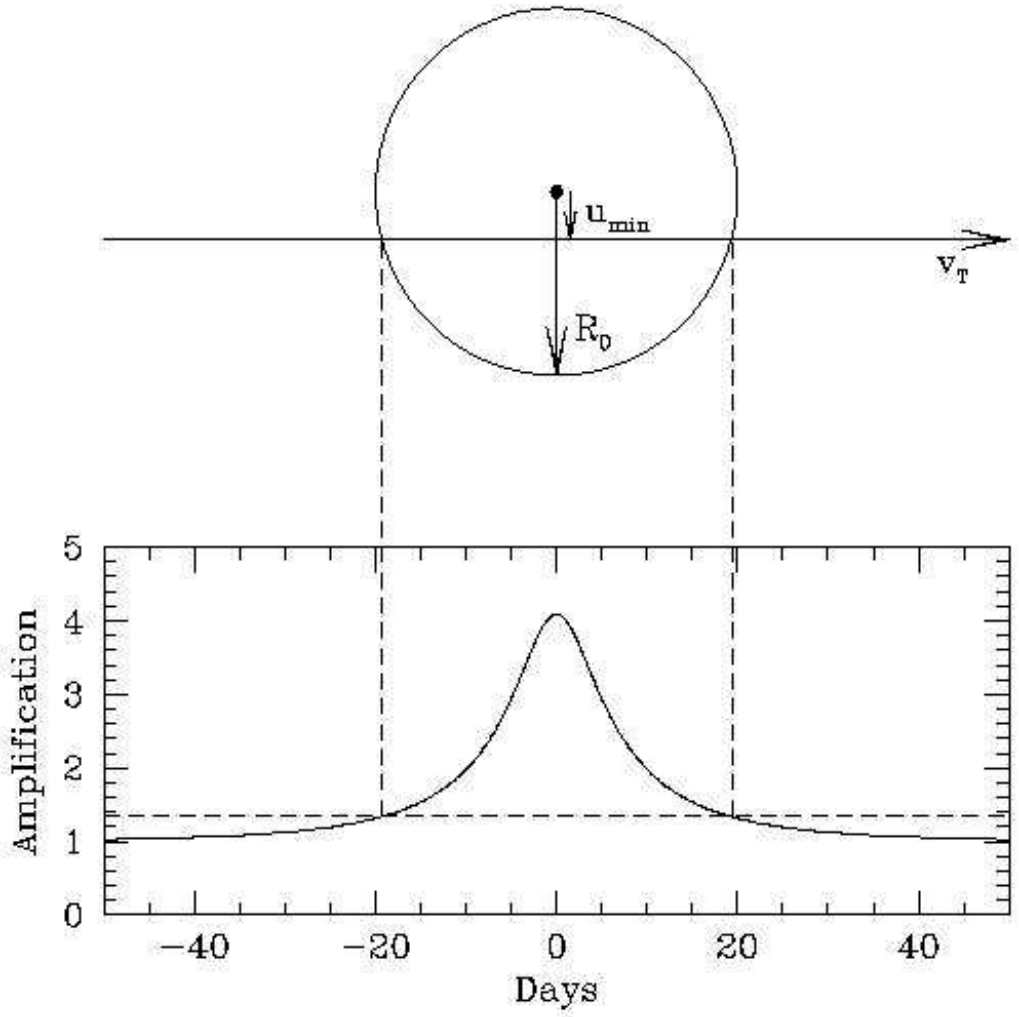

Fig. 2.4.2 shows how the magnification in magnitudes Δm changes with the impact parameter u_{min}. It is important to mention that the impact parameter is dimensionless, since it is the closest angular separation divided by the Einstein radius, meaning that for a source star passing at the Einstein radius from the lens, the impact parameter is equal to unity. In this case the magnification in magnitudes is $\Delta m = 0.3 mag$ (Fig. 2.4.2) We will accept this value for our modeling as a conventional minimum magnification for a microlensing event.

FIGURE 2.4.2. Magnification in as a function of impact parameter u_{min}. Magnification in magnitudes Δm (left) increases as u_{min}decreases, i.e. as the projected track of the source is closer to the lens (right).

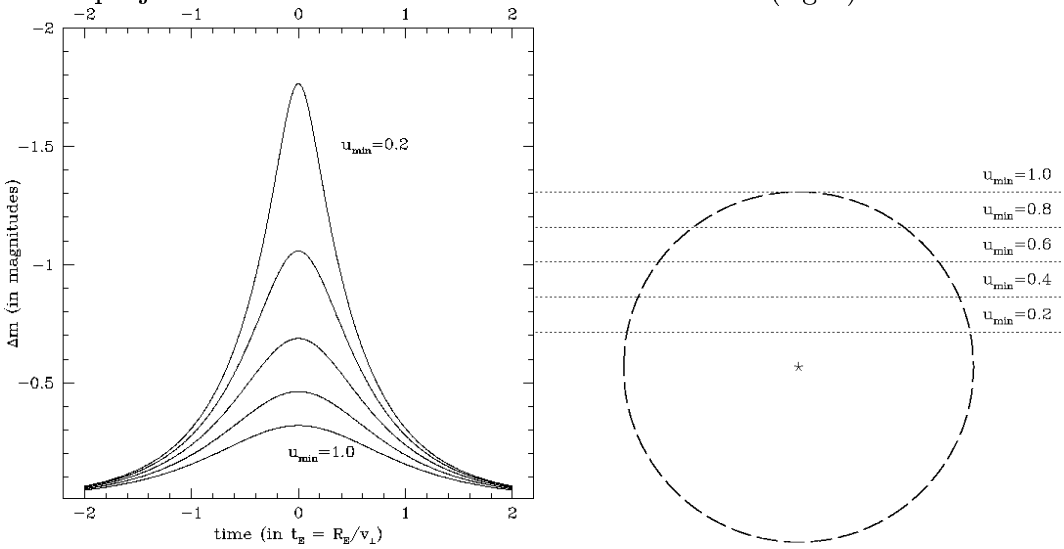

2.5. Binary lens single source microlensing events

A binary lens microlensing event is produced by a binary system acting as a lens. Depending on the mass ratio $q = m_2/m_1$ of the binary system, where m_1 is the mass of the more massive components, we have stellar binary lenses and planetary binary lenses. Typical mass ratios for stellar lenses are between $q = 1.0$ and $q = 0.1$, and typical planetary lenses for $q \leq 0.001$. For mass ratio of $q = 0.01$ we can have a planet, brown dwarf or a star as the less massive companion, depending on the total mass of the system:

$$M_{tot} = m_1 + m_2$$

For. ex. $q = 10^{-3}$ for a $M_{tot} = M_{\odot}$ means a Jupiter mass planet.

The theoretical study of binary lenses started in 1986, with the paper by Schneider and Weiss, where the equal masses case was considered in detail. The caustics were derived and they started to explore the non-trivial image dynamics underlying this model. The direct inversion of the binary lens equation can only be performed numerically. This point poses a major difficulty in the extraction of analytical results about the images of the binary lens. Dominik investigated static binary lens problem in detail (Dominik 1995) and later rotating binary systems (Dominik 1998). Bozza (2001) studied in detail the trajectories followed by single images during binary microlensing events. In Fig. 2.5.2 a magnification pattern of a binary lens is shown, produced by the code MICROLENS (Wambsganss 1990) for the total lens mass of 1 Solar mass, mass ratio $q = 0.3$ and the projected separation of the components of $d = 0.6R_E$. Caustics, typical for binary lenses, form an assymetric pattern, due to different masses of the components.

FIGURE 2.5.1. The first microlensing binary event OGLE 7, produced by a binary system with a mass ratio of $q = 1$, separated roughly 1 Einstein radius (Udalski et al. 1994). Caustic crossings are typical features for binary lens light curves.

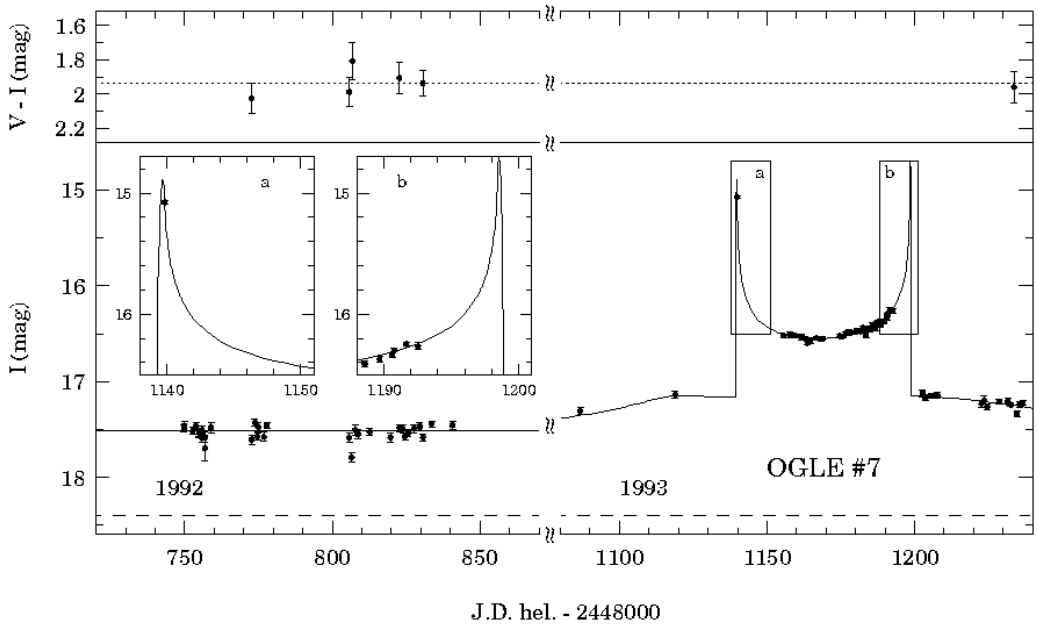

Binary lenses with separations d comparable to the Einstein radius R_E can produce lightcurves clearly different from a single lens lightcurve, through asymmetries and/or signatures of caustic crossings (Mao and Paczynski 1991, Dominik 1999, Bennet and Rhie 1999, Wambsganss 1997). In Fig. 2.5.1 the light curve of the first observed binary lens OGLE7 (Udalski et al. 1994) is shown.

2.5.1. Probability of observing a binary lens microlensing event. A large fraction of stars in the Milky Way are in binary systems. The exact fraction is still not known. Recent theoretical predictions give an estimate of the binary fraction of around 80% in the star-forming regions, with their fraction being an increasing function of the primary mass, while in the main sequence phase this percentage should drop to 40% (Delgado-Donate et al. 2003). In the solar neighbourhood the study of bright Solar-type stars gave 46% binaries vs. 42% singles, 9% triples and 2% quadruples (Abt & Levy 1976). Duquenney & Mayor (1991) found 53% of the main-sequence population I stars to be in binary or multiple systems. Among M-dwarves in the Solar neighbourhood 42% were found to be in binary systems (Fischer & Marcy 1992). The pre-main sequence stars in star-forming regions were found to be 80-100% in binary or multiple systems (Leinert et al. 1993). For the Population II stars a frequency of 20% was found (Zinnecker at al 2004). The binary fraction in the Galactic Bulge is still a big unknown.

Binary stars in the Milky Way have a logarithmic distribution in period. Duquenney & Mayor (1991) find that it is log-normal with a maximum around $P = 10^4$ days, for

FIGURE 2.5.2. Magnification for a binary lens of mass ratio $q = 0.3$ and a separation of $d = 0.6R_E$. The yellow cross marks the center of mass, and two yellow circles are positions of the two stellar components. The colors represent magnification. Dark blue is low magnification, red is the highest. Side length of a magnification pattern is $5R_E$.

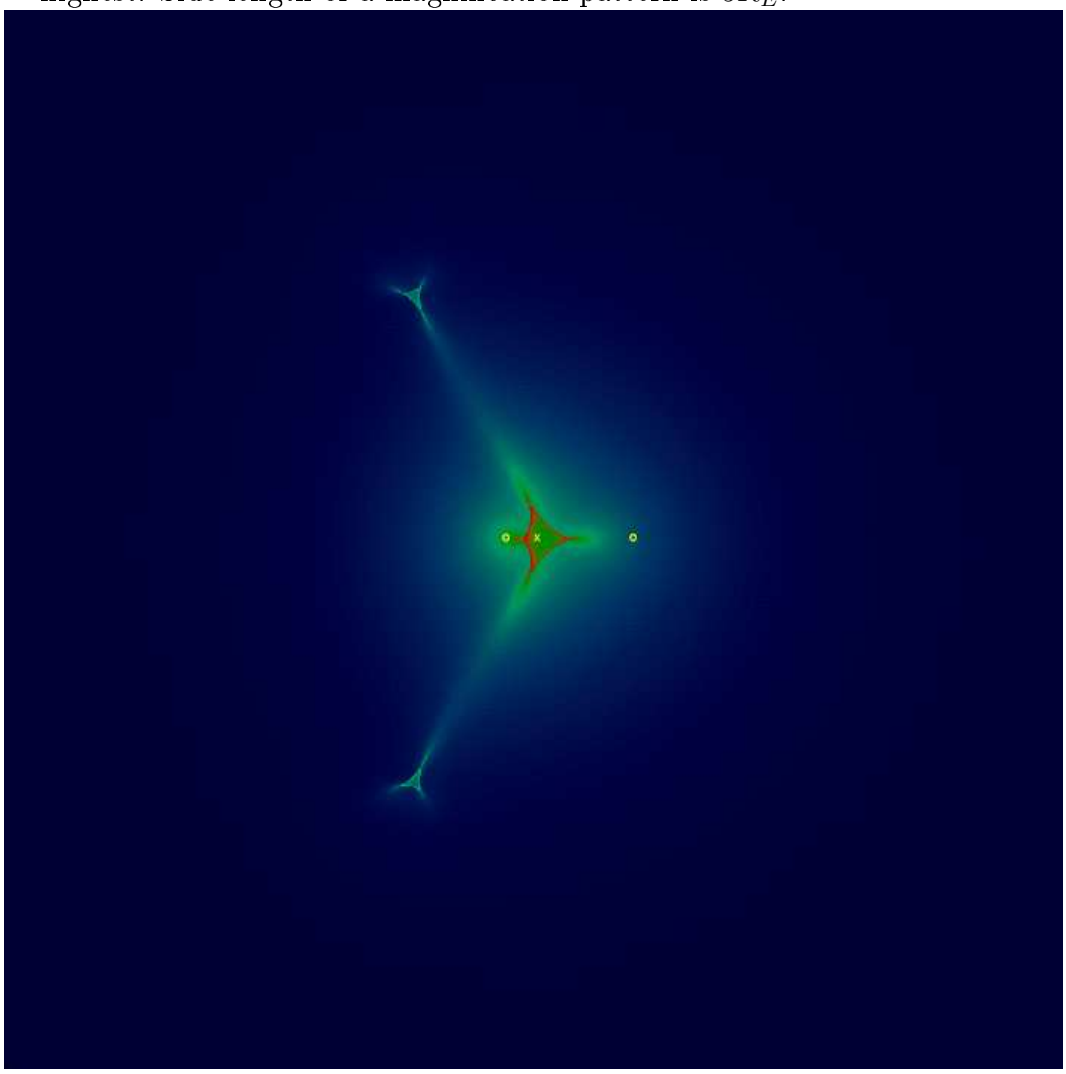

periods between 1 day and 10^{10}days. Mao & Paczynski (1991) used a flat distribution in $logP$ for the period range between 1 day and 10^9days. Mazeh et al. (2003) found that long period binaries have a non-uniform distribution depending on the mass ratio $q = m_2/m_1$, i.e. there are more binaries with higher mass ratios.

Binary lenses were first discussed in a general context by Schneider and Weiss (1986) and Paczynski (1986). In 1993, Galactic microlensing surveys published the first results (Alcock et a. 1993, Udalski 1993). The first observed binary microlensing event was OGLE#7 (Udalski et al. 1994), Fig. , with two caustic crossings. In the meantime, the microlensing surveys became more efficient, with fast alert systems (MOA, Bond

et al. 2001, and OGLE-III, Udalski 2003), yielding already thousands of observed microlensing events towards the Galactic Bulge In some cases the observational data is insufficient to distinguish between a single and a binary lens (Jaroszynski et al 2004), and especially to determine more detailed parameters of the lens systems. Occasionally, microlensing events with dense high-quality data can provide enough information for a full characterization of lens and source stellar systems in a binary lens events (Kubas et al. 2005).

Based on a rough estimate, the observed fraction of microlensing lightcurves produced by binary stars known from different microlensing surveys towards the Galactic Bulge (OGLE, PLANET, MOA etc.) so far is around 8%, as counted from the observed data of OGLE, PLANET and MOA surveys. This fraction is close to the rough estimate of 10% that Mao & Paczynski (1991) gave. However, this value can only be an absolute lower limit. We have to study the full parameter space of binary separations and mass ratios, in order to quantitatively determine the sensitivity of microlensing lightcurves for the detection of binary lenses. The ultimate goal would be to determine the efficiency of microlensing searches for the detecting of binary lenses and provide corrections factors for the real abundance of binary systems, based on the number of detected ones.

CHAPTER 3

Simulations

In this study we present calculations of microlensing lightcurves produced by binary stars with different parameters (separation, mass ratio, angle of the orbit inclination). We simulate observations by choosing various sampling and error bars, in order to determine the fraction of lightcurves produced by binary lenses which are likely to be misinterpreted as lightcurves produced by single lenses.

We perform two kinds of simulations, for "static" and for "rotating" binary systems. For the static approximation, the duration of the microlensing event is assumed to be much smaller than the orbital period of the binary. For events with duration roughly of the order of the binary orbital period, we take this orbital motion in account.

If the total mass of the two binary components is assumed to be equal to the solar mass:

$$m_{tot} = m_1 + m_2 = M_\odot$$

for a typical source distance of $D_S = 8.5kpc$ and a lens distance of $D_L = 6.0kpc$, the Einstein ring will be roughly of the order of $R_E = 1A.U.$ (Eq. 1.1.).

With transverse velocities of the order of 200 km s^{-1}, typical Einstein crossing times are of the order of few weeks. However, because the distribution of projected transverse velocities is very broad (Mao & Paczyński 1991), there is also a tail of (very) long-lasting events of many months or even years. For Solar mass binaries, a separation of $d = 1A.U.$ corresponds to an orbital period of 1 year. It is obvious that for separations which correspond to orbital periods larger than a fraction of the the event durations, we have to take the orbital motion in account, while for larger separation the static approximation will be good enough.

3.1. Magnification patterns

The simulations were performed using an optimized ray shooting program MICROLENS (Wambsganss 1990, 1997, 1999). In the ray shooting method, light rays follow a reversed path. They are shot onto the the lens plane under different angles from the observer, and then deflected from all mass elements in the lens plane. After deflection, they are collected on the source plane. This means that the density of the collected rays at the particular position in the source plane will be proportional to the source magnification at that position. In this way a so called magnification pattern is modeled, a uniform pixel grid map of the source plane, containing magnification at each pixel for that particular position. The size of the magnification pattern should not be to small compared to the size of the lens, in order not to lose too many rays.

A binary system is represented by two point masses, with the center of mass in the center of the lens plane; we chose the side length of the source plane to be $5R_E$. For each set of lens coordinates, we produce a two-dimensional magnification pattern of the size 1000×1000 pixels. One pixel size corresponds to $5R_\odot$ in the source plane. In Fig. 2.5.2 and Fig. 3.1.1 two such magnification patterns are shown for two binary systems of a mass ratio of $q = 0.3$, with separations of $d = 0.6R_E$ (Fig. 2.5.2) and $d = 3.0R_E$ (Fig. 3.1.1).

We investigate seven different mass ratio values $q = m_2/m_1$ of 10^{-5}, 10^{-4}, 10^{-3}, 10^{-2}, 0.1, 0.3, and 1.0, and 13 different binary separations of 0.1, 0.2, 0.3, 0.35, 0.4, 0.45, 0.5, 0.55, 0.6, 1.0, 2.0, 3.0 and 4.0 R_E, respectively. The orbit was assumed to be circular and seen under an inclination angle of 45 degrees.

3.2. Light curves

For each binary system, a set of 100 magnification patterns were calculated. For the "static" case, we use only one magnification pattern to construct light curves with 100 data points equally distributed in time. For the "dynamic" case, this corresponds to equal phase intervals, covering one full period of the binary.

Light curves were produced by convolving a uniform disk profile of a 10 $R_\odot$ giant at a distance of 8.5 kpc with the magnification patterns, for random starting and ending coordinates. That should simulate a source star passing with a random transverse velocity behind a rotating binary system acting as a lens. All the lightcurves have duration of one binary period, with a random phase shift. From perfect smooth simulated lightcurves, we select a given number of data points. We add Gaussian noise to the model lightcurves, in order to mimic real observations. Irregular data coverage has also been taken into account in the sense that a random subset of the data points is selected, in order to achieve a desired data coverage.

In order to analyze how the data quality influences the result, simulations for 10, 20, 30, 40, 50, 70 and 100 data points per lightcurve have been performed, and for different errorbars on the single data points, 0.03 mag, 0.01 mag and 0.1 mag at the baseline with some dependence on the magnitude. They decrease with brighter magnitude as

$$\sigma_m = \sigma_0 \frac{1}{1 + \Delta m} \tag{3.2.1}$$

where σ_m is the errorbar at the magnitude Δm above baseline, σ_0 at the baseline (nonmagnified magnitude), and σ_{min} the limiting minimum magnitude. The reason for that is higher accuracy of photometric observations of objects with brighter magnitude.

In Fig. 3.2.1 such a simulated 'ideal' light curve is shown for a rotating binary of mass ratio $q = 0.3$, orbital inclination of $i = 45^o$ and separation $d = 1R_E$. In Fig. 3.2.2 the simulated light curve with Gaussian noise is shown (left) and with 30 out of 100 randomly selected ed data points (right). Red line is the single lens single source fit to the data, showing how irregular data sampling can lead to a misinterpretation of a binary lens by a single lens.

FIGURE 3.1.1. Magnification pattern for a binary lens of mass ratio $q = 0.3$ for stars at projected separation $d = 3.0R_E$, calculated using MICROLENS. The yellow cross is marks the center of mass, and two yellow circles are positions of the two stellar component. The colors represent magnification. Dark blue is low magnification, red is the highest. Side length of a magnification pattern is $5R_E$.

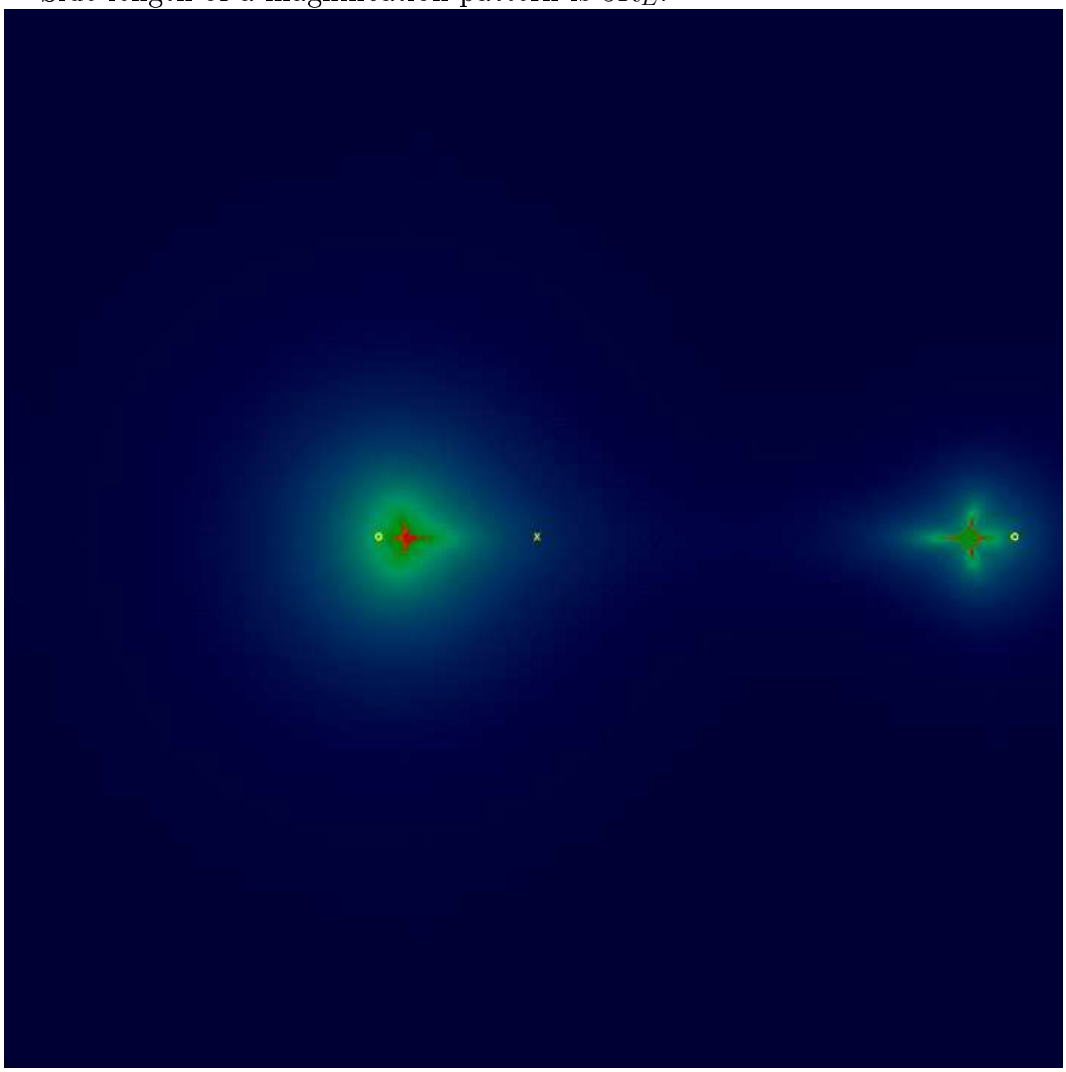

3.3. Fitting code using Downhill Simplex

In order to fit the simulated light curves, Downhill Simplex optimizing algorithm (Numerical Recipes, Press et al. 1992) was chosen. We want to fit simultaneously 3 parameters of a microlensing event for the each light curve produced:

$$u_0, t_E, t_{max}$$

FIGURE 3.2.1. A simulated light curve for a rotating binary system (mass ratio $q = 0.3$, inclination $i = 45^o$, separation $d = 1R_E$) . Black points are uniformly distributed data during one orbital period, each calculated by convolving a 10 solar radius giant star profile with one magnification pattern.

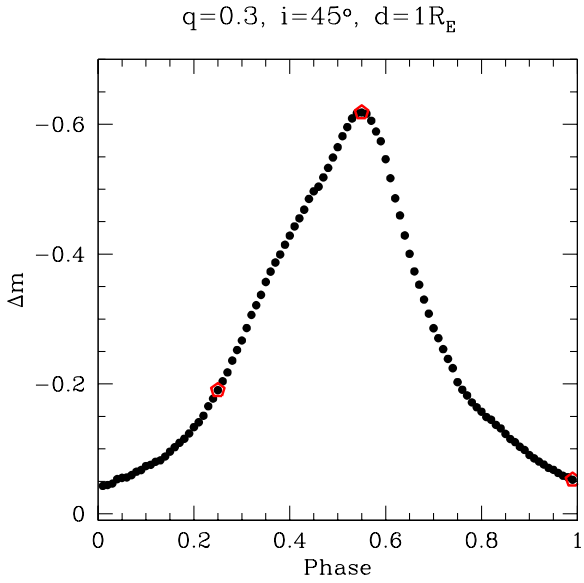

FIGURE 3.2.2. The light curve shown in Fig. 3.2.1, with Gaussian noise added (left) and irregular data sampling (right). The red lines are single lens fits the the simulated data.

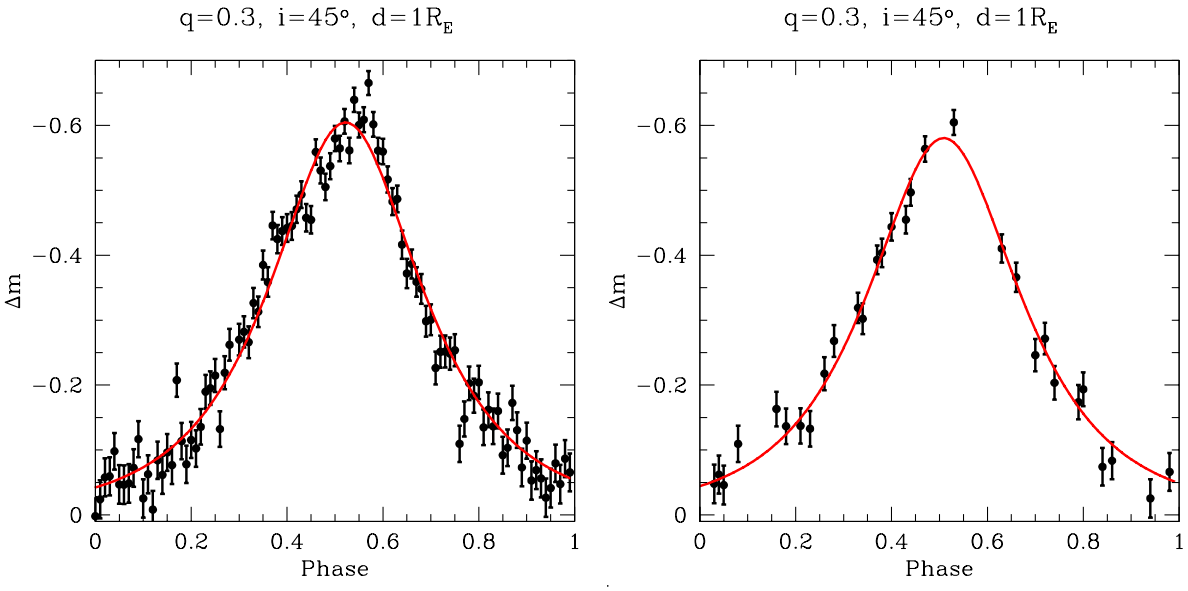

where u_0 is the impact parameter, t_E is the Einstein crossing time, and t_{max} is the time of the closest approach. We need to optimize a 3-dimensional non-linear inverse problem. The magnification A_{max} is then calculated from the impact parameter u_0 by using the Eq. 2.4.3.

The Downhill Simplex method requires only function evaluations, not derivatives. The algorithm maintains at each iteration a nondegenerate simplex (amoeba), a geometric figure in n dimensions of nonzero volume that is the convex hull of $n+1$ vertices, and their respective function values. In each iteration, new points are computed, along with their function values, to form a new simplex. The algorithm terminates when the function values at the vertices of the simplex satisfy a predetermined condition.

The reason for choosing Downhill Simplex for these calculations is that it is fast converging towards the local minimum, and thus suitable for statistical modeling requiring very large number of optimization runs. On the other hand, the theoretical underpinnings of the algorithm, such as its convergence properties, are not ideal. It has the disadvantage of falling into a local minimum, in the case of a complicated parameter space. However, a single lens light curve solution can be easily found by the this algorithm in the case we guess a proper starting simplex. This is done in the fitting code in such a way that from the simulated light curve we determine the maximum magnitude difference Δm_{max}, from which we calculate the estimate for the A_{max} starting value. The starting value for the Einstein crossing time t_E is roughly estimated es the FWHM of the single lens light curve. If we define the starting simplex in this way, the code will be stable in finding the solution for an automatic procedure of fitting a sequence of numerous light curves.

CHAPTER 4

Examples

4.1. Static approximation

An example of a lightcurve for a static binary, constructed in the way described above is shown in figures Fig. 4.1.1 and 4.1.2. The binary system has the mass ratio $q = 0.1$ and the separation of the components is $d = 1R_E$. The source star moves along a linear path behind the lens. The center of mass of the binary system is in the middle of the magnification pattern, which has a side length of $5R_E$ (Fig. 4.1.1).

The event duration is usually of the order of few weeks (Eq. 2.4.1), much smaller than the orbital period of the binary. Therefore we first study this static example. Let us assume that the Einstein crossing time for our example is 1 month (30 days). On Fig. 4.1.2 one can see the synthetic light curve produced for the trajectory shown on Fig. 4.1.1, divided into 100 equal time intervals.

The magnification was calculated by convolving the source star flat disk profile (i.e. without limb darkening) of radius $R_S = 10R_\odot$ with the magnification pattern along the chosen path. After the exact magnification is being calculated, we add Gaussian scatter, proportional to the size of the errorbars at the baseline.

The parameters of the best fit single-lens light curve for this example are:

$$A_{max} = 1.52; \quad u_0 = 0.81; \quad t_E = 10 \text{ days}; \quad \chi^2/d.o.f. = 1.23.$$

Irregular data sampling is modeled (Fig. 4.1.2), in a way that 30 out of 100 data points have been chosen randomly, with errorbars at the baseline of 0.03 magnitude, decreasing with the increasing maximum magnitude difference $\Delta m = m_b - m_{max}$, where m_b is the magnitude at the baseline.

$$A_{max} = 1.51; \quad u_0 = 0.81; \quad t_E = 10 \text{ days}; \quad \chi^2/d.o.f. = 0.83.$$

We see that the irregular data sampling did not change the fit parameters significantly, but the $\chi^2/d.o.f.$ decreases with fewer data points.

4.2. A rotating binary system

A binary system with mass ratio q=0.3 and a separation of $d = 0.6R_E$ is observed under an angle of inclination of $i = 45^o$ and rotating with an orbital period comparable to the event duration. The starting phase and the start and end coordinates of the background star were chosen randomly within the magnification pattern covering $5R_E \times 5R_E$ for each lightcurve. In this example case, the event start corresponds to the phase of 0.49, roughly about the time of the largest projected separation of the components.

FIGURE 4.1.1. Magnification pattern for a static binary system with projected separation $d = 1R_E$ and mass ratio $q = 0.1$. The line shows the path of the source star starting at the bottom. The scale is given in Einstein radii, with a side length of $5R_E$. The center of mass of the binary system is in the center of the magnification pattern, and the two stellar component lie on the y-axis.

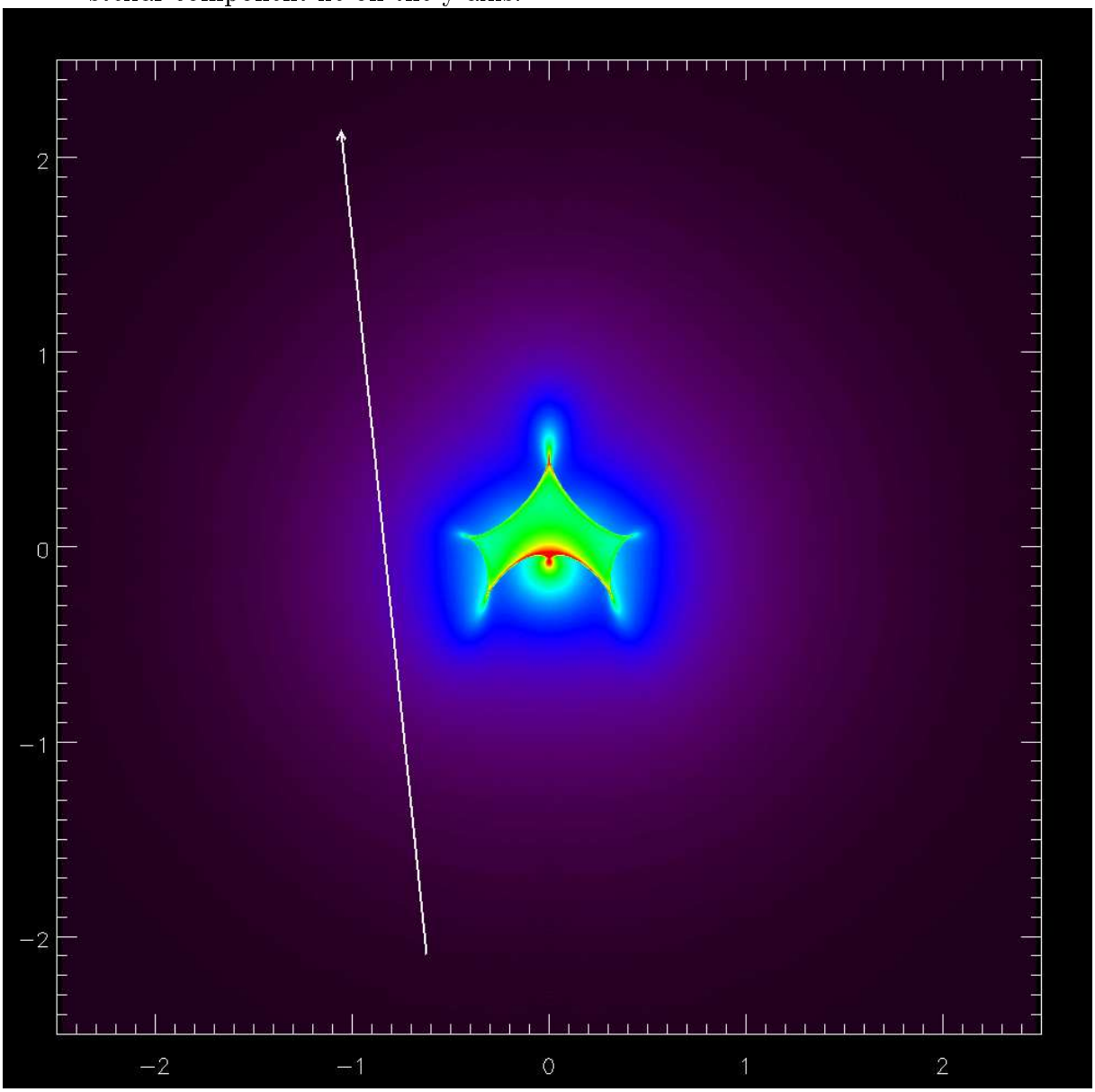

In Fig. 4.2.1 one can see the source track relative to magnification pattern of the rotating binary for 4 different epochs. Note that for each of the 4 patterns shown, the source star is positioned at the top of the arrow. Contrary to the static binary where the line marks the source star track in the pattern relative to the lens, in this case the

FIGURE 4.1.2. a) The light curve produced in the static approximation for the scenario shown on Fig. 4.1.1. $t_E \ll P_{binary}$;
b) Single-lens point-source fit to the binary-lens light curve assuming perfect data, no scatter;
c) 100 data points with Gaussian noise of $\sigma = 0.03mag$;
d) 30 randomly selected data points with Gaussian noise.

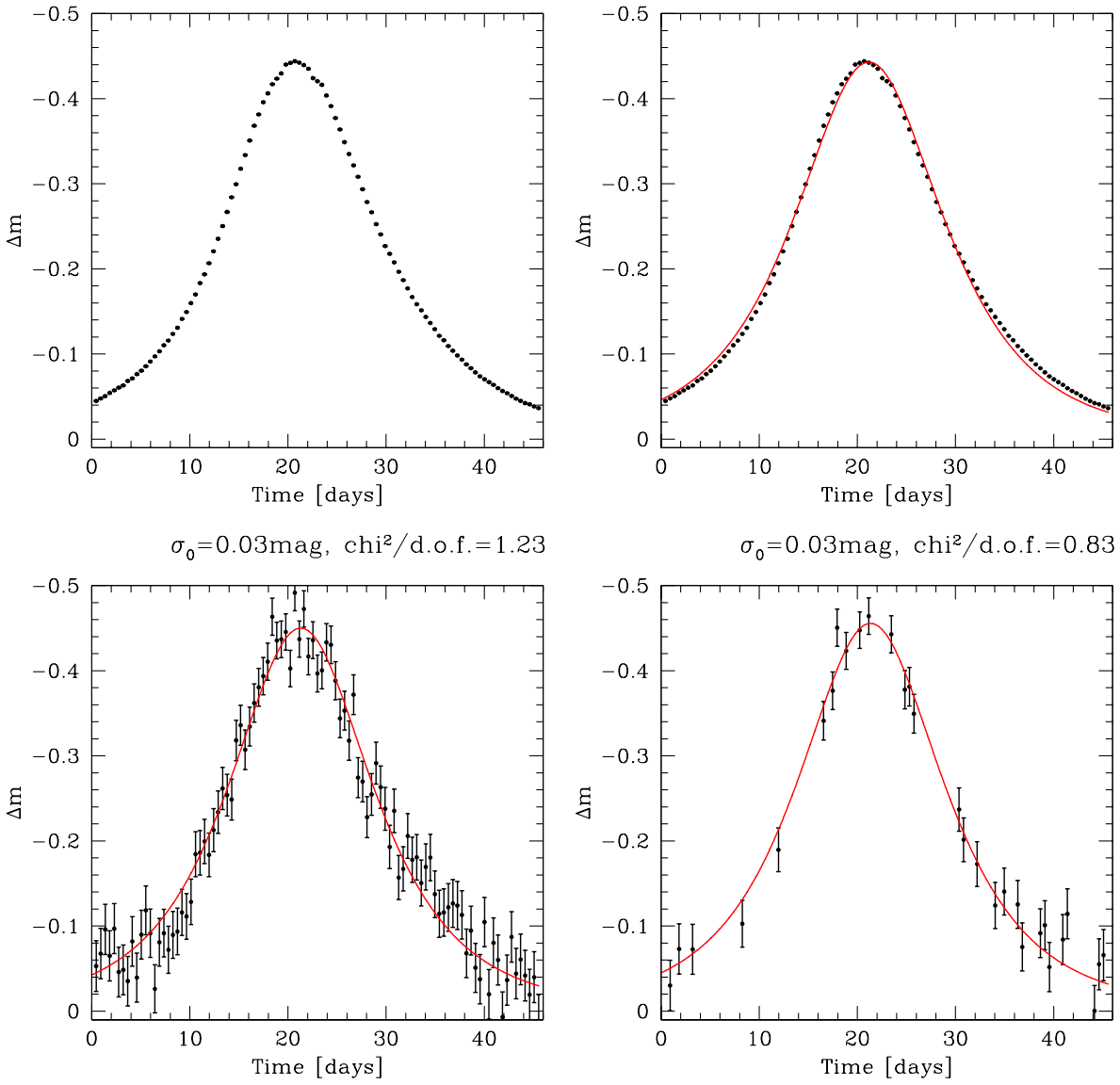

line represents only the track which the source star has passed, but at times where the magnification was different than in the given pattern, due to rotation.

On Fig. 4.2.2, the light curve corresponding to the tracks shown in Fig. 4.2.1 is plotted. The light curve in the top left panel consists of 100 regularly spaced data

FIGURE 4.2.1. Example for a magnification pattern of a rotating binary lens (mass ratio $q = 0.3$, inclination $i = 45^o$, separation $d = 0.6R_E$) for different phases of one orbital period: a) phase=0.25; b) time of highest magnification (phase = 0.47); c) phase=0.75; d) after one full binary rotational period (phase = 1.0). White lines show the path of the source star relative to the lens, with the arrow top at the source position. The scale is given in units of Einstein radius, with side length of $5R_E$.

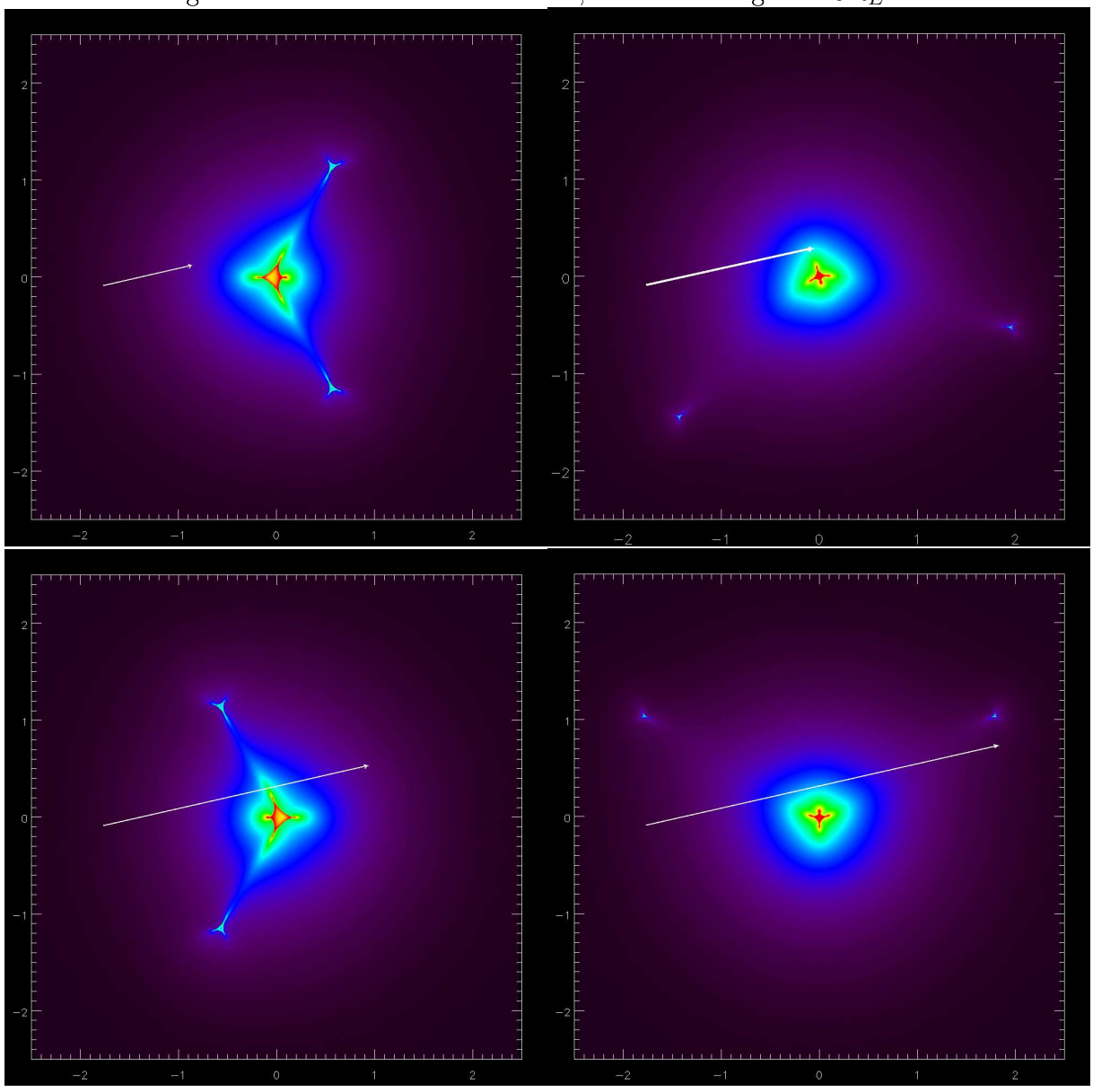

points covering one full orbital period. The magnitude was calculated by convolving the magnification pattern with a flat disk profile of the source star.

FIGURE 4.2.2. a) The light curve produced for the rotating binary constellation shown on Fig. 4.2.1, $t_E \sim P$; b) Single-lens point-source fit (red line) to the binary-lens light curve assuming perfect data, no scatter; c) 100 data points with Gaussian noise of$\sigma = 0.03mag$; d) 30 randomly selected data points with Gaussian noise.

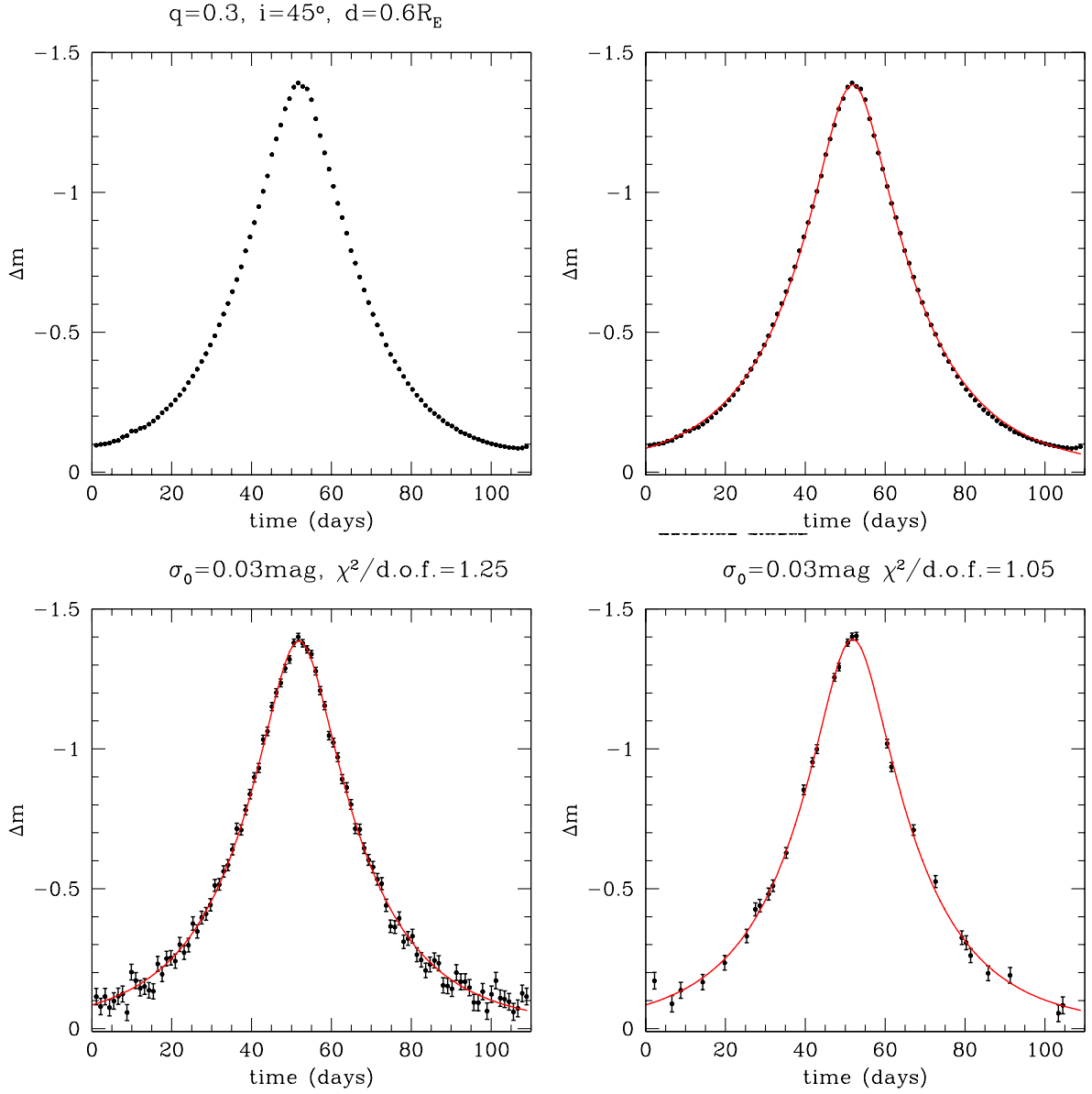

In Fig. 4.2.2, bottom right panel, a single-lens light curve was fitted for the 30 displayed randomly selected data points. The best solution was found to have the following parameters:

$$A_{max} = 3.61; \quad u_0 = 0.28; t_0 = 33.4 \text{ days}; \quad \chi^2/d.o.f. = 1.06.$$

The single-lens fit of the same lightcurve with all 100 data points results in $\chi/d.o.f. = 1.25$. This example shows that a rotating binary can produce a lightcurve that can be misinterpreted as a single-lens lightcurve.

CHAPTER 5

Results

5.1. Statistics

In order to quantitatively determine the probability for a binary-lens event to be misinterpreted as a single-lens event, we analyzed 10 000 light curves for each scenario defined by mass ratio, separation, inclination, number of data points, size of the error bars, random start and end points.

Depending on the exact trajectory, i.e. the impact parameter, light curves reach different maximum magnification. We only considered events which have at least one data point with a magnification higher than 0.3 magnitudes. For each light curve, we tried to fit a point-source single-lens light curve on the simulated data and determined the goodness-of-fit.

One important issue is the determination of the $\chi^2/d.o.f.$ cutoff value in defining "a good fit"; since the size of the error bars was fixed as one parameter, it does make sense to also discuss relatively large values of χ^2 per degree of freedom. The reason is that when performing real observations, errorbars are often underestimated.

To check the dependence of the $\chi^2/d.o.f.$ on different parameters, determine the $\chi^2/d.o.f.$ cutoff values to be considered as a merit in the simulations, and finally, to check if the models and codes work properly, we construct a magnification pattern of a single lens of one solar mass, and the corresponding light curves in the same way as we do for binary lenses.

The result of this simulations is shown in the Fig. 5.1.1, in the form of curves representing the dependence of the ratio of misinterpreted fits on the $\chi^2/d.o.f.$, and on the data sampling. Each color represents a curve for a different number of randomly selected data points out of 100. In the Table 5.1. we see the same result in the numerical form, for $\chi^2/d.o.f.$ cutoff of 1.0, 1.1, 2.0 and 3.0. So basically, the area under the given curve shows how for the total sample these light curves coincide with single lens fits we expect to fit.

We can conclude that the simulations behave as expected from the theory of statistic, but that if we really want a confidence level of more than 99%, we should take a $\chi^2/d.o.f.$ cutoff of 3.0. For the cutoff of 1.1 we get a confidence level of around 67% what corresponds to 1σ. We see immediately that for 10 out of 100 data points the statistic is not satisfactory enough, but the other values seem to be reasonable.

Our results are expressed as the percentages of binary-lens light curves which were fitted well by a point-source point-lens light curve, out of all light curves for which a microlensing signal was detected (i.e. with maximum magnification larger than 0.3 magnitudes).

FIGURE 5.1.1. Dependance of the percentage of cases with good fits on the number of data points for a single lens, shown as a function of the $\chi^2/d.o.f.$ cutoff, with the errorbar at the baseline of $\sigma_0 = 0.03mag$.
Different colors of lines stand for the number of randomly selected data points out of 100 (blue: 10/100, red: 20/100, green: 30/100 and black: 100/100).

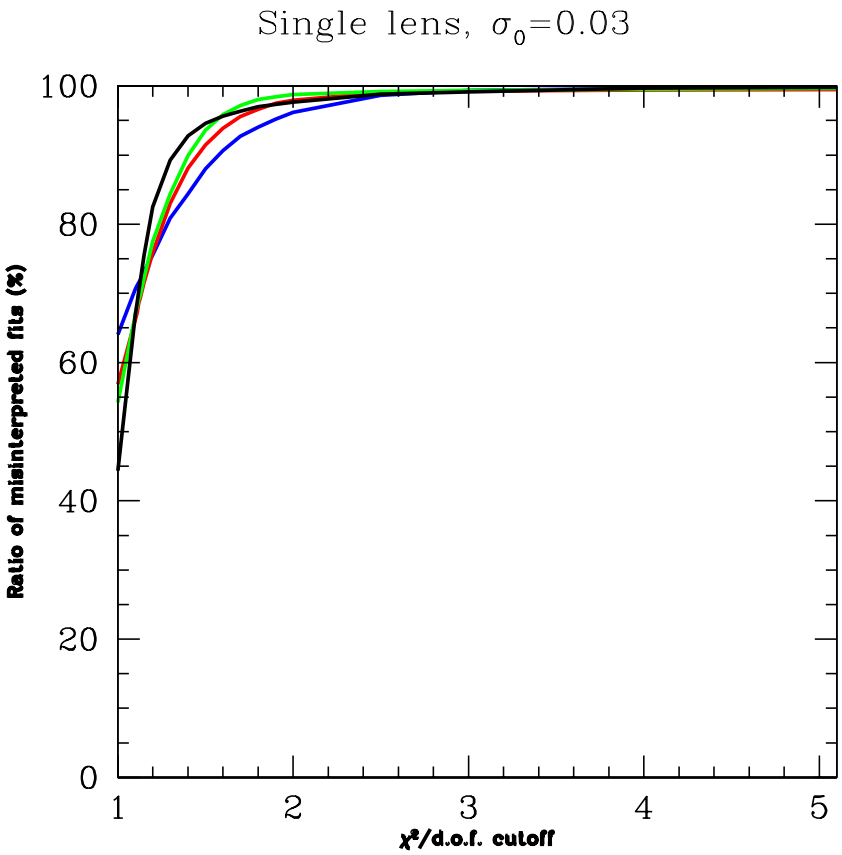

5.2. Dependence on number of data points

We investigated how the frequency of good point lens point source fits vary with the number of data points. It was found – not surprisingly – that the data coverage plays an important role.

If we compare this plot with the same kind of plot made for a single lens, we see that on one side, as expected, the number of single lens single lens fits increases with a higher $\chi^2/d.o.f.$ cutoff. On the other hand, if the data sampling is taken as a parameter, the trend is opposite for a binary lens than a single lens. That is consistent, since in the case of a single lens we make a wrong interpretation if we do not fit a single lens, while for a binary lens this is the other way round. We also see that 10 out of 100 data points seems to be not satisfactory enough, while already for 20 or 30 data points we get quite a satisfying result. Of course, we have to keep in mind that this dependence

n_{dp}	1.0	1.1	2.0	3.0
10	64.0	70.6	96.2	99.3
20	56.9	66.2	97.9	99.2
30	54.2	66.9	98.7	99.4
40	52.5	67.6	98.4	99.2
50	49.2	65.3	98.4	99.2
70	47.2	66.5	98.0	99.2
100	44.4	67.0	97.7	99.2

TABLE 1. Dependance of the ratio of misinterpreted fits on the $\chi^2/d.o.f.$ for a single lens, for different number of selected data points out of 100, and cutoffs for $\chi^2/d.o.f.$ of 1.0, 1.1, 2.0 and 3.0.

is satisfying for a mass ratio of $i = 0.3$, i.e. for a typical binary star. For lower mass ratios, particullary stars with planets, we need much denser data sampling.

n_{dp}	1.0	1.1	2.0	3.0
10	13.7	15.8	29.6	37.7
20	5.5	7.1	19.2	25.7
30	4.2	5.4	17.5	23.2
40	2.7	4.5	16.1	22.4
50	2.9	4.8	17.9	22.7
70	2.2	3.9	16.0	22.0
100	1.4	3.6	15.7	21.3

TABLE 2. Dependance of the ratio of misinterpreted fits on the $\chi^2/d.o.f.$ for a static binary lens, for different number of selected data points out of 100, and cutoffs for $\chi^2/d.o.f.$ of 1.0, 1.1, 2.0 and 3.0.

5.3. Dependence on binary mass ratio

q	1.0	1.1	2.0	3.0
10^{-5}	54.6	66.9	98.1	99.1
10^{-4}	54.6	67.5	97.8	98.9
10^{-3}	47.9	60.2	91.3	93.7
10^{-2}	27.9	35.9	65.6	71.4
0.1	7.7	10.7	27.7	34.5
0.3	4.2	5.4	17.5	23.2
1.0	3.3	4.6	14.5	19.9

TABLE 3. Dependance of the ratio of misinterpreted fits on the $\chi^2/d.o.f.$ for a static binary lens, for different mass ratios, and cutoffs for $\chi^2/d.o.f.$ of 1.0, 1.1, 2.0 and 3.0.

FIGURE 5.2.1. Dependance of the ratio of misinterpreted fits on the number of data points, shown as a function of $\chi^2/d.o.f.$ cutoff, with the errorbar at the baseline of $\sigma_0 = 0.03mag$, for a static binary lens with parameters: $q = 0.3$, $d = 1R_E$.
Different colors of lines stand for the number of randomly selected data points out of 100 (blue: 10/100, red: 20/100, green: 30/100 and black: 100/100)

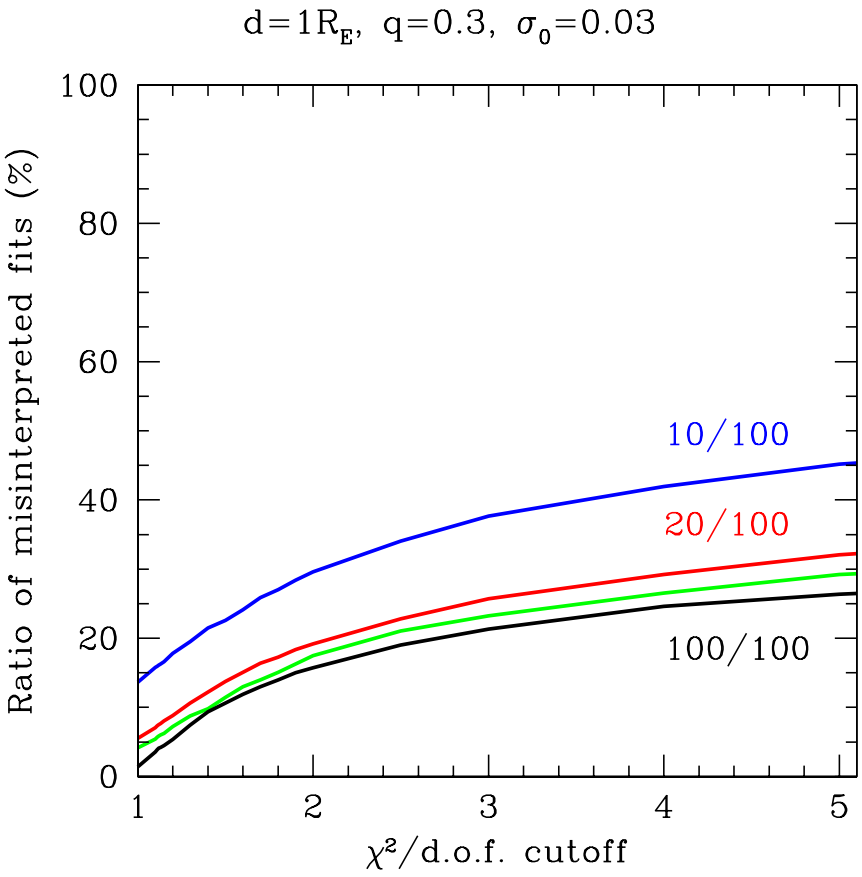

q	1.0	1.1	2.0	3.0
10^{-5}	28.4	45.7	85.4	90.5
10^{-4}	28.0	45.6	83.1	87.9
10^{-3}	23.1	37.3	69.5	74.1
10^{-2}	9.5	16.4	39.5	45.8

TABLE 4. Dependance of the ratio of misinterpreted fits on the $\chi^2/d.o.f.$ for a static binary lens, for different mass ratios, and cutoffs for $\chi^2/d.o.f.$ of 1.0, 1.1, 2.0 and 3.0.

The mass ratio of a binary system is an important parameter, since it tells us which kind of the companion the primary star has. For stellar binaries we assume a mass

FIGURE 5.3.1. Magnification pattern for $q = 0.01$

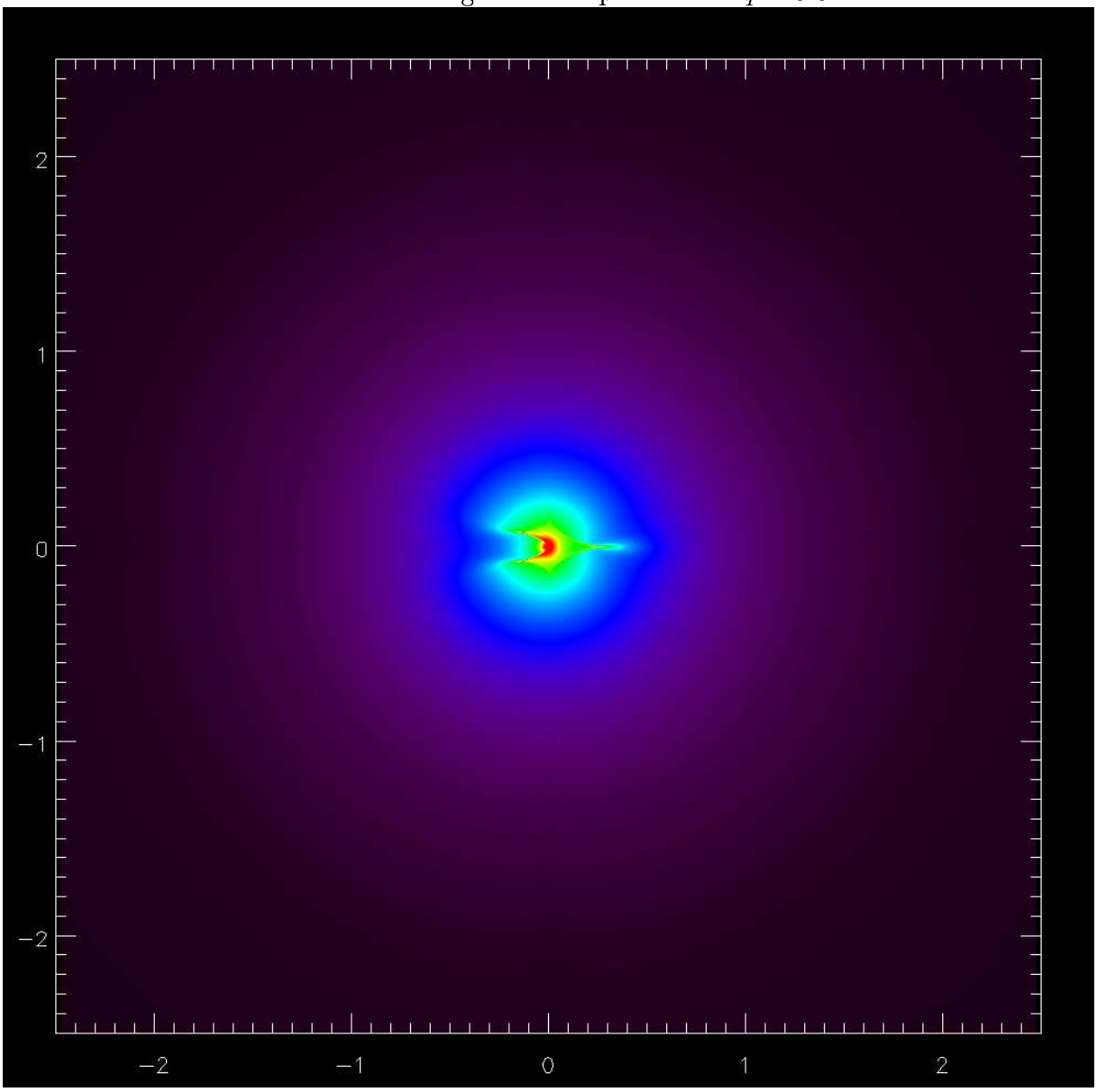

ratio between $q = 1.0$ and $q = 0.1$. If the mass ratio is of the order of $q = 10^{-2}$ the companion can be a brown dwarf, planet or a low-mass star, depending on the primary mass, while for a mass ratio of $q = 10^{-3}$ and a solar mass primary we have a Jupiter mass planetary companion, while for mass ratios of the order of $q = 10^{-5}$ we deal with planets of few Earth masses.

In Fig. 5.3.1 we see magnification patterns of systems with mass ratios of $q = 10^{-2}$, and in Fig. 5.3.2 for $q = 10^{-3}$. If we compare it to the magnification pattern of stellar binaries in the previous section ($q = 0.1, q = 0.3$), we can see how as the mass ratio decreases the system looks more and more similar to a single lens.

FIGURE 5.3.2. Magnification pattern for a Jupiter mass planet, $q = 0.001$

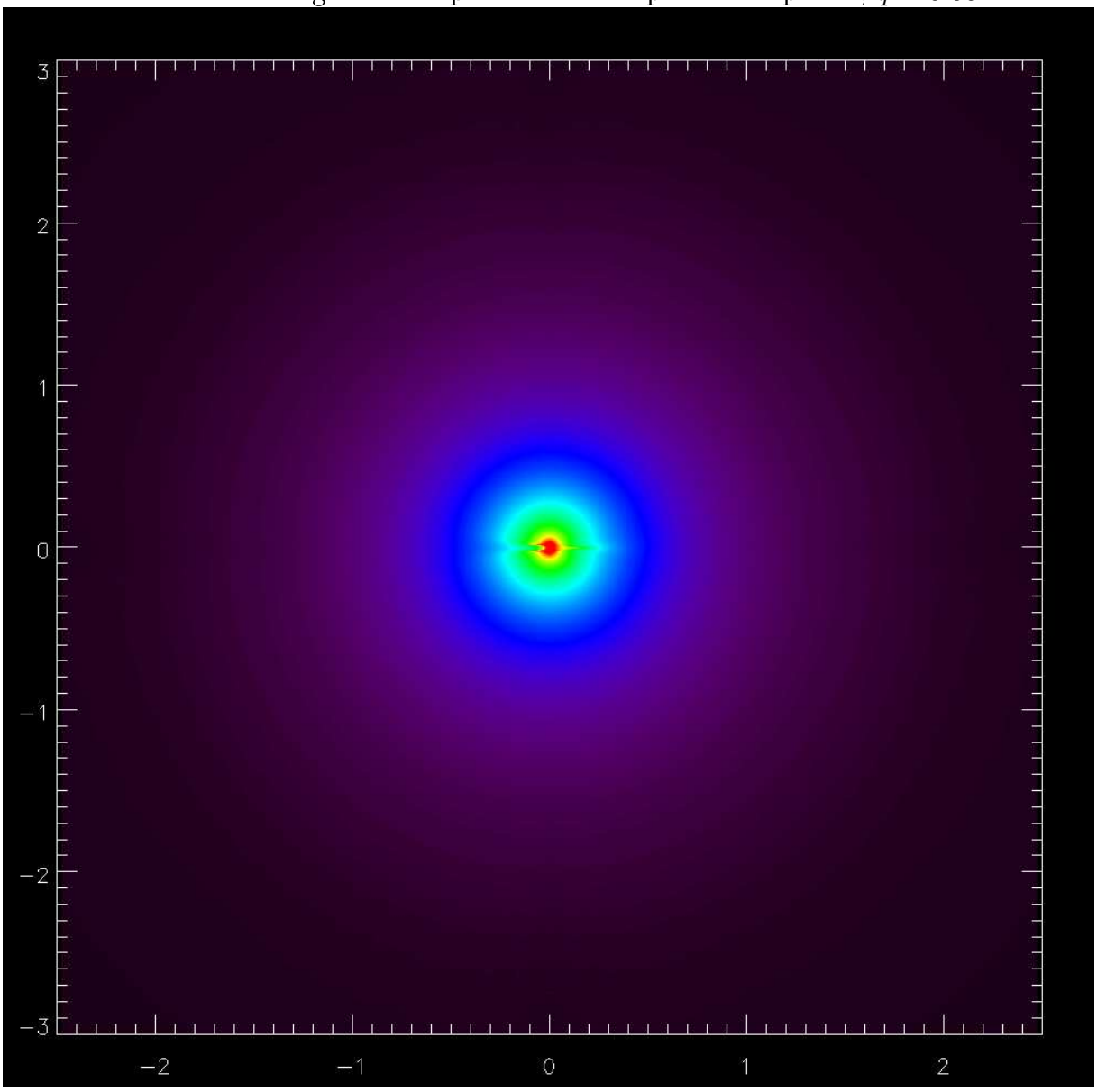

After the described analysis has been performed on static systems with fixed separation of $d = 1.0R_E$, and light curves with 30 out of 100 data points with $\sigma_0 = 0.03mag$, we got a family of curves with increasing ratios of misinterpreted fits as the mass ratio decreases (Fig. 5.3.3). This is in accordance with the intuitive guess one can get from looking at the magnification patterns. We see that for a Jupiter mass planet we still have a detectability, with few percent difference from a single lens fit, while for the lower mass ratios we cannot distinguish it from a single lens. If we decrease the errorbars to $\sigma_0 = 0.01mag$ and increase the data sampling to 100 out of 100 data points (Fig. 5.3.4)

FIGURE 5.3.3. Dependance of the ratio of misinterpreted fits on mass ratio shown as a function of $\chi^2/d.o.f.$ cutoff, for a static binary lens with separation of $d = 1R_E$, for stellar and planetary mass ratios, with the errorbar at the baseline of $\sigma_0 = 0.03mag$ and 30 out of 100 data points. Different colors of lines stand for the mass ratios: (cyan: 1.0, yellow: 0.3, magenta: 0.1, blue: 10^{-2}, green:10^{-3}, red: $10^{-4}$and black: single lens)

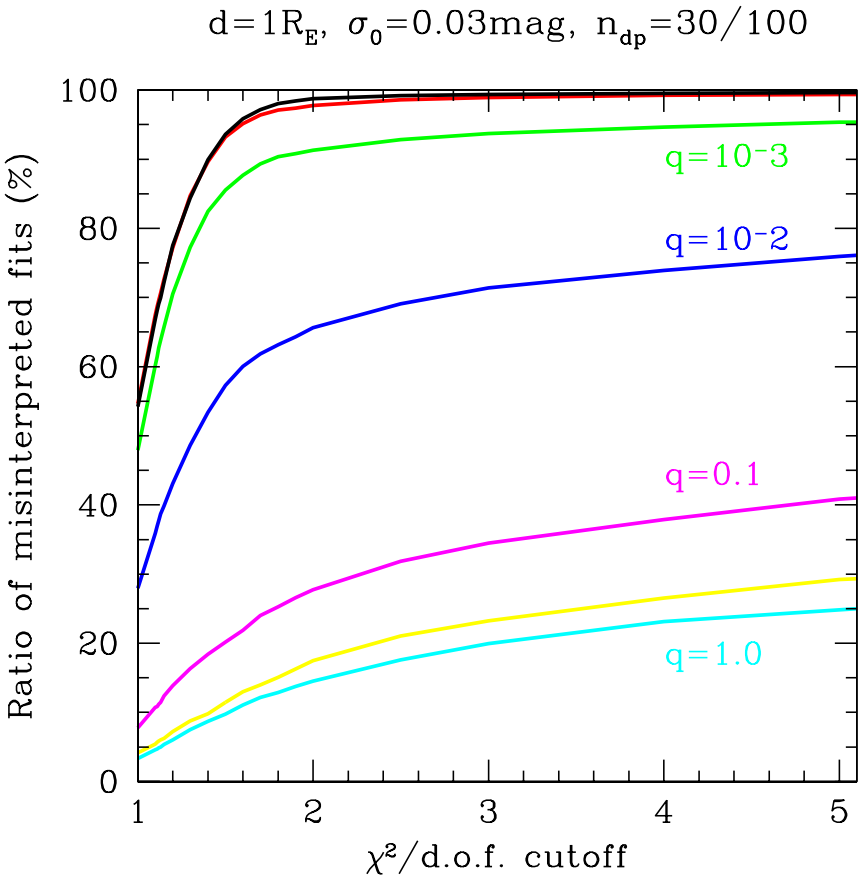

q	1.0	1.1	2.0	3.0
0.1	4.6	6.6	20.2	27.9
0.3	1.6	2.5	10.7	16.8
1.0	1.7	2.4	9.1	14.5

TABLE 5. Dependance of the ratio of misinterpreted fits on the $\chi^2/d.o.f.$ for a rotating binary lens, for different mass ratios, and cutoffs for $\chi^2/d.o.f.$ of 1.0, 1.1, 2.0 and 3.0.

we see that the detectability improves significantly for $q = 10^{-2}$ and Jupiters, and that even planet with a mass ratio of $q = 10^{-4}$ might be detected.

FIGURE 5.3.4. Dependance of the ratio of misinterpreted fits on mass ratio shown as a function of $\chi^2/d.o.f.$ cutoff, for a static binary lens with separation of $d = 1R_E$ for planetary mass ratios, with the errorbar at the baseline of $\sigma_0 = 0.01mag$ and 100 out of 100 data points
Different colors of lines stand for the mass ratios: (blue: 10^{-2}, green: 10^{-3}, red: $10^{-4}$and black: single lens)

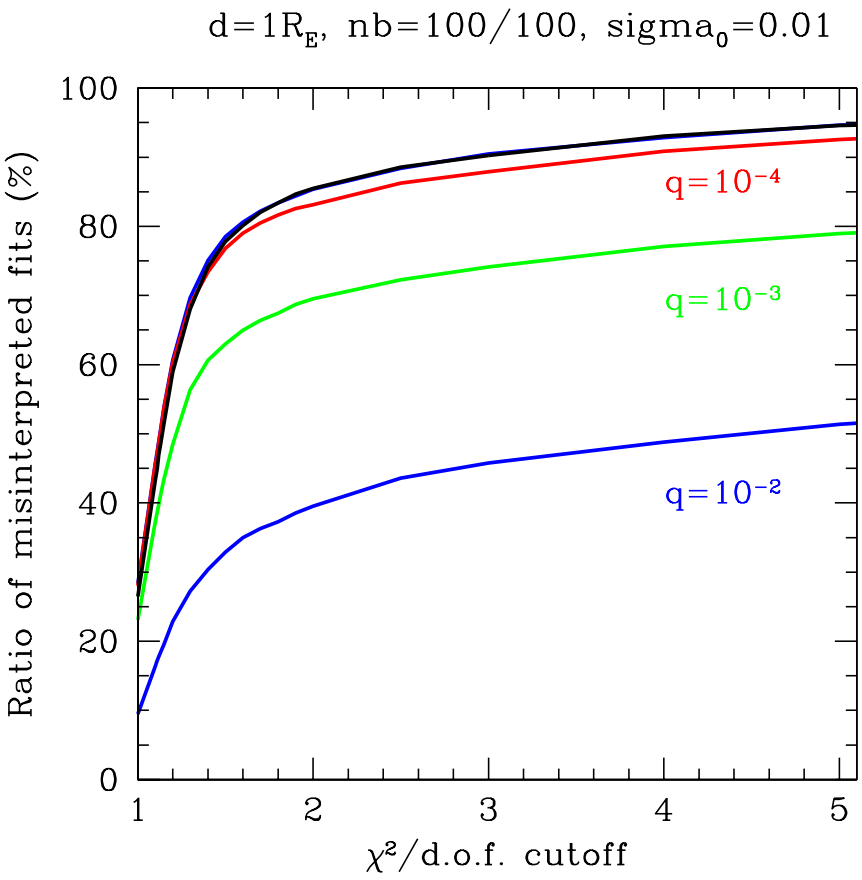

In Figure 5.3.5 we can see the same kind of calculations for a rotating stellar binary system, with mass ratios of 0.1, 0.3 and 1.0. The chance of misinterpretation is as expected smaller for bigger mass ratios, and also smaller than for the static case. This is mainly due to the fact that if the crossing time is of the order of the orbital rotation period, the chance is larger that a part of the magnification pattern which differs from that one for a single lens will be on the way of the source.

5.4. Dependence on binary separation

The dependence of the ratio of misinterpreted binary-lens fits with separation of the binary components is shown on Figs. 4.6 and 4.7, for a mass ratio of $q = 0.3$ and an angle of inclination of $i = 45^o$, for the rotating and static binary model, respectively.

FIGURE 5.3.5. Dependance of the ratio of misinterpreted fits on mass ratio shown as a function of $\chi^2/d.o.f.$ cutoff, for a rotating binary lens with separation of $d = 1R_E$, $i = 45^0$. Black line is the result obtained for a single lens.

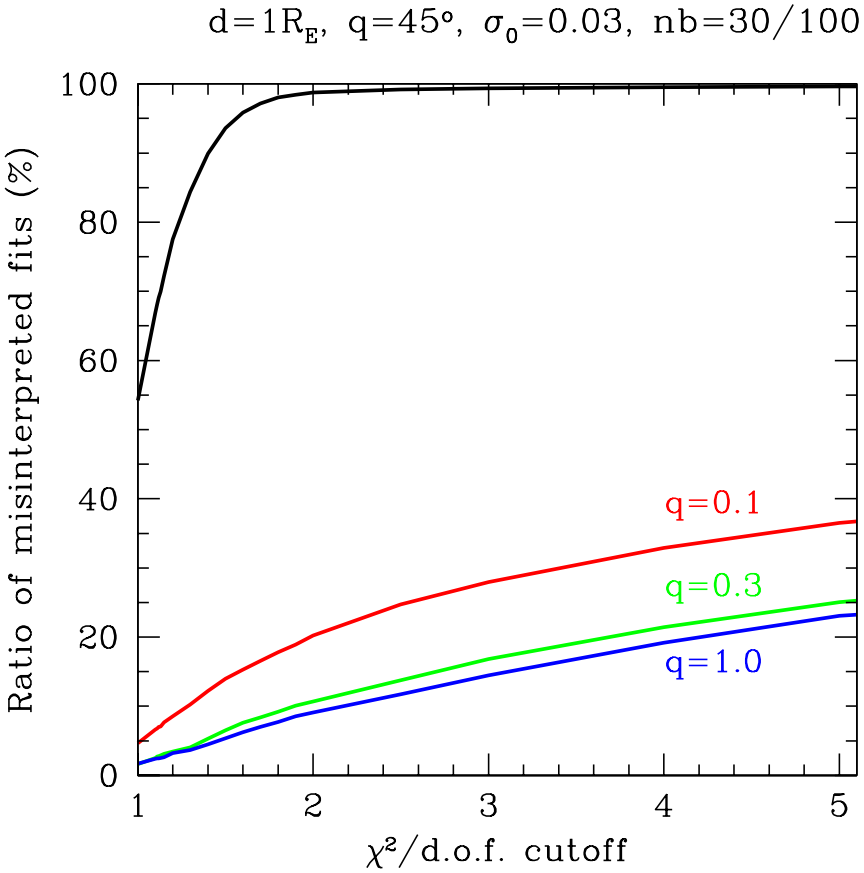

One can notice in both cases a steep decrease of the ratio of misinterpreted fits from very small separation up to a separation of about $0.6R_E$. When the two components are very close they behave as a single-lens, for both the static and the rotational model.

The results for the static approximation are shown in two panels in two plots, since for separation up to $d = 1.0R_E$ the ratio of misinterpreted fits is decreasing (Fig. 5.4.3), while for larger separation the trend is increasing again (5.4.2). For separations between $d = 0.6R_E$ and $d = 1.0R_E$ we reach the minimum, which seems to be flat in that range, since for $d = 0.8R_E$ we end up with the same values (black, red and green line at the bottom). For $d = 0.1R_E$ and $d = 0.2R_E$ the difference from the single lens can hardly be detected, while for the range between $d = 0.3R_E$ and $d = 0.5R_E$ the ratio of misinterpreted fits is uniformly decreasing. An interesting effect happens for $d = 0.55R_E$ (blue line): while the ratio of misinterpreted fits is almost the same as the one for the minimum range if the $\chi^2/d.o.f.$ cutoff is low, it increases steeper than the others for a high cutoff. To make sure this is not a random effect, we have performed

FIGURE 5.4.1. The percentage of misinterpreted fits for a static binary, $q = 0.3$, $\sigma_0 = 0.03mag$, 30/100 data points, for $d \leq 1.0R_E$. Black bottom line: $d = 1.0R_E$, red bottom line: $d = 0.8R_E$, green bottom line: $d = 0.6R_E$, blue bottom line: $d = 0.55R_E$, cyan bottom line: $d = 0.5R_E$, magenta: $d = 0.45R_E$, yellow: $d = 0.4R_E$, red top line: $d = 0.3R_E$, green top line: $d = 0.2R_E$, blue top line: $d = 0.1R_E$, black line: single lens.

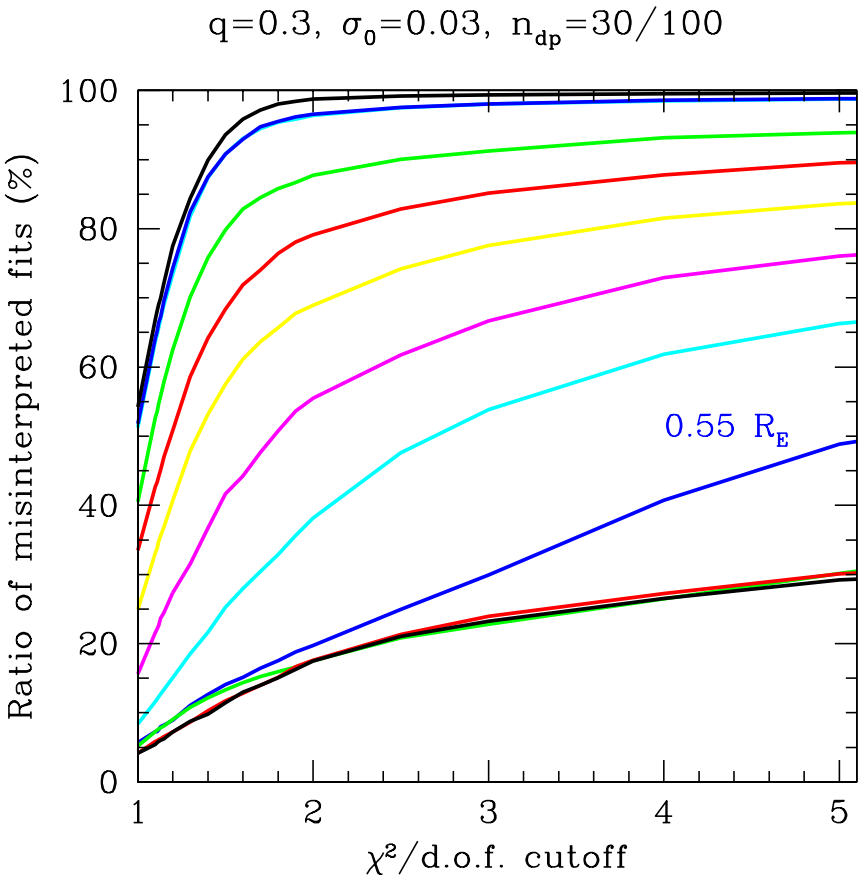

three different sets of calculations for this separation, with different random set of light curves, noise and data sampling, which have yielded same results. The reason for this is that around this separation we have the tiny triangular caustics (Fig. 5.4.4 and Fig. 5.4.5) which will give a signature of binarity only if we insist on a low $\chi^2/d.o.f$. For a separation larger than $d = 1.0R_E$ the trend is again uniformly increasing, since the two components, as they get more separated from each other, act as two single lenses.

The separation dependence for a rotating binary was calculated only up to the separation of $d = 2.0R_E$, since for larger separation we do not have events which are so long lasting as the rotational period. We see again the interesting effect for $d = 0.5R_E$ and $d = 0.6R_E$, for which the dependence on the $\chi^2/d.o.f$. cutoff seems to be stronger. This comes again from these small triangular caustics typical for these separations (see Figures 4.8 for $d = 0.5R_E$ and 3.3 for $d = 0.6R_E$). In the case of the rotating binary we

FIGURE 5.4.2. The percentage of misinterpreted fits for a static binary, $q = 0.3$, $\sigma_0 = 0.03mag$, 30/100 data points, for $d \geq 1.0R_E$. Black bottom line: $d = 1.0R_E$, red: $d = 2.0R_E$, green: $d = 3.0R_E$, blue: $d = 4.0R_E$, black line: single lens.

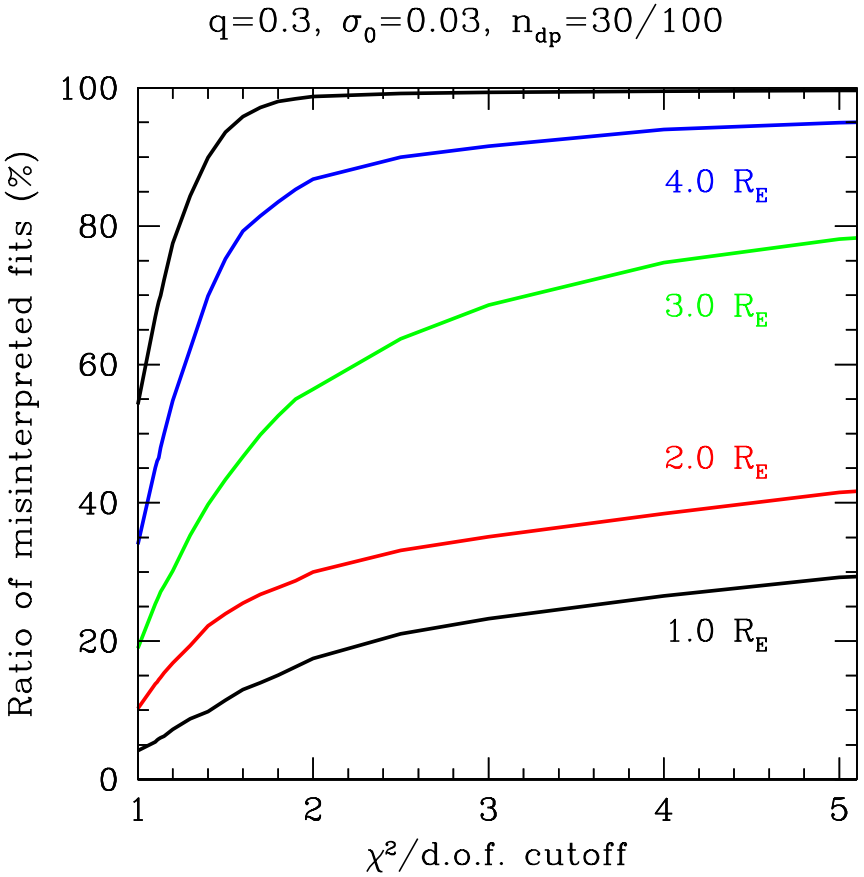

speak about the maximum separation which is observed only twice during one rotational period. However, for the assumed angle of inclination of $i = 45^o$, we reach the projected separations down to $i_{proj} = \cos i = \frac{1}{2}\sqrt{2}i = 0.707i$, so that we have a smaller projected separation than the physical separation.

For different angles of inclination $(0^o, 45^0, 90^o)$ no dependence of the ratio of misinterpreted fits was found.

5.5. Dependence on the maximum magnification

In Fig 5.5.1 the dependence of the ratio of misinterpreted fits on the magnitude at the maximum magnification of the lightcurve is shown, for one realization of a static binary $(q = 0.3, d = 1R_E)$. This example was especially chosen to show how the ratio of misinterpreted fits behaves in the binary separation most sensitive on signatures of microlensing.

$d[R_E]$	1.0	1.1	2.0	3.0
0.10	51.3	63.7	96.4	98.0
0.20	51.8	64.2	96.5	98.0
0.30	40.5	52.7	87.7	91.2
0.35	33.5	42.7	79.1	85.2
0.40	24.9	33.1	68.9	77.6
0.45	15.6	21.6	55.5	66.7
0.50	8.4	11.6	38.2	53.8
0.55	5.7	7.3	19.7	29.9
0.60	5.2	7.3	17.6	22.8
0.80	4.1	5.9	17.6	23.9
1.00	4.2	5.4	17.5	23.2
2.00	10.2	13.8	30.0	35.1
3.00	18.9	25.4	56.4	68.6
4.00	34.0	45.1	86.8	91.6

TABLE 6. Dependance of the ratio of misinterpreted fits on the $\chi^2/d.o.f.$ for a static binary lens, for different separations, and cutoffs for $\chi^2/d.o.f.$ of 1.0, 1.1, 2.0 and 3.0.

$d[R_E]$	1.0	1.1	2.0	3.0
0.40	14.2	20.2	63.6	79.5
0.50	5.5	7.7	30.1	47.2
0.60	2.8	3.9	13.3	23.3
1.00	1.6	2.5	10.7	16.8
2.00	10.2	13.8	30.0	35.1

TABLE 7. Dependance of the ratio of misinterpreted fits on the $\chi^2/d.o.f.$ for a rotating binary lens, for different separations, and cutoffs for $\chi^2/d.o.f.$ of 1.0, 1.1, 2.0 and 3.0.

It is obvious that the probability of a misinterpretation will be larger for smaller Δm. Overall, the fraction of misinterpreted binary events is low in this regime, of order of few percents. That is due to the fact that for larger magnification a caustic crossing usually takes place in the case of a binary lens event, which decreases the probability for misclassification.

5.6. Dependence on the size of errorbars

The sensitivity of the misinterpreation on the size of errorbars was also checked for one set of binary parameters ($q = 0.3, d = 1.0R_E$) and 30 out of 100 data points ($N_{data} = 30$) for a static binary.

On can see from Fig. 5.6.1, that this parameter plays an important role for the probability of misinterpreting the fits. This implies that in the case we have data sets with large errorbars, there is a big uncertainty on our model.

FIGURE 5.4.3. Rotating binary, $q = 0.3$,$i = 45^o$ $\sigma_0 = 0.03mag$, 30/100 data points

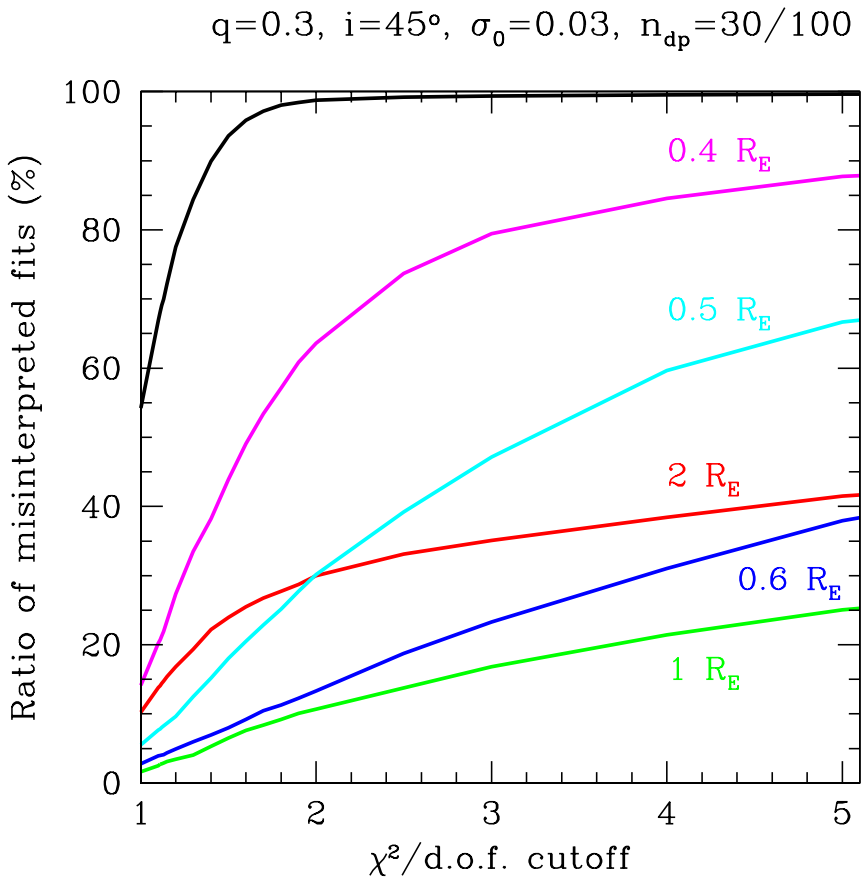

σ_0	1.0	1.1	2.0	3.0
0.01	0.5	0.8	2.6	5.7
0.03	4.2	5.4	17.5	23.2
0.10	13.9	18.4	37.3	44.0

TABLE 8. Dependance of the ratio of misinterpreted fits on the $\chi^2/d.o.f.$ for a static binary lens, for different size of errorbars, and cutoffs for $\chi^2/d.o.f.$ of 1.0, 1.1, 2.0 and 3.0.

5.7. Discussion

By studying stellar microlensing events towards the Galactic Bulge, we have found that it is realistic to expect that some binary lens lightcurves will be fitted well with single lens models and hence misinterpreted as single lens events; we quantitatively evaluated this effect. The probability for such a misinterpretation depends strongly on the separation of the two binary system components, reaching a minimum between projected separation of $0.6R_E$ and $1R_E$: for such binary lenses it is relatively unlikely

FIGURE 5.4.4. Triangular caustics for the rotating binary with separation of $d = 0.5R_E$. This figure shows phase=0.25, with the largest projected lens separation of $d_{proj} = 0.5R_E$

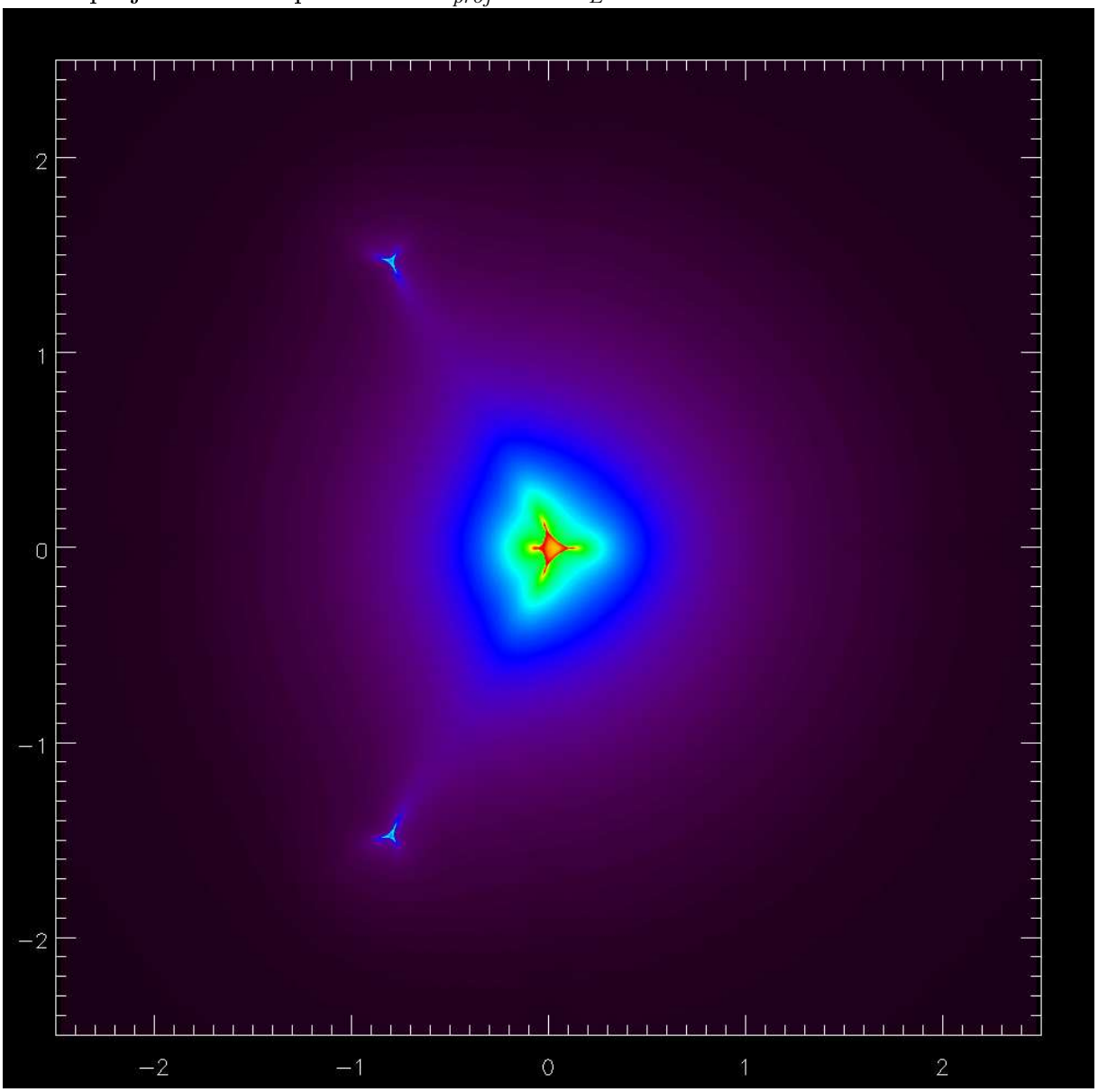

(probability of less than 10%) that they are misinterpreted. For smaller and larger separation, this probability will be larger, strongly depending on the separation.

For events with orbital period comparable to the Einstein crossing time of the order of a month or longer, that probability is reduced: the dynamic signatures of these lightcurves prevent them from being fit well by single-lens lightcurves. For events with Einstein crossing times of the order of days, the probability is larger, because the

FIGURE 5.4.5. Triangular caustics for the rotating binary with separation of $d = 0.5R_E$, shown for phase=0.50, and the smallest projected lens separation $d_{proj} = 0.707 \times d = 0.35R_E$. We see how the small triangular caustics slowly disappear as the projected separation decreases, making the binary lens more and more look like a single lens.

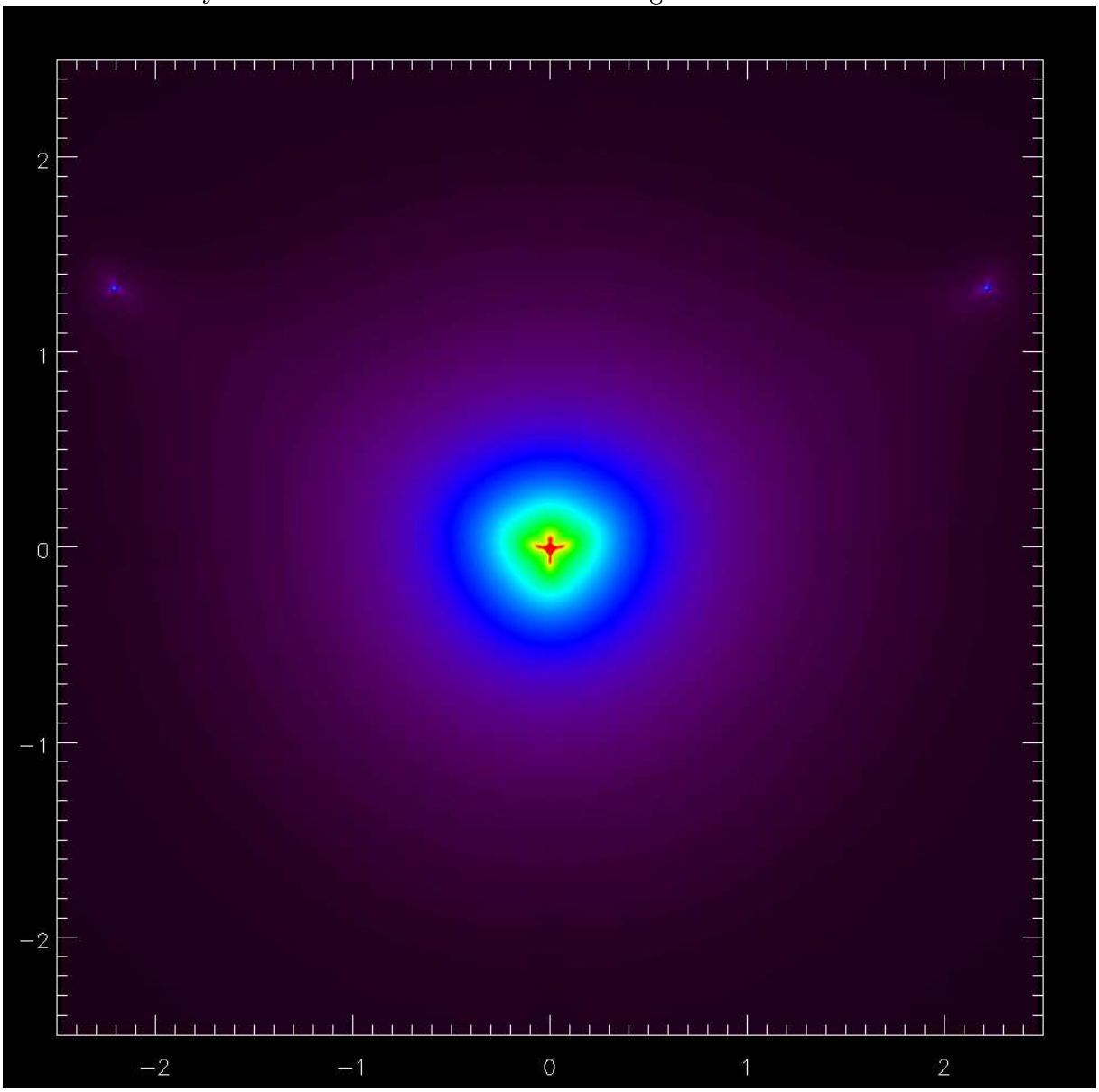

binary rotation will be neglected it the stars are at a large separation, and the system can behave as two separate single lenses.

The probability for misinterpretation increases for more extreme mass ratios. This is the reason why the detection probability for a binary system consisting of a star with a planet, is smaller that the detection probability for a stellar binary.

FIGURE 5.5.1. Dependance of the number of misinterpreted fits on the maximum magnification for one particular realization (static binary, $q = 0.3, d = 1R_E, \sigma_0 = 0.03mag$, 30/100 data points). Each point on this plot corresponds to one light curve fit.

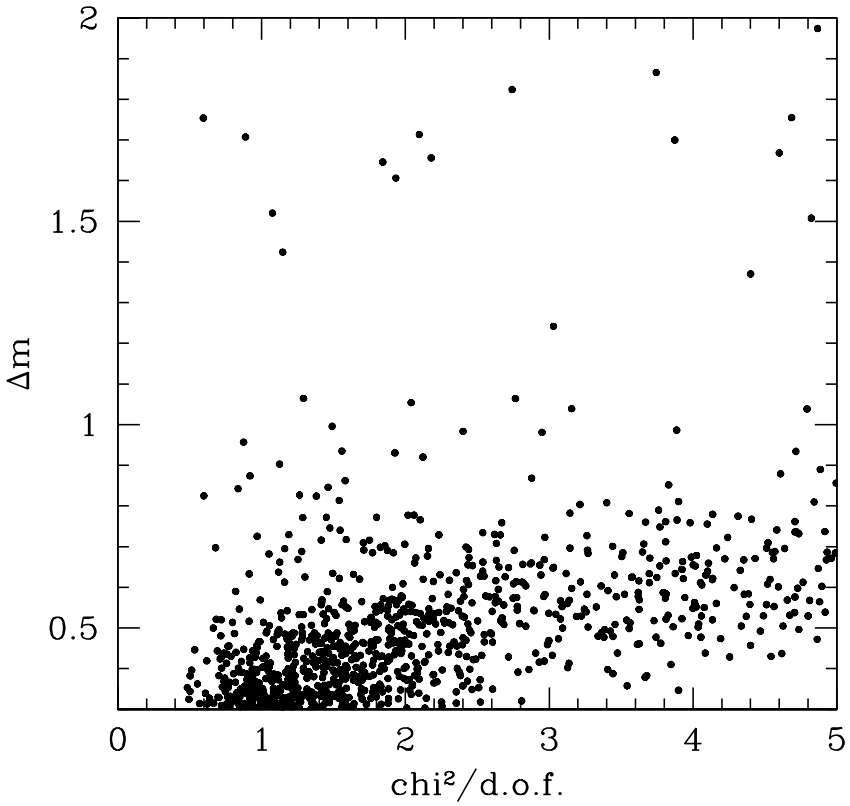

Good quality data , i.e. good data sampling and small errorbars decreases the probability for misinterepretation, but it is hard to imagine that it can be reduced to lower than a few percent.

From a statistical interpretation of a large number of observed binary microlensing events, the population of Galactic binary stars with certain separation limits can be determined. This study can help determine the percentage of binary stars in the Milky Way, by providing "correction factors" when using the observed samples of single-lens and binary-lens lightcurves from observations of towards the Galactic Bulge.

FIGURE 5.6.1. Dependence of the percentage of misinterpreted fits on the size of errorbars for $\sigma_0 = 0.01mag$ (green),$\sigma_0 = 0.03mag$ (red), $\sigma_0 = 0.1mag$ (blue), for a static binary, $q = 0.3$, $d = 1.0R_E$, 30/100 data points.

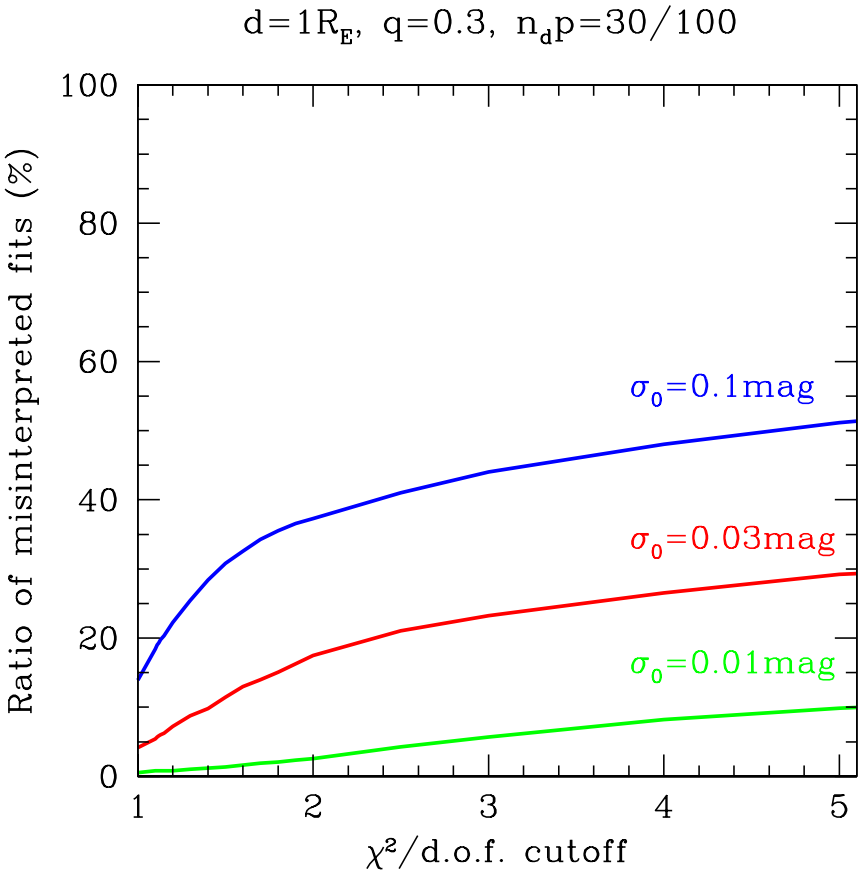

Part 2

Binary source modeling and PLANET events

CHAPTER 6

Binary source single lens microlensing events

As described in Part 1, about a half of the stars in our Galaxy are bound in binary systems. However, out of several thousands of microlensing events towards the Galactic Bulge, there have been only a few candidates for binary source microlensing events reported in literature so far (Gaudi and Han 2004, Jaroszynski at el. 2004, Collinge 2004). Fig. 6.0.1 shows an example of a binary source microlensing event OGLE-BLG-2003-067, observed by the OGLE team (Jaroszynski at el. 2004). Most of these candidates can be also fitted with a light curve produced by a single source, microlensed by a binary lens.

In order to understand this discrepancy, different authors carried out theoretical studies which could explain the mystery of lacking binary source events. Griest and Hu (1992) have performed a comprehensive study on the types of events which arise for binary sources. Depending on the type of the primary star star of the binary system, and the lens mass, they find that among binary source events, $60 - 95\%$ percent have a light curve which is primarily affected by only one of the objects.

Dominik (1998), showed that most of the binary source events show light curves which can be fitted with the simpler model of a blended single source. Blending is, as will be shown later in this work on the examples of microlensing events observed by PLANET, a big uncertainty factor when fitting both binary lens and binary source events. To account for the rarity of binary source events, Dominik pointed out that for a typical binary source event the separation between the component source stars is very large, resulting in a large difference in impact parameters between the component binary source stars. In these cases, the light curve of the highly amplified source star is barely affected by the light from the other star, making the observed binary source light curve difficult to distinguish from that of a single source lensing event.

This idea was later discussed by Han and Jeong (1998), who estimated the fraction of events with similar source star amplifications to be as much as 8%, and thus showed that the very low detection rate for binary source events cannot be explained by this effect alone. By carrying out simulations of binary source events, they found that a significant fraction of binary source events are additionally missed from detection due to a variety other reasons. First, if the flux ratio between the component stars is very large, the light curve of the bright star is hardly affected by the light from the faint star. Second, if the separation is too small, the binary source stars behave like a single star, making it difficult to separate the binary source event from a single event. Finally, although the probability of detecting binary source events increases as the source separation increases, still some fraction of binary source events will be missed

FIGURE 6.0.1. Binary source event OGLE-BLG-2003-067 (Jaroszynski at el. 2004). Red dots are data points observed by OGLE team, without errorbars shown. Solid green line is a binary source fit. Dotted greens lines show flux contribution from the two binary components, and blended light.

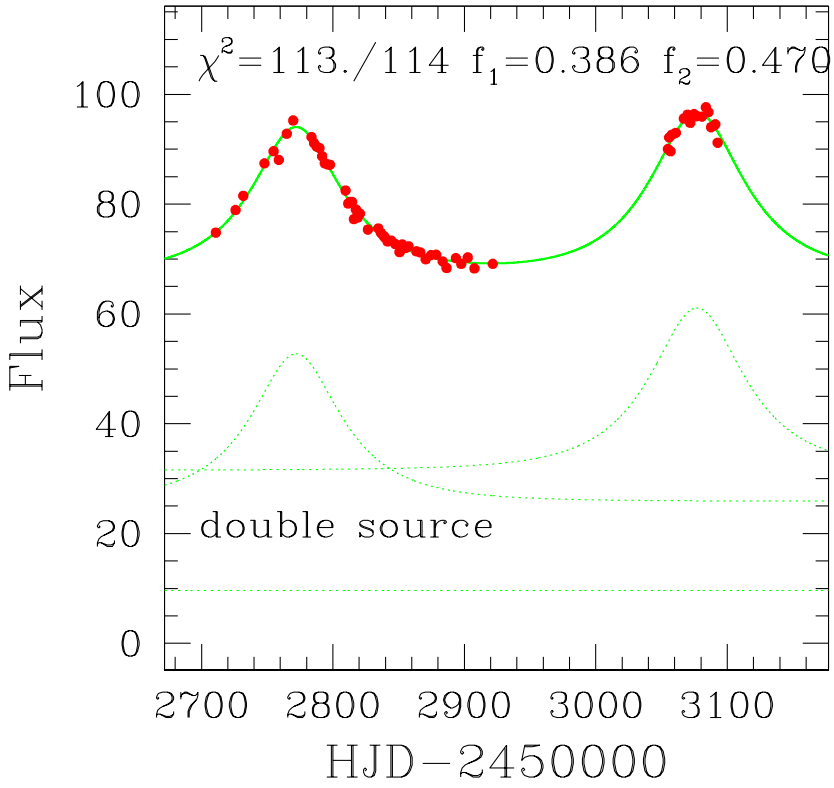

because the light curves of these events will mimic those of single source events with longer timescales and larger values of the impact parameter.

6.1. The problem of degeneracy

For binary source candidates reported in the literature so far, in most cases there exists a degeneracy in solution. This can also be one of the causes for observing so few binary source events, since they can often be interpreted as binary lens events.

Gaudi and Han (2004) report on various solutions on the light curve of the event OGLE-2002-BLG-055 observed by the OGLE team in 2002, which is characterized by a smooth, slightly assymetric single lens light curve with an isolated, secure data point which is 0.6 mag brighter than neighboring points (Fig. 6.1.1). A subset of binary lens fits consists of a family of continuously degenerate models whose mass ratios differ by an order of magnitude, even including a possible planetary companion to the lens

primary star. This deviant data point can also be explained by a binary source with flux ratio of 1 percent, microlensed by a single lens. The case of OGLE-2002-BLG-055 gave a very clear hint of a need for good follow up observations with very dense data sampling, in order to break the degeneracy. Collilnge (2004) presented degenerate binary lens and binary source solutions for event OGLE-2003-BLG-095. Jaroszynski et al (2004) presented several events from OGLE-III EWS database for seasons 2002 and 2003, showing degeneracy between binary lens and binary source solutions. However, the problem with the light curves observed only by OGLE team was very irregular data coverage. Many of the peaks in both models are not covered by data at all, which introduces a very high uncertainty factor. Examples of two such events are shown in Fig. 6.1.2.

Gaudi (1998) discussed in detail the degeneracy between extreme flux ratio binary source microlensing events, and planetary microlensing events. Extreme flux ratio binary source events can produce standard light curves with small, short-duration, positive perturbations. These perturbations can reproduce the gross features of one class of planetary perturbations: major image perturbations. The other class of planetary perturbations, minor image perturbations, cannot be reproduced by binary sources. For a binary source event to mimic a planetary event, the sources must have a small flux ratio ϵ, and the fainter source must pass close to the lens, with an impact parameter $\beta_2 \leq \frac{\epsilon}{\delta_{max}}$, where δ_{max} is the maximum fractional deviation from the unperturbed light curve. The detection probability for these events is$\sim \beta_2$.For $\epsilon = 0.01$ and $\delta_{max} = 0.05$, the probability is around 20 percent. In Fig. 6.1.3 one can see a comparison of light curves for a planetary event (solid curve) and a binary source event (short-dashed curve).

6.1.1. How to break the degeneracy? Gaudi suggested few ways to break the described degeneracy. One of them is to obtain accurate and dense sampling of the light curve. This was done successfully managed in the case of OGLE-2006-BLG-390 event (Beaulieau et al. 2006), which resulted in the discovery of a 5.5 Earth mass planet, OGLE-2006-BLG-390Lb. This discovery will be explained in more detail in Chapter 11.

Another way Gaudi suggested to break the degeneracy is to use color information. If the perturbation is due to a binary source, and the sources have different colors, there will be a color change during the course of the perturbation. The problem with this method is that if the flux ratio is very extreme, the color change will be difficult to observe. On the other hand, if dealing with binary source components of similar fluxes, the color difference cannot be large, due to mutual stellar evolution.

One possible method is to take spectra of the source both during and after the perturbation. If the perturbation is due to a binary source, both sources will be contributing to the spectrum during the perturbation, whereas after the perturbation, only the primary will contribute significantly to the spectrum.

Han (2002) suggested to observe lensing events astrometrically, in order to break the degeneracy between the binary source and the planetary lensing perturbations. This is possible because while the planet induced perturbation in the trajectory of the lensed source image centroid shifts points away from the opening of the unperturbed elliptical

FIGURE 6.1.1. Severely degenerate event OGLE-2002-BLG-055 (Gaudi and Han 2004). The points with errorbars show the light curve of event. The long-dashed magenta line shows the best single lens, single source, constant velocity model fit to the data, with the single high point and two neighboring points removed. The short dashed blue line shows the best single lens, single source, constant acceleration model fit to the same dataset. The dotted green line shows the best single lens, binary source, constant acceleration model to the entire data set. The solid red line shows the best single source, binary lens, constant acceleration model to the entire dataset. The inset shows a close up near the deviation.

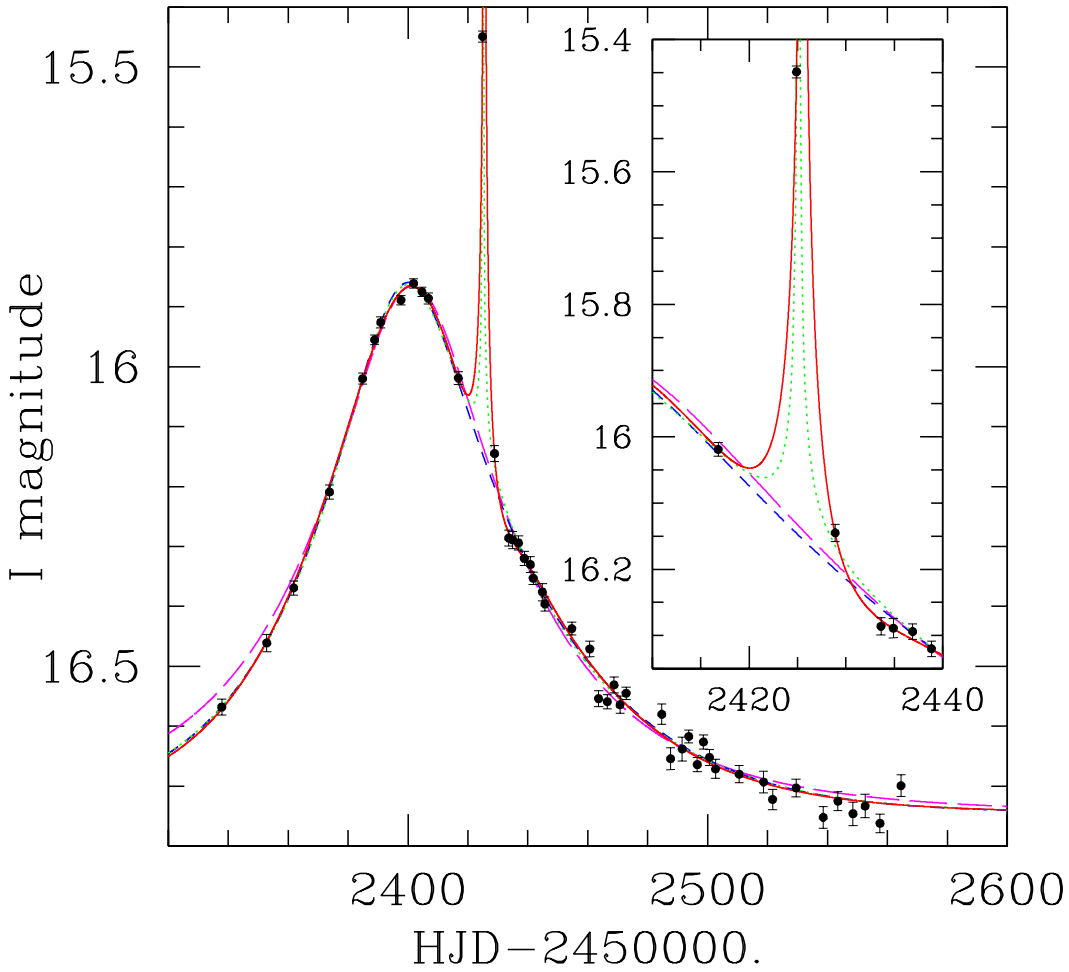

trajectory, the perturbation induced by the binary source companion will always point toward the opening. Astrometry will break not only degeneracy between binary lenses and binary sources, but also among several binary lens solutions to a photometric light curve (Gould and Han 2000). New astrometric facility PRIMA (Phase Referenced

FIGURE 6.1.2. Two examples of degenerate events OGLE-2002-BLG-256 and OGLE-2002-BLG-321 (Jaroszynski at el. 2004). In the left panels we see binary lens fits in magnitudes, in the right panels corresponding binary source fits in flux.

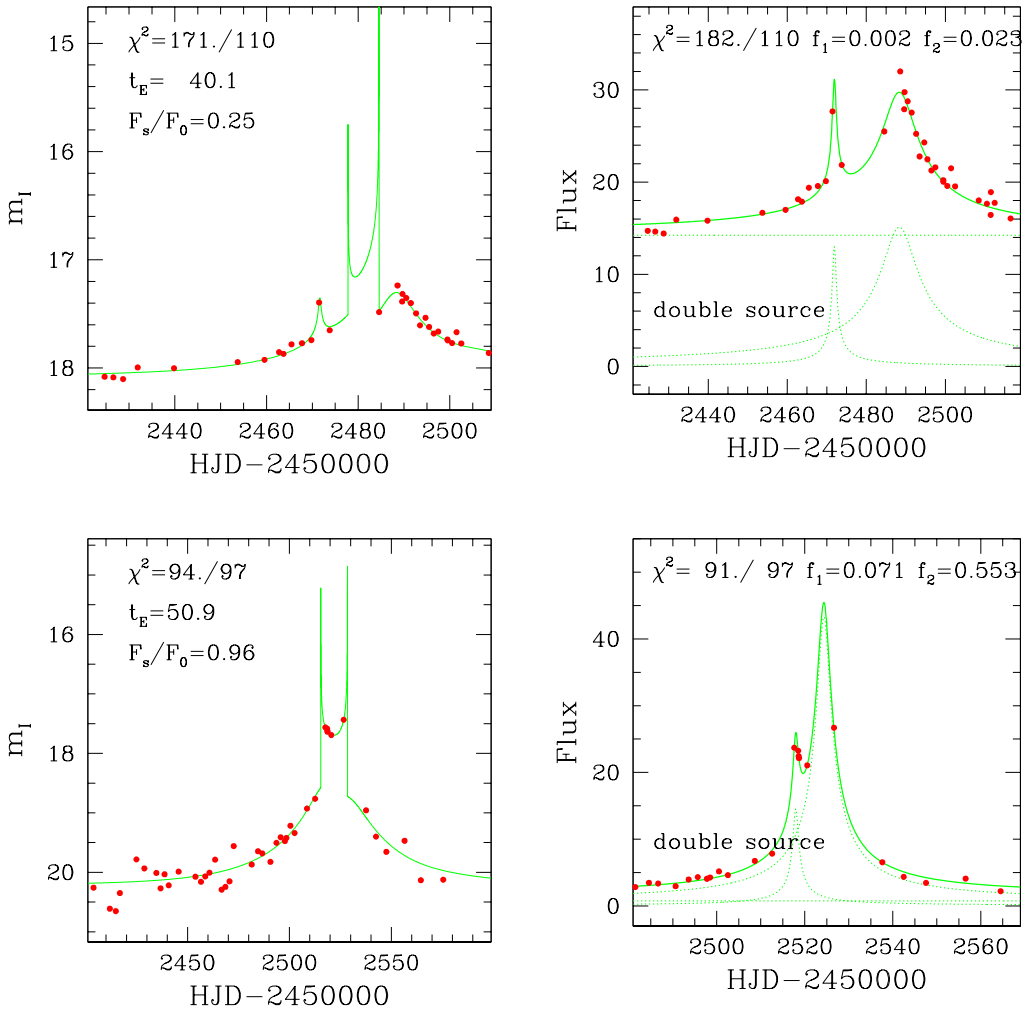

Imaging and Microarcsecond Astrometry) on the VLTI (see Part III for details), which should start functioning in 2008 (Delplancke et al. 2006), with expected high-precision of 10 micro arc sec, may allow breaking the degeneracy (Paresce et al. 2003).

6.2. Binary stars in the Galactic Bulge

In order to find a way to break the degeneracy, one has to understand the nature of stars in the Galactic Bulge.

The Galactic Bulge is hidden behind significant quantities of interstellar dust. Fortunately, we are able to 'peek' through Baade's Window (Fig. 6.2.1). It is a small clearing in the dust clouds of Sagittarius, near the globular cluster NGC 6522, through

FIGURE 6.1.3. Magnification as a function of time in units of the Einstein ring crossing time, t_E, for a planet/star system (solid curve) with a mass ratio $q = 10^{-3}$, a separation in units of the Einstein ring of $d = 1.3$, and angle between the planet-star axis and direction of source motion $\phi = 45^o$, and for a binary-source system (short-dashed curve) with flux ratio $\epsilon = 5 \times 10^{-3}$, projected separation in units of the Einstein ring $b = 0.5$, and angle between the binary-source axis and the direction of source motion $\theta = 44^o$. (Gaudi 1998)

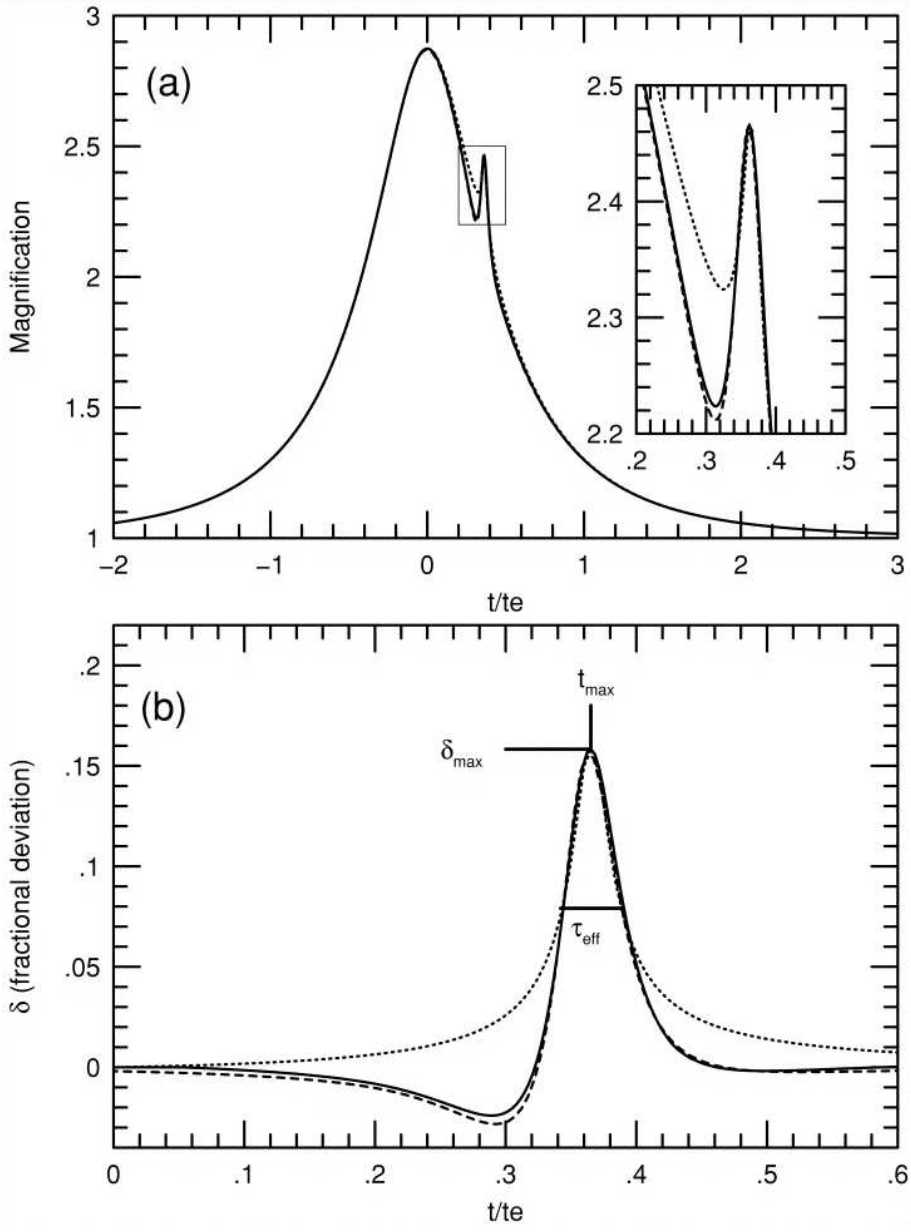

FIGURE 6.2.1. Stars and Dust Through Baade's Window. Copyright: David Malin (AAO), ROE, UKS Telescope

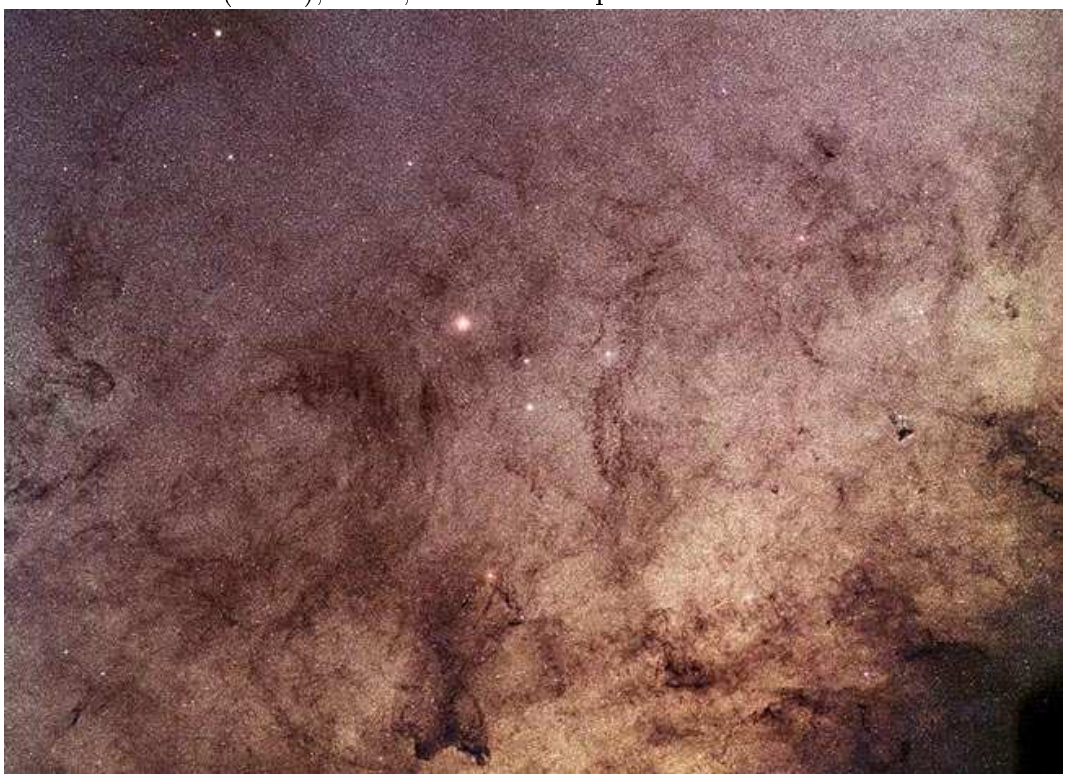

which we can observe stars in the Galactic Bulge. The window lies 3.9° south of the Galactic center.

Wozniak & Stanek (1996) proposed a new method to investigate interstellar extinction, based on two band photometry, which uses red clump stars as a means to construct the reddening curve. Stanek (1996) applied this method to the color-magnitude diagrams obtained by OGLE to construct an extinction map of (40') region of Baade's Window. He found that the total extinction in V photometric band A_V varies from 1.26 mag to 2.79 mag.

The Galactic Bulge is barred and rotates rapidly. Based on a comparison of color-magnitude diagrams, most of the stars in Baade's Window are coeval with the Bulge globular clusters and, therefore are old ($\sim 10 - 12 Gyr$). The Bulge stars have a broad [Fe/H] abundance distribution with mean at -0.25, and enhanced Mg and Ti abundances. Taken together, these findings strongly argue for an early, dissipative Bulge formation process (Gerhard 2000).

Zoccali et al (2003) determined the age of stars in the Bulge to be as old as that of Galactic globular clusters, $\geq 10 Gyr$. They used near-IR data from the 2MASS survey, from the SOFI imager at ESO NTT, as well as NICMOS camera on board HST, and were able to construct color-magnitude diagrams (CMD) and luminosity functions (LF) with good statistics and small photometric errors from the Asymptotic Giant Branch

(AGB) and Red Giant Branch (RGB) tip down to $\sim 0.15\ M_{\odot}$. They report that no trace is found for any younger stellar population.

Stellar binary pairs consisting of a giant primary with a main-sequence secondary star are more common than pairs of two giants. The reason for this is that stars live a short time on the giant branch, so if there is more than about 10% difference between the masses of the component, the secondary star will remain a dwarf until the primary has evolved to a white dwarf (Andersen 2006). This means that we expect more binary sources to have an extreme flux ratios. However, they are often hard to observe, for the reasons explained in the beginning of this chapter. More on flux ratios of binary sources will be discussed in Chapter 8.

In a binary system both stellar components are of the same age. As stars evolve, they change their stellar types, i.e. change photometric colors. A line connecting stars of different masses of the same age and metalicity is called an *isochrone*. If we plot $[V - I]$ color vs. I apparent magnitude of stars of the age of 10 Gyr for the distance of 8 kpc and the Solar metalicity, we get an isochrone shown in Fig. 6.2.2. This isochrone is calculated using the BaSTI (A bag of Stellar Tracks and Isochrones) database, explained in Pietrinferni et al. (2004), Bedin et al. (2005), Cassisi et al. (2004) and Pietrinferni et al. (2006). This can be used as a good approximation for the stars in the Galactic Bulge. The mass decreases as the magnitude gets fainter. At this age, low mass stars will still be on the main sequence for this age, while high mass stars have already evolved into the giant branch. The reddening vector will shift the isochrone towards the lower right corner of the plot, i.e., stars will appear fainter. The amount of reddening for an observed object can be determined from the extinction map in Baade's Window (Stanek 1996). Using isochrones and color information can help us determine the stellar type of the source, i.e. both source components in case of a binary source. It can be also used to determine the distance to the source (Cassan et al. 2006), i.e. to exclude non-physical solutions to a microlensing light curve, in the case of degenerate solutions.

6.2.1. The distance modulus. To convert the apparent magnitude (m) of a star into a real magnitude for the star (absolute magnitude, M), we need to know the distance (d) to the star. Alternatively, if we know the distance and the absolute magnitude of a star, we can calculate its apparent magnitude. Both calculations are made using:

$$m - M = -5 \log(d/10)$$

with m - M known as the distance modulus and d measured in parsecs.

So if we assume distance to the source of 8kpc:

$$m - M = -5 \log(800) = -14.5$$

FIGURE 6.2.2. Isochrone for stars of 10 Gyrs age at the distance of 8.0 kpc, without reddening (from BaSTI). [I-V] photometric color is plotted against apparent magnitude. Reddening will shift the isochrone towards the bottom right corner.

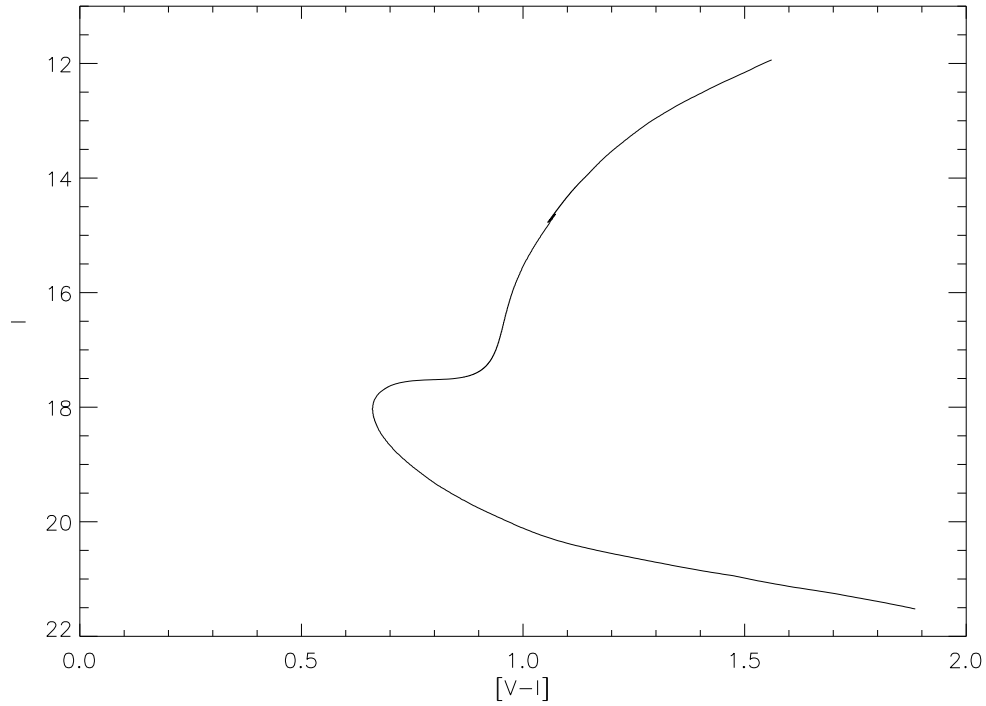

CHAPTER 7

Fitting binary source events

A binary system acting as a microlensing source will produce a light curve which will be a superposition of two single lens - single source light curves. In some cases one is able to recognize a double peak on the light curve, or at least some kind of assymetry of the single peak. By these features one can distinguish by visual inspection of the light curve, if the event is a binary source candidate. If there's a double peak in the light curve, for the Galactic microlensing scenario, it is most likely that the orbital period of the binary pair is of the order of years (i.e. separation of components of the order of few A.U.). It means that for the microlensing event with an Einstein crossing time of the order of a few weeks, the binary can be approximated as a static system consisting of 2 stars (source A and source B) moving with the same transverse velocity behind the lens. For such a system we can assume the common Einstein crossing time t_E for both components. However, they will have a different angular separation relative to the lens, i.e. different impact parameters $u_0(A)$ and $u_0(B)$. In most cases they are unlikely to reach the maximum magnification points at the same time, so we should expect two peaks with maximum magnification times $t_0(A)$ and $t_0(B)$.

When observing from different observing sites in parallel, one should expect different blended fluxes which add up to the magnified source flux. So for each observing site and photometric band set i, there will be a corresponding blended flux F^i_{blend}. The same applies for the source star fluxes. We measure unmagnified source component fluxes F^i_A and F^i_B, which are different from site to site. However, we expect the relative flux ratio $fr(k)$ of the two stellar components A and B, for a photometric band k:

$$fr(k) = F_A/F_B$$

to be constant for the given band k and independent from the observing site, under the assumption there is no star variability of any of the components.

The expression for the total flux at the site i as a function of time will be:

$$F^i(t) = F^i_A A_A(t) + F^i_B A_B(t) + F^i_{blend}$$

where $A(t)$ is magnification as a function of time for the given source star, defined through Einstein crossing time t_E , impact parameter u_0 and time of maximum magnification t_0:

$$A = \frac{u^2+2}{\sqrt{u^2+4}}$$

$$u = \sqrt{u_0^2 + (\frac{t - t_0}{t_E})^2}$$

Baseline flux (i.e. nonmagnified flux for the event) is:

$$F^i_{base} = F^i_A + F^i_B + F^{i,k}_{blend} \tag{7.0.1}$$

We define the so called blending factor $g^{i,k}$ as:

$$g^{i,k} = \frac{F^{i,k}_{blend}}{F^i_A + F^i_B}$$

In order to find the best solution of a microlensing light curve measured in the same time interval at n observing sites we will have to fit simultaneously the 6 site-independent parameters:

$$t_E, u_0(A), t_0(A), u_0(B), t_0(B), fr(k)$$

as well as $2n$ flux parameters corresponding to F^i_{blend} and F^i_A for each site, while F^i_B will be defined through flux ratio $fr(k)$.

The total number of parameters j_{par} to be fitted is:

$$j_{par} = (2n_{os} + 1)n_{pb} + 5$$

where n_{pb} is number of photometric bands, and n_{os} is the number of observing sites.

7.1. BISCO fitting code

If we have a binary source light curve with well separated peaks due to the binary components, observed at only one site, in only one photometric band, the light curve could be fitted with an optimizing routine which is not too sensitive on local minima, for example Simplex (see Section 3.3). However, for multi-site fitting, in two or more photometric bands, we get additional parameters explained above, for each site, and additional parameters for each photometric band. If the difference between the closest approach times for the two components $t_0(B) - t_0(A)$ is small compared to the Einstein crossing time t_E, the two peaks will merge, and it will be difficult to easily distinguish their contributions and estimate the times of the closest approach. All these difficulties, encountered for typical microlensing events observed by PLANET, suggested a need for a more robust optimizing tool to disentangle parameters for observed binary source events.

The fitting code BISCO (Binary Source Code for Optimization, Dominis 2005) uses the genetic algorithm general optimizing routine PIKAIA (Charbonneau 1995) in order to find the best solution of the $n_{pb} + 5$ site-independent parameters:

$$t_E, u_0(A), t_0(A), u_0(B), t_0(B), fr(k)$$

where t_E is the common Einstein crossing time, $u_0(A)$ and $u_0(B)$ are the impact parameters due to the two stellar components, $t_0(A)$ and $t_0(B)$ are the times of closest approach, and $fr(k)$ is the flux ratio in the given photometric band, in parallel with with

linear fitting routine $LFIT$ (Press et al. 1992) to fit the $2n$ observing site depending corresponding fluxes for each site.

In order to find how successful the code is in finding the solution of the binary source microlensing and stellar parameters from the measured light curves, different synthetic light curves were constructed to mimic light curves which could be produced through microlensing of a binary source in a Galactic Bulge with different component fluxes and blended flux of the same order of magnitude as source fluxes. For a given model, different kinds of synthetic light curves were constructed: a 'clean' light curve (no noise, regular data coverage), the same light curve with Gaussian scatter added, and a light curve where on the top of Gaussian scatter random data points were erased to simulate irregular data coverage. In Fig. 7.1.1 we see an example for such simulated light curves, for a hypothetical event with these parameters:

$t_E = 20days$, $t_A = 3330$[JD-2450000], $t_B = 3345$[JD-2450000], $u_A = 0.05$, $u_B = 0.30$, $fr = \frac{F_A}{F_B} = 0.2$, $g = \frac{F_{blend}}{F_A+F_B} = 0.33$.

Different synthetic binary source events were constructed to challenge BISCO and test its ability to find the best solution. More on the optimization method, and on performing these tests will be discussed in the following sections of this chapter.

7.2. Genetic algorithms

We now explain why a genetic algorithm was chosen as an optimization method for problems of optimizing observed light curves of binary source and binary lens microlensing events. Genetic algorithms (GAs) are a class of search techniques inspired from the biological process of evolution by means of natural selection. They can be used to construct numerical optimization techniques that perform robustly on problems characterized by ill-behaved search spaces.

An optimization scheme based on a genetic algorithm (GA) can avoid the problems inherent in more traditional approaches. Restrictions on the range of the parameter space are imposed only by observations and by the physics of the model. Although the parameter space is often quite large, the GA provides a relatively efficient means of searching globally for the best fit model. While it is difficult for GAs to find precise values for the set of best fit parameters, they are well suited to search for the region of parameter space that contains the global minimum. In this sense, the GA is an objective means of obtaining a good first guess for a more traditional method which can determine the precise values and uncertainties of the best-fit.

The underlying principles for genetic algorithms were inspired by Charles Darwin's (1859) notion of biological evolution through natural selection. The basic idea is to solve an optimization problem by evolving the best solution from an initial set of completely random guesses. The theoretical model provides the framework within which the evolution takes place, and the individual parameters controlling it serve as the genetic building blocks. Observations provide the selection pressure. A comprehensive description of how to incorporate these ideas in a computational setting was written by Goldberg (1989).

FIGURE 7.1.1. Synthetic light curves for a binary source event with parameters: $t_E = 20days$, $t_A = 3330$[JD-2450000], $t_B = 3345$[JD-2450000], $u_A = 0.05$, $u_B = 0.30$, $fr = \frac{F_A}{F_B} = 0.2$, $g = \frac{F_{blend}}{F_A + F_B} = 0.33$.
Top panel: red and green lines are magnitudes of the two binary components, black line composite magnitude of a binary source. Bottom panel: on the 'ideal' light curve (black line), Gaussian noise with errorbars of $\sigma_0 = 0.05mag$ at the baseline was added, and 100 out of 300 data points randomly selected.

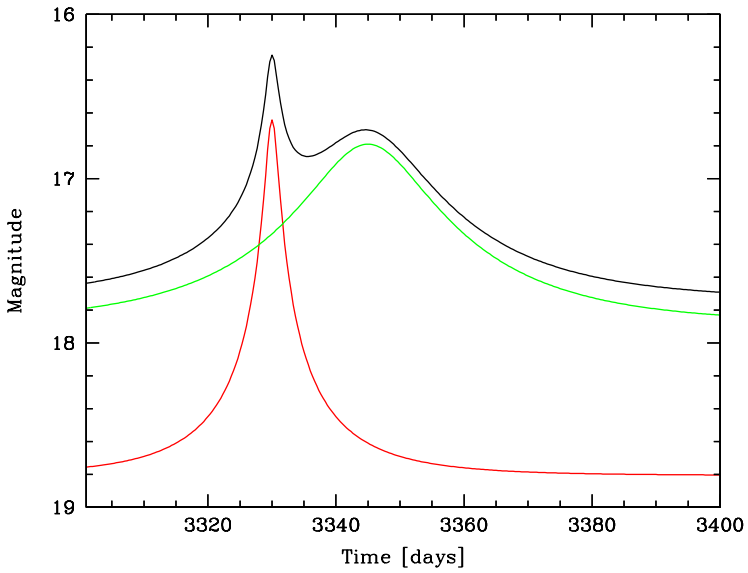

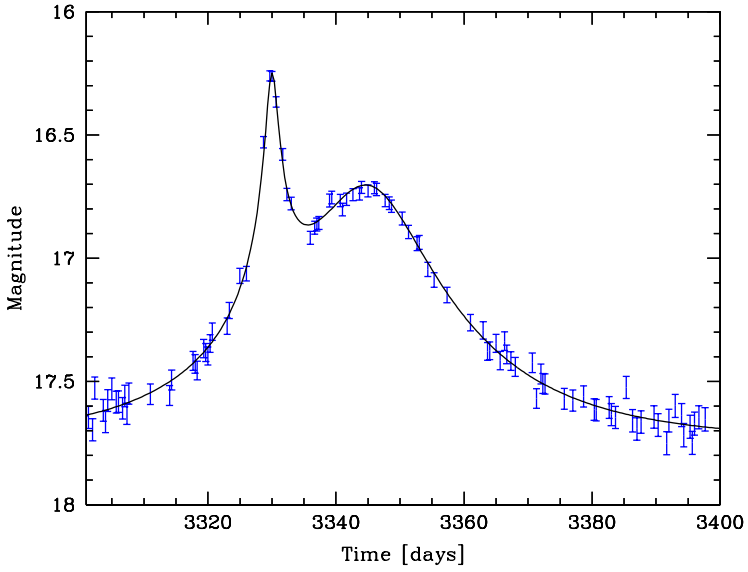

FIGURE 7.2.1. An example of a 2-D parameters space with many local maxima.

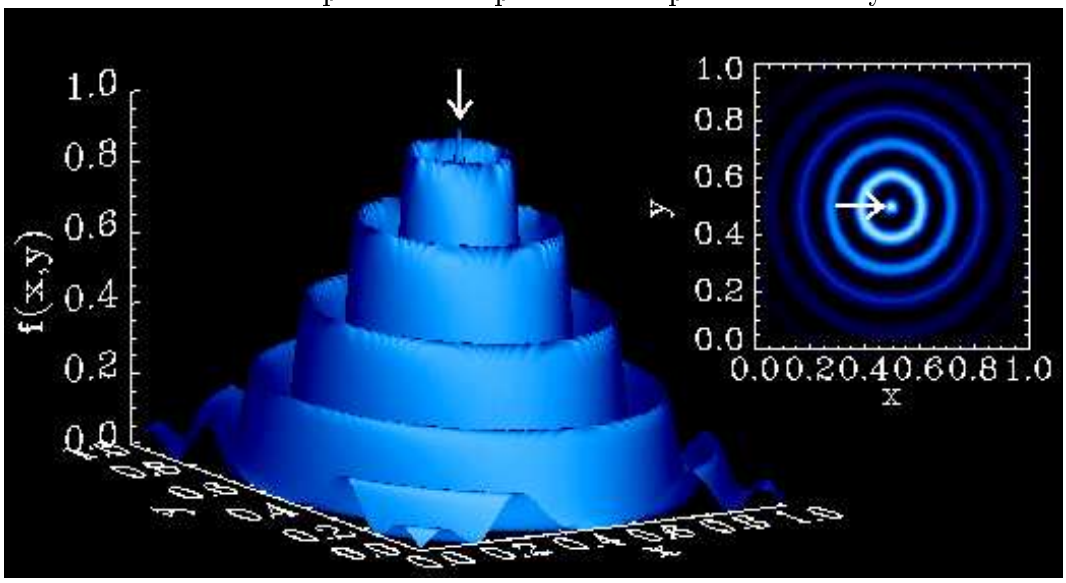

Initially, the parameter space is filled uniformly with trials consisting of randomly chosen values for each parameter, within a range based on the physics that the parameter is supposed to describe. The model is evaluated for each trial, and the result is compared to the observed data and assigned a fitness based on the relative quality of the match. A new generation of trials is then created by selecting from this population at random, weighted by the fitness f. Fitness is a function defined by the user of the genetic algorithm, constructed to determine the probability of an individual to be selected for breeding, and not to be deleted from the population. The larger the fitness, higher the probability for the survival of the individual. Fitness is defined in BISCO optimizing code (see Section 7.1) as $f = -\chi^2/d.o.f.$ between the observed data and the model light curve, for a given model.

Consider an optimization problem that consists of maximizing a function of two variables f(x,y), with x and y bounded between 0 and 1. The function defines a 2-D landscape, in which one is seeking the highest elevation point. If the landscape is smooth and simple this problem is readily treated with conventional hill-climbing methods. However a landscape such as the following would be a much more difficult task, as shown in Fig. 7.2.1.This space is a surface plot of the function f(x,y), and the inset in the upper right is a color-coded version of the same function. The global maximum (indicated by the arrow and located at (x,y)=(0.5,0.5), where f=1) is surrounded by concentric rings of secondary maxima, where a simple hill-climbing method would most likely fail. This problem is easily solved with a genetic algorithm, in the following way:

Start by generating a set (population) of trial solutions, usually by choosing random values for all model parameters; then:

1. Evaluate the goodness of fit (fitness) of each member of the current population (through a chi square measure with the data, for example).

2. Select pairs of solutions (parents) from the current population, with the probability of a given solution being selected made proportional to that solution's fitness.

3. Breed the two solutions selected in (2) and produce two new solutions (offspring).

4. Repeat steps (2)-(3) until the number of offspring produced equals the number of individuals in the current population.

5. Use the new population of offspring to replace the old population.

6. Repeat steps (1) through (5) until some termination criterion is satisfied (e.g., the best solution of the current population reaches a goodness of fit exceeding some preset value).

This method may look like some peculiar variation on the Monte Carlo theme, but there are two crucial differences. First, the probability of a given solution being selected to participate in a breeding event is made proportional to that solution's fitness (step 2); better trial solutions breed more often, the computational equivalent of natural selection. Second, the production of new trial solutions from existing ones occurs through breeding. This involves encoding the parameters defining each solution as a string-like structure (chromosome), and performing genetically inspired operations of crossover and mutation to the pair of chromosomes encoding the two parents, the end result of these operations being two new chromosomes defining the two offspring. Applying the reverse process of decoding those strings into solution parameters completes the breeding process and yields two new offspring solutions that incorporate information from both parents.

7.2.1. Algorithm PIKAIA. PIKAIA is a fully self-contained, general purpose optimization subroutine (Charbonneau 1995). The routine maximizes a user-supplied FORTRAN function, the name of which is passed in as an argument. A call to PIKAIA looks like:

call pikaia(funk,n,ctrl,xb,fb,status)

where funk is the name of the FORTRAN function to be maximized, n the dimension of the search space, and ctrl is a control vector whose elements determine the behavior of the algorithm (robust default values are built in). The output vector xb contains the optimal solution parameters, namely the best solution of the final population at the end of the evolution. The scalar f is the fitness of the solution (i.e., the value returned by $funk$ with f as input). The output variable status codes successful termination, or error conditions associated with illegal input parameter values. The (real) function ff must be declared as

function ff(n,x)

dimension x(n)

where the floating-point array x defines one point in the search space, and the function returns a (positive-definite) measure of fitness (or goodness of fit) associated with that point.

PIKAIA incorporates only the two basic genetic operators: uniform one-point crossover, and uniform one-point mutation. Unlike many GA packages available commercially or in the public domain, the encoding within PIKAIA is based on a decimal alphabet made of the 10 simple integers (0 through 9); this is because binary operations are usually carried out through platform-dependent functions in FORTRAN. Three reproduction

plans are available: Full generational replacement, Steady-State-Delete-Random, and Steady-State-Delete-Worst. Elitism is available and is a default option. The mutation rate can be dynamically controlled by monitoring the difference in fitness between the current best and median in the population (also a default option). Selection is rank-based and stochastic, making use of the Roulette Wheel Algorithm.

7.2.1.1. *Control vector.* PIKAIA behavior is controlled by the control vector array *ctrl*. It is an array of control flags and parameters, to control the genetic behavior of the algorithm, and also printed output. The choice of control parameters is not trivial, and depends very much on the problem to be solved. It is necessary to test every code on simulated data, using different control parameters, in order to find the best set which should be applied to real problems. The parameters of the control vector are:

ctrl(1) - number of individuals in a population (default is 100)

ctrl(2) - number of generations over which solution is to evolve (default is 500)

ctrl(3) - number of significant digits (i.e., number of genes) retained in chromosomal encoding (default is 6)

ctrl(4) - crossover probability; must be <= 1.0 (default is 0.85)

ctrl(5) - mutation mode; 1/2=steady/variable (default is 2)

ctrl(6) - initial mutation rate; should be small (default is 0.005) (Note: the mutation rate is the probability that any one gene locus will mutate in any one generation.)

ctrl(7) - minimum mutation rate; must be >= 0.0 (default is 0.0005)

ctrl(8) - maximum mutation rate; must be <= 1.0 (default is 0.25)

ctrl(9) - relative fitness differential; range from 0 (none) to 1 (maximum). (default is 1.)

ctrl(10) - reproduction plan; 1/2/3=Full generational replacement/Steady-state-replace-random/Steady- state-replace-worst (default is 3)

ctrl(11) - elitism flag; 0/1=off/on (default is 0) (Applies only to reproduction plans 1 and 2)

ctrl(12) - printed output 0/1/2=None/Minimal/Verbose (default is 0)

7.2.2. Breeding. In order to explain breeding in PIKAIA in the simplest terms, we show an example of maximization problem that consists in searching for the (x,y) pair that maximizes the output of a (given) function f(x,y), in a domain bounded between 0 and 1 in the x and y directions. This defines a two-parameter optimization problem.

7.2.2.1. *Encoding and Decoding.* Suppose that two parents (i.e., two (x,y) pairs) have been selected for breeding. The first step is to construct an encoding of each parent, in the form of a string-like structure or chromosome. PIKAIA proceeds by directly fragmenting each parameter into simple decimal integers, and splicing the resulting integers strings one behind the other. The number of digits (nd) to be retained in the encoding must be specified externally. For example, with nd=8 one would obtain

$$(x, y) = (0.123456789, 0.987654321) \rightarrow 1234567898765432$$

The length of the chromosome is then nd times the number of parameters (n) defining the solution. Here n=2 so the chromosome has length 16. Each digit can be thought

of as a gene occupying a chromosomal site for which there exists 10 possible possible gene values. Decoding is simply the reverse process:

$$1234567898765432 \rightarrow (0.12345678, 0.98765432) = (x, y)$$

It is important to point out that PIKAIA deals with numbers between 0 and 1. This means that when optimizing a physical problem, we always have to transform between real physical parameters and numbers between 0 and 1, for each parameter to be optimized. This is done in the way in which we define the limits in the physical space within a certain parameter may very, and these limits correspond to 0 and 1 in PIKAIA space.

7.2.2.2. *Crossing.* The first step of the breeding process proper is the application of the crossover operation to the pair of parent chromosomes. Consider now two parent chromosomes produced by the encoding process described in 7.2.2.1.

Randomly select one of the 16 sites, cut both chromosomes at that site, interchange the fragment right of and including the cutting site, and splice the fragments back together: for a cut at site #10, this would look like:

CUT: Ch1a:123456789 8765432 Ch2a:765432102 3456789

SWAP: Ch1b:123456789 3456789 Ch2b:765432102 8765432

SPLICE:

1234567893456789 Offspring #1

7654321028765432 Offspring #2

This results in two new offspring chromosomes, each containing intact chunks of chromosomal material from each parent. In the GA literature this is called one-point uniform crossover ; "one point" because there is only one cutting site per chromosome pair, "uniform" because each site is equally likely to be selected for the cut/swap/splice operation. In general one introduces a probability Pc that the crossover operation is to occur; unlike the mutation probability (see below), Pc should not be much smaller than one.

7.2.2.3. *Mutation.* The second step of the breeding process is the application of the mutation operator to each offspring chromosome. For each gene of each offspring chromosome, a random number between 0 and 1 is generated, and if this number is smaller than a preset mutation probability Pm then the gene value is randomly changed to any other legal value. For example, the following is a mutation at site 2:

7654321028765432

$7m54321028765432$

7154321028765432

In the GA literature this is called one-point uniform mutation ; "one point" because there is only one gene affected at a time, "uniform" because each gene is equally likely to be subjected to mutation, independently of the site it occupies along the chromosome.

The effects of crossover and mutation on the decoded version of a parameter set can be drastic (if one of the leading digits is affected) or quite imperceptible (if one of the least significant digit is affected). The result is that the breeding process can cause large jumps in parameter space, as well as slight displacements. The resulting search algorithm can therefore explore parameter space efficiently, as well as perform

fine tuning. In the case of the two parameter example used here, we would have gone from two parents:

$$P1 : (x, y) = (0.12345678, 0.98765432)$$

$$P2 : (x, y) = (0.76543210, 0.23456789)$$

to two offsprings:

$$O1 : (x, y) = (0.12345678, 0.98765432)$$

$$O2 : (x, y) = (0.76543210, 0.23456789)$$

Clearly the offsprings have taken sizable jumps through parameter space, as compared to their parents.

7.2.3. Applications of PIKAIA in astronomy. Genetic algorithms have been used a great deal for optimization problems in various fields. The application of GAs to problems of astronomical interest was promoted by Charbonneau (1995), who demonstrated the technique by fitting the rotation curves of galaxies, a multiply-periodic signal, and a magneto-hydrodynamic wind model. Many other applications of GAs to astronomical problems have appeared in the recent literature. Hakala (1995) optimized the accretion stream map of an eclipsing polar. Lang (1995) developed an optimum set of image selection criteria for detecting high-energy gamma rays. Kennelly et al. (1995) used radial velocity observations to identify the oscillation modes of a δ Scuti star. Lazio (1997) searched pulsar timing signals for the signatures of planetary companions. Charbonneau et al. (1998) performed a helioseismic inversion to constrain solar core rotation. Wahde (1998) determined the orbital parameters of interacting galaxies. Dominis et al. (1998, 2005) and Metcalfe (1999) used a GA to fit the light curves of eclipsing binary stars. Kubas (2005) optimized microlensing light curves of binary lenses using GA. There are many more publications in astronomy, using PIKAIA, and can be found on PIKAIA homepage (http://www.hao.ucar.edu/Public/models/pikaia/pikaia.html).

The applicability of GAs to such a wide range of astronomical problems is a testament to their versatility.

7.3. Fitting synthetic binary source light curves using BISCO

In order to test the code in finding the best solution of a binary source system from an observed light curve and determine errors, we simulate a binary source microlensing event. We choose the parameters in a way such that the difference between the maximum magnification time for the two binary components, $t_0(B) - t_0(A)$, is comparable to the Einstein crossing time t_E. In such events it is much harder to resolve the contributions of the two componets because the light curves merge and there is no clear secondary maximum.

The two microlensing events observed by PLANET, OGLE-2003-BLG-222 and OGLE-2004-BLG-347 are of this nature (Fig. 7.3.1), so we want to be sure that to code is

FIGURE 7.3.1. Light curve for OGLE-2003-BLG-222 event (top panel) and OGLE-2004-BLG-347 (bottom) observed by OGLE team. Large errorbars at the baseline of OGLE-2003-BLG-222 are due to a very faint magnitude.

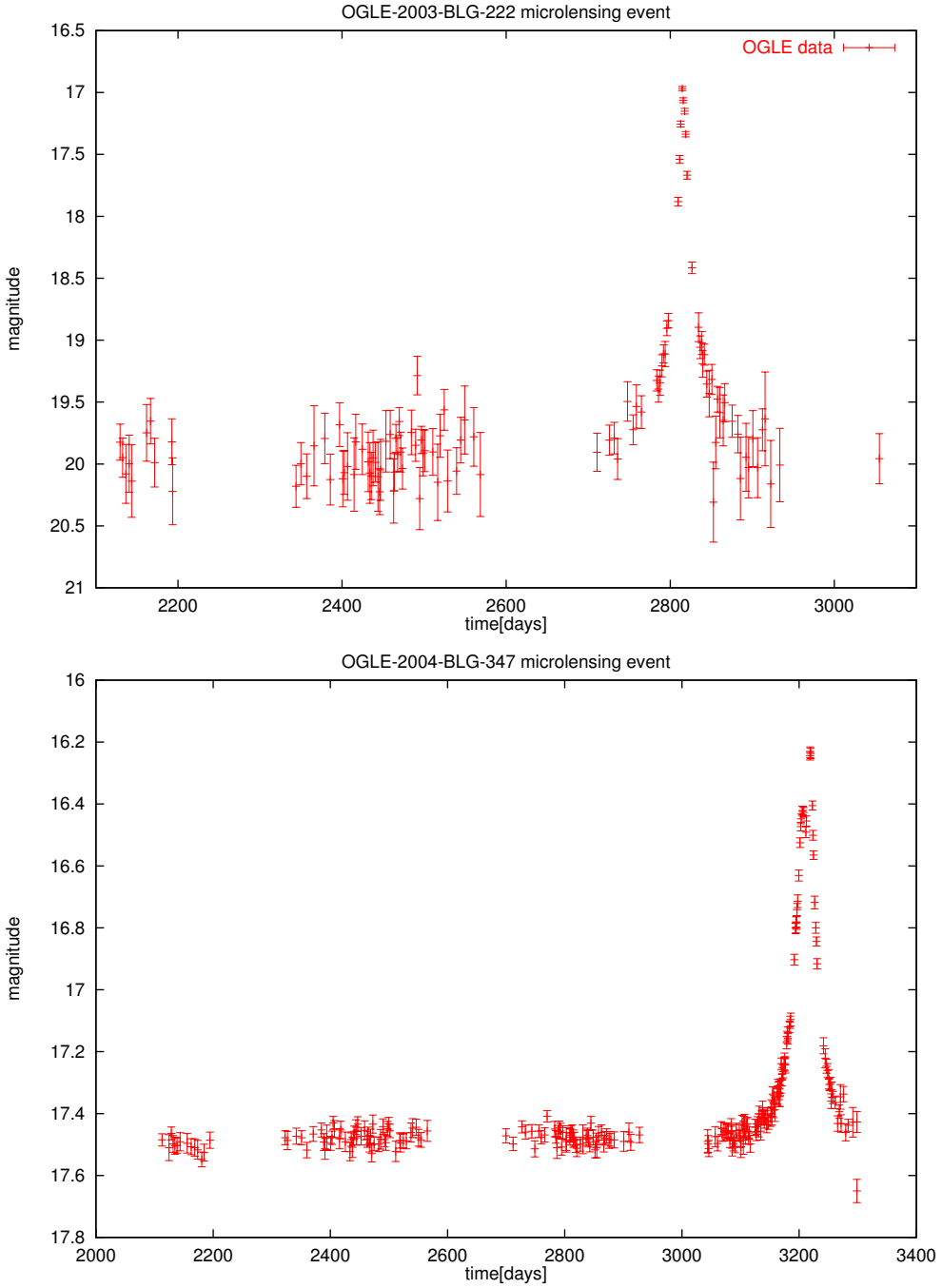

capable of solving this problem. We also want to find out how to perform the optimization process in the best way, i.e. how many optimization runs we need to perform per object, which control parameters we should use for PIKAIA genetic algorithm, as well as determine the errors of fits for particular microlensing event parameters.

For the set of parameters: $t_E = 13days$, $t_A = 1030$[JD-245000], $t_B = 1035$[JD-245000], $u_A = 0.1$, $u_B = 0.2$, $fr = \frac{F_A}{F_B} = 0.75$, $g = \frac{F_{blend}}{F_A+F_B} = 0.43$, we construct a light curve shown in Fig. 7.3.2, for 200 equally distributed time intervals.

Starting from such an ideal light curve, we add errorbars of different sizes $\sigma_0 = (0.02, 0.05, 0.1)mag$, decreasing with magnitude in the way explained in section 3.2. Out of these light curves, we construct parallel sets of light curves which contain only 70 out of 200 randomly selected data points, to mimic irregular data sampling.

7.3.1. Finding the best PIKAIA control vector parameters. We fit these light curves using different sets of PIKAIA control vector parameters, explained in subsection 7.2.1.1. ni is number of individuals in the population, and ng is the number of generations over which the population evolves. In order to find out how these parameters influence the convergence towards the global minimum, we test three different versions:

a) ni=500, ng=50,

b) ni=100, ng=200, and

c) np=500, ng=200.

In Fig. 7.3.3 and Fig. 7.3.4 we see three different examples of light curves produced for different parameters, for the three versions a) b) and c). These are only examples. In order to test the code several fits of all various combinations were performed, with different random seeds in creating the simulated light curves, and different random seeds for PIKAIA. The example in Fig. 7.3.3 shows that even for very dense and regular data sampling, small errorbars, and the corresponding 'perfect fit' to the initial light curve (one can barely see the difference between the initial and the fitted light curve), there is intrinsic uncertainty in the blending factor.

In Fig. 7.3.5 we see how $\chi^2/d.o.f.$ decreases with each next generation, in the cases a), b) and c) explained above.

Another very interesting parameter is elitism., i.e. protecting the best individual in the population from random deletion. This option is used by default in PIKAIA. However, it is not always the best option, especially in parameter spaces with smooth minima. For this reasons this is tested as well on the synthetic light curves.

7.3.2. Determining the error. For the example simulated light curve shown in Fig. 7.3.6, having s baseline magnitude of $\sigma_0 = 0.05mag$ and data sampling of 70 out of 200 data points, we perform 50 optimization runs using BISCO, with the same limits of allowed parameters to be optimized. In each run, a population of 500 individuals is optimized over 200 generations. These limits are first set to a very wide range, since in the case of a real observed light curve we do not know the starting parameters, and have to allow the code to search in a large range. For every run of BISCO we take different random seeds for PIKAIA.

FIGURE 7.3.2. Light curves for a binary source event (black line), and for the contributions of the two binary source components (component A - red line, component B -green line), for a simulated microlensing events with parameters: $t_E = 13days$, $t_A = 1030$[JD-245000], $t_B = 1035$[JD-245000], $u_A = 0.1$, $u_B = 0.2$, $fr = \frac{F_A}{F_B} = 0.75$, $g = \frac{F_{blend}}{F_A+F_B} = 0.43$

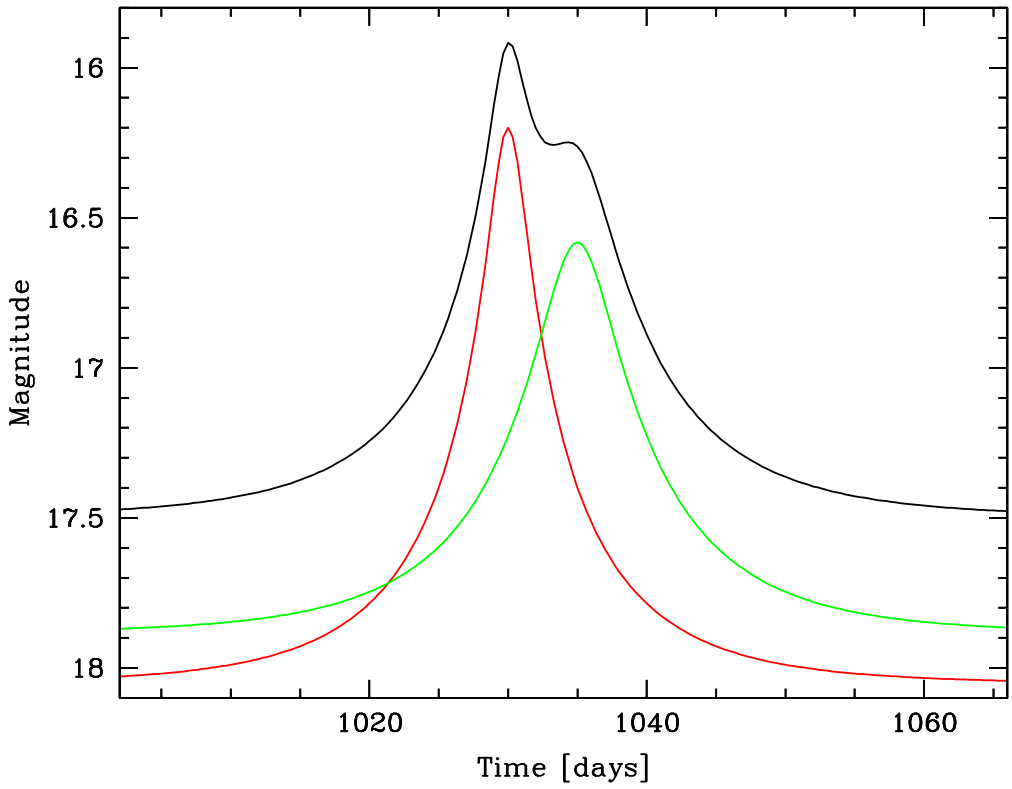

For a wide range of parameters limits we obtain the results given in the Tab. 1. We see that one has to do several runs with PIKAIA, but it will yield very accurate mean values. For some parameters the standard deviation is large, mainly for the blending factor g which one obtains using linear fit $LFIT$ (Numerical Reciepes, Press et al. 1992). However, the reason for this is not the method, but the fact that blending is in principle difficult to fit very accurately, especially in binary sources where the baseline flux is as given in Eq:7.0.1. The flux ratio deviation is also large, but ending with a very good mean value, which is very satisfactory. The light curves for these mean values are plotted in Fig. 7.3.7, next to the initial ideal light curves used to produced the simulated

FIGURE 7.3.3. An example of a synthetic light curve fit, for 200 out of 200 data points, and errorbars of $\sigma_0 = 0.02mag$. PIKAIA parameters were ni=100, ng=200. Dotted lines correspond to the original light curves for the two binary components and the composite binary source curve, solid lines are the curves for the best fit to the simulated data (blue bars). $\chi^2/d.o.f. = 1.13$

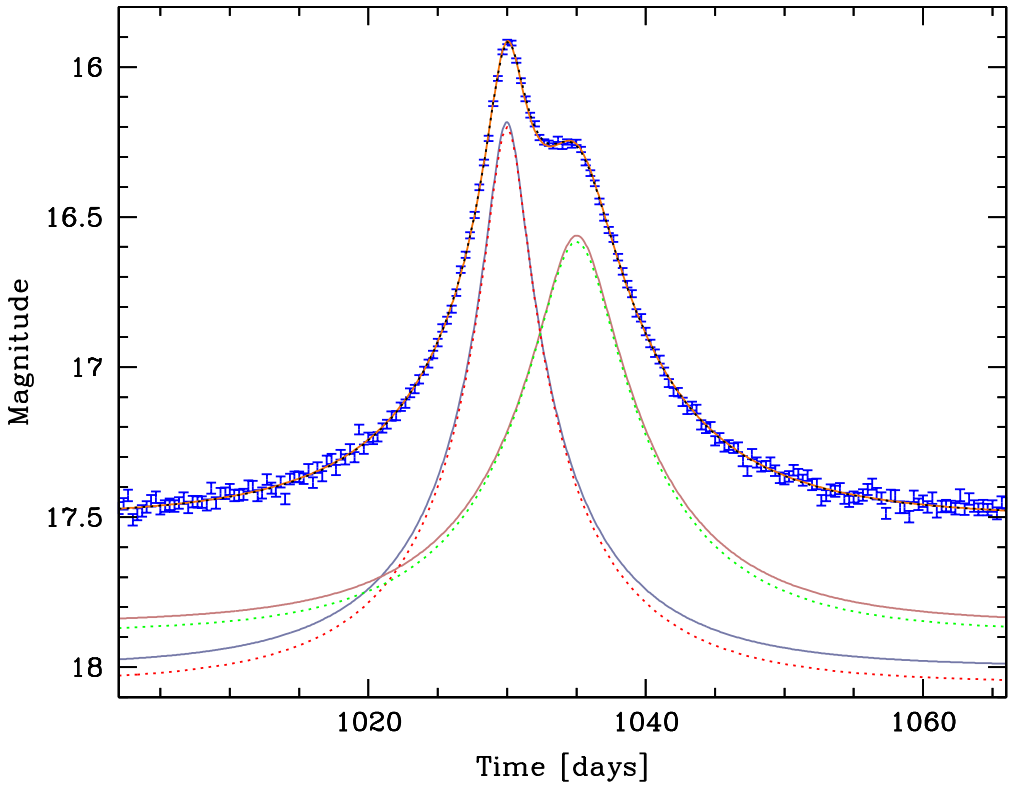

data. We see that the fitted light curves are in the better agreement with simulated data than the initial light curves, what explains the slight discrepancy between the best fit parameters and the initial parameters. However, this shows that the code BISCO, after performing several optimization runs with different random parameters, is very suitable in finding the best model which fits data points of a binary source microlensing event.

If we want to get the more accurate result, we can make the second set of run within more narrow parameter range, i.e. around the mean value within the standard

FIGURE 7.3.4. The same as in Fig. 7.3.3, for 70 out of 200 data points. Errorbars of $\sigma_0 = 0.1mag$, ni=500, ng=50, $\chi^2/d.o.f. = 1.12$(top panel) and $\sigma_0 = 0.05mag$, ni=500, ng=200 $\chi^2/d.o.f. = 0.99$(bottom panel).

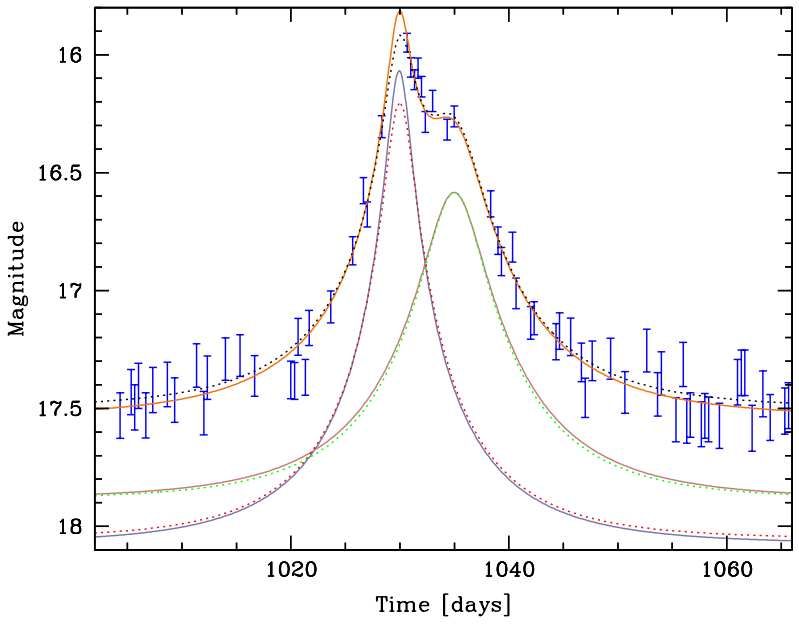

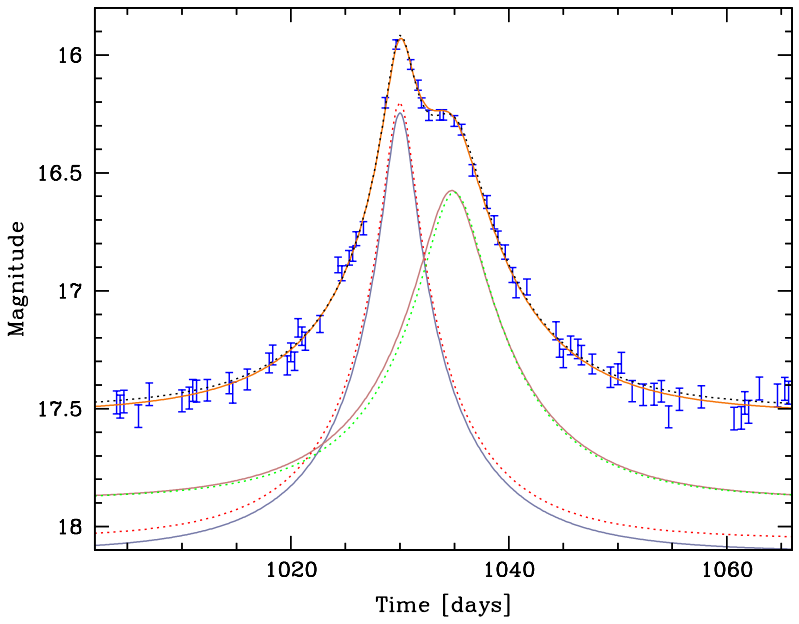

FIGURE 7.3.5. Convergence of PIKAIA towards the best solution for different population sizes, for the simulated light curve shown in Fig. 7.3.6. Red line is a fit with 100 individuals, blue line with 500 individuals.

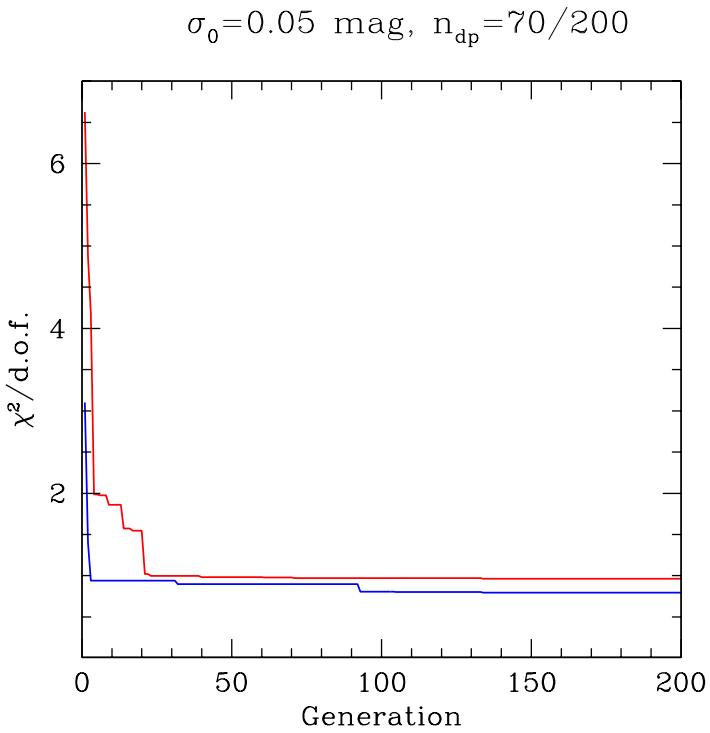

deviation of the first set of runs. However, it it very important to keep the same range of parameters for all the runs in one set. The result obtained for such an additional run is shown in Tab. 2. We see that luittle progress was made, except for a slightly better solution of the flux ratio.

We also compare how the result changes for different number of optimization runs (for 5,10,30,30,50 runs). With 20, even with 10 runs we already get very satisfactory results.

Finally, we compare the same example, with same parameter limits, for sets of optimization runs with and without elitism. Results are compared in tables Tab. 2 and Tab. 3. We can immediately see that the runs without elitism have smaller scatter, i.e. smaller error. This is the result of the smoothness of the parameter space minima. In the case of non-linear spaces with sharp minima, elitism is necessary. However, in smooth minima there are often many close solutions with similar $\chi^2/d.o.f$. If we insist on keeping the best individual in the population, this one will breed more often and produce more offsprings, i.e. we might force the code to converge towards some particular solution. So on one hand, one single solution, obtained using elitism, is more likely to be very close to the initial set of parameters, i.e. the best solution. On the other hand, if more runs are performed, using elitism can ensure very good mean values, and initial values being within the errorbars.

TABLE 1. Parameters optimized by BISCO for the synthetic light curve, for the example shown in Fig.7.3.6 for a wide range of parameters.

Parameter	Initial value	Low limit	High limit	$Mean_{fit}$	σ_{fit}
t_E	13.0	7.0	20.0	13.07	1.42
$t_0(A)$	1030.0	1027.0	1033.0	1030.017	0.054
$t_0(B)$	1035.0	1032.0	1040.0	1034.72	0.23
$u_0(A)$	0.10	0.01	0.50	0.101	0.014
$u_0(B)$	0.20	0.01	0.50	0.209	0.039
fr	0.75	0.1	1.0	0.73	0.13
g	0.43	-	-	0.42	0.24
$\chi^2/d.o.f.$	-	-	-	1.09	0.03

TABLE 2. The same as in Tab. 1, for a narrow parameter range.

Parameter	Initial value	Low limit	High limit	$Mean_{fit}$	σ_{fit}
t_E	13.0	11.5	14.5	13.20	1.49
$t_0(A)$	1030.0	1029.9	1030.1	1030.024	0.048
$t_0(B)$	1035.0	1034.5	1035.0	1034.74	0.23
$u_0(A)$	0.10	0.099	0.111	0.101	0.014
$u_0(B)$	0.20	0.199	0.211	0.205	0.039
fr	0.75	0.61	0.87	0.76	0.13
g	0.43	-	-	0.44	0.25
$\chi^2/d.o.f.$	-	-	-	1.10	0.03

So we can therefore conclude that for fitting binary source light curves one does not need to perform additional fitting with more narrow parameter limits, but rather repeat the optimization runs for the same limits and PIKAIA control vector parameters, using different random seed inputs, in order to get the best mean value and errors of the fit at the same time. In the case of very many data points, i.e. lack of computer time, which needs to restrict us to only one optimization run, or in the case of test runs to see where we are close to a solution, it is reccomended not to use elitism. On the other hand, if we can afford at least 10 (or possibly more) optimization runs, elitism as an option is preferred.

Considering the population size ni and number of generations ng, it was shown in case of restricted computer time, better convergence is achieved with a large population evolving for a moderate number of generations. This is a characteristic of a smooth parameter space. We take $ni = 500$ and $ng = 200$ for each optimization run, what is different to PIKAIA default values, and perform 20 optimization runs per model.

FIGURE 7.3.6. Example of a simulated binary source light curve. Red and green dotted lines are the single source light curves for the two binary components, black dotted line is the binary source light curve, and blue bars are simulated data points, for $\sigma_0 = 0.05 mag$ and $n_{dp} = 70/100$. Parameters used to simulate the binary source light curve are given in Tab. 1, column 2.

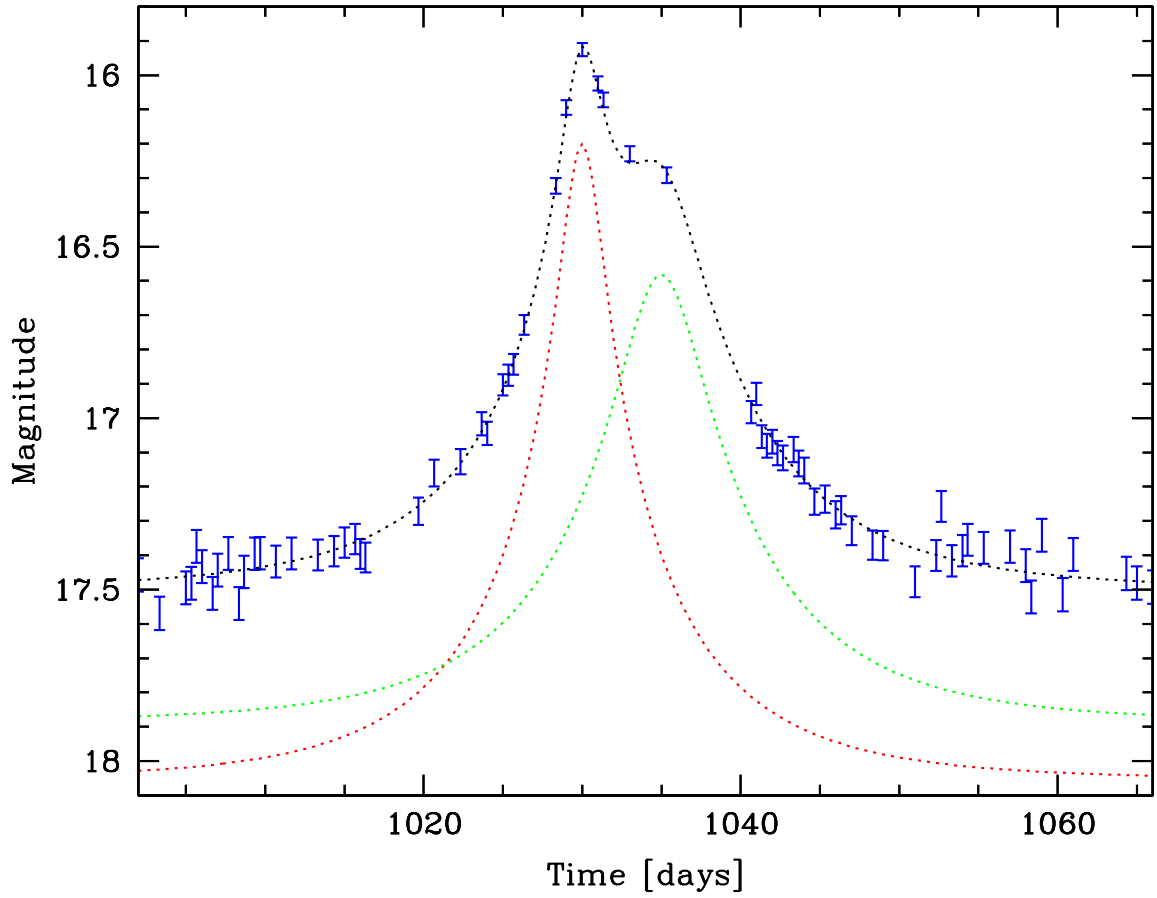

TABLE 3. The same as in Tab. 2, without elitism.

Parameter	Initial value	Low limit	High limit	$Mean_{fit}$	σ_{fit}
t_E	13.0	11.5	14.5	12.62	0.10
$t_0(A)$	1030.0	1029.9	1030.1	1030.024	0.014
$t_0(B)$	1035.0	1034.5	1035.0	1034.79	0.036
$u_0(A)$	0.10	0.099	0.111	0.105	0.002
$u_0(B)$	0.20	0.199	0.211	0.208	0.003
fr	0.75	0.61	0.87	0.75	0.02
g	0.43	-	-	0.36	0.02
$\chi^2/d.o.f.$	-	-	-	1.046	0.002

FIGURE 7.3.7. The best fit to the simulated binary source light curve obtained using BISCO. Dotted lines and simulated data are the same as in Fig. 7.3.6. Full lines correspond to the best fit parameters, given in Tab. 1, column 5.

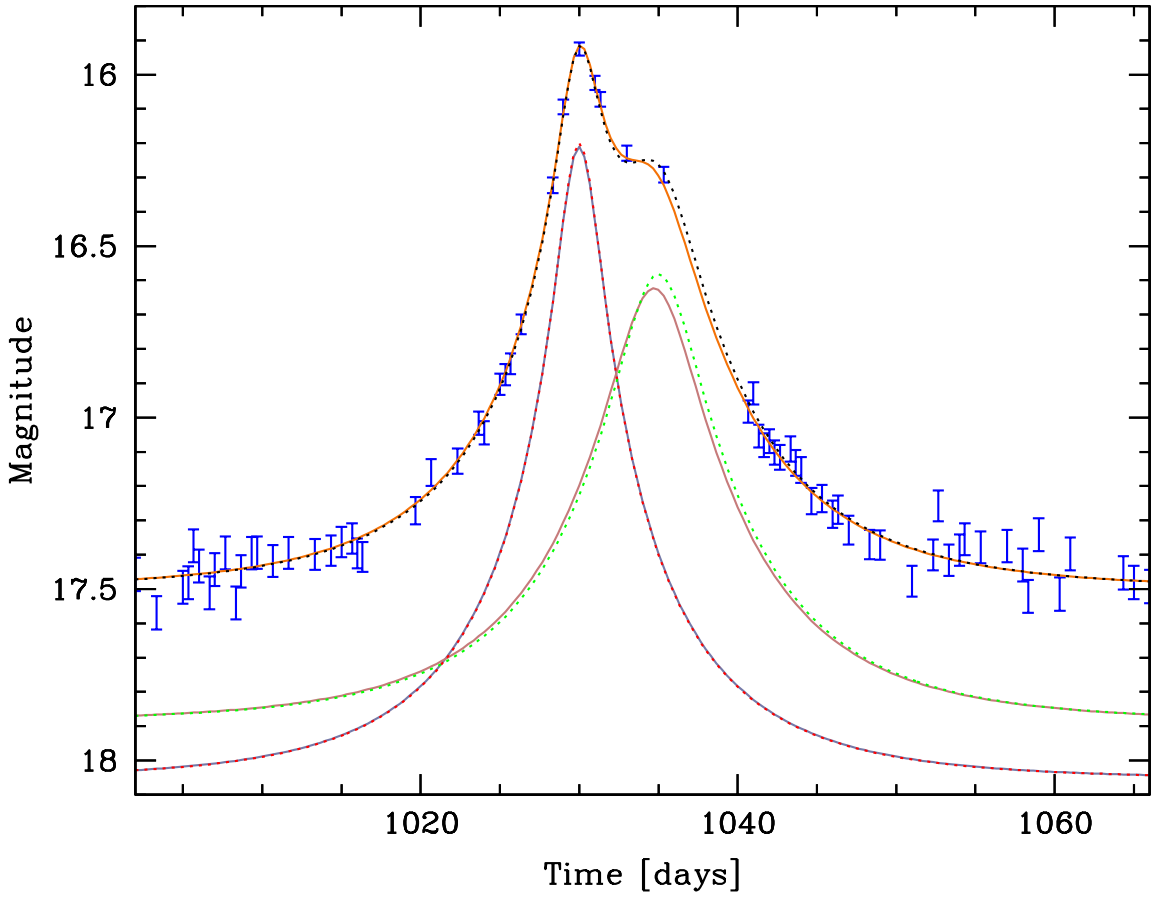

CHAPTER 8

The flux ratio method

As explained on various examples in Chapter 6, there is a degeneracy in the solution of many microlensing photometric light curves, which can be fitted as either a binary source, or binary lens events. So if we are not in the position to take a spectrum of the source, which would potentially show a signature of binarity in case of a binary source, we have to think of method which would use simple photometric data, without significant increase in observing time i.e. require no extra observing cost. Our idea comes from the assumption that for a binary source, if the stars have different spectral types, the nonmagnified flux ratio of the two binary stellar components A and B will in general be different and constant for two different filter bands, particullary I and V bands:

$$fr(I) = F_A(I)/F_B(I) \neq fr(V) = F_A(V)/F_B(V)$$

In the case of an extreme flux ratio (i.e. fluxes of the components are of the same order of magnitude) we probably deal with a pair of giants. In this case the flux ratio difference will be small, and we will need observations of very good quality for this method. This will be discussed later on the example of the OGLE-2004-BLG-347 microlensing event observed by PLANET.

However, for a large (or more extreme) flux ratio, we probably deal with a giant-dwarf pair. This kind of a binary is probably more common in the Galactic Bulge. What is especially interesting in this case, is that such a pair will produce a light curve which has a solution degenerate to the solution of a light curve produced by a lens containing a low mass planet, as discussed by Gaudi (1998), see Fig. 6.1.3. In such cases we need very good data quality and a bit of luck to obtain very dense data sampling, in order to distinigush between a planet and a binary source. One such low-mass planet of 5.5 Earth masses was detected by Beaulieu et al. (2005), OGLE-2005-BLG-390Lb, and disthiguished from a binary source model, which was also a fit to the data (see 11), due to high quality data sampling. If we had been less lucky to have such a dense data coverage, we would have ended up with a degenerate case. However, even with less dense data in I band, and with few data points in V band, one could distinguish between a binary lens and a binary source in such a case by using this method of flux ratios.

In the next section, such an example will be discussed, on a simulated set of data which is designed to be similar to those in the OGLE-2005-BLG-390 microlensing event.

TABLE 1. Initial parameters of a binary source event

t_E	11.37days
$u_0(A)$	0.340
$u_0(B)$	0.006
$t_0(A)$	JD: 3582.5
$t_0(B)$	JD: 3592.5
$fr(I)$	500
$fr(V)$	a) 200 and b) 1000
F_{blend}	$0.5F_A$
m_0	15.4mag

8.1. Simulating a high flux ratio microlensing binary source event

Let us model a light curve similar to the observed light curve for the OGLE-2005-BLG-390 event, and the solution we obtained for the binary source model. The flux ratio in I band was around $fr(I) \sim 500$ (the best fit model gave $fr(I) = 515$) , and the color index corrected for reddening was $(V - I)_0 = 0.85$. Since there were no V data during the two peaks, one could have not applied this method.

For the V band, the flux ratio $fr(V)$ the can differ by a factor of two or more from $fr(I)$, depending on how far the components lie on the isochrone (Fig. 6.2.2). Contrary to the flux ratio difference for a pair of giants, where we can predict the sign and the amount of change, for a giant-dwarf pair the sign can be positive or negative, since the components can be on the both branches of the isochrone, depending on their evolutionary state. This means that the difference cannot be predicted, so we have to fit it as a free parameter. We will show examples for $fr(V) = 200$ and $fr(V) = 1000$, given $fr(I) = 500$. We model a binary source microlensing event with parameters given in Tab. 1:

We show such a modeled light curve in Fig. 8.1.1 (I band) and Fig. 8.1.2 (V band), showing the contribution of both components. It is obvious that in the case of a less extreme flux ratio it is easier to detect the signal of the B component, what means that for the higher flux ratios we would need much better quality of data.

We add Gaussian noise to the model lightcurves, in order to mimic real observations. Irregular data coverage has also been taken into account in the sense that a random subset of the data points is selected, in order to achieve a desired data coverage.

In order to analyze how the data quality influences the result, simulations for different number of points per lightcurve have been performed, and for different errorbars on the single data points, 0.02 mag and 0.01 mag at the baseline with some dependence on the magnitude. They decrease with brighter magnitude as

$$\sigma_m = \sigma_0 \frac{1}{1 + \Delta m} \tag{8.1.1}$$

FIGURE 8.1.1. Light curve of a binary source event in I band with flux ratio of $fr(I) = 500$. Black line shows the total light curve. Light curve of the A source component (red dotted line) and the light curve of the B component (blue dotted line).

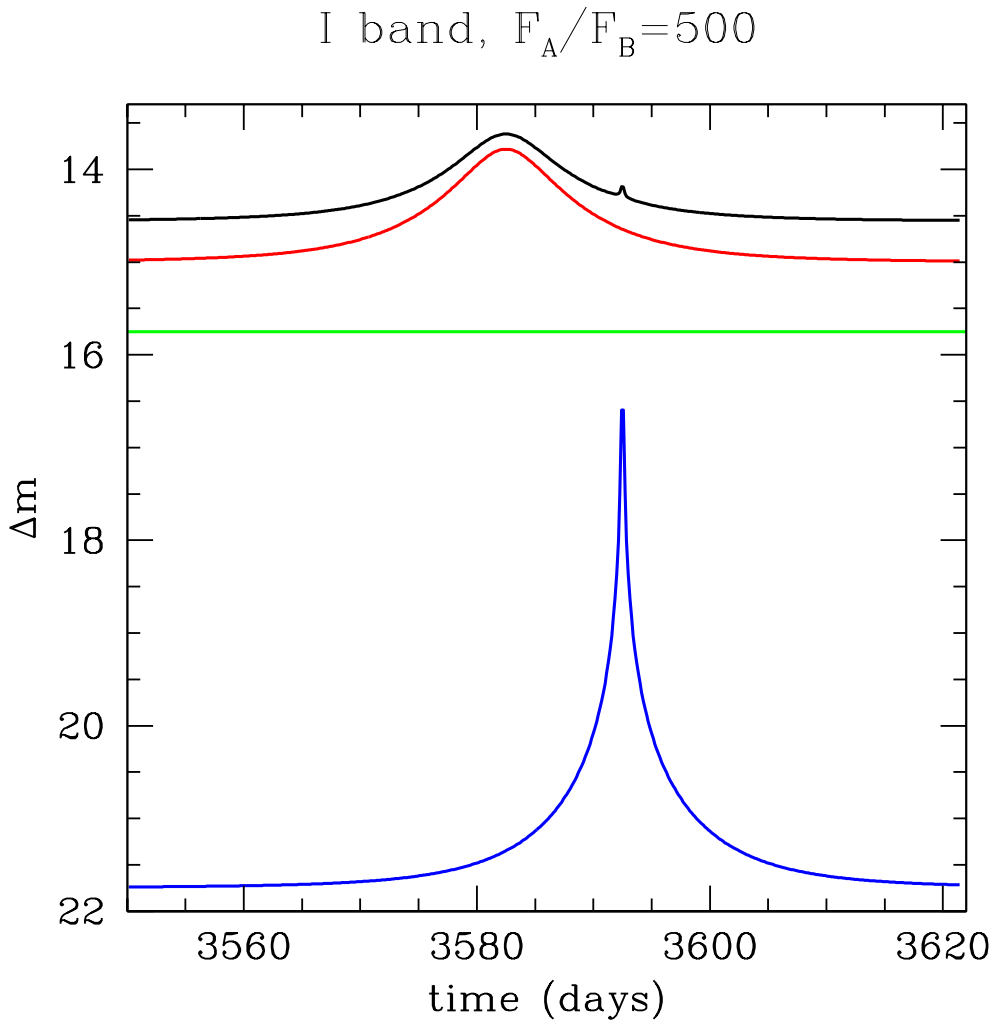

where σ_m is the errorbar at the magnitude Δm above baseline, σ_0 at the baseline, and σ_{min} the limiting minimum magnitude. The reason for that is higher accuracy of photometric observations of objects with brighter magnitude.

Out of 500 data points which cover 70 days, we select at random 200 points. This corresponds to roughly 3 data points per day, with irregular random gaps which mimic the weather conditions. This is a reasonable assumption comparable with PLANET events with even low priority, in practice we usually have much denser data for high priority events. The baseline magnitude for this example is $\sigma_0 = 0.02mag$. We construct two light curves in the same way for I and V bands, in the case $fr(V) = 200$ (Fig. 8.1.1 and Fig. 8.1.2). If $fr(V) = 1000$, such errorbars with corresponding scatter will be

FIGURE 8.1.2. Light curve of a binary source event in V band with flux ratios of $fr(V) = 200$ (left panel) and 1000 (right panel) . Light curve of the A source component (red), light curve of the B component (blue), blending(green) and the total light curve in magnitudes (black).

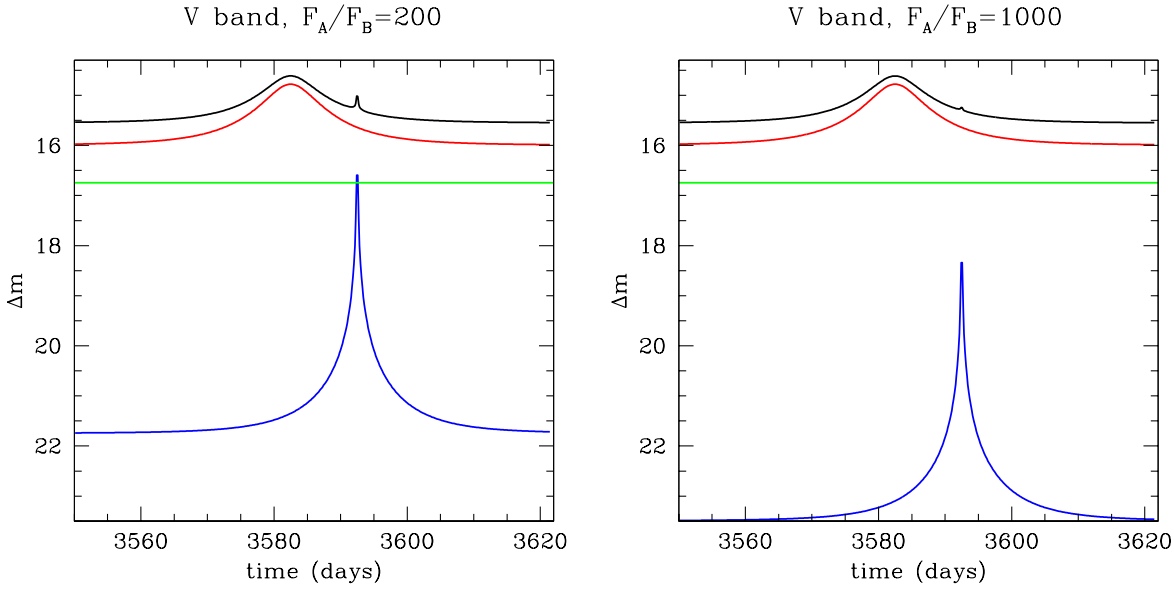

too large compared to the signal of the B component, which means that in this case we would need better data quality of $\sigma_0 = 0.01mag$, and this is still within the realistic range of PLANET observations (Fig. 8.1.2.).

8.2. Fitting the light curves using BISCO

We fit the simulated light curves in the way described in section 7.3, i.e. in the way we would fit an observed light curve using genetic algorithms. This means, with a large range of parameters, setting all parameters free at the same time.

We fit simultaneously 7 parameters using the PIKAIA genetic algorithm:

$$t_E, t_0(A), t_0(B), u_0(A), u_0(B), fr(I), fr(V)$$

where the first five parameters are common for the both I and V dataset. Two more parameters per dataset corresponding to the nonmagnified flux and blended flux are fit using a linear fit, from which we calculate the blending factors $g^{i,V}$ and $g^{i,I}$, where i correponds to the observing site.

Particullary, for the Example 1, we start with a very wide range of flux ratios, from $fr_{min} = 100$ to $fr_{max} = 700$ for both I and V band. After 30 optimization runs per model, each with 500 generations and a population of 500 individuals, the code finds the global minimum to correspond to the parameters given in Tab. 2. These parameters are very close to the initial paramteres used to construct the ideal light curve, with all initial parameters within the errorbars of the fit (Fig. 8.2.1). This means that the code really find the best fit to the data, even for such a large parameter range, and avoids

FIGURE 8.2.1. Different flux ratio in I and V bands, case for a bluer secondary component, $\sigma_0 = 0.02mag$. Red line: binary source fit, blue dotted line: magnification of the primary, red dotted line: magnification of the secondary component.

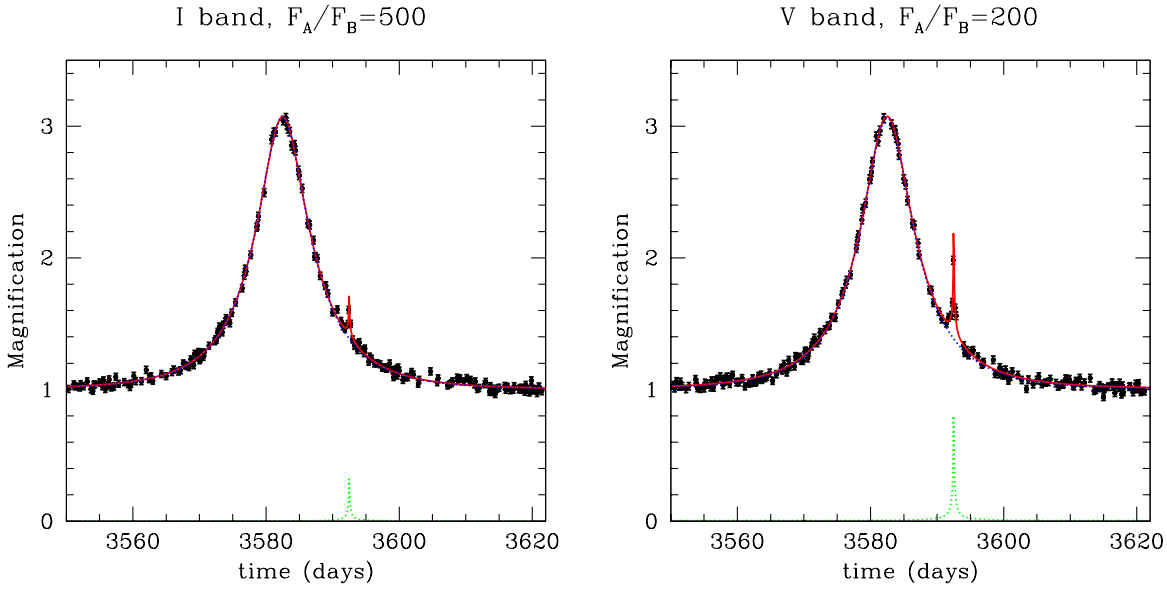

FIGURE 8.2.2. Different flux ratio in I and V bands, case for a redder secondary component, $\sigma_0 = 0.01mag$. Red line: binary source fit, blue dotted line: magnification of the primary, red dotted line: magnification of the secondary component.

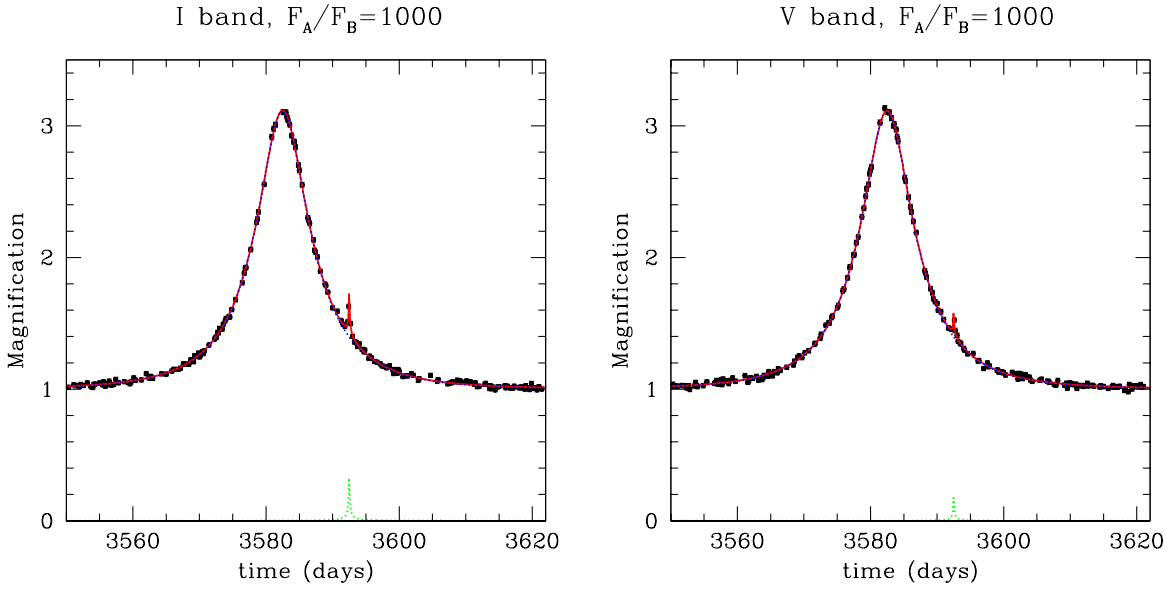

TABLE 2. Parameters optimized by BISCO for the synthetic light curve, example 2 (many data points).

Parameter	Initial value	Low limit	High limit	$Mean_{fit}$	σ_{fit}
t_E	11.37	7.0	20.0	11.90	0.65
$t_0(A)$	3582.5	3581.0	3584.0	3582.531	0.028
$t_0(B)$	3592.5	3584.0	3591.0	3592.496	0.035
$u_0(A)$	0.340	0.2	0.5	0.320	0.024
$u_0(B)$	0.0060	0.001	0.010	0.0052	0.0027
$fr(I)$	500	200	700	526	79
$fr(V)$	200	50	500	201	35
g	0.50	-	-	0.51	0.14
$\chi^2/d.o.f.$	-	-	-	1.07	0.03

TABLE 3. Parameters optimized by BISCO for the synthetic light curve, example 2 (5 data points in V).

Parameter	Initial value	Low limit	High limit	$Mean_{fit}$	σ_{fit}
t_E	11.37	7.0	20.0	11.52	0.51
$t_0(A)$	3582.5	3581.0	3584.0	3582.496	0.017
$t_0(B)$	3592.5	3584.0	3591.0	3592.499	0.014
$u_0(A)$	0.340	0.2	0.5	0.338	0.022
$u_0(B)$	0.0060	0.001	0.010	0.0055	0.0019
$fr(I)$	500	200	700	534	63
$fr(V)$	200	50	500	200	15
g	0.50	-	-	0.41	0.11
$\chi^2/d.o.f.$	-	-	-	1.03	0.02

TABLE 4. Parameters optimized by BISCO for the synthetic light curve, example 1.

Parameter	Initial value	Low limit	High limit	$Mean_{fit}$	σ_{fit}
t_E	11.37	7.0	20.0	11.62	0.53
$t_0(A)$	3582.5	3581.0	3584.0	3582.502	0.006
$t_0(B)$	3592.5	3584.0	3591.0	3592.504	0.013
$u_0(A)$	0.340	0.2	0.5	0.333	0.022
$u_0(B)$	0.0060	0.001	0.010	0.0055	0.0018
$fr(I)$	500	200	700	500	35
$fr(V)$	1000	500	1500	992	79
g	0.50	-	-	0.45	0.12
$\chi^2/d.o.f.$	-	-	-	1.00	0.03

FIGURE 8.2.3. Different flux ratio in I and V bands, case for a bluer secondary component, $\sigma_0 = 0.02mag$, and only 5 data points in V. Red line: binary source fit, blue dotted line: magnification of the primary, red dotted line: magnification of the secondary component.

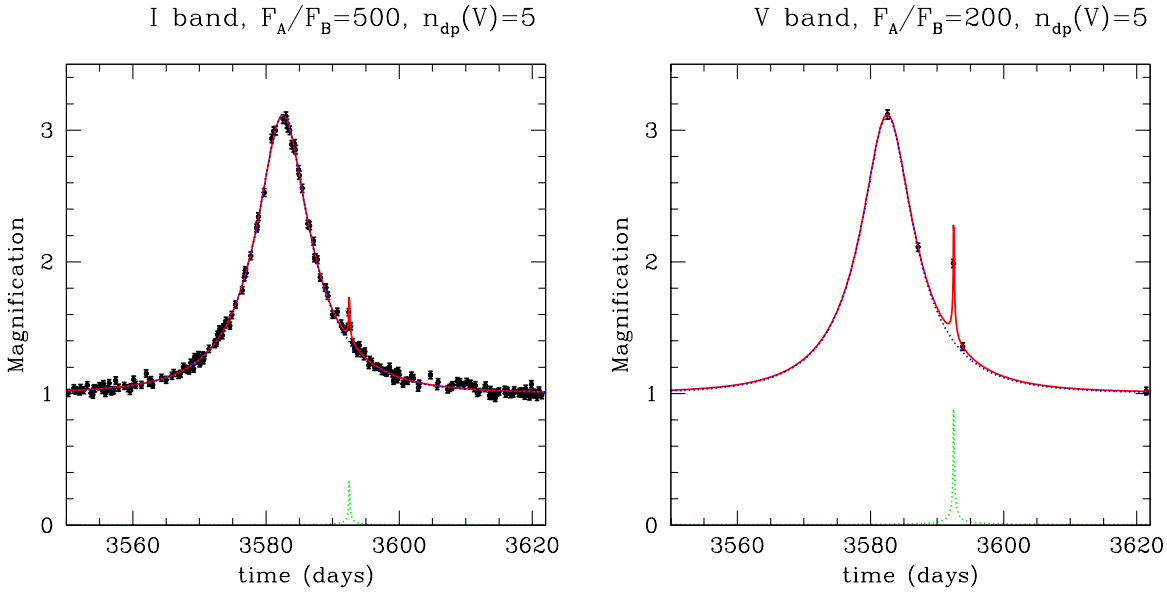

the trap of local minima. The corresponding fit for fr(V)=1000 is given in the Fig. 8.2.2 and Tab. 4.

We will take in account that taking the equal number of data points in V band as in I band increases the complexity of observations, and takes too much telescope time. So let us consider that next to the light curve of the equal sampling like in the former examples, we have only 5 data points in V band for the whole light curve, taken in the following times: first data point is taken during the event peak, second, few days later, third during the second peak, fourth just after the second peak and the last one more days later, to find the baseline. This really does not require too much observational time, and can be carried for multiple events during observations in I band. In the next example we see the fit we get for fr(V)=200, with such light curves, i.e. only 5 data points in V. The first gues for the parameters of the microlensing event like $t_E, t_0(A), t_0(B)$ can be estimated in advance with a higher precision from the I light curve only, so these can be restricted to a narrow range. The flux ratios and impact parameters can vary over a wide range. Again, even with a very large range, we get a very good solution (Fig. 8.2.3, Tab. 3). And what is more important, the flux ratios for I and V can clearly be distinguished, which suggests that the microlensing event was caused by a binary source.

If we tune the code in such a way that the relative weight of the $\chi^2/d.o.f.$ of V dataset is equal that of the I band, despite the difference in the number of data points, we get even a better fit to the flux ratios. Further calculations show that even for poor data sampling of the I dataset one could break the degeneracy and prove a binary source

FIGURE 8.2.4. The $10Gyr$ isochrone in the (V,V-I) color-magnitude diagram for a metalicity of Z=0.01 (50% of the Solar metalicity), from $0.5M_{\odot}$ to the onset of the asymptotic giant branch for a distance of $D = 8kpc$. Also shown is the ZAMS until $5M_{\odot}$(dashed line). The $8Gyr$ and $10Gyr$ isochrones (thick and thin dotted lines, respectively) do not differ significantly from the $10Gyr$ isochrone. The exact age of the stellar population is therefore not an important issue. As examples of binaries, a giant-giant binary (diamonds) and giant-dwarf (asterisk) are shown. The reddening vector is indicated by the thick bar. The isocrhrones are calculated using the BaSTI database (see

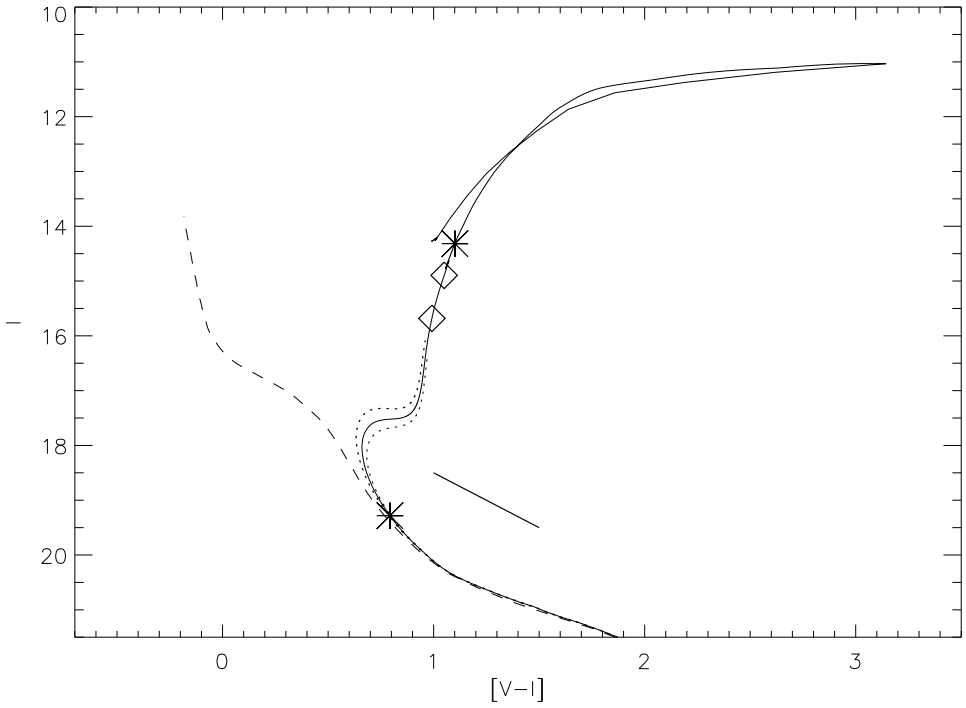

if any, but this kind of data sampling would not allow to determine the planetary mass in the case of a binary lens.

8.3. Discussion

The two described models with the flux ratios in V band $fr(V) = 200$ and $fr(V) = 1000$, both with flux ratio in I band $fr(I) = 500$, show that if we observe two light curves in I and V band, we can distinguish a binary source event from an binary lens event, especially if we have an extreme flux ratio. The problem with flux ratios of the same order of magnitude is that the two binary component lie to close on the isochrone, i.e. have difference in [V-I] color which is comparable with the fit error.

We are aware that there is one special case for which the degeneracy cannot be broken using the flux ratio method. That is, in case the two stars have such positions

on the iscochrone (Fig. 6.2.2), which correspond to the same color [V-I] but lie on different branches (i.e., the brighter component is already on the giant branch, while the dwarf is on the main-sequence branch). We have shown only two cases with large differences between $fr(I)$ and $fr(V)$, mainly since this idea for the flux ratio method came very recently, i.e. during the late phase of writing this thesis. We plan to develop this idea further using numerical simulations. We will construct synthetic binary source light curves in I band for different flux ratios $fr(I)$, each with a corresponding set of light curves in V band for different $fr(V)$, for different sizes of errorbars, data sampling, absolute magnitudes etc. We will calculate the solutions in parallel using BISCO code for for a binary source events, and TANGO code (Kubas 2005) for a binary lens event. The fit comparisons will enable to find the desired data quality and the best observing modes for breaking the degeneracy between binary lens and binary source solutions, depending on the light curve type and the flux ratios. In addition, we will determine the probability of not being able to detect a binary source in the special case described above, i.e. in the case they have the same [V-I] colors despite of an extreme flux ratio. This probability will be derived in dependence of the data quality and flux ratios $fr(I)$ and $fr(V)$.

The BISCO optimizing code has shown to be capable of finding the right solution even with a large span of starting parameters, though the benefits of the genetic algorithm PIKAIA used. This case is of a special interest since it is degenerate to a solution of a lens with a low mass planet, as will be shown in Chapter 11. In the case of restricted observing time, we suggest keeping dense data sampling for the I band in order to be able to determine the parameters of a possible planet as precisely as possible, but securing at least few V data points, to distinguish it from a binary source event. It is important to take V data during the both peaks, in order to determine the flux ratios of the components in both I and V bands.

CHAPTER 9

Modeling binary lens events

In a microlensing event, the unit of length is given by the Einstein ring radius R_E, as described in Chapter 1.

In units of R_E, a complete binary lens model is described by the lens equation, and we call d the binary lens separation and q the mass ratio between the two components ($q < 1$). The trajectory of the source is described following Kubas et al. (2005) by α, the angle between the symmetry axis of the binary lens and the source trajectory, t_E the time for the source to cross the Einstein radius, and t_0 the time when the trajectory is at the closest distance u_0 to the lens center of gravity. It may also be affected by parallax effect, for which we add π_E and ψ to model the absolute deviation amplitude from the straight line and the orientation of the caustic patterns in the sky. The whole amplification model therefore requires 8 parameters, plus baseline magnitude and blending parameters for each site.

PLANET is using several observing sites to monitor Bulge events, implying different CCD responses, sky conditions, photometry quality. Hence it is necessary to treat each telescope separately, with only the amplification model (which depends on physical parameters of the model) in common. The observed magnitude can be written for a given site s:

$$m^s(t) = M^s_{\text{base}} - 2.5 \log_{10} \left[\frac{A(t) + g^s}{1 + g^s} \right], \tag{9.0.1}$$

where M^s_{base} is the observed baseline magnitude and $g^s = \frac{F^s_B}{F^s_S}$ is the ratio between the blend flux, not comprising the source, and the source flux (Cassan 2006).

The first set of model parameter spaces (the geometrical ones) is explored using non-linear methods, such as a genetic algorithm, a gradient method or simplex, generally used in combination. The photometric parameters (M^s_{base}, g^s) are directly computed given the model magnification and the data points using a least squares fit. Moreover, we have refined this to put limits on baselines and blending during the fitting process, to avoid computing non-physical models.

The modeling strategy follows in its main lines the one which we adopted in Kubas et al. (2005). The main points are recalled in the following subsections.

9.1. Validity of the point-source approximation

The typical source size in a microlensing event is of the order of 0.001 of the Einstein radius. Consequently, in most parts of the light curve, the magnification gradient over the source is negligible compared to its size, allowing us to consider the source as a

point (the so-called point-source approximation). For each event, we first look at the data, and exclude all the points which seem to be affected by extended source effects. Indeed, in our chosen sample of binary lenses, the most relevant excluded points are related to caustic crossings and cusp approaches. In case the data coverage is not dense enough in these regions, and do not allow a precise localization of the beginning or end of the extended source effect (as it is often the case in caustic entry, which are usually unexpected), we prefer removing more data than less to be sure to catch a set of first guess solutions compatible with point-source.

Hence, this first point-source exploration of the parameter space provides us with a set of potential solutions for the fits. Depending on the nature of the event and its coverage, the solution may or may not be well defined. To go further, one needs to have more informations mainly on the source size, to build a complete model including all the data and extended source effects. Unfortunately, the computation power needed to directly implement an extended source fitting method scheme (e.g. integration over the source disk, contour integration in the lens plane using Stokes theorem, etc.) is clearly out of reach of our current resources. Therefore, we choose first to model the caustic crossings (entry and/or exit) to extract some relations between the point-source model and the source size.

9.2. Caustic crossing and limb darkening

We first define the regions in which the caustic crossings are supposed to occur, based on the previous point-source models, and keep only the corresponding data points. We assume a uniform motion for the source, and we neglect both the curvature of the caustic and the variation of its strength along the caustic within the source disk. As stated in Cassan et al. (2004), this approximation significantly reduces the computation time; moreover, it takes naturally into account limb darkening, and is a very good method to derive limb-darkening coefficients. We restrict ourselves to the first order of the classical limb darkening power-law expansion, namely to the linear coefficient (in very high amplification or well sampled events, one may add a square root coefficient $\gamma^s_{1/2}$ to the law). Let us express the limb-darkening of the source as

$$I(r) = \frac{I^s_S}{\pi}\left[1 - \gamma^s_1\left(1 - \frac{3}{2}\sqrt{1-r^2}\right)\right], \tag{9.2.1}$$

where r is the fractional radius of the source ($r \in [0,1]$); I^s_S is the total flux of the source, which depends only on the chosen photometric observing band. Note that in the following, we remove the s superscript, to simplify the notation (c.f. M.D.). Given this, the caustic crossing model takes the form:

$$A(\eta) = a_{\rm crit}\ G(\pm\eta, \gamma_1) + a_{\rm other}\ \left(1 + \Delta t\ \omega\ (\eta \pm 1)\right), \tag{9.2.2}$$

where $\eta = \frac{t - t_{cc}}{\Delta t}$ and

$$G(\eta, \gamma_1) = G_0(\eta) - \gamma_1\ [G_0(\eta) - G_{1/2}(\eta)]$$

(see Albrow et al. (1999) for the definition of the G_n functions). Δt denotes the time for the radius of the source to cross the caustic, and the origin of time t_{cc} is chosen so that $A(\eta) = a_{\rm other}$ the instant when the limb of the source enters a caustic (i.e. $+$ corresponds to a caustic entry in Eq. (9.2.2), and $-$ to an exit). Finally $a_{\rm crit}$ is related to the local strength of the caustic.

For some events both the entry and exit were well sampled, whereas for some we could only get a satisfactory model of only one crossing. We can easily establish a relation between the radius of the source $\rho_{\rm srce}$ (in Einstein unit), the impact angle ϕ to the caustic, defined as the angle between the tangent to the caustic and the source trajectory, t_E (both coming from the point-source model) and Δt (from the caustic crossing model):

$$\rho_{\rm srce} = \frac{\Delta t \ \sin\phi}{t_E}. \tag{9.2.3}$$

Measuring ϕ, and knowing t_E and Δt, one can infer the source radius. When two caustic crossings are modeled, the two measurements can may agree and then give a better estimate of the radius, or disagree, which probably means that the assumed caustic geometry was not appropriate.

CHAPTER 10

Two degenerate PLANET events

Out of the microlensing events observed up to date by PLANET, we have found two candidates which, from the visual inspection of the light curves, seem as binary source and binary lens candidates at the same time: OGLE-2003-BLG-222 and OGLE-2004-BLG-347 (Fig. 7.3.1). The light curves are of a similar type, both showing two peaks with small difference in maximum magnitude, merged into one peak. We fit the binary source source using the BISCO optimizing code (Dominis 2005), based on genetic algorithm optimization, and binary lens model by the GOBI code (Cassan 2004), using the Powell optimization method.

10.1. Photometry data

We have searched the 2MASS Point Source Catalog through the Aladin interface for these objects, but without success. We also computed the extinction toward these objects from Schlegel (Schlegel et al. 1998) and Sumi (Sumi et al. 2004) maps.

The error bars reported by DoPhot do not account for some noise sources - e.g. photon shot noise from pre-subtracted dark current, or systematic effects. To give systematic error scaling between sites, and for all images, the error bars for each microlens measurement are scaled using the other field stars measured in each image. For a large (1000) set of the lowest-scatter stars in the field (as measured over all images), the mean magnitude for each is calculated. Then, for each image, the value $\sum_i \left(\frac{m_i - <m_i>}{\sigma_i}\right)^2$, is calculated, where m_i is the magnitude of star i in that image, $< m_i >$ its mean magnitude over all images and σ_i is the formal error for m_i.

This is the χ^2 sum for fitting all the stars in the set to constant values, and dividing by the number of stars gives the χ^2 per degree of freedom ($\chi^2/\mathrm{d}of$). The error scale factor used is simply the square root of $\chi^2/\mathrm{d}of$. Multiplying all the star formal errors by this factor would bring the above χ^2 residual per d.o.f. to 1.0 for each image, for the 1000-star reference set. Multiplying the microlens formal error by this scale factor normalizes the error bars for the microlens, assuming the same statistical and systematic errors apply to the microlens measurement. This prevents site-to-site and image-to-image variation in the unmeasured noise component from driving the fitting process.

Since OGLE, MOA, and MicroFun only publish the microlensed magnitude, or that plus a couple of reference stars, the unscaled published error bars are used for these data sets.

10.2. OGLE-2003-BLG-222

Event OGLE-2003-BLG-222 has been observed by the OGLE team for 3 years before it peaked on 23 June 2003, with a high magnification of roughly $\Delta m = 3mag$. With the baseline magnitude in I band observed by the OGLE team of $I_0 = 19.901 \pm 0.018$, it is one of the faintest objects observed by PLANET team. In the finding chart (Fig. 10.2.1) we can see it is much fainter than most of the stars in its neighborhood, contaminated with significant blended light from its neighbors. In Fig. 7.3.1 we see the complete light curve of the event shown in magnitudes, observed by OGLE. One can see that the errorbars at the baseline have a very large scatter, while as the magnitude is increasing they become much smaller and have less scatter. For that reason it is very important to have a good baseline observed over a long time interval in the case of such a faint object, in order to make a good model of the event.

According to the equations explained in (6.2.1) we can estimate the brightness and the mass of the source from its magnitude. It is very likely that it is either a single source Solar type star, or a binary pair of G dwarfs. Such binary pairs are very common in the Milky way, which means that for a binary source in the Galactic Bulge, we can with high probability expect two stars of similar brightness.

10.2.1. Model comparison. We fitted the observed data from two PLANET observing sites (Danish telescope in La Silla, Chile, and SAAO in South Africa) and OGLE data simultaneously, for a binary lens and a binary source model, using fitting codes BISCO (Sec. 7.1) for a binary source model, based on genetic optimization, and GOBI for the binary lens model, used Powell optimization method. For a binary source, 100 optimization runs, with PIKAIA population sizes of 500 individuals and 200 generations each, were performed over a very large parameter range in order to find the best solution and corresponding errors to the fit. We obtained the following sets of parameters for a binary source and a binary lens model:

BINARY SOURCE MODEL:
Einstein ring radius crossing time: $t_E = (68.4 \pm 1.1)days$
Closest approach of the A component: $u_0(A) = (0.0251 \pm 0.0012)R_E$
Closest approach of the B component: $u_0(B) = (0.0325 \pm 0.0007)R_E$
Time of closest approach (A): $t_0(A) = (2814.13 \pm 0.06)JD - 245000$
Time of closest approach (B): $t_0(B) = (2817.52 \pm 0.05)JD - 24500$
Flux ratio $F_A(I)/F_B(I)$: $fr(I) = (0.965 \pm 0.094)$
Baseline magnitudes in [mag] and blending factors for each site:
$m_{base}(OGLE) = 19.94$, $g(OGLE) = 0.926$
$m_{base}(Danish) = 20.65$, $g(Danish) = 1.135$
$m_{base}(SAAO) = 21.01$, $g(SAAO) = 0.001$
$\chi^2/d.o.f. = 454/235$

FIGURE 10.2.1. Finding chart for OGLE-2003-BLG-222. RA (J2000.0) 17:37:08.04, Dec (J2000.0) -22:15:16.0. The very faint source is close to several bright neighbors in the field, suggesting high blending factor.

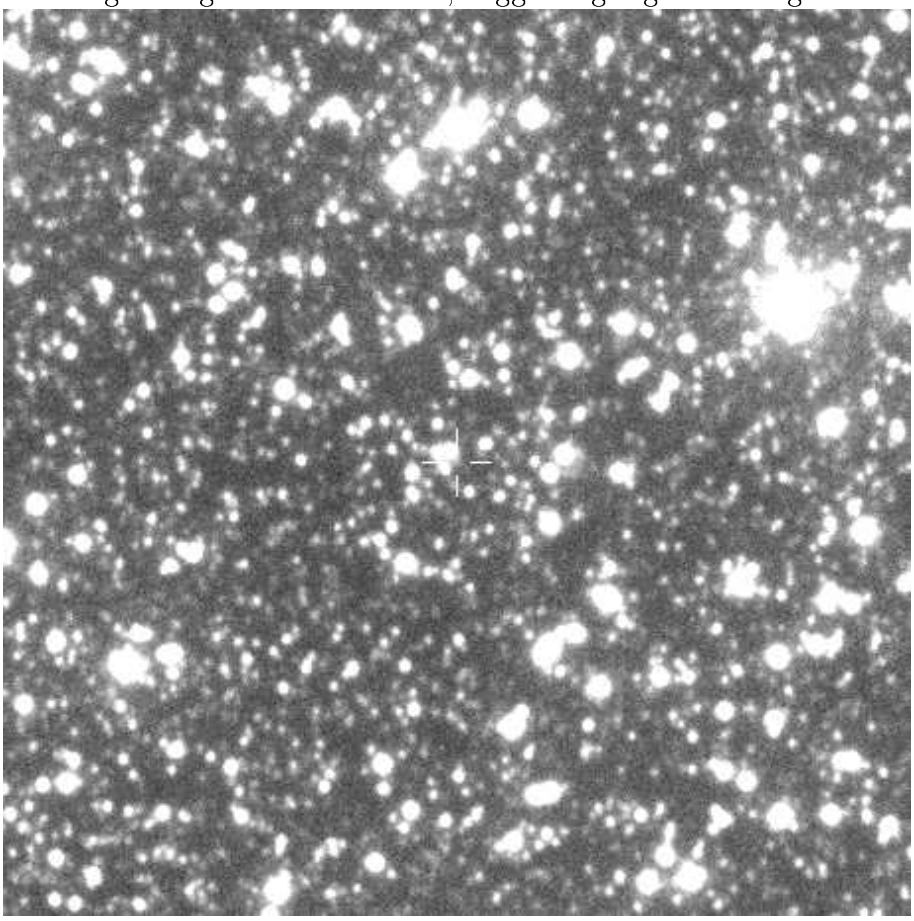

BINARY LENS MODEL :
Binary separation: $(d = 0.258^{+0.002}_{-0.026})R_E$
Mass ratio: $q = (0.1022^{+0.0748}_{-0.0007})$
Einstein ring radius crossing time: $t_E = (68.1^{+0.3}_{-7.6})days$
Closest approach: $u_0 = (0.036^{+0.002}_{-0.0009})R_E$
Time of closest approach: $t_0 = (2815.64^{+0.01}_{-0.02})JD - 245000$
$\Theta = (2.574^{0.001}_{0.01})rad$
Baseline magnitudes in [mag] and blending factors for each site:
$m_{base}(OGLE) = 19.95$, $g(OGLE) = 0.694$
$m_{base}(Danish) = 20.68$, $g(Danish) = 0.926$
$m_{base}(SAAO) = 20.89$, $g(SAAO) = 0.000$
$\chi^2/d.o.f. = 487/235$

In Fig. 10.2.2 we see a binary source fit shown in magnification, performed for all observing sites in parallel. In Fig. 10.2.3 this fit is shown in magnitudes, with light

FIGURE 10.2.2. Binary source best model for OGLE-2003-BLG-222 for OGLE and PLANET data points, plotted as amplification

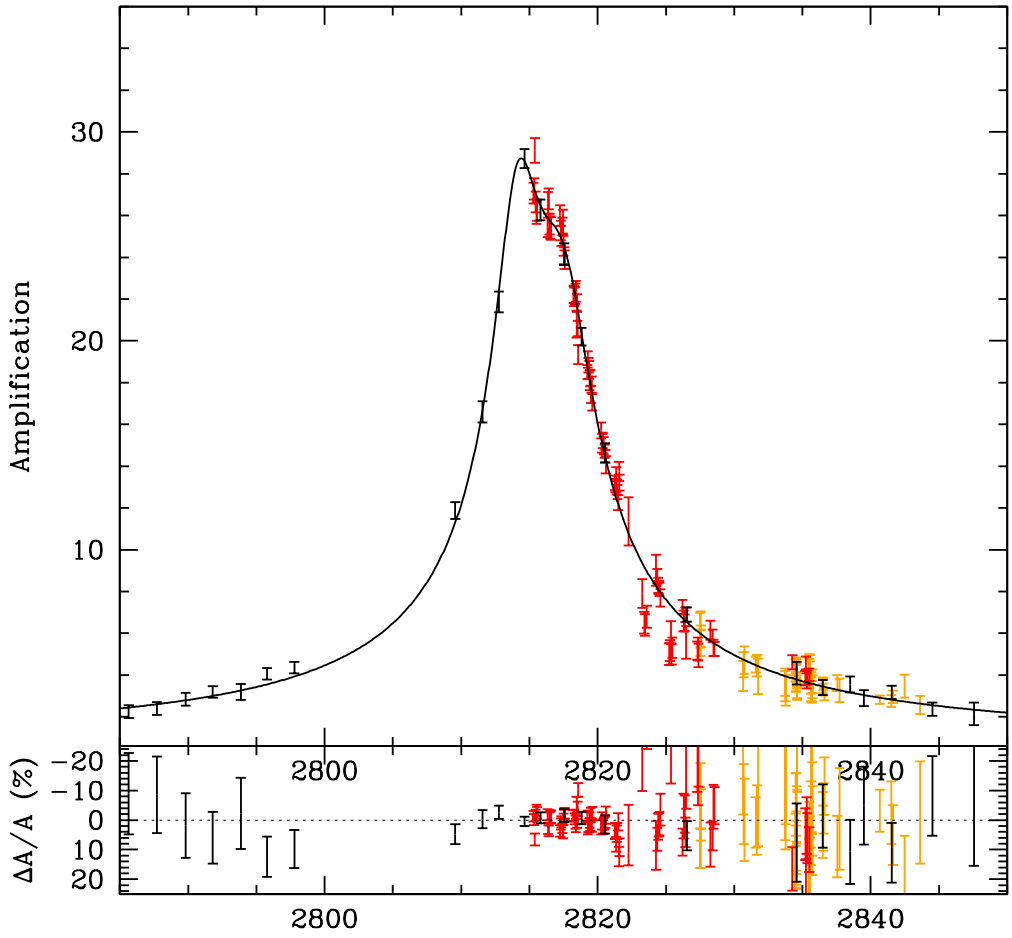

curves of the two binary components plotted. It is plotted only with OGLE data is because each observing site has different baseline magnitude. For the binary source model, a flux ratio almost equal to unity was obtained, what suggests that it can be a pair of G dwarfs, with slightly different impact parameters. This is in agreement with the theoretical assumptions explained earlier in this chapter, predicting such pairs to be very common in the Milky Way, and makes such a model plausible. We also calculated constraints on the binary separation from difference in the impact parameters $u_0(A)$ and $u_0(B)$, and $t_0(B) - t_0(A)$ compared with the Einstein crossing time t_E, finding that for the projected R_E in the source plane, this corresponds to a realistic binary system in the Galactic Bulge.

If it is a binary pair, it means the stars are of the same age. If they have the same brightness and the same age, it means they will have the same photometric color, so

FIGURE 10.2.3. Binary source fit for event OGLE-2003-BLG-222 shown in magnitudes

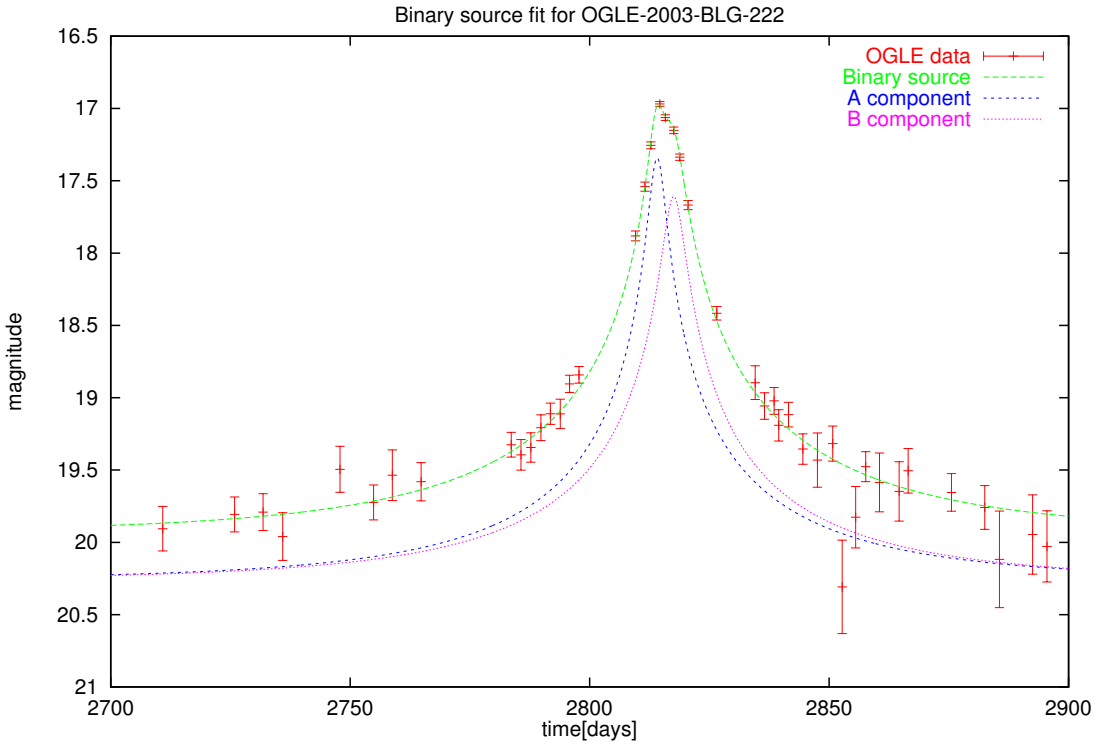

the flux ratio method suggested earlier in this work cannot be applied to show if there is a binary source.

For the binary lens two good models were obtained, a wide binary model with separation of the binary lens components of $d = 2.97R_E$, and a close binary model with $d = 0.26R_E$ (Fig. 10.2.4).

When we compare the sum of squared residuals per degree of freedom for the three mentioned models, we see that they they do not differ very much, all being around $\chi^2/d.o.f. \sim 2$. Since the errors are not Gaussian, and we did not rescale the errorbars, we do not expect them to be as small as $\chi^2/d.o.f. \sim 1$. So we prefer to compare just the sums of squared residuals χ^2.

The binary source model has the smallest $\chi^2 = 454$, compared to the binary lens models with $\chi^2 = 486$ (close) and $\chi^2 = 503$ (wide). Also at the peak the binary source model fits better the observed data, which speaks in favor of the binary source model. However, the difference in $\chi^2/d.o.f.$ is too small, to to prefer the binary source model using only the light curve fit. Even the blending factors g for different observing sites do not differ much, what makes it more difficult to favor one particular model.

It is obvious that in the case of OGLE-2003-BLG-222 we have encountered a degeneracy between a binary lens single source, and a binary source single lens model, despite very good data coverage. Unfortunately, it seems that it is impossible to break the degeneracy, taking in account equal fluxes of the components in the binary source

FIGURE 10.2.4. The best binary lens model for OGLE-2003-BLG-222

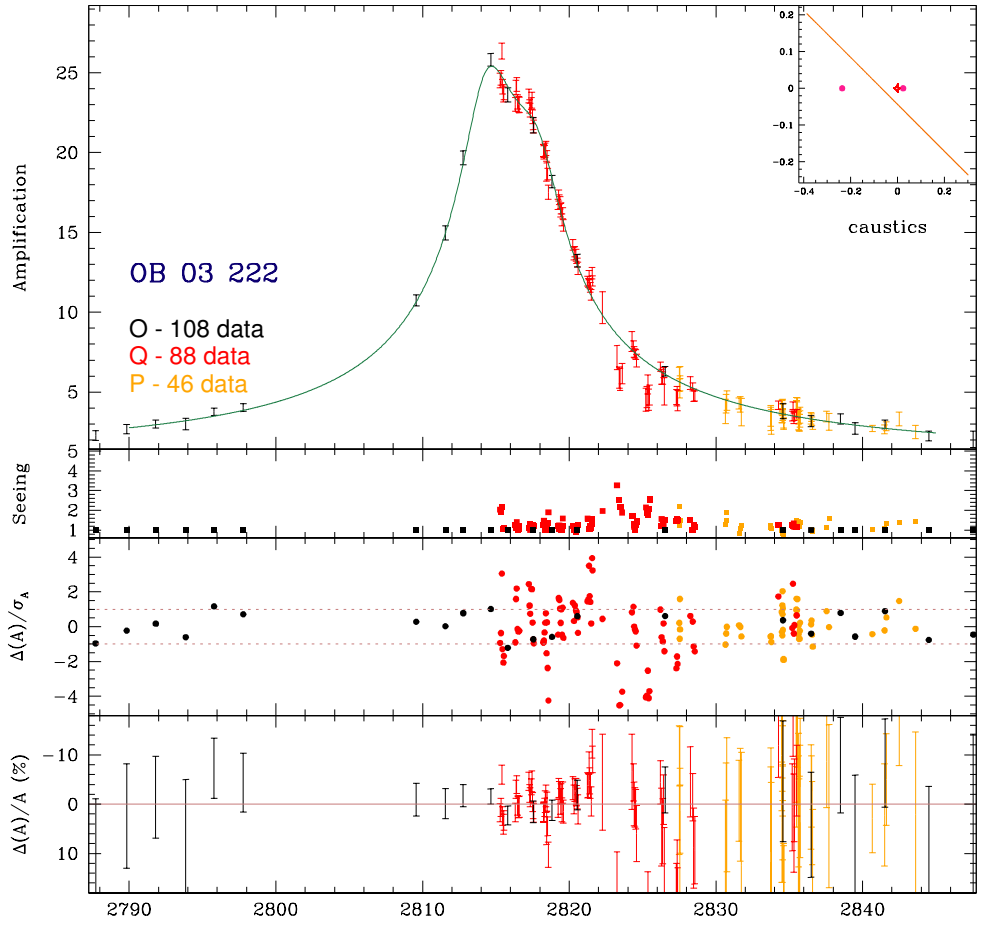

model. On the other hand, the nonmagnified source is very faint, contaminated by blending of a brighter neighbor star, so even taking spectra would not help in order to break the degeneracy.

10.3. OGLE-2004-BLG-347

Event OGLE-2004-BLG-347 peaked first on 1 August 2004, and then 5 days later again, with slightly higher magnification. With maximum magnification of roughly $\Delta m = 1.2 mag$ and the baseline magnitude in I band observed by the OGLE team of $I_0 = 19.901 \pm 0.018$, it represents a typical anomalous event observed by the PLANET team. In the finding chart (Fig. 10.3.1) we can see it is relatively bright compared to the stars in its neighborhood, but contaminated by some blending from its very close neighbor star.

FIGURE 10.3.1. Finding chart for OGLE-2004-BLG-347. RA (J2000.0) 17:45:53.14, Declination (J2000.0) -36:29:38.The source is brighter than the stars in the close neighborhood in the field. However there is a neigbout which can contaminate by blending.

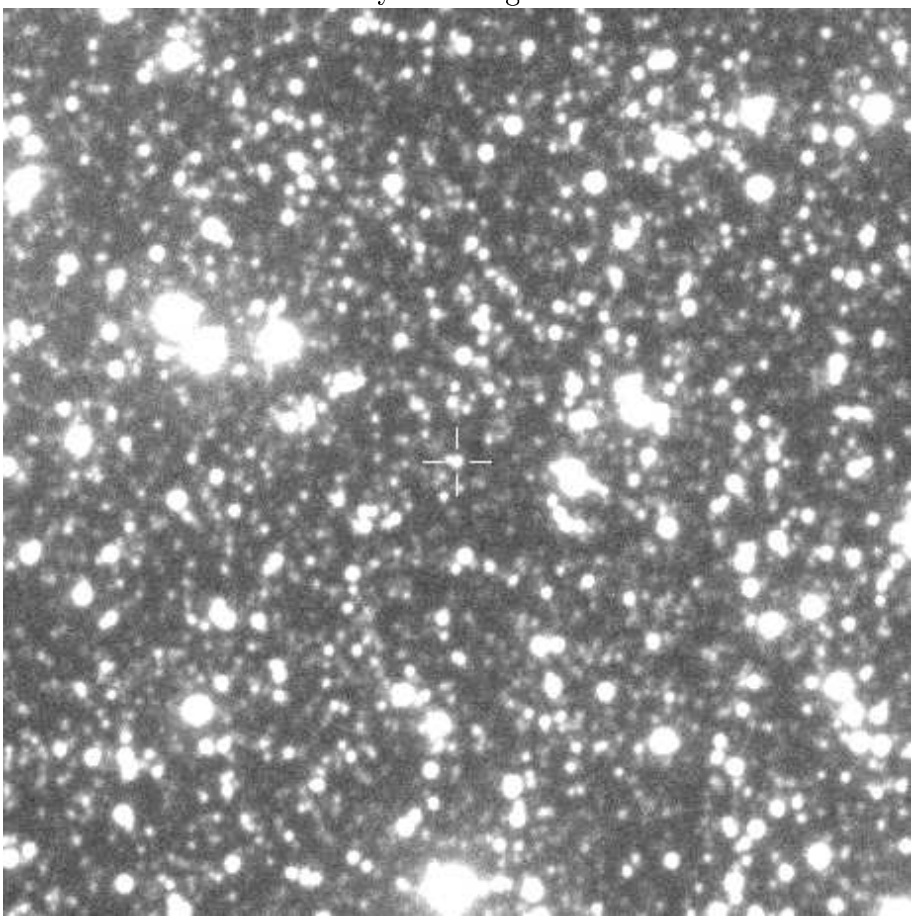

10.3.1. Model comparison. The optimization was performed in the same way as described for the OGLE-2003-BLG-222 event, for the OGLE data, and PLANET data from four observing sites (Danish telescope in La Silla, Chile, and SAAO in South Africa, Mt Canopus in Horbart, Tasmania, and Perth, Australia). We obtain the following sets of paramteres for the binary source and binary lens models:

FIGURE 10.3.2. Binary source fit for event OGLE-2004-BLG-347 (black line).

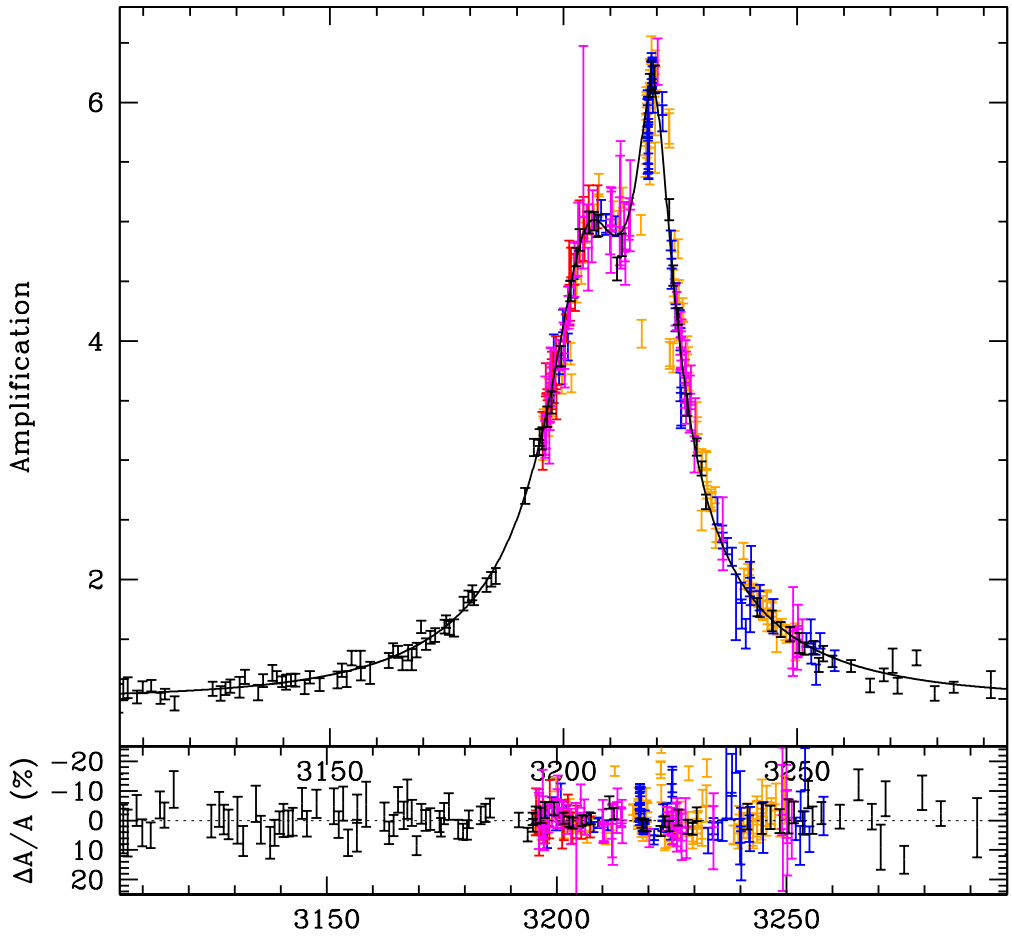

BINARY SOURCE MODEL:
Einstein ring radius crossing time: $t_E = (45.7 \pm 2.2) days$
Closest approach of the A component: $u_0(A) = (0.081 \pm 0.005) R_E$
Closest approach of the B component: $u_0(B) = (0.182 \pm 0.013) R_E$
Time of closest approach (A): $t_0(A) = (3219.63 \pm 0.06) JD - 245000$
Time of closest approach (B): $t_0(B) = (3205.45 \pm 0.16) JD - 245000$
Flux ratio $F_A(I)/F_B(I)$: $fr(I) = (0.468 \pm 0.036)$
Baseline magnitudes in [mag] and blending factors for each site:
$m_{base}(OGLE) = 17.48$, $g(OGLE) = 1.422$
$m_{base}(Danish) = 16.92$, $g(Danish) = 1.494$
$m_{base}(SAAO) = 17.66$, $g(SAAO) = 2.078$
$m_{base}(Hobart) = 17.99$, $g(Hobart) = 1.605$
$m_{base}(Perth) = 17.49$, $g(Perth) = 1.510$
$\chi^2/d.o.f. = 1221/552$

FIGURE 10.3.3. Binary lens fit for event OGLE-2004-BLG-347 (black line).

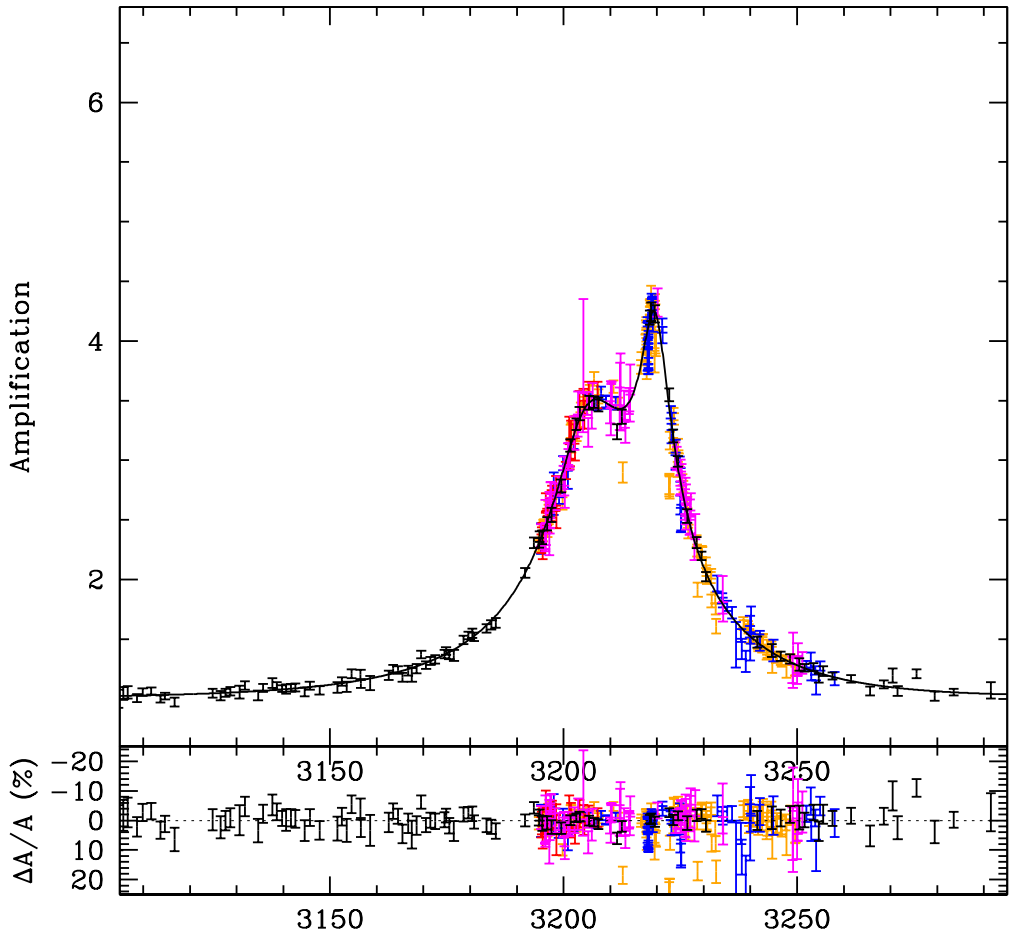

BINARY LENS MODEL:
Binary separation: $(d = 3.0717^{+0.001}_{-0.0009})R_E$
Mass ratio: $q = (0.74969^{+0.000003}_{-0.0001})$
Einstein ring radius crossing time: $t_E = (50.082^{+0.005}_{-0.004})days$
Closest approach: $u_0 = (0.5902^{+0.0002}_{-0.0002})R_E$
Time of closest approach: $t_0 = (3254.58\pm^{+0.001}_{-0.0})JD - 24500$
$\Theta = (2.42171^{+0.00005}_{-0.00002})rad$
Baseline magnitudes in [mag] and blending factors for each site:
$m_{base}(OGLE) = 17.47$, $g(OGLE) = 0.510$
$m_{base}(Danish) = 16.90$, $g(Danish) = 0.593$
$m_{base}(SAAO) = 17.64$, $g(SAAO) = 0.943$
$m_{base}(Hobart) = 17.97$, $g(Hobart) = 0.683$
$m_{base}(Perth) = 17.47$, $g(Perth) = 0.596$
$\chi^2/d.o.f. = 1171/552$

FIGURE 10.3.4. Binary source fit for event OGLE-2004-BLG-347 shown in magnitudes

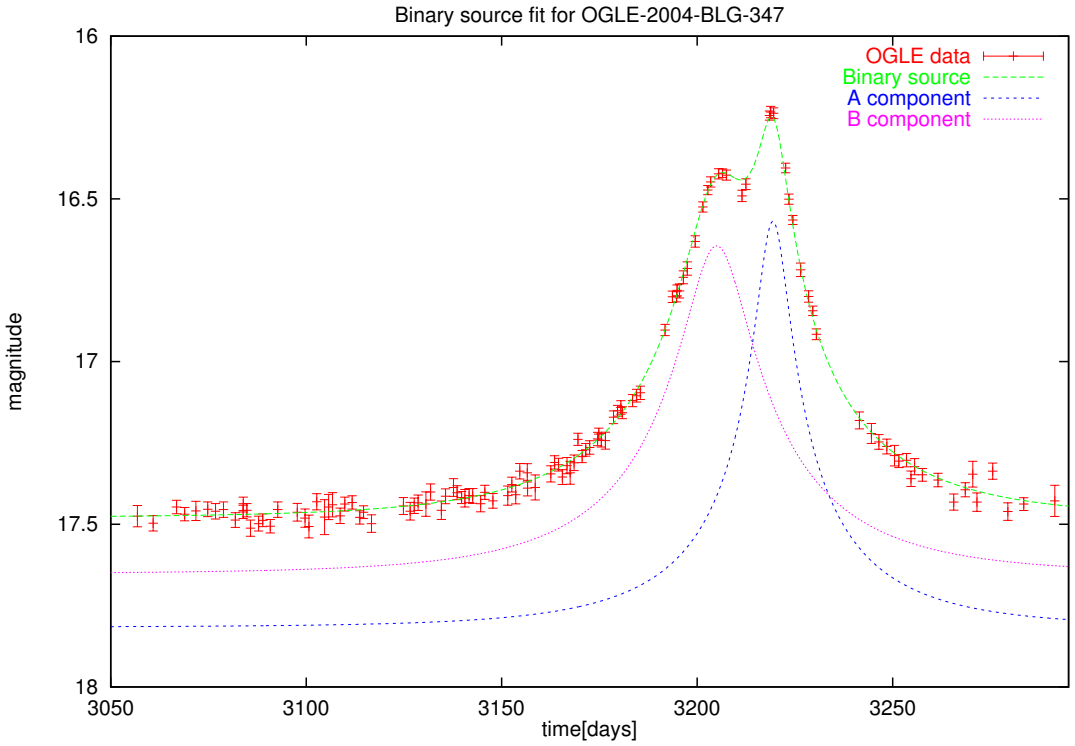

Both binary lens and binary source models fit very nicely the observations. Residuals show no trend in either none of the two cases. In the binary lens case (Fig. 10.3.3), a wide binary model is preferred, with $d = 3.0R_E$. One should note that for such large separations the caustics are very small so that there is a whole family of binary lens solutions with similar $\chi^2/d.o.f.$

The binary source model (Fig. 10.3.2) has slightly larger $\chi^2/d.o.f.$ than the binary lens model, and again as in the case of OGLE-2003-BLG-222, the difference is too small to be confident about the choice of the model. In Fig. 10.3.4 we see a plot of the binary source fit for OGLE-2004-BLG-347, with the light curves of both binary components plotted in magnitudes. Again, the fit is the same as in (Fig. 10.3.2), and plotted only against OGLE data. We see that that the magnitudes of the two components do not differ significantly at the baseline, only for roughly $0.2mag$. This corresponds to the obtained flux ratio of $f = 0.47$.

We also tried to fit this event for different flux ratios in I and R bands, since the data from the Danish telescope in Chile were taken for R band. We get a difference in flux ratios of $fr(I)$-$fr(R) = 0.50 - 0.46 = 0.04$. In Fig. 10.3.5 the two fits obtain in parallel or plotted against the data taken at La Silla in R band (bottom panel) and the data taken in I band at all other observing sites (top panel). In the bottom panel we see the difference for the both fits, where the cyan line is the fit to the La Silla R data on the plot (fr(R)=0.46), and the yellow line is the fit to the I data (fr(I)=0.50),

FIGURE 10.3.5. Different flux ratio fits for I (top panel) and R (bottom panel) photometric bands, for the event OGLE-2004-BLG-347.

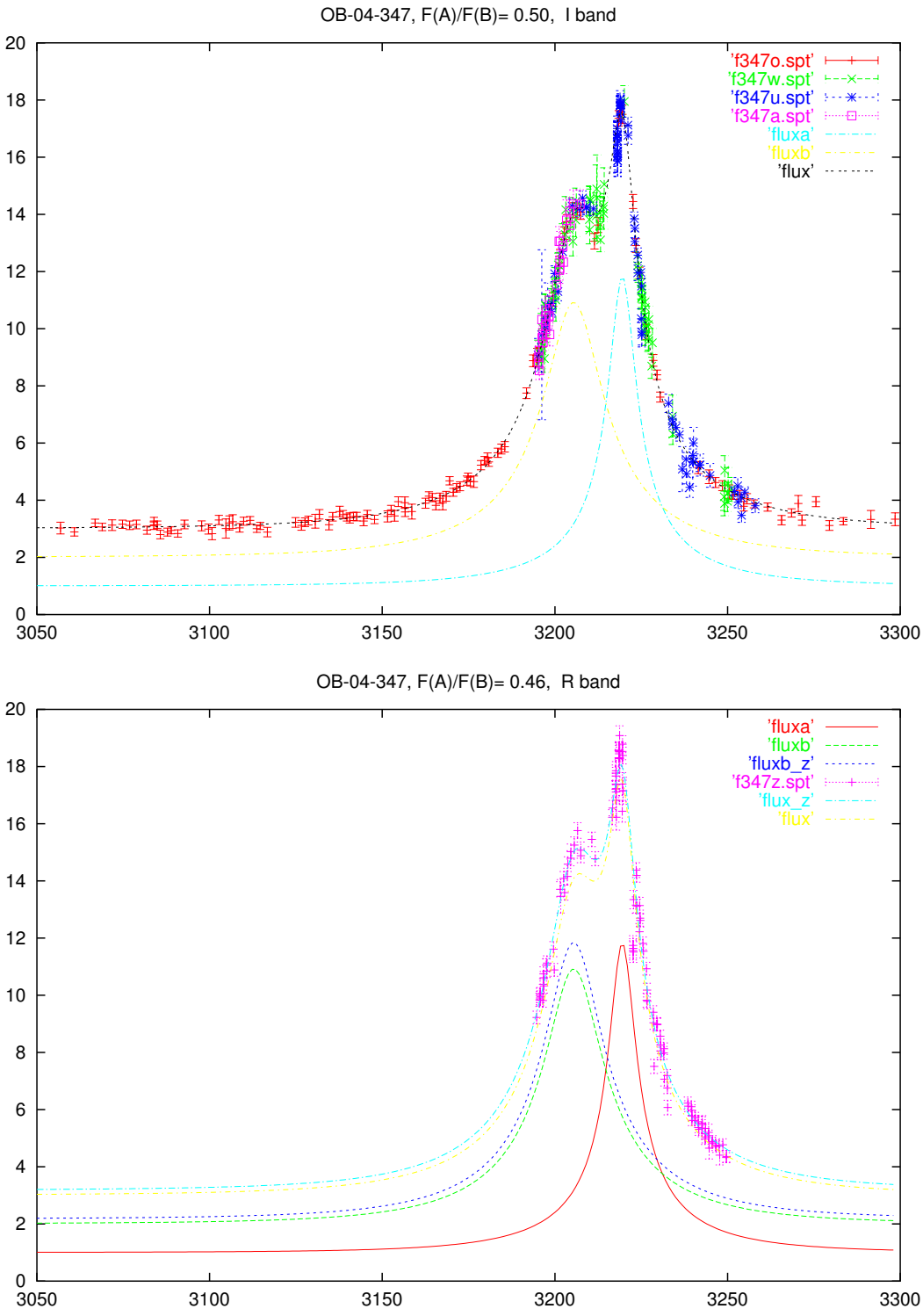

shown for the comparison. In the same way as explained before, we predict the stellar types of the source components from the magnitude. The magnitudes suggest a pair of giants, with similar mass. Such pairs exist in the Milky way, but are quite rare, much less common that giant+dwarf pairs, or pairs of two main-sequence stars. The obtained difference in flux ratios agrees with a model of such a pair of giants, however, it is at the order of error for the flux ratio fit. It would be much better if we had data for the two photometric bands taken at the same observing site, since the uncertainty in blending produces too much bias for the right interpretation. Taking additional data in the V band instead in the R band would be better, since the difference of the colors would be larger, increasing the relative difference and the detectability.

However, the binary source model yields much larger blending factors g than the binary lens model. Since the source star is brighter than in the OGLE-2003-BLG-222, we expect blending not to be very large. This means that the binary lens model can be preferred to the binary source model. Taking high S/N spectra of the source could help breaking the degeneracy for the event OGLE-2004-BLG-347.

CHAPTER 11

Planet discovery: OGLE-2005-BLG-390Lb

The importance of high-quality, densely sampled data, and accurate binary lens and binary source modeling has come to its point in 2005, resulting in the discovery of a 5.5 Earth mass planet by microlensing, OGLE-2005-BLG-390Lb. For the first time we were able to break the degeneracy between a planetary binary lens and extreme flux ratio binary source, explained in Section 6.1. Discovery of OGLE-2005-BLG-390Lb has been published in Nature, as a joint paper led by the PLANET collaboration, with OGLE and MOA collaborations (Beaulieu at al. 2006). To this date this is the lowest-mass planet discovered outside of the Solar System.

On 11 July 2005 the OGLE Early warning System announced the microlensing event OGLE-2005-BLG-390 with a relatively bright clump giant star as a source. In Fig. 11.0.1 we see the source star in the OGLE finding chart. With its baseline magnitude in the the I band $I_b = (15.664 \pm 0.021) mag$ it is relatively bright compared to its neighbors, and well-separated from them. Subsequently, PLANET, OGLE and MOA monitored it with their different telescopes. After peaking at a maximum magnification of $A_{max} = 3.0$ on 31 July 2005, a short duration deviation from a single lens light curve was detected on 9 August by PLANET. This deviation was due to a low-mass planet orbiting the lens star.

The reddening-corrected photometric colors and the magnitude for the source star were derived from color-magnitude diagrams: $[V-I]_0 = 0.85$, $[V-K]_0 = 1.9$,$I_0 = 14.25$. The angular star radius of $5.25 \pm 0.73 \mu as$ was derived used the surface brightness relation linking the emerging flux per solid angle of a light-emitting body to its color, calibrated by interferometric observations. This radius corresponds to a source radius $R = 9.6 \pm 1.3 R_{Sun}$, for a source star at the distance of 8.5 kpc. The colors indicate a 5200K giant of a G4III spectral type.

The observed light curve in I photometric band, consisting of data points taken at several observing sites by PLANET, OGLE and MOA collaborations, was modeled for binary lens and binary source microlensing events, to find which one fits better.

Fig 11.0.2 shows the best fit binary lens and binary source models. The parameters for the best binary lens and binary source fits are:

BINARY LENS MODEL:
Binary separation: $(d = 1.610 \pm 0.008)R_E$
Mass ratio: $q = (7.6 \pm 0.7) \times 10^{-5}$
Einstein ring radius crossing time: $t_E = (11.03 \pm 0.11)days$
Closest approach: $u_0 = (0.359 \pm 0.005)R_E$
Time of closest approach: $t_0 = (3582.231 \pm 0.005)JD - 245000$
Source star radius crossing time: $(0.282 \pm 0.10)days$
$\Theta = (2.756 \pm 0.003)rad$
$\chi^2/d.o.f. = 562/631$

BINARY SOURCE MODEL:
Einstein ring radius crossing time: $t_E = (11.37 \pm 0.17)days$
Closest approach of the A component: $u_0(A) = (0.34 \pm 0.01)R_E$
Closest approach of the B component: $u_0(A) = (0.0059 \pm 0.0009)R_E$
Time of closest approach (A): $t_0(A) = (3582.690 \pm 0.005)JD - 245000$
Time of closest approach (B): $t_0(B) = (3592.767 \pm 0.004)JD - 245000$
Flux ratio $F_A(I)/F_B(I)$: $fr(I) = 515 \pm 26$
$\chi^2/d.o.f. = 608/632$

In Fig. 11.0.4 the caustic pattern for the binary lens model is shown in units of Einstein radius. The best binary source model is shown in Fig. 11.0.3 (top panel) in magnitudes, with contributions of the both binary components. The difference in the two models spans over the time range of less than one day (bottom panel). In case of a binary lens microlesning event by a point source, the difference between the secondary peaks due to a planet, and due to a binary source, would be even smaller (Fig. 6.1.3).

Binary lens model gives a better fit to the observed data, not only from comparing $\chi^2/d.o.f.$ for the two models, but also from the visual inspection of the light curve. It is clear that in the case of light curves of the type observed in OGLE-2005-BLG-390, the number of data points distinguishing different models is small compared to the total number of data points, and $\chi^2/d.o.f.$ is not the best criterion for making a decision on which model should be accepted. We must inspect the light curve visually and compare it to each fit, in order to recognize the typical features of particular models.

For this event, only one data point in V band has been observed, after the two peaks, closely to the baseline. This means that the flux ratio method (Chapter 8) could not have been applied in this case to make an additional check to the model.

We agreed to accept the binary lens model, indicating a planet in the orbit of the lens parent star. The planet is designated OGLE-2005-BLG-390Lb, where the 'Lb' means the secondary component of the lens system with a planetary mass ratio $q = (7.6 \pm 0.7) \times 10^{-5}$. We cannot directly determine the planet and the lens star masses, but we can derive their probability densities. We have performed a Bayesian analysis employing the Galactic models and mass functions described in Bennet and Rhie (2002) and Dominik (2005). We averaged over the distances and velocities of the lens and the source stars, subject to the constraints due to the angular diameter of the source and the measured microlensing event parameters. We obtain a 95% probability

FIGURE 11.0.1. Finding chart for OGLE-2005-BLG-390 with the coordinates: RA(J2000.0)17:54:19.19, Dec(J2000.0)-30:22:38.3.The relatively bright source is well separated form its bright neighbors in the field.

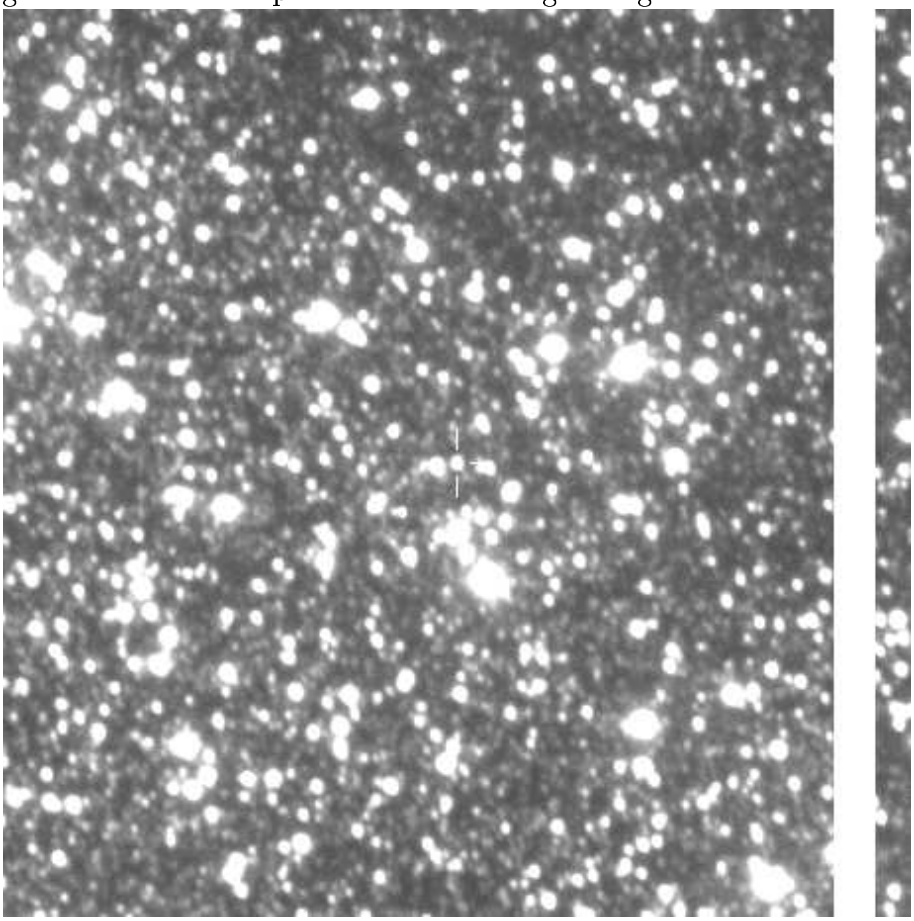

that the planetary host star is a main-sequence star, a 4% probability that it is a white dwarf, and less than 1% probability that it is a black hole or a neutron star. The medians of the lens parameter probability distributions yield:

Mass of the planet: $m_p = 5.5^{+5.5}_{-2.7} m_{Earth}$
Mass of the lens star: $m_s = 0.22^{+0.21}_{-0.11} M_{Sun}$
Orbital separation: $d = 2.7^{+1.5}_{-0.6} A.U.$
Distance to the lens: $D_L = 6.6 \pm 1.0 kpc$

These parameters imply that the planet receives radiation from its host star of roughly 0.1% of radiation received by Earth by the Sun, what means that the planet surface temperature can be around 50K. The parameters of this event are near the limits of microlensing planet detectability for a giant source star. If we wanted to detect an Earth-mass planet, we would need larger telescopes, in order to achieve a better data quality for fainter stars. Or in other words, we would need a planetary signal which is

FIGURE 11.0.2. The observed light curve and best-fit models for event OGLE-2005-BLG-390, plotted as a function of time. Colors stand for different observing sites, given in the plot. In the left top corner, the full light curve observed by the OGLE collaboration is shown. Yellow short-dashed line is the single source single lens fit to the data, grey long-dashed line the best binary source single lens fit, and black solid line the best single source binary lens fit, with a planet of 5.5 Earth masses at the separation of 2.7A.U. from a 0.22 Solar mass red dwarf in the lens system. In the right top corner the secondary peak is shown zoomed in, showing the broken degeneracy.

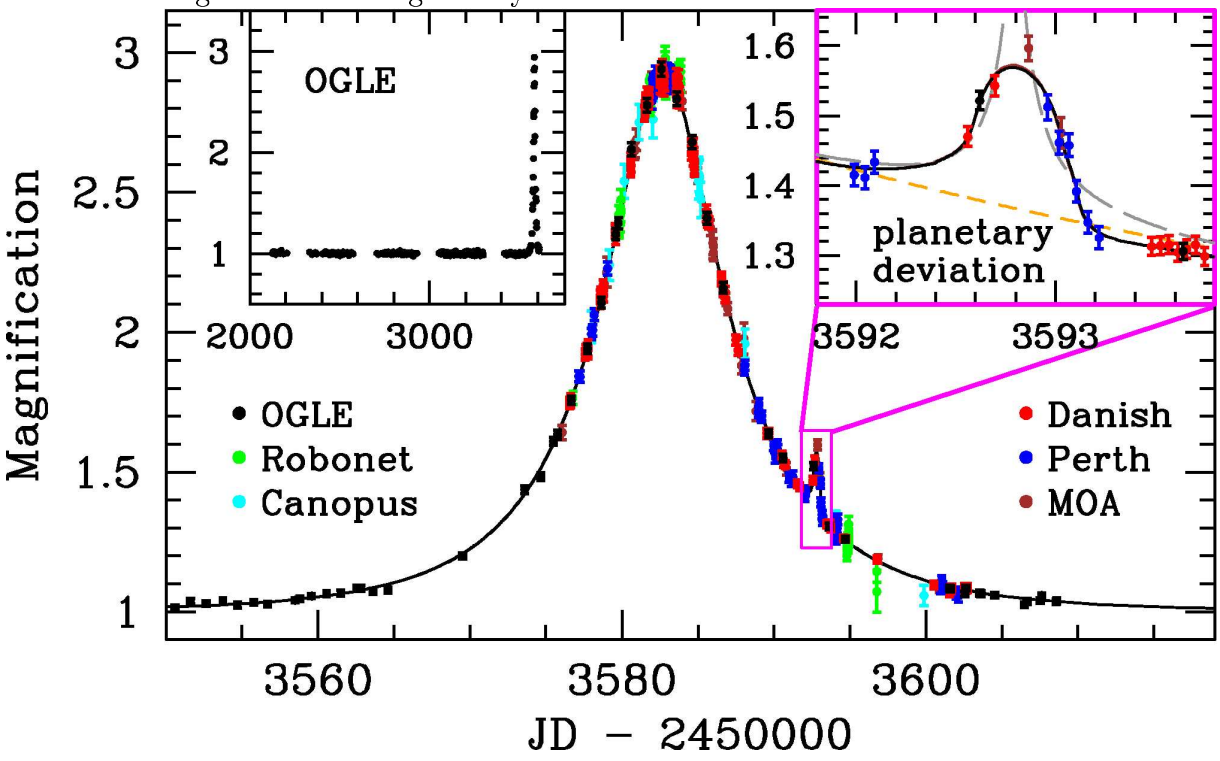

significantly larger than the observational error. In this way we could observe main-sequence stars which are not extended, which would allow detecting lenses of more extreme mass ratios. However, as explained in Chapter 8, the flux ratio method allows distinguishing binary lenses from binary sources for data with larger errorbars and less dense data sampling, than in the case of the OGLE-2005-BLG-390Lb discovery. This means that by using the flux ratio method, i.e. taking a few additional data points in V photometric band, even with existing facilities Earth-mass planets will be detectable. On the other hand, we are aware that the flux ratio method only will not allow such an accurate determination of the planet parameters, but rather concentrate on breaking the degeneracy between a binary lens and a binary source.

More details on the described planet discovery can be found in Beaulieu et al., Discovery of a Cool Planet of 5.5 Earth Masses Through Gravitational Microlensing, Nature, 439, 437 (2006)

FIGURE 11.0.3. Top: Binary source model for event OGLE-BLG-2005-390 shown in magnitudes. 500 times fainter dwarf binary component (blue dotted line) than the primary source star (red dotted line) can be fitted to the observed light curve of OGLE-BLG-2005-390, shown in Fig. 11.0.2. Black line is the binary source fit. Bottom: Figure #: Degeneracy in the solution. Green line: binary lens model, black line: binary source model. Very dense and accurate data sampling breaks this degeneracy.

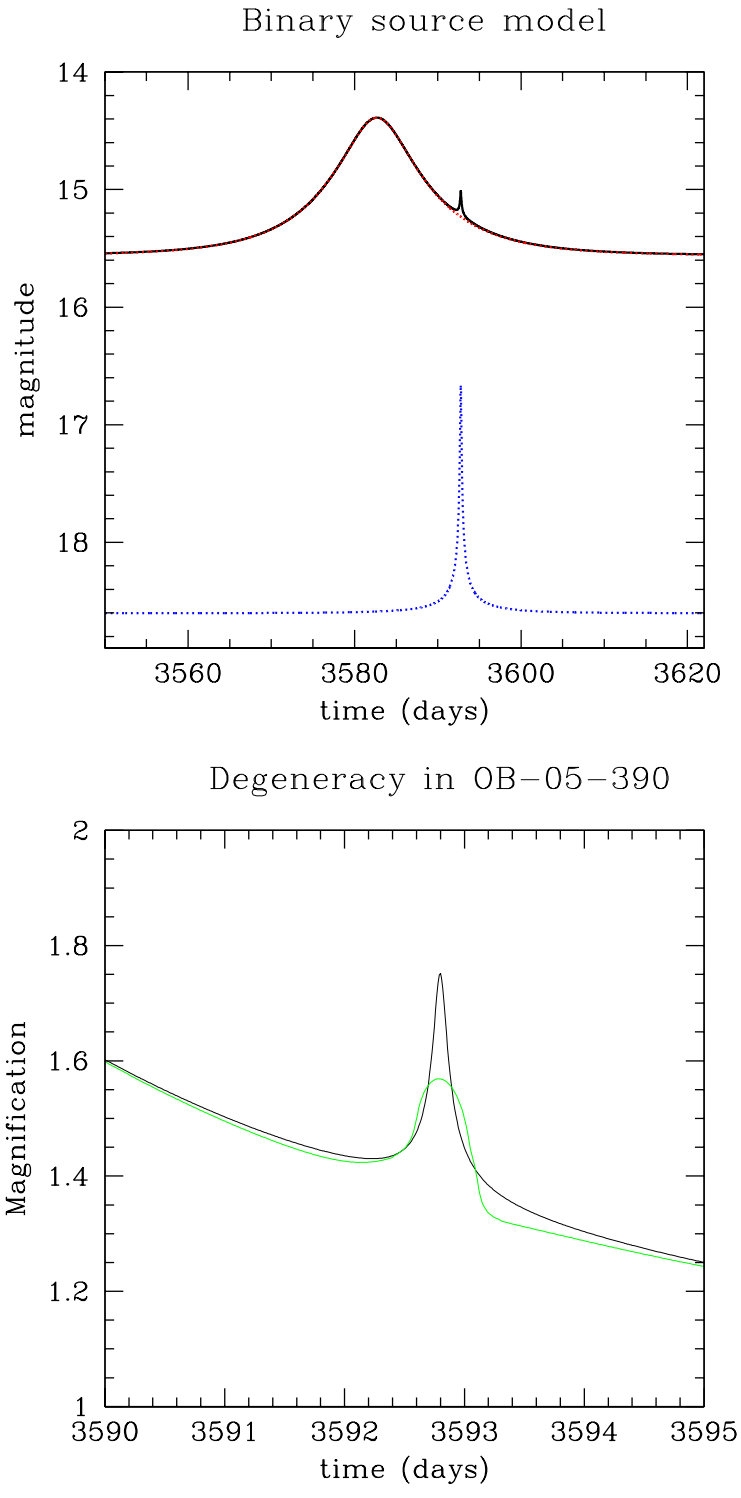

FIGURE 11.0.4. Caustics pattern for the event OGLE-BLG-2005-390. Orange disk represents the source star of the finite size, blue disk is the position of the planet, red is the area of high magnification. Small diamond caustic (bottom panel) is characteristic for planetary events (Figures by Kubas 2006).

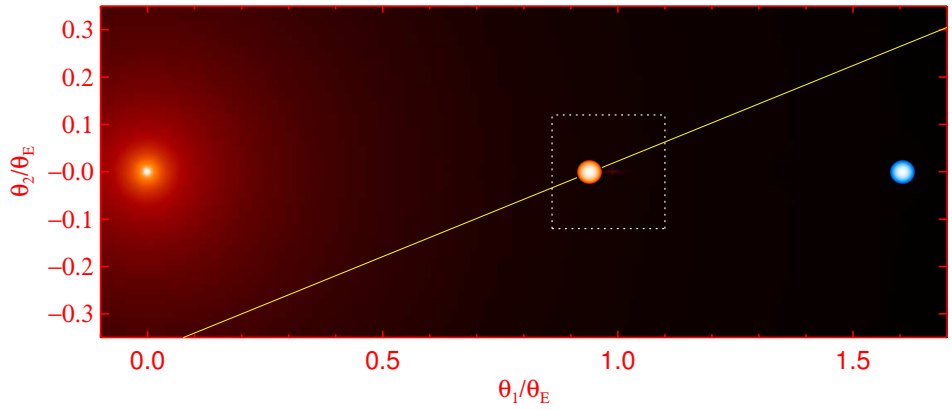

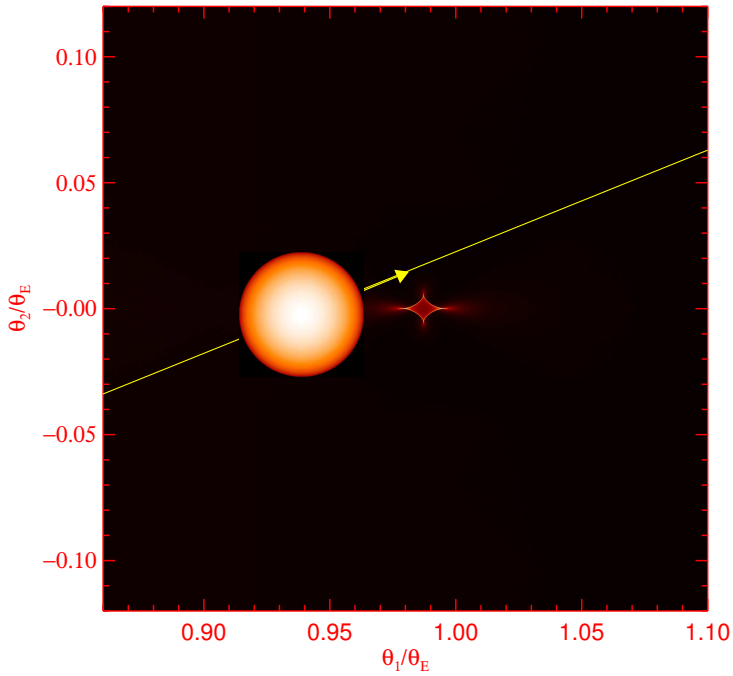

CHAPTER 12

Other PLANET events

Besides binary source modeling for the PLANET collaboration, I have been observing a large number microlensing events for the PLANET, including OGLE-2003-BLG-222, OGLE-2004-BLG-347 and OGLE-2004-BLG-254 events, described in this work. In observing season 2003 I was observing at the Observatory Mt. Canopus, Hobart, Tasmania, and in season 2004 in La Silla Observatory (ESO) in Chile. I was also helping Daniel Kubas in developing TANGO code for fitting binary lens light curves, using the genetic algorithm PIKAIA. This work has yielded co-authorships in two PLANET papers, which will be briefly described in this chapter.

12.1. Full characterization of binary-lens event OGLE-2002-BLG-069 from PLANET observations

We analyze the photometric data obtained by PLANET and OGLE on the caustic-crossing binary-lens microlensing event OGLE-2002-BLG-069. Thanks to the excellent photometric and spectroscopic coverage of the event, we are able to constrain the lens model up to the known ambiguity between close and wide binary lenses (Fig. 12.1.1). The detection of annual parallax in combination with measurements of extended-source effects allows us to determine the mass, distance and velocity of the lens components for the competing models. While the model involving a close binary lens leads to a Bulge-Disc lens scenario with a lens mass of $M = (0.51 \pm 0.15)M_{\odot}$ and distance of $DL = (2.9 \pm 0.4)kpc$, the wide binary lens solution requires a rather implausible binary black-hole lens ($M \geq 126M_{\odot}$). Furthermore we compare current state-of-the-art numerical and empirical models for the surface brightness profile of the source, a G5III Bulge giant. We find that a linear limb-darkening model for the atmosphere of the source star is consistent with the data whereas a PHOENIX atmosphere model assuming LTE and with no free parameters does not match our observations (see Kubas et al. 2005 for more details).

12.2. OGLE-2004-BLG-254: a K3 III Galactic Bulge Giant Spatially resolved by a single microlens

We present an analysis of OGLE-2004-BLG-254, a high-magnification ($A_{max} \sim 60$) and relatively short duration ($t_E = 13.3$ days) microlensing event in which the source star, a Bulge K-giant, has been spatially resolved by the point-like lens. A high signal-to-noise ratio spectrum taken while the source was still magnified by ~ 20 showed that the source was a K3 III Bulge giant with $T_{eff} = 4250 \pm 50$ K, $\log g = 2.1 \pm 0.1$ and $Z \sim Z_{\odot}$, situated at $D_S = 14kpc$. From the light curve modeling, we derive an angular size of the Einstein ring $R_E = 134\mu as$, and a relative lens-source proper motion $\mu_{rel} = R_E/t_E =$

FIGURE 12.1.1. Comparison of wide and close binary light curve best fits for event OGLE-2002-BLG-069

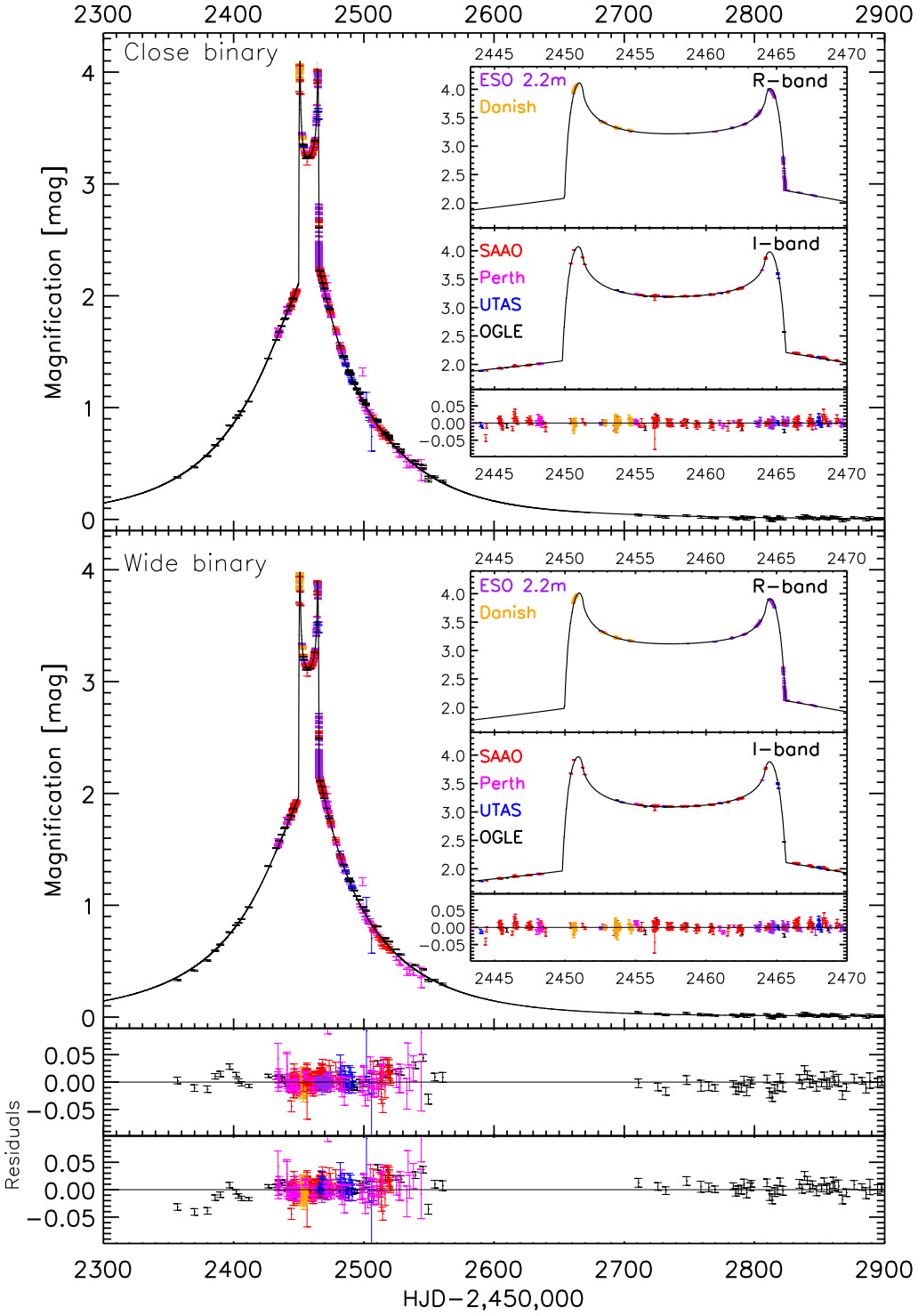

3.7 mas/yr, whereas no significant constraint can be obtained from parallax effects. We use a galactic model for the mass and velocity distribution of the stars to put bounds on the most likely lens position, $D_L = 8.7 \pm 1.8$ kpc. Our dense data coverage of this event, however, allows us to obtain a limb-darkening coefficients involving GK giant stars, with predictions from ATLAS (Claret 2000) atmosphere models. After underlining the good agreement for G-giants, we discuss the case of K-giants and essentially find a disagreement between limb-darkening measurements and model predictions, which would indicate that atmosphere models for K-giant stars would miss some relevant physics (see Cassan et al. 2005. for more details).

12.3. Summary on modeling of the PLANET events

Microlensing events should be observed in such a way to produce light curves with dense and regular data sampling, and possibly small scatter, so that we can distinguish binary lens from binary source events. Thus, it is important that follow-up observations, like those performed by the PLANET collaboration, are made upon alerts of the monitoring teams OGLE and MOA.

In modeling binary source and binary lens microlensing events, robust optimization methods, capable of avoiding local minima, should be used for finding the best solution. The genetic algorithm PIKAIA is a powerful tool for binary source light curve modeling, what is demonstrated in this work with the examples solved by the BISCO optimizing code. It is also a very good tool for solving binary lens light curves, as shown in Sec. 12.1.

Very good data quality and dense data sampling, combined with accurate binary lens and binary source modeling, yielded the discovery of the lowest-mass planet found outside of the Solar System so far, OGLE-2005-BLG-390Lb, having only 5.5 Earth masses. This was the first observed microlensing event in which the degeneracy between a planetary binary lens and an extreme flux ratio binary source model has been broken. What should be pointed out is that joint efforts, expertise and observed data of the three microlensing collaborations involved, PLANET, OGLE and MOA, were necessary for this planet discovery.

The flux ratio method is suggested in this work for breaking degeneracy between binary lens and binary source light curves. Even a few additional data points in photometric V band, together with a full light curve in I band, can give much information on the source stellar system, and enable breaking the degeneracy between binary source and binary lens microlensing events. With this method, it can be possible to observe even fainter sources than in the case of OGLE-2005-BLG-390 event, and still break the degeneracy in the solution. This means, it can allow finding planets with masses below a few Earth masses, using the existing PLANET facilities, keeping in mind that the source size is the limiting detection factor on the planet mass. The flux ratio method is reccomended for events for which binary source components have fluxes of different orders of magnitude. For the same order of magnitude, the difference in colors is too small, considering the two source stars are of the same age.

For events OGLE-2003-BLG-222 and OGLE-2004-BLG-347, degeneracy was encountered despite very dense data sampling. From light curve modeling and stellar

evolution theory, there was a slight preference to explain OGLE-2003-BLG-222 as a binary source event, and OGLE-2004-BLG-347 as a binary lens event. However, without spectra, this degeneracy cannot be fully broken. So for these kind of events, with fluxes of the components being of the same order of magnitude, taking spectra during the magnification is reccomened in order to break the degeneracy.

Part 3

Astrometric search for planets around white dwarfs in wide binary systems

CHAPTER 13

Introduction

Astrometry is a well-known procedure whereby unseen companions to stars can be detected by measuring the slight deviation in the target star's proper motion due to the gravity of the companion. Since two objects orbit around the common center of mass, if a star has planets in orbit around it then it will exhibit this deviation if the geometry is favorable. By measuring the deviation and the period it exhibits, it is possible to estimate orbital parameters and the mass of the object causing the wobble in the proper motion of the star. This assumes one knows the mass of the star in question. As an example, e.g. Jupiter causes an astrometric wobble of on order of 1 milliarcsecond in the Sun's proper motion, if seen from the distance of 10pc (Croswell, 1997). This is extremely small, but is measurable using modern equipment. Future instruments like the PRIMA facility at VLTI (the Phase Referenced Imaging and Micro-Arcsecond Astrometry facility at VLTI) and global astrometry mission GAIA will be capable of surveying the Solar neighborhood for the astrometric signatures of planets around stars.

The amplitude of the astrometric wobble (signal) in arc seconds is:

$$A" = \frac{m_P a_P}{m_S D} \tag{13.0.1}$$

where m_P is the mass of the planet, a_P is the orbital separation of the planet in A.U., m_S mass of the star and D distance of the system in pc (Schneider 1999). For example, for $m_P = 1 m_{Jupiter}$, $m_S = (2/3) m_{Sun}$, $a_P = 5 A.U.$ and $D = 20 pc$, $A" = 0.37 mas$. For this example the orbital period of the planet in a circular orbit is 13 years. So if one would observe for 1 or 2 years only with large intervals, that would be sufficient to detect a signal and confirm a planet. However, if we would want to calculate the planet mass and the orbital parameters, one should observe the whole orbit. It is clear from the formula that the planets at large separations from low mass stars will be good candidates for astrometric measurements.

Our attempt is to model how to perform high precision astrometry observations of nearby white dwarfs in wide binary systems in order to find planets around white dwarfs. We selected a sample of targets which should be observed by PRIMA, and modeled the observations which can be achieved for these targets. We want to show whether it is possible to fit the orbit and find the parameters of the potential planets, for the simulated observations.

13.1. Planets around white dwarfs

No planet was found so far around a white dwarf, though it is believed that white dwarfs should have Jupiter-like planets in wide orbits. Burleigh et al. (2002) suggest

that Jovian planets should survive the late stages of stellar evolution, and that white dwarfs will retain planetary systems in wide orbits (>5A.U.). They suggest infrared imaging with 8-m class telescopes. Duncan and Lissauer (1998) made detailed simulations of the evolution of planetary orbits through the solar mass loss phase at the end of the Sun's main-sequence lifetime. They found that those terrestrial planets that survive the Sun's red giant phase are likely to remain stable for (possibly much) longer than a billion years and those of the giant planets are likely to remain stable for (possibly much) more than ten billion years. They predict that the giant planets will be moved from 1 A.U. to the separations of 3 to 5 A.U. from the star.

Zinnecker et al. (2005) tried to find massive giant planets (6-12 Jupiter masses) around the known seven single white dwarfs in Hyades cluster at sub-arcsec separations by direct imaging with NICMOS/HST and NACO/VLT. They did not find any evidence for planetary mass companions with masses down to about 10 Jupiter masses nor brown dwarfs around any of the seven white dwarfs for separations larger than 0.5 arcsec. Wilson (2003) made an observational survey, using the Iowa Robotic Observatory, with the goal of detecting a transiting extrasolar planet around a white dwarf. An initial number of the local sample (within 20 parsecs) of white dwarfs was chosen, with 84 targets remaining out of 105 initial targets after known binary systems were removed. Of these 84 white dwarfs, 75 were observed and 128 light curves generated. No eclipse events were detected, which led to the conclusion that planets surviving very close to the Roche limit (within a few hundredths of an AU) are not common.

13.1.1. Planets around red dwarfs in binary systems with white dwarfs. There are two planets found so far in orbits around red dwarfs which are in binary systems with white dwarfs. Els at el. (2001) report the discovery of a close companion to HD 13445B via AO imaging, identifying the companion as a T-dwarf based on its colors. The recent publication of Mugrauer et al. (2005) identifies this companion as a cool white dwarf based on its spectrum, claiming the first white dwarf discovery in a planetary system. However, HD 147513 was the first white dwarf discovery in a planetary system, reported by Mayor et al. (2004). We now have two known systems with evidence of planets surviving the post-main-sequence evolution of a stellar companion, with this one being the closest known white dwarf companion to an exoplanet host (at a projected separation of just 21 AU). HD 147513B was the first white dwarf detected in an exoplanet system (Mayor et al 2004). The planet discovery paper notes the wide white dwarf companion at a projected separation of 5360 AU. They also mention a possible explanation for the wide separation being ejection of the white dwarf from an originally quadruple system. If this were true, this planet has survived post main sequence evolution of a companion as well as ejection of its parent star from a multiple system.

13.2. The mass loss

Probably all stars with initial masses up to about eight solar masses finally end up as white dwarfs. Stars with more than about 8 solar masses explode as type II supernovae after a lifetime of only a few million years and become neutron stars or black holes. 90% of all stars finally become white dwarfs when their nuclear energy generation has

ceased. With typically 0.6 solar masses and radii of about 0.01 solar radii the mean densities of white dwarfs are of the order of $\rho \sim 10^5 - 10^6 g/cm^3$ so that these stars can be considered as laboratories for matter at extreme densities and pressures. White dwarfs are stabilized against a gravitational collapse by the pressure of the degenerate electron gas in the interior.

Investigation of white dwarfs provide important constraints on the theory of stellar evolution. E.g. the existence of white dwarfs in young stellar clusters (with turn-off masses of about 5 solar masses) show that massive stars must loose the bulk of their matter during their lifetime until they become a white dwarf with about 1.15 solar masses. The majority of white dwarfs have masses of about 0.6 solar masses and stems from progenitor with about 2 solar masses. The mass-loss processes during the stellar evolution is not well understood; the largest quantity is lost on the asymptotic giant branch (AGB) when the energy in a star is produced by alternating ignitions of a hydrogen and helium burning shell ("thermal pulses") in the interior. At the end of this phase about 0.1-0.3 solar masses are lost when the outer layers are blown away; this matter subsequently becomes visible as a planetary nebula. The nebula emits light since it is ionized by the hot (typically 50-200 kK) remnant. This central star of a planetary nebula is the direct progenitor of a white dwarf. After about 30000 years the nebula becomes invisible and the white dwarf cools down before they eventually become invisible. The coolest white dwarfs known have an age of about 9-10 billion years.

Zinnecker at al (2005) discussed the consequences of the mass loss on the orbits of giant planets. They predict that the giant planets which are far enough not to be swallowed by the red giant, will be pushed towards the outer orbits due to conservation of the specific angular momentum.

If v_k is the Kepler velocity, $M_*$is the mass of the star, and a_{pl} planet separation, due to conservation of specific angular momentum:

$$v_{k,pl} a_{pl} = const$$

$$(\frac{GM_*}{a_{pl}})^{1/2} a_{pl} = const$$

$$M_* a_{pl} = const$$

which means that as the mass loss takes place, i.e. as M_* is decreasing, a_{pl} will be increasing. They derive:

$$\frac{a_{pl}(final)}{a_{pl}(initial)} = \frac{M_*(initial)}{M_*(final)}$$

This gives the motivation to look for planets around white dwarfs by astrometry, since the decreased star mass and the increased planet separation will increase the astrometric signal (Eq. 13.0.1).

CHAPTER 14

Interferometric astrometry

14.1. Interferometry with the VLTI

Interferometers are facilities that measure interference or other properties associated with interference of an electromagnetic field, produced by the combination of two (or several) telecopes. Interferometers provide access to high angular resolution information at a small fraction of the price of conventional single-aperture telescopes with similar angular resolution. In other words, the resolution is much better than the resolution achievable with conventional single-aperture telescopes. While the diffraction limit of a telescope is inversely proportional to its diameter, the angular resolution reached by an interferometer depends on the length separating the two telescopes projected onto the plane of the sky, also called the baseline. The baseline vector between two telescopes is the three-dimensional vector relying the intersection of the altitude and azimuth axes of a pair of telescopes.

The Very Large Telescope Interferometer (VLTI) is an interferometer on Cerro Paranal in Chile composed of four unit telescopes (UTs) and three Auxiliary telescopes (ATs). In order to produce interference, the signal of the two telesopces observing a distant source have to be combined coherently, i.e. corrected for the existing optical path difference, by using delay lines. The purpose of the delay lines is twofold, to equalize optical path length differences (OPD) and to transfer a pupil at a fixed location inside the interferometry laboratory. Considering the case of the VLTI, with two telescopes observing a distant source, the Optical Path Difference (OPD) is the sum of the external path difference and the internal path difference (Fig. 14.1.1). The external optical path difference is the geometric difference between the optical path length from the observed object to each telescope. It depends on the object position and on the baseline vector, and varies in time as Earth rotates (sidereal motion). The internal optical path difference is the difference in the optical path length, due to the interometer layout, from the telescope to the detector. It is also called delay offset or delay constant. The Unit Telescopes (UTs) are the four main telescopes of the VLTI. They have a diameter of 8.2m and are fixed on the ground. The Auxiliary telescopes (ATs), are smaller and are not fixed. With a diameter of 1.8m, the ATs will provide the best imaging capability of VLTI by complementing the array of the four 8.2m telescopes. The Auxiliary Telescopes can be placed on any of the 30 possible stations and provide therefore many interferometric baselines. The ATs will be used in the "Narrow Angle Astrometry" mode of VLTI (measuring extremely accurate positions of objects in the sky). This requires long baselines as well as regular and long-term monitoring, not achievable with the 8.2m telescopes.

FIGURE 14.1.1. Optical Path Difference for the VLTI

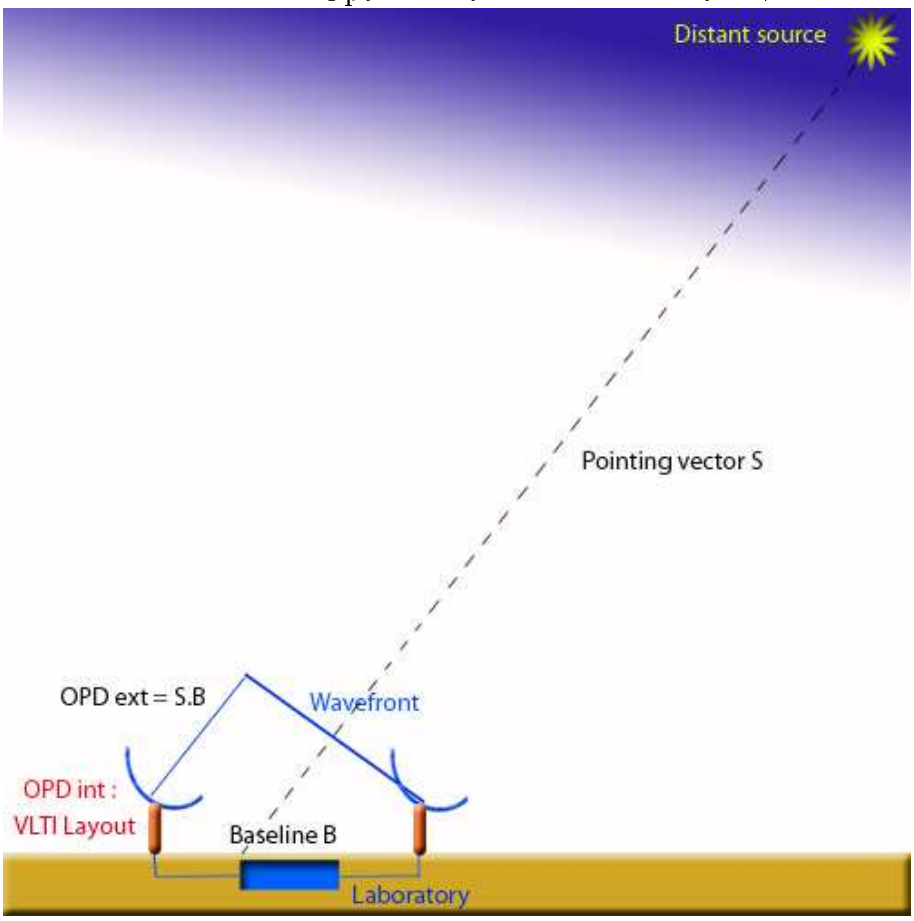

14.2. Basics of interferometry

Let's consider a monochromatic point source located at infinity and two telescopes that are observing the source in the direction **S**. The telescopes are on the x-axis, x-coordinates $x_1$and x_2.

They are separated by a baseline B given by: $B = x_2 - x_1$, where x_1 and x_2 are the positions of the two telescopes. The source being very far, the wavefronts can so be considered as plane. The waves observed by the telescopes are given by:

$$f_1 \sim exp(-ikx_1 s)exp(-ivt)$$

$$f_2 \sim exp(-ikx_2 s)exp(-ivt)$$

If we take for example $x_1 = 0$, the expressions become:

$$f_1 \sim exp(-ivt)$$

$$f_2 \sim exp(-ikBs)exp(-ivt)$$

The negative sign of the first exponential of f2 is due to the fact that the plane wavefront arrives later on the telescope 1.

The interferometer is equipped with delay lines that offer the possibility to add a supplementary OPD. If we consider that the first delay line adds the $OPD1 = d_1$ to the travel of the beam observed by the first telescope and $d_2 = OPD2$ added by the other delay line, the expressions become:

$$f_1 \sim exp(ikd_1)exp(-ivt)$$

$$f_2 \sim exp(ikd_2)exp(-ikBs)exp(-ivt)$$

The beams are then combined by a beam combiner. The resulting interferences have the following form:

$$f = f_1 + f_2 \sim exp(-ivt)[exp(ikd_1) + exp(ikd_2)exp(-ikBs)]$$

The resulting intensity is not merely the simple addition of the intensities 1 and 2 but is modulated by the phenomenon of interference:

$$moy \sim f * fconj = 2(1 + cos(k[sB + d_1 - d_2]))$$

$$Imoy = 2Io(1 + cos(kD))$$

That gives the traditional fringe scheme: I(D) as a function of OPD (shown in 14.2.1), with a sinusoidal form, varying between 0 and 2Io, with Io proportional to AF (and not equal because of some loss in the VLTI optical train concerning F) where A is the collecting area of the aperture and F the incident source flux power in units of incident energy per units time per units cross-sectional area. Two peaks are separated by: $kD = 2\pi$ (Fig. 14.2.1, top panel)

For a polychromatic source, the interferometers have a limited bandwidth, and a transmissivity depending on the frequency ν given by $h(\nu) : F(\nu) = Fh(\nu)d\nu$.

The fringe pattern will look like in Fig. 14.2.1 (bottom panel).

14.2.1. The isoplanatic angle. The light from two astronomical objects which are separated on the sky by a small angle will travel on slightly different paths through the Earth's atmosphere, as shown schematically in Figure 14.2.2. If layers of turbulence exist within the atmosphere, the light from the two objects will travel through slightly different parts of each turbulent layer. For two objects separated by a small angle $\Delta\theta$, the offset x in the position of the light paths as they intersect a layer at a height h is given by:

$$x = h\Delta\theta$$

If the offset x between the paths is sufficiently large, the atmospheric perturbations applied to the light from the two astronomical targets will differ. This variation in the atmospheric perturbations with angle is closely analogous to the change in the atmospheric perturbations as time elapses and the turbulence patterns within the atmospheric layers move past the telescope.

FIGURE 14.2.1. Theoretical fringes ($I/(2I_0) = f(D)$) for a monochromatic (top panel) and a polychromatic source (bottom panel).

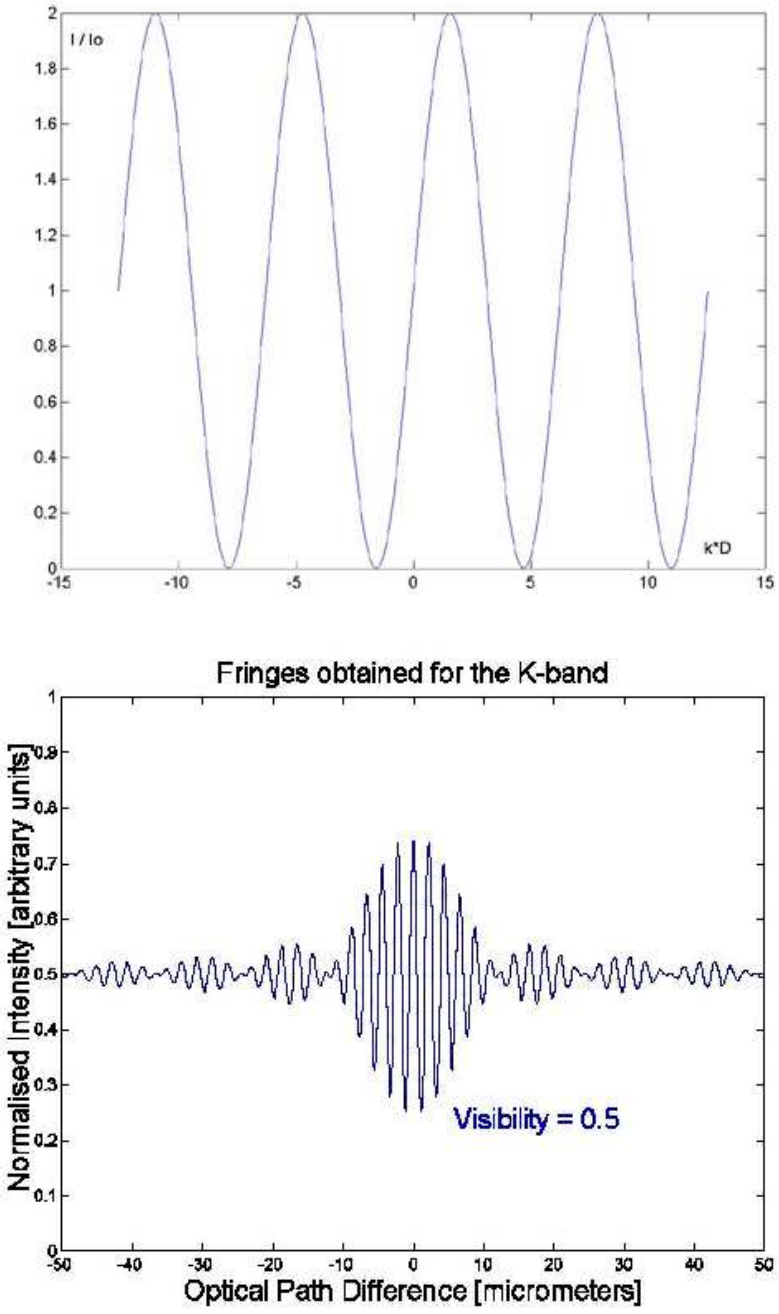

The angular separation $\Delta\theta_0$at which the atmospheric perturbations applied to the light from the two stars becomes uncorrelated is called the isoplanatic angle.

The isoplanatic angle is increasing function of wavelength. Typical values for observations at wavelength $500nm$ (V-band) are in the range of 1.5 arcsec to 5 arcsec. For

FIGURE 14.2.2. Schematic showing off-axis observations through an atmosphere with two turbulent layers. The off-axis beam passes through the turbulent layers at a position which is offset by an amount proportional to the height of the layer above the telescope (and indicated by x_1 and x_2 in the figure).

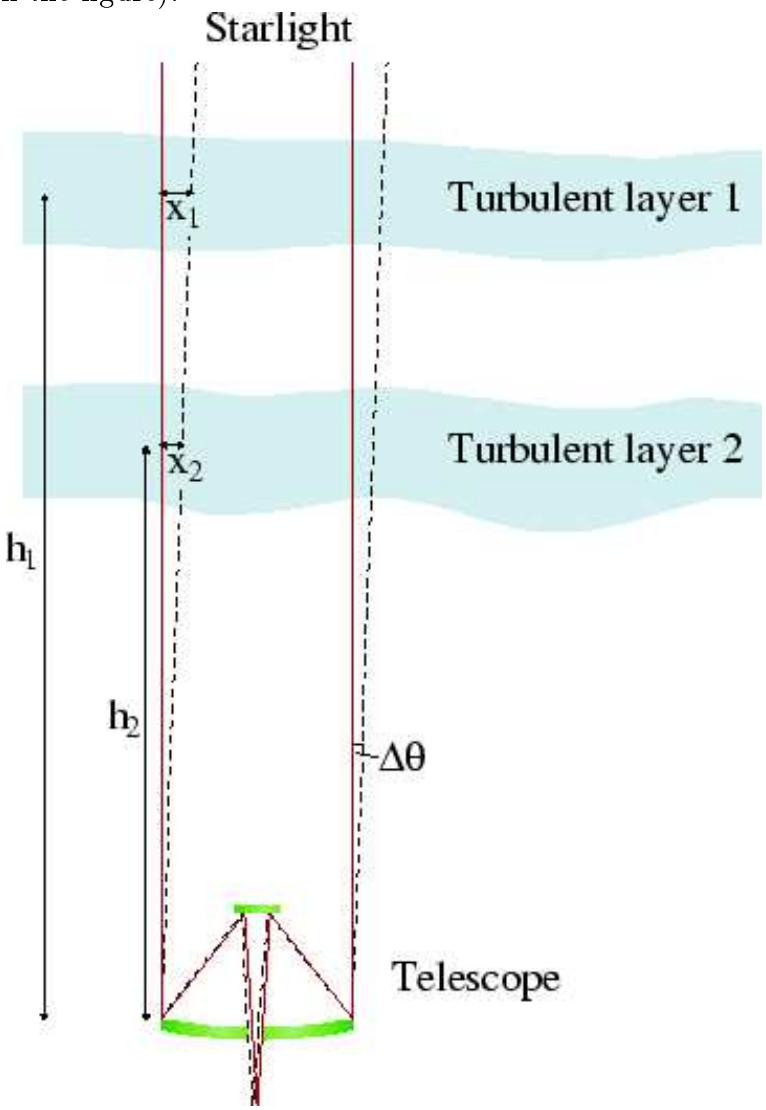

observations at the I-band it is around 30 arc sec, while for the K-band it is as large as 1 arc minute.

14.3. Astrometry with PRIMA

The PRIMA facility (Phase Referenced Imaging and Micro Arcsecond Astrometry) on the Very Large Telescope Interferemoter (VLTI) is a system designed to enable simultaneous interferometric observations of two objects - each with a size of at most 2 arcsec - that are separated by up to 1 arcmin, which corresponds to the isoplanatic

FIGURE 14.3.1. Increasing limiting magnitude with PRIMA and AMBER

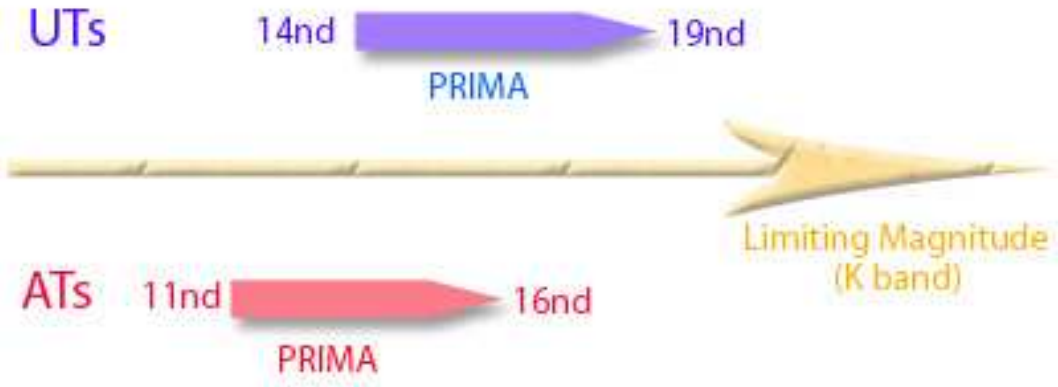

angle in the K-band, without requiring a large continuous field of view. Actually until nowadays the interferometry is limited in the sensitivity of observing faint objects by the atmospheric turbulence: the integration time must be short enough to freeze the fringe jitter. PRIMA will improve the sensitivity by using the bright guide star near the fainter object we want to image, in order to stabilize the fringe motion due to atmospheric turbulence. In the astrometry mode, due to its efficient fringe stabilization, PRIMA can be used to measure the angular separation between the two objects with high accuracy.

PRIMA will always practice interferometry with two telescopes. That's why the results are dependent primarily on one baseline. PRIMA will allow VLTI instruments like MIDI (The Mid-Infrared interferometric instrument) or AMBER (The near infrared/red VLTI focal instrument) to observe objects up to ~ 5 magnitudes fainter than in the single field mode (corresponding to a factor 100 to the brightness of the star). For example, it will enable AMBER to reach the K-band magnitude of 19 with the UTs (14.3.1).

There is always a 3 magnitude difference between the UTs and the ATs (so a performance attained for magnitude M on the UTs will be reached only for magnitude M-3 on the ATs). "Bright stars" are K-magnitude < 13 for the UTs, and < 10 for the ATs. We need to find one bright star to track the fringes. It could be a star close to the object of interest, for example, a bright binary companion. The estimate of the limiting magnitude on the faint object is $\sim 18-19$ mag in K-band with the UTs ($\sim 15-16$ mag on the ATs). But this will also depend on the stellar background and on the dynamic range of the detector. For the large noise, we expect a Gaussian or Poissonian data scatter of the astrometric signal (Delplancke 2005, Launhardt 2005).

14.3.1. Micro-arcsecond Astrometry. PRIMA high accuracy metrology and astrometric camera will also allow to measure relative angular positions of stars with a 10 μas accuracy (Delplancke et al. 2001, Launhardt 2005). Detection of Jupiter like

planets and characterization of gravitational micro-lensing events on the galactic center and on the Magellanic Clouds will then be possible. (Delplancke et al. 2001)

Interferometric astrometry is a complementary method to the radial velocity technique for extrasolar planet detection and characterization. Firstly, the radial velocity gives only an evaluation of the planet mass, depending on the orbital plane inclination i. Combined with astrometry, it gives its exact mass. Secondly, the applicability domains of both methods are complementary, astrometry being limited to nearby stars but being able to detect Jupiter-like planets far from the star while radial velocity can only detect planets close to the star (see Eq. 13.0.1).

Let us consider the simple case of a binary system with a star and a planet. In fact, both the star and the planet are orbiting around the mass center. However this system is moving with a common velocity. Thus the position of the mass center is oscillating around the line of translation of the system, corrected for the parallactic motion. This oscillation is called "the wobble" and is in this case sinusoidal. By observing the wobble we can infer the presence of a Jupiter-like planet and determine its mass. Note that if there are few planets around the star, the wobble isn't sinusoidal any more. Combined with the radial velocity techniques, the wobble observation and the shift of the wavelengths due to the Doppler effect allows determining the inclination of the orbital plane and the exact mass of the planet.

Precisely, the PRIMA astrometric mode will allow observing simultaneously two fields separated by 2 to 60 arcsec, to detect and track the fringes on the brightest object, to detect the fringes on the faintest, and to measure the phase of the secondary set of fringes relative to the primary one, with an accuracy of l/1000 at 2 μm. Indeed, the differential delay is measured with a very high accuracy (5nm rms) and is related to the angle between the two observed stars. The 200m baseline would give a figure of merit of 10 μas for a 10" separation angle, in only 30 min integration time.

The differential phase between the reference star and the object measured by PRIMA is given by:

$$OPD_{Ref-star} - OPD_{Object} = \Delta SB + \frac{\lambda}{2\pi}\phi_{Object} + OPD_{Atm} + OPD_{int}$$

where $OPD_{Ref-star}$ is the position of the fringes for the reference star, OPD_{Object} the position of the fringes for the studied object, ΔS the angular separation vector on the sky between the star and the object (i.e. the astrometric signal), B the baseline vector, ϕ_{Object} the object intrinsic phase (i.e. the imaging information), OPD_{Atm} the random differential OPD due to the atmospheric turbulence, and OPD_{int} the internal OPD introduced by the VLTI. What we ultimately want to measure is ΔS.

The first light on PRIMA is expected in the beginning of 2008 (Delplancke et al. 2006).

14.4. Selection of targets

Our targets are nearby white dwarfs in wide binary systems with main sequence companions, preferably red dwarfs. One reason is that observations in red (K-band) allow the largest isoplantic angle, which increases the possible number of reference stars. Red dwarfs will be best visible in K-band. The other reason is that these are old binary

systems, where the companion of the higher mass has already passed into the WD stage, with supposed planets migrated, and the lower mass companion can only be a red dwarf.

If the angular separation between the WD and the companion is between 2 and 60 arcsec, the companion can be used as an ideal phase reference star for PRIMA, having the same proper motion. If the two stars in the binary system are at a large absolute separation, the potential error coming from the orbital motion of the stars relative to each other will be small, due to the very long orbital period. If taking only the red companion as a reference star, only the relative star separation can be measured. If we have another phase reference star with known proper motion, this will give us additional information, i.e. we will be able to determine the absolute position changes of both binary components, red dwarf and white dwarf.

It is interesting to discuss how the red dwarf companion can influence the result. Red dwarfs can have significant oscillations of their center of light due to stellar spots. Can stellar spots induce 'false' planetary signals? They probably can't, because red dwarfs in binary systems with white dwarfs are old, and such old stars have low stellar activity. According to Bryden (2006), these oscillations for old red dwarfs can be up to 5 percent and for distances between 10 and 30 pc cannot influence the astrometric signal. Another question is, what happens if it is a red dwarf that has a planetary companion (see 13.1.1). In the case of measuring only the relative separation between the red dwarf and the white dwarf center of light, a planetary companion can produce a signal that can also be interpreted as a planetary signal of a white dwarf companion. Thus it will be necessary to take aditional data using another phase reference star.

The systems should be close enough so that the astrometric wobble due to a planet is detectable (i.e. to be larger than 0.1 mas). For a Jupiter in a circular orbit around a WD at 5 A.U. this is satisfied up to approx. 30pc. They should be observable from Paranal, in case of using PRIMA, have preferably southern declination, i.e. not larger than +30 degrees North.

The astrometric accuracy of PRIMA will be higher with brighter magnitude, so we need stars not fainter than the limiting magnitudes given in Fig 14.3.1. Crowded fields are problematic, we need both target and phase reference stars with clear fields of view within 2". So we want to look into the Galactic plane and not the Galactic Center region.

We show an example of an appropriate system. A 2MASS (Cutri et al. 2003) Ks band image of a 90 arcsec by 90 arcsec field, with the red dwarf white dwarf pair L 923-21/22 at the distance of $D = 10.4pc$, and the angular separation of the two stellar components of 27 arc sec is shown in Fig. 14.4.1. The K magnitude of the white dwarf is Ks=12.4 mag, well above the PRIMA limiting magnitude of 16 mag. The red dwarf is very bright, with Ks=7.4 mag, and can be used as a phase reference star. There is an another very bright background star in the field with Ks=9.0 mag. In Fig. 14.4.2 we see the same field taken in the optical blue passband (SuperCOSMOS Sky Surveys, Bj, Hambly et al. 2001) 15 years before the 2MASS observation. The white dwarf is the brightest object in this image. The common proper motion of the white dwarf/red dwarf pair is clearly visible.

FIGURE 14.4.1. The DC white dwarf L 923-21 (circled) and its red dwarf (dM5) common proper motion companion L 923-22. The red dwarf is the brightest star (Ks=7.4) in the 90 arcsec by 90 arcsec field, and overlaps with a relatively bright background star (Ks=9.0), which could be used as an additional reference star in PRIMA observations. The magnitude of the white dwarf is Ks=12.4, the separation between L 923-21 and L 923-22 is 27 arcsec. The red dwarf has an accurate ground-based parallax (more accurate than the Hipparcos parallax of the white dwarf) placing the system at about 10 pc distance.

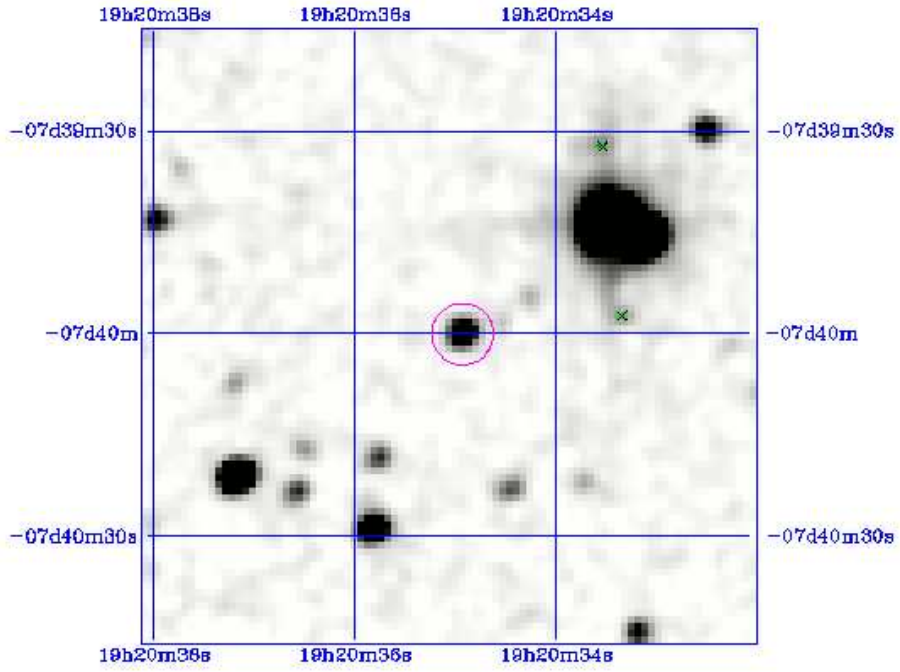

FIGURE 14.4.2. The same field as in 14.4.1taken in the optical blue passband (SuperCOSMOS Sky Surveys, Bj) 15 years before the 2MASS observation. The white dwarf is the brightest object in this image. The common proper motion of the white dwarf/red dwarf pair is clearly visible.

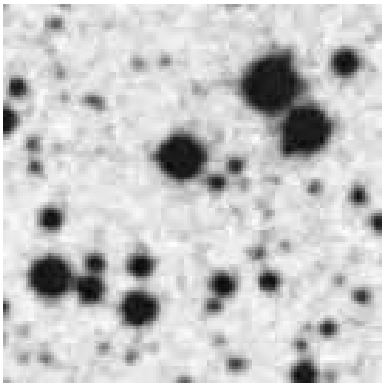

TABLE 1. List of the brightest southern observing targets (from Oswalt and Strunk 1994). First two columns are the coordinates (right ascension and declination), columns 3 and 4 are two photographic magnitudes for the two stellar components, column 5 is 2MASS red dwarf K magnitude, column 6 is the distance to the system (P - photometric, S - spectroscopic, and T - trigonometric), and the last column gives the physical separation of the components in arc seconds.

$R.A.(1950)$	$\delta(1950)$	$Phot(WD)$	$Phot(RD)$	$K(RD)$	$D(pc)$	$d_1["]$
$00h27m30s$	$-54^o58'00"$	15.8	15.7	8.9	14.6(P)	3.5
$01h58m32s$	$-16^o00'36"$	14.8	17.4	11.2	-	7
$03h26m45s$	$-27^o18'36"$	13.9	15.6	-	-	7
$04h43m18s$	$-27^o32'00"$	15.6	15.9	10.1	8.8(S)	49
$06h28m08s$	$-02^o03'42"$	15.3	16.8	9.9	-	4.5
$08h20m42s$	$-58^o32'00"$	16.2	17.0	9.7	-	21
$08h45m18s$	$-18^o48'00"$	15.1	12.8	9.0	-	31
$09h26m51s$	$-03^o57'00"$	15.3	16.7	10.4	-	19
$13h34m18s$	$-16^o04'00"$	15.1	15.2	9.5	62.1(P)	14
$13h48m30s$	$-27^o19'00"$	15.1	13.9	8.4	-	9
$15h55m22s$	$-08^o59'30"$	15.6	15.9	9.9	58.5(P)	10
$19h17m54s$	$-07^o45'00"$	12.2	13.7	7.4	10.1(T)	27
$19h32m54s$	$-13^o36'00"$	14.9	15.5	9.9	113.3(P)	28
$20h44m42s$	$-04^o18'00"$	16.4	16.6	11.8	-	17
$21h54m24s$	$-51^o14'00"$	14.9	11.5	5.9	16.2(T)	28
$21h54m48s$	$-43^o42'00"$	14.4	15.9	9.5	-	9
$22h24m36s$	$-34^o27'00"$	14.1	13.9	9.0	-	9
$23h23m30s$	$-24^o10'54"$	16.1	16.8	12.5	-	12
$23h41m45s$	$-16^o27'30"$	16.3	15.8	10.3	-	5
$23h51m31s$	$-33^o32'48"$	14.5	15.0	8.6	25.9(P)	7

White dwarfs in binary systems with red dwarfs were observed by Oswalt & Strunk (1994). In Tab. 1 we give our list of selected targets from their sample. We show only the targets with shouthern declination, because they will be closer to zenith and thus ensure better data observational quality. There are also some possible targets up to +30 degrees North in the sample. Oswald & Strunk give photometric colors of the two binary components. We have searched 2MASS catalogue for K photometric magnitudes and distances. For those objects with known distances, most of them are up to 30 pc. Three object have large distances, but we did not exclude them from the sample, since these distances may be very inaccurate, derived photometrically for white dwarfs.

We suggest to observe all the listed targets during the first 2 years. Even with only one or two data point per year for each object, what would require little telecope time, this would make it possible to select the candidates for which there is any signal (astrometric wobble) detected. When we select these candidates, these should be observed

until we cover the full orbit with denser data sampling in order to calculate the orbital parameters and the planet mass.

CHAPTER 15

Orbit modeling

For a triple system [(WD+Planet)+RD] at the distance of $D = 10pc$ the astrometric wobble and the relative star separation is shown in Fig. 15.0.1, showing changes in relative separation for a red dwarf of the mass $M_{RD} = 0.25M_{\odot}$in binary system with a white dwarf with mass $M_{RD} = 0.50M_{\odot}$ and a Jupiter-mass planetary companion to the white dwarf, for one orbital period of the binary system WD+RD. This model is already corrected for the annual parallax, which will be of the order of 0.1 arc sec.

We simulate a circular orbit by calculating the theoretical coordinates of the WD relative to the RD, in order to find out the limits on planetary mass, distance to the system, astrometric accuracy etc. We need to achieve the detection of planets around white dwarfs. For this study, a circular orbit is taken for simplicity, since it does not change the detectability significantly. The only important difference is that for an elliptic orbit, we need to take data during at least one full orbital period to determine the system parameters. In case we manage to take some data in the future which are promising for a planet detection, a more complicated fitting code will be designed, including eccentricity.

We perform our simulations for the following sets of parameters:

- Separation WD-Planet of 3, 5, and 10 A.U.
- Planet mass of 10 Jupiters, 1 Jupiters, and 10 Earths
- WD mass of 0.5 and 1.0 M_{Sun}
- Distance to the system: 10, 20, and 30 pc

The magnitude ranges of the models are in the range of magnitudes from the selected target sample, with minimum and maximum magnitudes for ATs and UTs. This corresponds to the limits given for PRIMA. We model the best accuracy limit (10 μas) down to 100 μas, which we still find accurate enough for planet detection. In addition, we model for astrometric accuracy of 1mas, in order to find out what can be reached using the existing operating facilities on the ground.

After calculating the theoretical orbits we add the simulated Gaussian noise to the data proportional to the error bars, and fit the orbits to such simulated observed orbits, for different densities of data sampling. In this way we are able to determine the astrometric accuracy and data sampling needed to detect a planet for a given set of parameters.

We assume the error bars to be the same in all directions, and for simplicity the orbit to be tilted such that it is rotated around the x-axis for an angle of inclination of i degrees. Considering the data sampling, we need to take in account that observing from the southern hemisphere means half-year gaps in the data sampling. So we model the data in such a way that we take one data point every two months, all together 3

FIGURE 15.0.1. Astrometric wobble for a triple system [(WD+Planet)+RD] for a Jupiter mass planet, during one orbital period of the binary system WD+RD. The solid line is the red dwarf, the short-dashed line the white dwarf, and the long-dashed line the planetary companion to the white dwarf (the one with the shortest period).

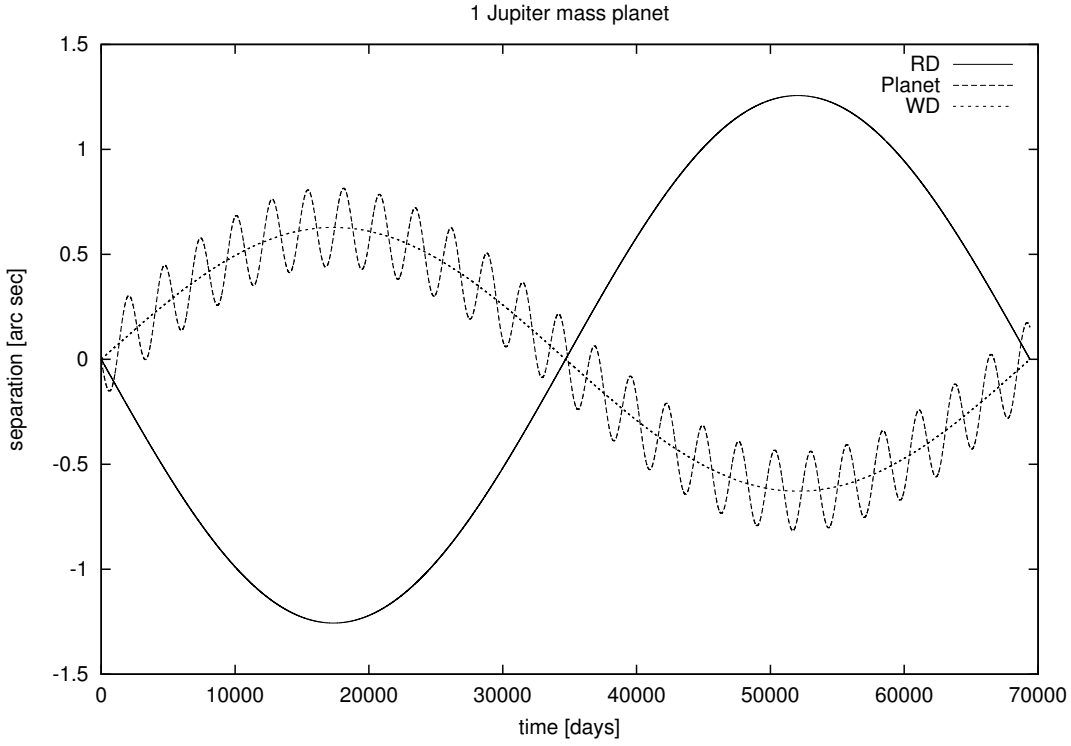

data points per year. We also model up to one point per month, and down to 1 point per year.

15.1. Fitting the orbits

The orbit of a white dwarf is defined through Kepler's laws. The squares of the periods of the planets are proportional to the cubes of their semi major axes:

$$T_a^2/T_b^2 = R_a^3/R_b^3 \tag{15.1.1}$$

The orbital period P of a planet around a star of mass M will vary as:

$$MP^2 \sim R^3 \tag{15.1.2}$$

where R is the semi major axis of the star-planet system.

a FORTRAN-90 optimizing code is constructed to fit the simulated orbits, and the best set of parameters fitting the data. We fit simultaneously three parameters: the mass ratio of the planet and the white dwarf $q_2 = \frac{m_{planet}}{m_{WD}}$, the separation between the planet and the white dwarf d_2, and the angle of inclination of the system to the observer i. We assume that the two stellar components and the planetary companion orbit in the same orbital plane, so that there is only one angle of inclination. The parameters which are held fixed for each run are: the distance to the system D in pc, the mass ratio of the white dwarf to the red dwarf $q_1 = \frac{m_{RD}}{m_{WD}}$, the astrometric accuracy in arc sec, and the data sampling mode. We also test the fit for the whole orbital period of the planet versus some parts of the orbital period (one half, one quarter) to find out how long we need to observe at least to get the rough orbit. This problem is easy with the circular orbit: observing one half of the orbit or even more than a quarter can be sufficient. However, in the case of a real planet, we do not know if the orbit is elliptical and thus need to observe the whole orbital period if we want the true parameters. For this study, a circular orbit is taken for simplicity, since it does not change the detectability as a function of other listed parameters, which is our goal. We do not fit the parallax, since the data will be taken for the objects of known distance i.e. known parallax, for which the observed data will be corrected before fitting.

The Downhill Simplex optimizing algorithm (Section 3.3) from Numerical Recipes (Press et al. 1992) was chosen as the optimizing routine, with 2-dimensional $\chi^2/d.o.f.$ (for the x and y coordinates fitted simultaneously) taken as a criterion of the goodness of fit. For each set of parameters, a minimum of 3 optimizing runs with different starting guessed Simplex values, possibly far enough from the initial set of parameters, was performed, in order to determine for which sets of parameters the orbits can be fitted, and to determine the error.

15.2. Examples

For the distance to the system of $D = 10pc$ and for a 10 Jupiter planet mass orbiting in a circular orbit a white dwarf of the mass $M_{WD} = 0.5M_{\odot}$ ($q_2 = 0.02$), and for a separation between the planet and the white dwarf of $d_2 = 5A.U.$ for a system observed under the angle of inclination $i = 45^0$, the astrometric wobble for one full orbital period of the planet will be an ellipse shown in Fig. 15.2.1.

We now simulate the data as explained in the previous section, with astrometric accuracy of $\sigma = 10\mu as$, and 3 data points per year taken every 2 months, with a half year gap. We add the Gaussian noise to the data, in such way that 1σ(standard deviation) of the Gaussian distribution is equal to the size of the error bar. In Fig. 15.2.2 we see the comparison of the fitted orbit (red line) vs. initial orbit (blue dotted line). The same fit is shown as the change of astrometric signal in x-coordinate vs. time in Fig. 15.2.3. The comparison of the fitted data for the initial orbit, and the orbit fitted to the simulated data is given in Tab. 1. We see that the fit is very close to the initial parameters, and can conclude that with the astrometric accuracy of $\sigma = 10\mu as$ we can fit the orbit with a high confidence.

FIGURE 15.2.1. Astrometric wobble during one rotational period of the planet P=13 years. The planet has 10 Jupiter masses, and is at the distance of 10 pc.

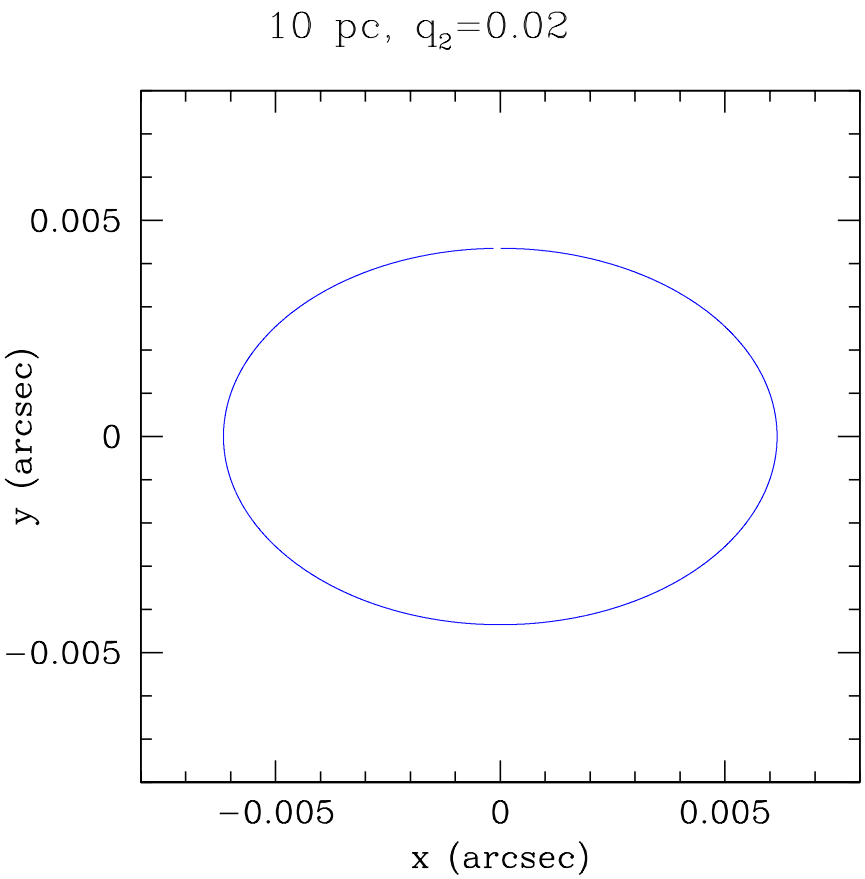

For planets of 1 Jupiter mass, the astrometric detection accuracy of $\sigma = 10\mu as$ yields with very confident models for 10 and 20 pc (Fig. 15.2.4, Tab. 2). For $\sigma = 100\mu as$, we still get good models for 10 pc (Fig. 15.2.5, 3), while for 20 pc the fits are not very accurate, however, still within reasonable limits.

We also want to find out what is possible with the existing astrometric facilities on the ground, i.e. for the astrometric accuracy of $1mas$.(Leinert et al, 2001) We test a 10 Jupiter mass planet at 10pc, and at 20pc. For 20pc the fit is shown in Fig. 15.2.6 (Tab. 5). It is clear from the figure that we can hardly fit anything on these data. In this case, for initial guess parameters far from the solution, we are more likely to get a very bad fit. For the same accuracy and the same system at 10 pc, we come very close to the initial parameters. It is obvious that the distance to the system plays an important role for the detectability. However, this detection requires almost 15 years of regular observations, which is not realistic.

TABLE 1. Parameter comparison for the fit shown in Fig. 15.2.2 and in Fig. 15.2.3. Upper row: initial parameters. Bottom row: parameters fitted to the simulated data. We have fitted simultaneously the 3 parameters determining the solution: distance between the planet and the white dwarf d_2, mass ratio of the planet to the WD q_2, and the inclination angle i.

$d_2[A.U.]$	$q_2(10^{-2})$	$i[^o]$	$\chi^2/d.o.f.$
5.00	2.00	45.00	
5.05	1.98	44.93	1.01

TABLE 2. Parameter comparison for the fit shown in in Fig. 15.2.4. Upper row: initial parameters. Middle row: parameters fitted to the simulated data for 10 pc and (Bottom row) 20 pc.

$d_2[A.U.]$	$q_2(10^{-2})$	$i[^o]$	$\chi^2/d.o.f.$	$D[pc]$
5.00	2.00	45.00		10/20
4.64	2.15	45.21	0.99	10
4.62	2.16	45.03	0.95	20

TABLE 3. Parameter comparison for the fit shown in Fig. 15.2.5. Upper row: initial parameters. Bottom row: parameters fitted to the simulated data.

$d_2[A.U.]$	$q_2(10^{-2})$	$i[^o]$	$\chi^2/d.o.f.$
5.00	2.00	45.00	
5.09	2.01	49.91	1.07

TABLE 4. Parameter comparison for the fit shown in Fig. 15.2.6. Upper line: initial parameters. Lower line: parameters fitted to the simulated data.

$d_2[A.U.]$	$q_2(10^{-2})$	$i[^o]$	$\chi^2/d.o.f.$
5.00	2.00	45.00	
3.19	2.52	21.38	1.02

TABLE 5. Parameter comparison for the fit shown in Fig. 15.2.6. Upper line: initial parameters. Lower line: parameters fitted to the simulated data.

$d_2[A.U.]$	$q_2(10^{-2})$	$i[^o]$	$\chi^2/d.o.f.$
5.00	2.00	45.00	
5.44	1.92	43.58	0.98

FIGURE 15.2.2. Simulated orbit from Fig. 15.2.1 for 3 data points taken per year (dots). The orbital period is 13 years. Blue dotted line - initial orbit. Red line - orbit fitted to the data.

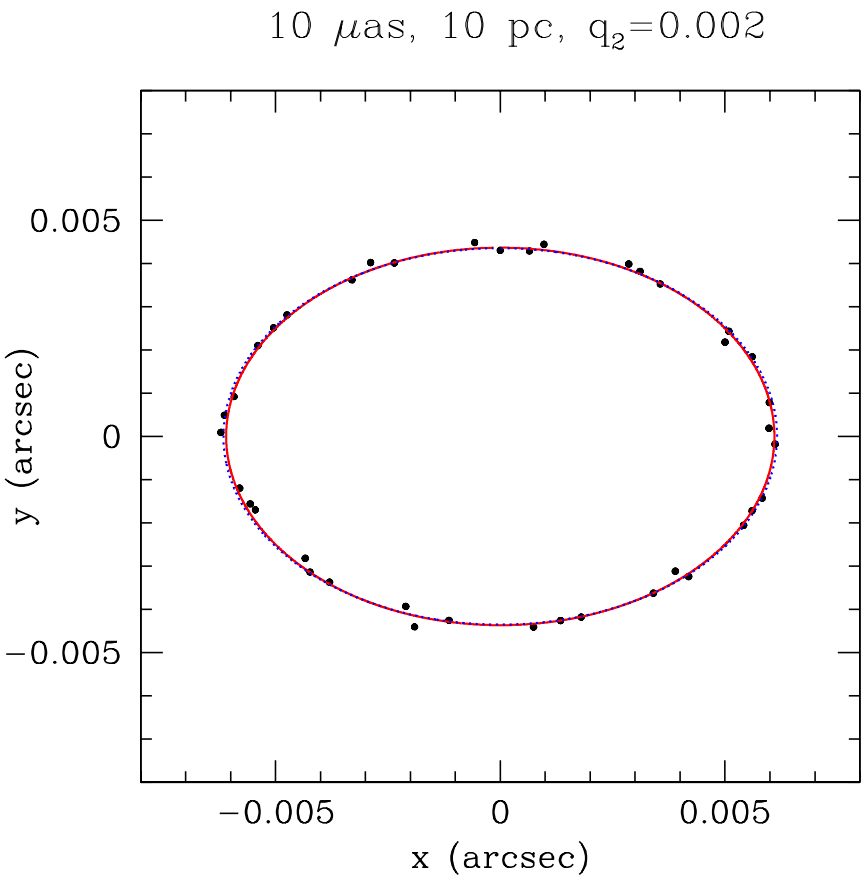

15.3. Results

We have performed at least 3 numerical simulations for different combinations of parameters given at the beginning of this chapter, and for different densities of data sampling. We decide to express the result in the simple tabular form which will be a guideline for the detectability. For each simulated case (one set of parameters) we give a judgment based on the visual inspection of the simulated data, and convergence of the fitting code towards the initial parameters. Instead of calculating errors from the 3 fits for the each set of parameters (performed for different random values for the data scatter, plus for different initial simplex), which might still have some systematic errors hidden, we rather decide to compare these 3 fits to judge which level of confidence they show in finding the solution. We assign three different 'grades' for the each set of parameters:

1. D = Detectable (very good detectability, confident determination of the system parameters)

FIGURE 15.2.3. The same fit as in 15.2.2, shown in x-coordinate vs. time.

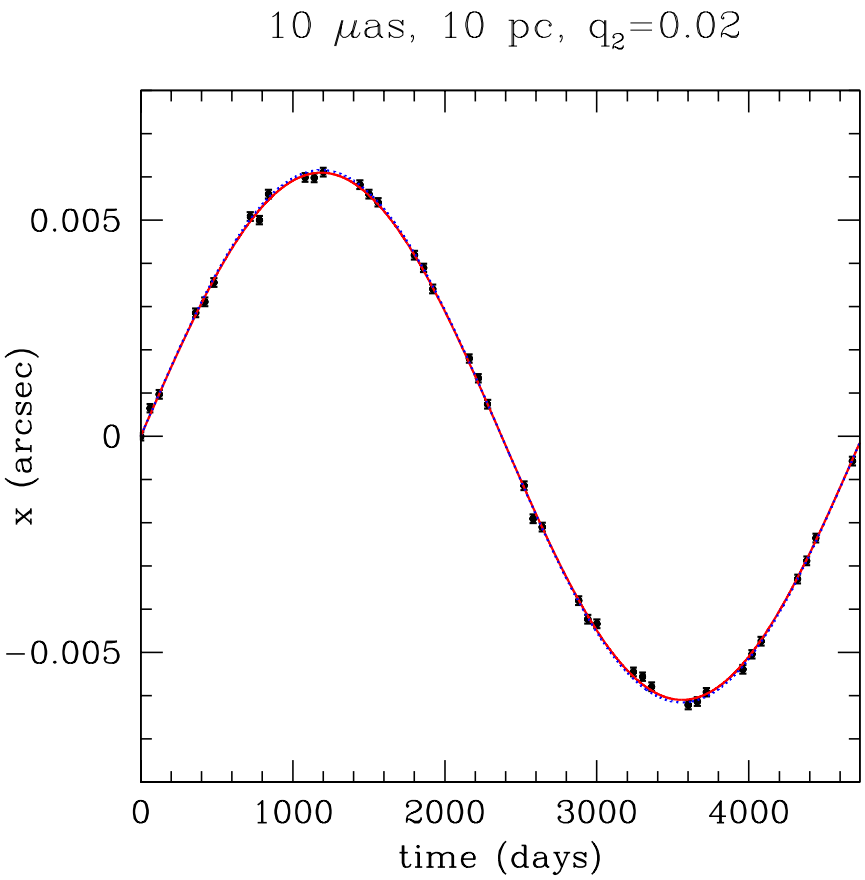

2. N = Not detectable (the planet might not be detected, the noise is of the order of magnitude of the signal)

3. L = on the Limit of being detectable (we can detect the presence of the planet, but cannot determine with high confidence the system parameters like the mass ratios, angle of inclination, separation etc., or the time for the detection is too long).

When applied to the examples shown in the last section, we assign them the following grades:

D: Fig. 15.2.2 and Fig. 15.2.4

N: Fig. 15.2.6

L: Fig. 15.2.5 and Fig. 15.2.7

For planets of the order of 1 Earth and 10 Earth masses, no detectability is possible. For the separations of 10 A.U. the rotational period is very long, and it would require too many years of observing. In particular 32 years for 1 Solar mass white dwarf according to Eq. 15.1.2 (unfortunately scientific projects do not get funded on such times scales, and even it they would, there might be problems with inheritance of the project after the scientist's death). On the other hand, if we would have this time available, detectability would increase, due to the larger separation (eq. 13.0.1). Separation of 3 A.U. has an

FIGURE 15.2.4. Comparison of the simulated orbits and fits to the data for the distance to the system of 10 and 20 pc, both for 1 Jupiter mass planet and $10\mu as$ accuracy.

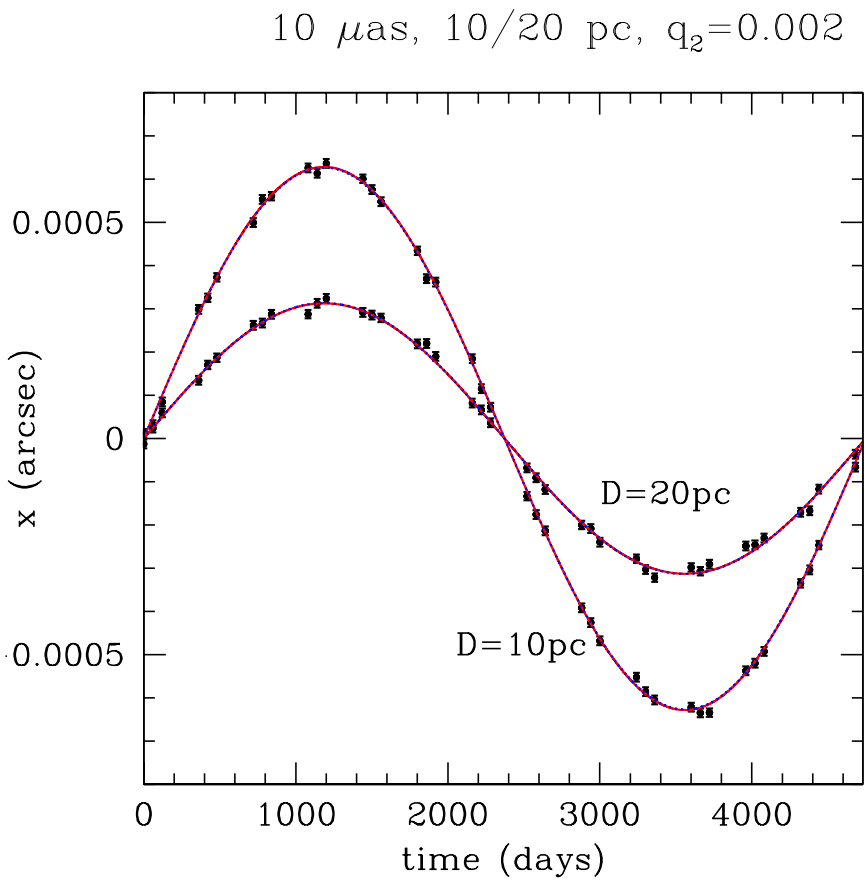

advantage of the short orbital period (roughly 7 years for a 0.5 Solar mass white dwarf). A disadvange is not only the decreased astrometric signal, but also the question whether the planet will survive the red giant phase. This will however be an interesting task to find out by astrometry, and that's why we suggest that it will be worth covering a 7 year period for nearby WDs, in case we manage to achieve the expected $10\mu as$ for PRIMA. In the case of a circular orbit, even 3.5 years of monitoring (a time scale of a PhD or a typical project funding) may be sufficient.

Considering data sampling, it was found that taking 3 data points per year is sufficient for determining the orbital parameters of a circular orbits, even for planet separations of 3 A.U. Simulations with 1 data point per year have also yielded relatively satisfying fits. However, we do not propose such data sampling for determination of the orbit parameters, but rather only for the first phase of the project, in case we cannot get more telescope time. In that case, for the first 3 years, the telescope time will be used in a more optimal way by taking data points for all the initial targets, with 1 data point per year per target. Once we have the candidates, we suggest following only the

FIGURE 15.2.5. 1 Jupiter mass planet and $100\mu as$ accuracy.

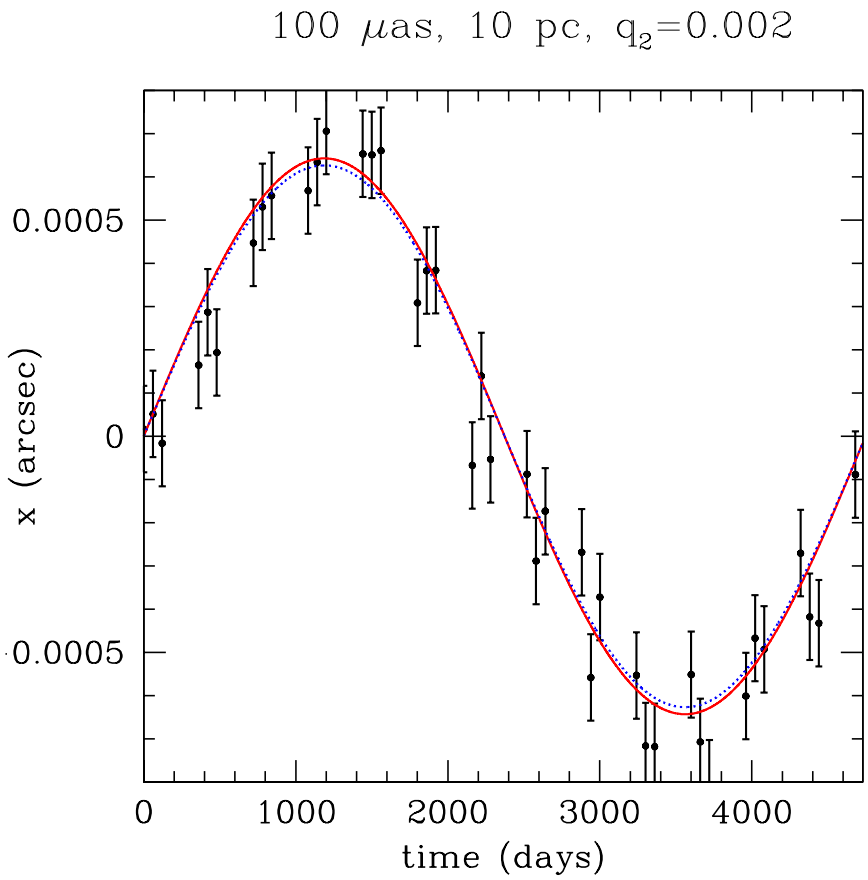

candidates with 3 or more data points per year. We do not mark the systems with separations larger than 5 A.U. as detectable, since the time for detection is too long. The planets at the separation of 3 A.U. are interesting, since covering one half of the orbit takes less than 4 years, which is realistic.

We performed calculations for different combinations of parameters until we have reached the limit at which the planets were not detectable any more, i.e. where we could not fit the orbit any more. We obtain the following detectability for 3 data points per year, for the following sets of parameters, where σ is the astrometric accuracy, D distance to the system, d_2 separation between the white dwarf and a planet, and q_2 mass ratio of the planet vs. WD:

1. $\sigma = 10\mu as$, $D = 10pc$,$d_2 = 5A.U.$, $q_2 = 0.02$: D
2. $\sigma = 10\mu as$, $D = 20pc$,$d_2 = 5A.U.$, $q_2 = 0.02$: D
3. $\sigma = 10\mu as$, $D = 30pc$,$d_2 = 5A.U.$, $q_2 = 0.02$: D
4. $\sigma = 10\mu as$, $D = 10pc$,$d_2 = 3A.U.$, $q_2 = 0.02$: D
5. $\sigma = 10\mu as$, $D = 20pc$,$d_2 = 3A.U.$, $q_2 = 0.02$: D
6. $\sigma = 10\mu as$, $D = 30pc$,$d_2 = 3A.U.$, $q_2 = 0.02$: D
7. $\sigma = 10\mu as$, $D = 10pc$,$d_2 = 5A.U.$, $q_2 = 0.002$: D

FIGURE 15.2.6. The same fit as in 15.2.3, for a 10 Jupiter mass planet, accuracy of 1mas, and distance of 20 pc.

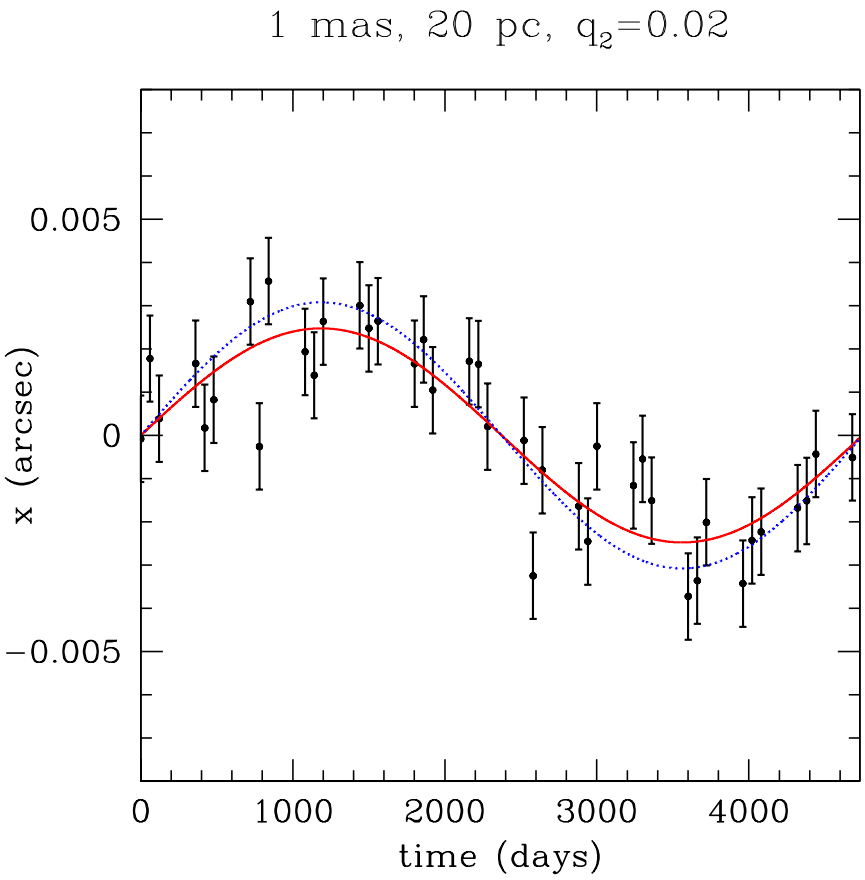

8. $\sigma = 10\mu as$, $D = 20pc$,$d_2 = 5A.U.$, $q_2 = 0.002$: D
9. $\sigma = 10\mu as$, $D = 30pc$,$d_2 = 5A.U.$, $q_2 = 0.002$: D
10. $\sigma = 10\mu as$, $D = 10pc$,$d_2 = 3A.U.$, $q_2 = 0.002$: D
11. $\sigma = 10\mu as$, $D = 20pc$,$d_2 = 3A.U.$, $q_2 = 0.002$: D
12. $\sigma = 10\mu as$, $D = 30pc$,$d_2 = 3A.U.$, $q_2 = 0.002$: D
13. $\sigma = 100\mu as$, $D = 10pc$,$d_2 = 5A.U.$, $q_2 = 0.02$: D
14. $\sigma = 100\mu as$, $D = 20pc$,$d_2 = 5A.U.$, $q_2 = 0.02$: D
15. $\sigma = 100\mu as$, $D = 30pc$,$d_2 = 5A.U.$, $q_2 = 0.02$: L
16. $\sigma = 100\mu as$, $D = 10pc$,$d_2 = 3A.U.$, $q_2 = 0.02$: D
17. $\sigma = 100\mu as$, $D = 20pc$,$d_2 = 3A.U.$, $q_2 = 0.02$: L
18. $\sigma = 100\mu as$, $D = 30pc$,$d_2 = 3A.U.$, $q_2 = 0.02$: N
19. $\sigma = 100\mu as$, $D = 10pc$,$d_2 = 5A.U.$, $q_2 = 0.002$: D
20. $\sigma = 100\mu as$, $D = 20pc$,$d_2 = 5A.U.$, $q_2 = 0.002$: L
21. $\sigma = 100\mu as$, $D = 30pc$,$d_2 = 5A.U.$, $q_2 = 0.002$: N
22.$\sigma = 100\mu as$, $D = 10pc$,$d_2 = 3A.U.$, $q_2 = 0.002$: L
23. $\sigma = 100\mu as$, $D = 20pc$,$d_2 = 3A.U.$, $q_2 = 0.002$: N

FIGURE 15.2.7. The same fit as in 15.2.6, for $D = 10pc$.

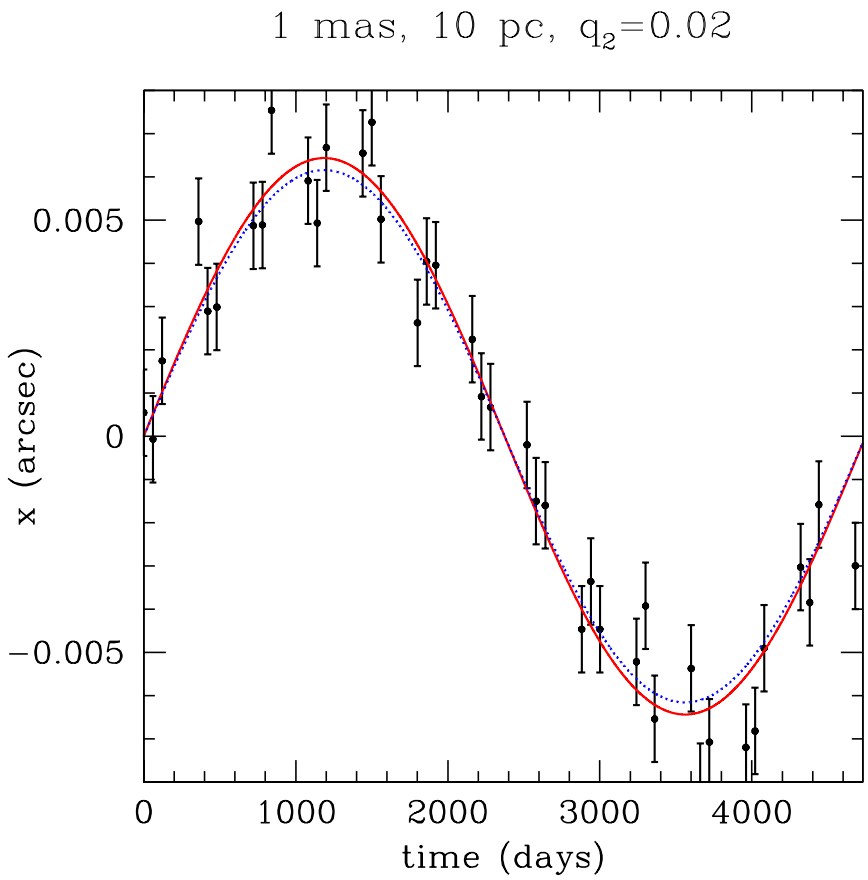

24. $\sigma = 100\mu as$, $D = 30pc$,$d_2 = 3A.U.$, $q_2 = 0.002$: N
25. $\sigma = 1mas$, $D = 10pc$,$d_2 = 5A.U.$, $q_2 = 0.02$: L
23. $\sigma = 1mas$, $D = 20pc$,$d_2 = 3A.U.$, $q_2 = 0.02$: N
24. $\sigma = 1mas$, $D = 30pc$,$d_2 = 3A.U.$, $q_2 = 0.02$: N

15.4. Conclusion

The PRIMA facility at VLTI will be able to detect planets around white dwarfs once it is operating, by detecting the astrometric wobble of the WD due to a planet companion. It is desirable to observe one full orbital period of the planet, especially since we don't know if the orbit is elliptical. For circular orbits one half of the orbital period should be sufficient. We find that we can detect planets of 1 and 10 Jupiter masses around WDs up to distance of 30 pc without a problem with the PRIMA VLTI facility, even if we consider that the accuracy can go down from the expected $10\mu as$ to $100\mu as$. For an accuracy of $1mas$, corresponding to the existing astrometric facilities, we might detect 10 Jupiter mass planets at the distance of 10 pc for a separation between the planet and the WD of 5 A.U., but this is the limiting value. For separations larger than 5 A.U., detection would be easier, but we would need too many years to cover

the orbit. The sample of white dwarfs in wide binary systems should be observed with PRIMA over a time range of $\sim$ 10 years in order to detect the astrometric wobble caused by the orbital motion of its planet of the WD relative to its stellar companion, and relative to at least one more phase reference star with known proper motion.

CHAPTER 16

Summary and perspectives

In Part I of this work, by studying simulated stellar microlensing events towards the Galactic Bulge, we have found that some binary lens light curves will be fitted well with single lens models and hence misinterpreted as single lens events. We have quantitatively evaluated this effect. The probability for such a misinterpretation depends strongly on the separation of the two binary system components, reaching a minimum between projected separation of $0.6R_E$ and $1R_E$. For such binary lenses it is relatively unlikely (probability of less than 10%) that they are misinterpreted. For smaller and larger separation, this probability will be larger, strongly depending on the separation. The probability for misinterpretation increases for more extreme mass ratios, explaining why the detection probability for a binary system consisting of a star with a planet is smaller than the detection probability for a stellar binary. Good quality data, i.e. good data sampling and small errorbars, decreases the probability for misinterpretation. From the correction factors obtained in this statistical interpretation of a large number of observed binary microlensing events, the population of Galactic binary stars with certain separation limits can be determined in the future.

In Part II, we fitted synthetic and observed light curves, in order to break the degeneracy between binary lens single source and single lens binary source microlensing events. An optimizing code BISCO (Binary Source Code for Optimization) was constructed using the genetic algorithm PIKAIA, in order to fit simultaneously light curves of binary source microlensing events observed in I, R, and V photometric bands at different observing sites. It was shown that the BISCO optimizing code is capable of finding the right solution even with a large span of starting parameters, through the benefits of the PIKAIA, suitable for finding the best solution in parameter spaces with many local minima.

In this work we have suggested the flux ratio method to break the degeneracy between the binary lens and the binary source events from photometric light curve solutions. The method suggests taking a few data points in the V photometric band in addition to the light curve in the I band, especially concentrated on the times of high magnification due to the two stars. For two stars of different spectral types, the flux ratio of the nonmagnified fluxes of the two stellar components in V band $fr(V) = F_A(V)/F_B(V)$ will differ from the flux ratio in the I band $fr(I) = F_A(I)/F_B(I)$. The method was tested using the BISCO code on synthetic light curves. The two models, with the flux ratios in V band $fr(V) = 200$ and $fr(V) = 1000$, both with flux ratio in I band $fr(I) = 500$, show that if we observe two light curves in I and V band, we can distinguish a binary source event from a binary lens event. This will depend on the flux ratio: for extreme flux ratios this method is more successful. This case is of

a special interest since it is degenerate to a solution of a lens with a low mass planet. The problem with flux ratios of the same order of magnitude is that the two binary components lie too close on the isochrone, i.e. have a difference in [V-I] color which is comparable with the fit error. We plan to extend this study in the near future, performing a large number of additional simulations for a large span of parameters, using binary source and binary lens fitting codes BISCO and TANGO, to find out how the efficiency of this method changes with different parameters involved.

For the microlensing events observed by the PLANET collaboration, OGLE-2003-BLG-222 and OGLE-2004-BLG-347, degeneracy between a binary lens and a binary source solution was encountered despite very dense data sampling. From light curve modeling and stellar evolution theory, there was a slight preference to explain OGLE-2003-BLG-222 as a binary source event, and OGLE-2004-BLG-347 as a binary lens event. However, without spectra, this degeneracy cannot be fully broken. So for this kind of events, with component fluxes being of the same order of magnitude, taking spectra during the magnification is recommended in order to break the degeneracy. For the event OGLE-2005-BLG-390, this degeneracy was successfully broken, due to the high-quality densely sampled data, collected by the PLANET, OGLE, and MOA collaborations. As the best light curve solution, a binary lens with the mass ratio of $q = (7.6 \pm 0.7) \times 10^{-5}$ was found. By performing a Bayesian analysis employing the Galactic models and mass functions, a planet of the mass $m_p = 5.5^{+5.5}_{-2.7} m_{Earth}$, at the orbital separation of $d = 2.7^{+1.5}_{-0.6} A.U.$ from a red dwarf with the mass of $m_s = 0.22^{+0.21}_{-0.11} M_{Sun}$ was found, named OGLE-2005-BLG-390Lb. This is the lowest-mass planet found up to date (June 2006) outside of the Solar system.

In Part III, we studied whether planets around white dwarfs in wide binary systems can be detected astrometrically. We performed numerical simulations of astrometric orbits, for different sets of parameters, and selected a list of observing targets. We have found that the PRIMA facility at VLTI will be able to detect planets around white dwarfs once it is operating, by detecting the astrometric wobble of the WD due to a planet companion. If we want to determine the system parameters with high accuracy, it is desirable to observe one full orbital period of the planet, especially since we do not know the orbital eccentricity. For circular orbits one half of the orbital period should be sufficient. For the pure detection of a planet existence, astrometric monitoring covering of 2 to 3 years with taking only 1 or 2 data points per year may be sufficient. We find that we can detect planets of 1 and 10 Jupiter masses around WDs up to distances of 30 pc without a problem with the PRIMA VLTI facility, even if we consider that the accuracy can go down from the expected $10 \mu as$ to $100 \mu as$. For an accuracy of $1 mas$, corresponding to the existing astrometric facilities, we might detect 10 Jupiter mass planets at the distance of 10 pc for a separation between the planet and the WD of 5 A.U., but this is the limiting value. Once PRIMA is operating in the near future, we will apply for observing time, and monitor the selected white dwarfs in wide binary systems in the hope to detect the presence of Jupiter-like planets around white dwarfs.

Acknowledgments

While working on this thesis, I have had the pleasure of interacting scientifically with different people, and their different ways of thinking. These personalities have enriched and broadened not only my scientific perception, but also my perception of the Universe and society from a human point of view. I am very grateful to these beautiful minds for giving me such an opportunity to develop myself. What I found especially fascinating, was that working with people with different ways of thinking helps one develop one's own potentials in the best way.

I wish to thank my supervisor Prof. Joachim Wambsganss for his patience and efforts in helping me with this work, and for providing me financial support. He managed to delight me with a new fascinating topic, microlensing, that made me change my field of research. This is something I never regretted. I especially appreciate that he taught me to work systematically, approach new problems in an efficient way, and present my work in a visual way, which has become a great pleasure for me.

I am thankful to my co-supervisor Hans Zinnecker for his brilliant ideas, for supporting me and helping to continue and finish this work. From the start, he has been enriching me with ideas emerging from his wide knowledge and strong scientific intuition. He has been supporting me in following my own scientific intuition and work on the topics which were inspiring me. I appreciate this very much.

This work would have not been possible without the PLANET collaboration. Observing PLANET events, and being able to work on these data afterwards, has been a very exciting experience, which I would like to continue in future. I am thankful to all of the members, especially Jean-Philippe Beaulieu for teaching me many useful things, and supporting me in working on PLANET modeling. To Daniel Kubas, Arnaud Cassan, Martin Dominik, Dave Bennet, Pascal Fouque and Dan Bramich for very constructive discussions and work interactions. To John Greenhill for introducing me to the Tasmanian telescope and the pleasure of observing. To Uffe Jorgensen for funding my observational stay in Chile. I am also thankful to the MOA and OGLE collaborations for providing me with their data and the exchange of ideas with some members.

Thanks to the organizers of the Saas-Fee Winter school in gravitational lensing, IAC Winter School, and Michelson Summer School in Astrometry, for the valuable knowledge and financial support these schools have provided.

Some people have enriched me with their knowledge through our scientific discussions, spending their time to help me in proceeding with this work: Ralf-Dieter Scholz, Michael Andersen, Francoise Delplancke, Ralf Launhardt, Robert Schmidt, Ralf Klessen, Petar Mimica, Serge Correia, Geoff Bryden, Joris Gerssen, and many others,

and to people who have read parts of this thesis and commented on it for either scientific or language aspects.

Our astro-secretary Andrea Brockhaus at the University of Potsdam has been taking care of me since I arrived in Potsdam, not only with my work, but also helping me to start feeling at home here with very much success. I am also very grateful to Prof. Wolf-Rainer Hamman and Prof. Matthias Steinmetz for the financial support to finish the thesis in Potsdam, to the staff, especially Christine Rein, and my colleagues at the University of Potsdam and the Astrophysikalisches Institut Potsdam who have been so friendly and helpful to me in different ways, turning my working environment into a very pleasant place (extra credits to the "1 o'clock lunch crew"). Interactions with the two working groups (the Star Formation group of Hans Zinnecker at the AIP and the former Gravitational Lensing group of Prof. Wambsganss at the University of Potsdam) have been a pleasure for both exchanges of scientific ideas and social interactions. Special thanks to Stefan, for organizing the Social Meetings of PhD students in Potsdam, Spyros and Katharina for making coffee, and to Isabelle for the moral support during the weekend and night shifts while writing this thesis. I will allow myself to be a bit informal at this point, some of us named the SF group meetings "The group therapy", due to the good and relaxed atmosphere with a lot of humor involved and smiling faces.

I should not forget to mention that I would not have ended up in Potsdam without Prof. Lutz Wisotzki, who advertised Potsdam to me as a nice place for an astrophysicist, and Prof. Rolf Kudritzki, to whom I'm thankful for ending up in Germany, my second 'at home'.

Last but not least, I want to stress that this work would not have been possible without love of my dearest ones who have supported me in both happy and tough times: Predrag, my parents, family and friends.

Bibliography

[1] Abt H.A., Levy S.G., ApJS, 30, 273 (1976)

[2] Alcock, C., et al. Nature, 365, 621 (1993)

[3] Albrow M. et al, ApJ, 509, 687 (1998)

[4] Albrow M. et al, ApJ, 522, 1022 (1999)

[5] Andersen, M., private communication (2006)

[6] Beaulieu, J.P., D.P. Bennett, P. Fouque, A. Williams, M. Dominik, U.G. Jorgensen, D. Kubas, A. Cassan, C. Coutures, J. Greenhill, K. Hill, J. Menzies, P.D. Sackett, M. Albrow, S. Brillant, J.A.R. Caldwell, J.J. Calitz, K.H. Cook, E. Corrales, M. Desort, S. Dieters, D. Dominis, J. Donatowicz, M. Hoffman, S. Kane, J.-B. Marquette, R. Martin, P. Meintjes, K. Pollard, K. Sahu, C. Vinter, J. Wambsganss, K. Woller, K. Horne, I. Steele, D. Bramich, M. Burgdorf, C. Snodgrass, M. Bode (PLANET) A. Udalski, M. Szymanski, M. Kubiak, T. Wieckowski, G. Pietrzynski, I. Soszynski, O. Szewczyk, L. Wyrzykowski, B. Paczynski (OGLE), the MOA Collaboration, Discovery of a Cool Planet of 5.5 Earth Masses Through Gravitational Microlensing, Nature, 439, 437 (2006)

[7] Bedin L.R., Cassisi S., Castelli F, Piotto G., Anderson J., Salaris M., Momany Y., and Pietrinferni A., MNRAS - vol. 357, 1038 (2005)

[8] Bennet, D.P., Rhie, S.H., ApJ, 574,985-1003 (2002)

[9] Bond, I.A. et al, MNRAS, 327, 868 (2001)

[10] Bond, I. A.; Udalski, A.; Jaroszynski, M.; Rattenbury, N. J.; Paczynski, B.; Soszynski, I.; Wyrzykowski, L.; Szymanski, M. K.; Kubiak, M.; Szewczyk, O.; Zebrun, K.; Pietrzynski, G.; Abe, F.; Bennett, D. P.; Eguchi, S.; Furuta, Y.; Hearnshaw, J. B.; Kamiya, K.; Kilmartin, P. M.; Kurata, Y.; Masuda, K.; Matsubara, Y.; Muraki, Y.; Noda, S.; Okajima, K.; Sako, T.; Sekiguchi, T.; Sullivan, D. J.; Sumi, T.; Tristram, P. J.; Yanagisawa, T.; Yock, P. C. M., OGLE 2003-BLG-235/MOA 2003-BLG-53: A Planetary Microlensing Event, ApJ, 606L, 155B (2004)

[11] Bozza V., A&A 374, 13-27 (2001)

[12] Bryden Geoff, private communication (2005)

[13] Burleigh, M.R., Clarke, F.J., Hodgkin, S.T., MNRAS, 331, L41-L45 (2002)

[14] Cassan, A., PhD Thesis, Univ. Paris (2006)

[15] Cassan, A, J.P. Beaulieu, D. Kubas, P. Fouque, U.G. Jorgensen, J. Greenhill, M. Dominik, C. Coutures, J.A.R. Caldwell, D. Bennert, M.D. Albrow, J.J. Calitz, K. Cook, D. Dominis, J. Donatowicz, K. Hill, M. Hoffman, K. Horne, V.R. Miller, S. Kane, J.B. Marquette, R. Martin, P. Meintjes, J. Menzies, K.R. Pollard, K.C. Sahu, C. Vinter, J. Wambsganss, A. Williams (The PLANET Collaboration), A. Udalski, M.K. Szymanski, M. Kubiak, G. Pietrzynski, L. Soszynski, K. Zebrun, O. Sxewczyk, L. Wyrzykowski (The OGLE collaboration), D. Heytovsky, OGLE 2004-BLG-254: a K2 III Galactic Bulge Giant spatially resolved by a single microlens, submitted to Astronomy and Astrophysics (manuscript no. AC254n12) (2005)

[16] Cassisi S., Salaris M., Castelli F and Pietrinferni A., ApJ, 616, 498 (2004)

[17] Claret, A., A&Am 363, 1081, (2000)

[18] Collinge, M. J., astro-ph/0402385 (not published yet) (2004)

[19] Charbonneau, P.ApJS,101,309(1995)

[20] G. Chauvin; A.M. Lagrange; C. Dumas; B. Zuckerman; D. Mouillet; I. Song; J.-L. Beuzit; P. Lowrance, A&A, 425, L29 (2004)

[21] Croswell, K., Lunar and Planetary Exploration, book (1997)

[22] Cutri, R.M., Skrutskie, M.F., Van Dyk, S., et al. The 2MASS All-Sky Catalog of Point Sources, University of Massachusetts and Infrared Processing and Analysis Center (IPAC/California Institute of Technology) (2003)
[23] Darwin, C., On the origin of species, John Murray, London (1859)
[24] Delplancke, F., Gorski, K.M., Richichi, A., A&A 375, 701, 710 (2001)
[25] Delplancke, F., private communication (2005)
[26] Delplancke et al. - slides- (2006)
[27] Di Stefano, R., Perna, R., ApJ 488, 55 (1997)
[28] Di Stefano, R., Mao, S., ApJ 457, 93 (1996)
[29] Di Stefano, R., Scalzo, A., ApJ 512, 564 (1999a)
[30] Di Stefano, R., Scalzo, A., ApJ 512, 579 (1999b)
[31] Delgado-Donate E.J., Clarke C.J., Bate M.R., Hodgkin S.T., Mon. Not. R. Astron. Soc., 000, 1-14 (2003)
[32] Dominik M., A&A, 349,108 (1999)
[33] Dominik, M., astro-ph(0507540), (2005)
[34] Dominik, M., A&A 333, 893 (1998)
[35] Dominik, M., Ph.D. thesis, Univ. Dortmund (1998)
[36] Dominis, D., Pavlovski, K., Mimica P., Tamajo E., Astrophysics and Space Science, 296, 189 (2005)
[37] Duquenney A, Mayor M., A&A, 248, 485(1991)
[38] Durisen R.H., Sterzik M.F., A&A, 286, 84(1994)
[39] Duncan, Martin J.; Lissauer, Jack J., Icarus, Volume 134, Issue 2, pp. 303-310 (1998)
[40] Els, S.G., Sterzik, M.F., Marchis, F., Pantin, E., Endl, M., Kurster, M., AAP, 370, L1 (2001)
[41] Fischer D.A., Marcy G.W., ApJ, 396, 178 (1992)
[42] Friedrich, S., Zinnecker, H., Brandner, W., Correia, S., McCaughrean, M., ASP Conference Series, 334, 431(2005)
[43] Gaudi, S., ApJ, 506:533-539 (1998)
[44] Gaudi, S., Han, C., ApJ, 611:528-536 (2004)
[45] Gerhard, O., Dynamics of Galaxies: from the Early Universe to the Present, 15th IAP meeting held in Paris, France, July 9-13, 1999, Eds.: Francoise Combes, Gary A. Mamon, and Vassilis Charmandaris ASP Conference Series, Vol. 197, ISBN: 1-58381-024-2, 2000, p. 201.
[46] Gould, A., Han, C., The Astrophysical Journal, Volume 538, Issue 2, pp. 653-656
[47] Gould, A., Udalski, A., D. An, D.P. Bennett, A.-Y. Zhou, S. Dong, N.J. Rattenbury, B.S. Gaudi, P.C.M. Yock, I.A. Bond, G.W. Christie, K. Horne, J. Anderson, K.Z. Stanek, D.L. DePoy, C. Han, J. McCormick, B.-G. Park, R.W. Pogge, S.D. Poindexter, I. Soszynski, M.K. Szymanski, M. Kubiak, G. Pietrzynski, O. Szewczyk, L. Wyrzykowski, K. Ulaczyk, B. Paczynski, D.M. Bramich, C. Snodgrass, I.A. Steele, M.J. Burgdorf, M.F. Bode, C.S. Botzler, S. Mao, S.C. Swaving, ApJL, submitted, Astro-ph/0603276 (2006)
[48] Griest, K., Hu, W., ApJ, 397(2), 362 (1992)
[49] Han, C., ApJ, 564(2), 1015-1018 (2002)
[50] Hakala, P. J., A&A, 296, 164 (1995)
[51] Hambly, N.C., MacGillivray, H.T., Read M.A., et al. 2001a, MNRAS, 326, 1279
[52] Holberg, J.B, Oswalt, T.D., Sion, E.M., ApJ, 571, 512-518 (2002)
[53] Horne, K, private communication (2005)
[54] Jaroszynski M. et al., Acta Astronomica, 54, 103, (2004)
[55] Kennelly, E.J, ASPC,76, 568 (1995)
[56] Kubas D., PhD Thesis, University of Potsdam (2005)
[57] Kubas D., A. Cassan, J.P. Beaulieu, C. Coutures, M. Dominik, M.D. Albrow, S. Brillant, J.A.R. Caldwell, D. Dominis, J. Donatowicz, P. Fouque, U.G. Jorgensen, J. Greenhill, K. Hill, K. Horne, S. Kane, J.B. Marquette, R. Martin, J. Menzies, K.R. Pollard, K.C. Sahu, C. Vinter,J. Wambsganss, R. Watson, A. Williams (The PLANET Collaboration), C. Fendt, J. Heinmueller, C. Thurl, A&A, 435 (2005)

[58] Lang, M. J., Irish Astronomical Journal, 1995, 22(2), 167 (1995)
[59] Lazio, T. J., PASP,109,1068 (1997)
[60] Launhardt, R., private communication (2006)
[61] Launhardt, R., slides from the lecture at the AIP (2005)
[62] Leinert C., Zinnecker H., Weitzel N., Christou J., Ridgway S.T., Jameson R., Haas M., Lenzen R., A&A, 278, 129 (1993)
[63] Leinert et al., A&A, 367,183 (2001)
[64] Mao, S., Paczynski, B., ApJ, 374, L3 (1991)
[65] Marcy, G.W.; Fischer, D.A.; McCarthy, C.; Ford, E.B., PASP Conference series, 338, 191 (2005)
[66] Mayor, M. Queloz, D., Nature 378, 355-359. (1995)
[67] Mayor, M., Udry, S., Naef, D., Pepe, F., Queloz, D., Santos, N.C., Burnet, M., AAP, 415, 391(2004)
[68] Mazeh T., Simon M., Prato L., Markus B., Zucker S, ApJ, 599,1344 (2003)
[69] Metcalfe, T.S., AJ, 117, 2503 (1999)
[70] Muraki, Y., Prog. Theor. Phys. Supp. 133, 233-246 (1999)
[71] Mugrauer, M., Neuhauser, R.2005, MNRAS, L50 (2005a)
[72] Neuhauser, R, Guenther, E.W, G. Wuchterl; M. Mugrauer; A. Bedalov; P.H. Hauschildt (2005)."Evidence for a co-moving sub-stellar companion of GQ Lup". A&A, 435, L13
[73] Oswalt, T.D., Strunk, D., American Astronomical Society, 184th AAS Meeting, Bulletin of the American Astronomical Society, 26, 901 (1994)
[74] Paczynski B., ApJ, 304, 1 (1986)
[75] Paczynski B., Ann. Rev. Astron. Astrophys. 34, 419 (1996)
[76] Paresce et al., Interferometry for Optical Astronomy II. Edited by Wesley A. Traub. Proceedings of the SPIE, 4838, 486 (2003)
[77] Pietrinferni A., Cassisi S., Salaris M. and Castelli F., ApJ, 612, 168 (2004)
[78] Pietrinferni A., Cassisi S., Salaris M. and Castelli F., ApJ, 642, 797 (2006)
[79] Press W.H., Teukolsky S.A., Vetterling W.T., Flanery B.P., Numerical recipes (Cambridge: University Press), (1992)
[80] Schneider P., Weiss A., A&A, 164, 273 (1986)
[81] Silvestri, N.M., Oswalt, AJ, T.D., 124, 1118-1126 (2002)
[82] Udalski A., Szymanski M., Kaluzny J., Kubiak M., and Mateo M., Acta Astron. , 42, 253 (2002)
[83] Udalski, A.; Szymanski, M.; Kaluzny, J.; Kubiak, M.; Krzeminski, W.; Mateo, M.; Preston, G. W.; Paczynski, B., Acta Astronomica, 43(3), 289 (1993)
[84] Udalski A., Szymanski M., Mao, S., ApJL, 436, L103. (1994)
[85] Udalski, A.; Szymanski, M.; Mao, S.; Di Stefano, R.; Kaluzny, J.; Kubiak, M.; Mateo, M.; Krzeminski, W., ApJ, 2 , 436, 2, L103 (1994)
[86] Udalski A., Acta Astronomica, 53, 291 (2003)
[87] Udalski, A.; Jaroszynski, M.; Paczynski, B.; Kubiak, M.; Szymanski, M. K.; Soszynski, I.; Pietrzynski, G.; Ulaczyk, K.; Szewczyk, O.; Wyrzykowski,; Christie, G. W.; DePoy, D. L.; Dong, S.; Gal-Yam, A.; Gaudi, B. S.; Gould, A.; Han, C.; Lépine, S.; McCormick, J.; Park, B.-G.; Pogge, R. W.; Bennett, D. P.; Bond, I. A.; Muraki, Y.; Tristram, P. J.; Yock, P. C. M.; Beaulieu, J.-P.; Bramich, D. M.; Dieters, S. W.; Greenhill, J.; Hill, K.; Horne, K.; Kubas, D., A Jovian-Mass Planet in Microlensing Event OGLE-2005-BLG-071, ApJ...628L, 109 (2005)
[88] Wahde, M., A&ASS, 132, 417, (1998)
[89] Wambsganss J., Ph.D. Thesis, Munich University, (1990)
[90] Wambsganss J., MNRAS, 284, 172 (1997)
[91] Wambsganss, J. Living Reviews in Relativity 1, 1-80 (1998)
[92] Wambsganss J., Journal of Computational and Applied Mathematics, 109, 353-372 (1999)
[93] Wilson, M.J, Master Thesis, Universtity of Iowa (2003)
[94] Yock, P. Pub. Aston. Soc. Aust. 104, 35-44 (2000)
[95] Zinnecker, H., Bioastronomy 2002, Proceeding IAU Symposium 213, 45 (2003)

[96] Zinnecker, H.; Köhler, R.; Jahreiß, H., The Environment and Evolution of Double and Multiple Stars, Proceedings of IAU Colloquium 191, Edited by Christine Allen & Colin Scarfe. Revista Mexicana de Astronomía y Astrofísica (Serie de Conferencias) 21, 33-36 (2004)

[97] Zoccali, M., A. Renzini, S. Ortolani, L. Greggio, I. Saviane, S. Cassisi, M. Rejkuba, B. Barbuy, R. M. Rich and E. Bica, A&A 399, 931-956 (2003)